UC Irvine
UC Irvine Electronic Theses and Dissertations

Title
The Kinetics of Reactions of Criegee Intermediates with Functionalized Ketones

Permalink
https://escholarship.org/uc/item/3d92w18s

Author
Cornwell, Zachary Albert

Publication Date
2024

Peer reviewed|Thesis/dissertation

eScholarship.org Powered by the California Digital Library
University of California

UNIVERSITY OF CALIFORNIA,

IRVINE

The Kinetics of Reactions of Criegee Intermediates with Functionalized Ketones

DISSERTATION

Submitted in partial satisfaction of the requirements

for the degree of

DOCTOR OF PHILOSOPHY

in Chemistry

By

Zachary A. Cornwell

Dissertation Committee:
Professor Craig Murray, Chair
Professor Sergey Nizkorodov
Professor James Smith

2024

Chapter 2 © 2021 American Chemical Society

Chapter 3 © 2023 Wiley Periodicals LLC

Chapter 4 © 2024 American Chemical Society

All other materials © Zachary A. Cornwell

DEDICATION

To

my friends and family

who supported me along the way

and to my papa

apologies for not finishing my thesis in time

As our "clothes stay impregnated with strong and characteristic odours;
we follow the initiates of Hermes by their scent. In such an environment,
how is it possible not to be productive?"

—Victor Grignard

TABLE OF CONTENTS

LIST OF FIGURES vi

LIST OF TABLES xi

ACKNOWLEDGMENTS xiii

VITA xv

ABSTRACT OF THE DISSERTATION xix

1 INTRODUCTION 1

1.1 ATMOSPHERIC OZONE 1

1.2 ALKENE OZONOLYSIS 2

1.3 LABORATORY PRODUCTION AND DETECTION 4

1.3.1 Electronic Structure 5

1.3.2 Electronic spectroscopy (UV-Vis) 7

1.3.3 Rovibrational Spectroscopy (IR) 9

1.3.4 Rotational Spectroscopy (Microwave) 10

1.4 REACTION KINETICS 11

1.4.1 Unimolecular Decomposition 11

1.4.2 1,2-Addition Reactions 12

1.4.3 1,4-Addition Reactions 14

1.4.4 Cycloaddition Reactions 16

1.5 RESEARCH GOALS 17

2 KINETICS OF THE REACTIONS OF CH_2OO WITH ACETONE, A-DIKETONES, AND B-DIKETONES 19

2.1 ABSTRACT 20

2.2 INTRODUCTION 21

2.3 EXPERIMENTAL AND COMPUTATIONAL METHODS 25

2.4 RESULTS 27
2.4.1 Reactant absorption spectroscopy and calibration *27*
2.4.2 Transient absorption spectroscopy *31*
2.4.3 Modeling and systematic uncertainties in k_{loss} *38*
2.4.4 Computational results *42*
2.5 DISCUSSION 50
2.5.1 Systematic uncertainties in k_{loss} *50*
2.5.2 Previous measurements *51*
2.5.3 Mechanism and reactivity trends *52*
2.5.4 Atmospheric implications *57*
2.6 CONCLUSIONS 58
3 TEMPERATURE-DEPENDENT KINETICS OF THE REACTIONS OF CH_2OO WITH ACETONE, BIACETYL, AND ACETYLACETONE 60
3.1 ABSTRACT 61
3.2 INTRODUCTION 62
3.3 EXPERIMENTAL AND THEORETICAL METHODS 65
3.4 RESULTS 68
3.4.1 Experimental kinetics measurements *68*
3.4.2 Computational Results *75*
3.5 DISCUSSION 80
3.6 CONCLUSIONS 86
4 TEMPERATURE-DEPENDENT KINETICS OF THE REACTIONS OF THE CRIEGEE INTERMEDIATE CH_2OO WITH HYDROXYKETONES 87
4.1 ABSTRACT 88
4.2 INTRODUCTION 89
4.3 METHODS 91
4.4 RESULTS 93

4.4.1 Reactant Concentration Measurements *93*

4.4.2 Kinetics Measurements *98*

4.4.3 Computational Results *103*

4.5 DISCUSSION 108

4.6 ATMOSPHERIC IMPLICATIONS 114

4.7 CONCLUSIONS 115

5 STRUCTURE ACTIVITY RELATIONSHIPS FOR CYCLOADDITION REACTIONS WITH CRIEGEE INTERMEDIATES: A COMPUTATIONAL STUDY 117

5.1 ABSTRACT 118

5.2 INTRODUCTION 119

5.3 METHODS 123

5.4 RESULTS AND DISCUSSION 124

5.4.1 Standard Transition State Theory (TST) *124*

5.4.2 FMO Theory: Carbonyl Substituents R_1 & R_2 ..... *126*

5.4.3 Hammett Parameters: Carbonyl Substituents R_1 & R_2 ..... *130*

5.4.4 FMO Theory: Criegee Substituents R_1 & R_2 ..... *131*

5.5 CONCLUSION 136

6 DISSERTATION SUMMARY 137

7 REFERENCES 140

LIST OF FIGURES

Figure 1.1 UV-Vis absorption spectra of CH_2OO. Sheps (red) and Beames (black) were scaled to the spectrum of Ting et al. (blue). The more recently measured spectra by Foreman and Mir are shown in grey and green respectively. 7

Figure 1.2 Absolute UV-Vis absorption spectra of several different CIs: CH_2OO (blue)[51], CH_3CHOO (green)[59], $(CH_3)_2COO$ (black)[54], MVKO (yellow)[58], and MACRO (red)[58]. 9

Figure 2.1 Acetone (2-propanone, Ac), the α-diketones acetylpropionyl (2,3-pentanedione, AcPr) and biacetyl (2,3-butanedione, BiAc); and the β-diketones acetylacetone (2,4-pentanedione, AcAc) and 3,3-dimethyl-2,4-pentanedione (dMAcAc). The enolone and diketone tautomers of AcAc are both shown but the former is predominant in the gas phase. 24

Figure 2.2 Gas phase absorption spectra at 295 K of acetone, BiAc, AcPr, AcAc, and dMAcAc. The AcAc absorption cross section values have been reduced by a factor of fifty; the dashed line is the measurement of Messaadia *et al.*,[46] which captures the peak absorption. Shaded areas are 1σ uncertainties from repeated measurements. 28

Figure 2.3 (a) Typical experimental absorbances (black) due to BiAc measured using the same selection of choked-flow orifice as in the kinetics experiments. Best-fit scaled BiAc absorption spectra are also shown (purple). (b) Calibration plot of measured concentrations, $[BiAc]_{exp}$, determined from the spectra plotted against estimated concentrations, $[BiAc]_{est}$. The gradient, $[BiAc]_{exp}/[BiAc]_{est}$ <1, indicates that reactant concentrations are slightly over-estimated. The shaded area is a 2σ prediction band. 29

Figure 2.4 Broadband transient absorption spectra, recorded over the range 365–390 nm at the indicated time delays after photolysis (a) in the absence of any reactant and (b) in the presence of $[Ac]_{exp} = 2.47\times10^{16}$ cm^{-3}. (c): Time-dependent concentration profiles for CH_2OO and IO (inset) derived from the transient absorption spectra. 32

Figure 2.5 Observed pseudo-first order loss rates (symbols), and linear (solid line) and quadratic fits (dashed line) for the reaction of CH_2OO with Ac at 295 K and 67 Torr. The shaded areas represent 2σ prediction bands. 35

Figure 2.6 Observed pseudo-first order loss rates (symbols) and fits (lines) for the reaction of CH_2OO with BiAc (circle, purple), AcPr (square, blue), AcAc (triangle, green) and dMAcAc (diamond, yellow) at 295 K and 67 Torr. The shaded areas represent 2σ prediction bands. 37

Figure 2.7 Simulated $[CH_2OO]_t$ and $[IO]_t$ profiles at various concentrations of BiAc and Ac. In panel (a) [BiAc] / 10^{15} cm^{-3} = 0 (solid), 0.4 (dotted), 0.8 (short dash), 1.6, long dash), 3.2 (dash-dot). In panel (b) [Ac] / 10^{16} cm^{-3} = 0 (solid), 0.5 (dotted), 1.0 (short dash), 2.0, long dash), 4.0 (dash-dot). Average experimental profiles in the absence of BiAc and Ac are shown as blue and red lines respectively, with 1σ uncertainties shaded. Inset: pseudo-first order loss rates plotted as a function of the reactant determined from analysis of simulated $[CH_2OO]_t$ profiles. Linear fit is shown with shaded area representing 2σ prediction band. 40

Figure 2.8 Stationary points on the potential energy surfaces for reactions of CH_2OO with representative carbonyls acetone (Ac), biacetyl (BiAc) and both diketone and enolone tautomers of acetylacetone (AcAc). Energies of reactants (R), entrance channel van der Waals complex (vdW), cycloaddition transition state (TS_{SOZ}), and secondary ozonide products (SOZ) are shown for each reaction. Energies were calculated at the CBS-QB3 level of theory (see Table 2.3) as described in the text. Free energies (ΔG; 298 K) and zero-point corrected electronic energies (ΔE + ZPE; 0 K) are shown in red and black, respectively. 42

Figure 2.9 Schematic molecular orbital diagram, for the 1,3-dipolar cycloaddition reaction between CH_2OO and HCHO. Relative orbital energies are based on M06-2X/aug-cc-VTZ calculations. The "antisymmetric" combination (gray) has a large energy gap ΔE_A and gives rise to the Ψ_1, Ψ_3 bonding and anti-bonding molecular orbitals. The "symmetric" combination (black) has a smaller energy gap ΔE_S and gives rise to the Ψ_2, Ψ_4 pair. Red arrows: effect of electron-donating substituents; blue arrows: effect of electron-withdrawing substituents 47

Figure 2.10 Pressure dependence of rate constants for the CH_2OO + acetone reaction. Previous results from Taatjes *et al*. [T_P12],[4] Berndt *et al*. [B_O15],[5] and Elsamra *et al*. [EJBMG16J[6] are compared to the current results [CHM21]. A linear fit to the data of Elsamra *et al*. is shown in red, with the shaded area representing a 1σ prediction band. 52

Figure 2.11 Inverse correlation between ln k and the energy gap between the carbonyl π* orbital (LUMO) and the n_0 orbital (HOMO) of CH_2OO. Orbital energies were calculated at the M06-2X/aVTZ level. Filled circles are measurements from this work, open circles are results of previous work. A linear fit with 2σ prediction band is shown (R^2 = 0.83). Reactions indicated in the dashed box were not included in the fit. 54

Figure 2.12 Plot showing correlation between observed rate constants and the sum of the *para* position Hammett constants, σ_p, for each substituent on the carbonyl. Closed circles are from this work, open circles are results of previous work. A linear fit with 2σ prediction band is shown (R^2 = 0.93). 57

Figure 3.1 Laser fluence dependence of $[CH_2OO]_t$ at 335 K to show increasing $[CH_2OO]_0$ and increasing curvature at 15 mJ (light gray circles), 20 mJ (gray squares), and 25 mJ (black triangles). Fits to determine k_{loss} and k_{self} are also shown, with shading representing 1σ prediction bands. Data and fits are sequentially offset horizontally for clarity (+250 μs), indicated by the horizontal arrows 69

Figure 3.2 Complete data set of pseudo-first order kinetics for the CH_2OO + X reactions over the experimental temperature range, 275 K (circles), 295 K (squares), 315 (triangles), and 335 K (stars). X = (a) Ac (black), (b) BiAc (red), and (c) AcAc (blue).Solid lines are linear fits with shaded areas representing 1σ prediction bands. 70

Figure 3.3 Pseudo-1st order plots of observed k_{loss} against reactant concentration at (a) 335 K and (b) 275 K for the reactions of CH_2OO with Ac (black), BiAc (red), and AcAc (blue). 71

Figure 3.4 Arrhenius plots for the reactions of CH_2OO with (a) Ac (black circles), (b) BiAc (red squares), and (c) AcAc (blue triangles) over the temperature range 275–335 K. Shaded areas represent 1σ prediction bands for the linear fits. Fit parameters are summarized in Table 3.3. 73

Figure 3.5 Left: Observed CH_2OO loss rates for the reactions with Ac, BiAc, and AcAc at 295 K over the total pressure range 50–100 Torr. Reactant concentrations: [Ac] = 8.60×10^{15} cm^{-3}, [BiAc] = 9.36×10^{14} cm^{-3}, [AcAc] = 4.33×10^{15} cm^{-3}. Horizontal lines are average values of $\langle k_{loss}\rangle$ across the pressure range, with shaded areas representing the 1σ standard deviation. Right: Observed background loss rates in the absence of reactant. Horizontal lines are average values of $\langle k_{loss}\rangle$ across the pressure range, with shaded areas representing the 1σ standard deviation. 75

Figure 3.6 Stationary point (a) energies at 0 K (ΔE+ZPE, solid lines) and (b) free energies at 298 K ($\Delta G°$, dotted lines) cycloaddition reactions of CH_2OO with acetone (Ac, black), biacetyl (BiAc, red), and the enol tautomer of acetylacetone (AcAc, blue) to form a secondary ozonide (SOZ). 76

Figure 3.7 Transition state structures for reactions of the enolone tautomer of AcAc. (a) Cycloaddition at the C=C bond with O atom attack at the β-C atom; (b) cycloaddition at the C=C bond with O atom attack at the α-C atom; (c) 1,2-addition at the OH group; and (d) cycloaddition via a seven-membered cyclic adduct involving the carbonyl O atom and β-C atom. 78

Figure 3.8 Plots of k_X against T for the reactions of CH_2OO with (a) Ac (black circles), (b) BiAc (red squares), and (c) AcAc (blue triangles). The solid lines are fits to Equation E 3.5 (see text), used to extract thermodynamic parameters for the rate-limiting TS. Shaded areas represent 1σ prediction bands. Previous high-P limit measurements in this temperature range from Berndt et al.[22] (B15, gray circle with dot), Chhantyal-Pun et al.[25] (CP19, gray circle with plus), Cornwell et al.[26] (C21, gray circle with cross) are also shown. 83

Figure 3.9 Temperature dependence of the ratio of Ac (black) and BiAc (red) loss rates due to reaction with CH_2OO and OH. Calculated ratios based on estimated approximate daytime (dashed lines) and nighttime (solid lines) concentrations of CH_2OO and OH are shown. 85

Figure 4.1 Headspace FT-IR spectra of AcOH (red) and 4H2B (blue). Also shown is the AcOH spectrum (black) obtained from the PNNL IR spectral database.[1] 93

Figure 4.2 UV absorption spectra of AcOH (red) and 4H2B (blue). The shaded area indicates the wavelength range covered by the 280 nm LED used for concentration measurements. Solar flux (black) is also shown. 95

Figure 4.3 Calibration plots of experimental versus estimated concentrations of (a) AcOH on the left and (b) 4H2B on the right in the range 275–335 K, blue to red respectively. 96

Figure 4.4 Scale factors determined from gradient of $[X]_{exp}$ versus $[X]_{est}$ calibration plots as a function of temperature. Solid lines are the T-independent average, while shaded areas represent the estimated experimental uncertainty, based on the variability of the measurements. Values >1 or <1 indicate that reactant concentration is underestimated (AcOH) or overestimated (4H2B), respectively. 97

Figure 4.5 Broadband transient absorption spectra recorded at various time delays after photolysis at 295 K. (a) Spectra recorded in the absence of any additional reactive species, (b) spectra recorded with [AcOH = 5.1×10^{15} cm^{-3}. (c) [CH_2OO] time profiles resulting from fitting the experimental transient spectra. 98

Figure 4.6 Pseudo-1st order plots for the reactions of CH_2OO with (a) AcOH and (b) 4H2B across the experimental temperature range 275–335 K, blue to red respectively. Vertical and horizontal error bars represent statistical uncertainties (1σ) in the loss rates determined from fitting [CH_2OO] time profiles and uncertainties in the hydroxyketone concentration calibration measurements, respectively. Weighted linear fits to the experimental data are also shown, with shaded area representing 1σ prediction bands. 100

Figure 4.7 Arrhenius plots for the reaction of CH_2OO with AcOH (red) and 4H2B (blue), with 1σ statistical uncertainties. The AcOH data has been offset vertically for clarity. Solid black lines are linear fits with shaded areas representing 1σ prediction bands. 102

Figure 4.8 Pressure dependence of CH_2OO loss rates in the presence of AcOH (red, [AcOH] = $(5.1\pm0.3)\times10^{15}$ cm^{-3}) and 4H2B (blue, [4H2B] = $(8.0\pm1.1)\times10^{14}$ cm^{-3}) at 295 K. Total pressure was varied by changing only the flow rate of the N_2 buffer, with all other gas flows held constant. The solid lines indicate the average loss rates determined from the kinetics measurements. Shaded areas represent 1σ uncertainties. 103

Figure 4.9 Low-energy conformers of AcOH (left) and 4H2B (right), calculated at the B3LYP/cc-pVDZ level. The zero-point corrected energy (kcal mol^{-1}) of each conformer relative to the most stable cyclic H-bonded structures is indicated. 105

Figure 4.10 CBS-QB3 energy and free energy profiles for the CH_2OO + AcOH (red) and 4H2B (blue). Panel (a) shows Δ(E+ZPE) at 0 K and panel (b) shows ΔG at 298 K for both reactions. Solid lines connect stationary points for cycloaddition A, dotted lines for cycloaddition B, and dashed lines for 1,2-addition at the OH group. The inset shows a magnified view of the entrance channel van der Waals complex (vdW) and the transition state (TS) for the cycloaddition pathways. 106

Figure 4.11 Optimized transition state geometries for the 1,3-dipolar cycloaddition reactions of CH_2OO with AcOH (a, b) and 4H2B (c, d). The orientation of the central O atom of CH_2OO oriented towards (a,c) or away (b,d) from the hydroxyl group of the hydroxyketone identifies cycloaddition A or B, respectively. Red arrows indicate displacement vectors along the reaction coordinate. 107

Figure 4.12 Frontier orbital energies calculated at B3LYP/cc-pVDZ level for CH_2OO and the carbonyls formaldehyde, acetone, and the hydroxyketones AcOH and 4H2B. Red: S orbitals (non-bonding n(p_C–p_O) for CH_2OO, π* LUMO for carbonyls), black: A orbitals (π bonding orbitals of carbonyls, π* antibonding for CH_2OO), gray: non-bonding (n_O orbitals). 108

Figure 4.13 Inverse correlation between reported experimental rate constants at room temperature for the reactions of CH_2OO with a series of carbonyl compounds and the energy gap $|\Delta E_S|$ between the π^* orbital of the carbonyl and the n(p_C–p_O) orbital of CH_2OO. Orbital energies were calculated at the B3LYP/cc-pVDZ level. A linear fit is shown, where the shaded area represents 1σ prediction bands. Experimental rate constants are drawn from various sources – see text for details. Reactions involving α,β-unsaturated carbonyls (gray) were excluded from the fit. 112

Figure 5.1 Molecular orbital diagram for the cycloaddition reaction between CH_2OO (left) and formaldehyde (right). The "symmetric" orbitals interact to form the molecular orbitals (S, S*) in the black trace, and the "antisymmetric" orbitals form the molecular orbitals (A, A*) in the grey trace. The effect of EDGs in red and EWGs in blue are shown by the corresponding arrows on the carbonyl π and π^* orbital energies. 120

Figure 5.2 Panel (a) MO diagram for the cycloaddition reaction between CH_2OO and the seven carbonyls listed in Table 5.3. The A and S energy gaps between the orbitals are shown in panel (b) (red or black) with the same common bottom axis. 128

Figure 5.3 The energies of the carbonyl π^* (a) and π (b) orbitals plotted against the experimental rate constants for the bimolecular cycloaddition reaction of the specified carbonyls with CH_2OO..... 129

Figure 5.4 The carbonyl π^* orbital energies are plotted as a function of Hammett parameters. Panel (a) and (b) show the relationship based on the *para-* (σ_p) and *meta-* (σ_m) substituted positions on benzoic acid. The substituents (R_1, R_2) that correspond to the summed σ_p and σ_m values are indicated with text adjacent to the points on the plot..... 130

Figure 5.5 Molecular orbital diagram for the cycloaddition reaction between CH_2OO (left) and sulfur dioxide (right). The "symmetric" orbitals interact to form the molecular orbitals (S_1, S_2) in the black trace, and the "antisymmetric" orbitals form the molecular orbitals (A_1, A_2) in the grey trace. The effect of EDGs in red and EWGs in blue are shown by the corresponding arrows on the carbonyl π and π^* orbital energies..... 132

Figure 5.6 The log of the rate constant of the CIs for the reaction with SO_2 plotted as a function of the $n_{pc\text{-}po}$ orbital energies. The reported experimental values are shown in black, and the *syn-* conformer of CH_3CHOO was masked from the fit. $ClCHOO$ (red) and CH_3OCHOO (purple) are shown with the corresponding arrows to indicate where they would end up on the trend. 135

LIST OF TABLES

Table 1.1 Several different CIs produced in the presence of oxygen, with their corresponding photolytic precursors. 6

Table 1.2 Compiled rate constants of CH_2OO with different carbonyl compounds and the substituents separated as R_1 and R_2. This is a summarized version of Table 4.4, where the references are shown along with the corresponding rate constants. For simplicity, only the weighted means are shown here. 18

Table 2.1 Reactant vapor pressures ($P_{vap,X}$), bimolecular rate constants derived using experimental ($k_{X,exp}$) reactant number densities, and ratio of experimentally measured reactant concentrations to those estimated ($[X]_{exp}/[X]_{est}$). The asterisk on the value of $P_{vap,BiAc}$ indicates that the liquid sample was held at 273 K rather than 295 K. All reported rate constants were derived from the *overall* fits of the experimental data (see text). Uncertainties are 1σ. 30

Table 2.2 Mechanism and reaction rate constants used to simulate $CH_2I + O_2$ reaction from Ting *et al*. following the photolysis of diiodomethane (R1).[164] 41

Table 2.3 Relative energies (ΔE+ZPE at 0 K), including zero-point contributions, and free energies (ΔG at 298 K), evaluated using RRHO partition functions, calculated at the M06-2X/aug-cc-pVTZ and CBS-QB3 levels for the SOZ pathway (see Figure 2.8) for reactions of CH_2OO with acetone (Ac), biacetyl (BiAc), and the enolone and diketone tautomers of acetylacetone (AcAc). All energies are reported in kcal mol^{-1}. 44

Table 2.4 Rate constants at 298 K calculated using the two-step model (E 2.8 – E 2.9) and the values of ΔG at the M06-2X/aug-cc-pVTZ and CBS-QB3 levels of theory (see Table 2.3). 46

Table 2.5 Frontier orbital energies calculated at the M06-2X/aVTZ level. 49

Table 2.6 Hammett substituent constants for carbonyl compounds. Data taken from Table 1 of Hansch *et al*.[7] 56

Table 3.1 Compiled rate constants for CH_2OO + acetone reaction at or near room temperature. Uncertainties are 1σ. 62

Table 3.2 Temperature-dependent bimolecular rate constants ($\times 10^{-13}$ cm^3 s^{-1}) for the reactions of CH_2OO with Ac, BiAc, and AcAc at 80 Torr. Reported errors are 1σ based on estimated 8% uncertainties in the reactant concentration and statistical uncertainties from the fits. 72

Table 3.3 Arrhenius and thermodynamic parameters for rate-limiting TS. 74

Table 3.4 Relative energies (ΔE+ZPE at 0 K), including zero-point contributions, and free energies ($\Delta G°$ at 298 K), calculated at the CBS-QB3 levels for the SOZ pathway (see Figure 3.6) for reactions of CH_2OO with acetone (Ac), biacetyl (BiAc), and the enolone tautomer of acetylacetone (AcAc). All energies are reported in kcal mol^{-1}. 77

Table 3.5 Relative energies (ΔE+ZPE at 0 K), including zero-point contributions, and free energies ($\Delta G°$ at 298 K) calculated at the CBS-QB3 levels for all reaction pathways for the enolone tautomer of acetylacetone (AcAc). TS energies are for the inner transition states (see Figure 3.7). All energies are reported in kcal mol^{-1}. 79

Table 4.1 *T*-dependent bimolecular rate constants, Arrhenius parameters, and standard enthalpies, entropies, and Gibbs energies of activation at 298 K for the reactions of CH_2OO with hydroxyacetone and 4H2B. Uncertainties are 1σ statistical uncertainties from the fits. 101

Table 4.2 CBS-QB3 thermochemistry for the reactions of CH_2OO with AcOH and 4H2B: ΔE+ZPE @ 0K ($\Delta H°$ @298 K) [$\Delta G°$@ 298 K] in kcal mol^{-1}. 104

Table 4.3 B3LYP/cc-pVDZ calculated orbital energies (eV) of HCHO, AcOH, 4H2B, and Ac. CH_2OO π* E = –2.422 eV, n(pC–pO) E = –6.694 eV. $|\Delta E_A|$ is the magnitude of the energy difference between the occupied π orbital of CH_2OO and unoccupied π*of the carbonyl (dominant). $|\Delta E_S|$ is the magnitude of the difference between the unoccupied π* orbital of CH_2OO and the occupied π orbital of the carbonyl. The $|\Delta E_A|$ interaction is always smaller. 111

Table 4.4 Experimental rate constants for CH_2OO + R_1R_2CO reactions at room temperature. 116

Table 5.1 Hammett parameters for a range of different substituents that are EDGs or EWGs, represented as the *para*- (σ_p) and *meta*- (σ_m) substituted coefficients. 122

Table 5.2 Calculated zero point corrected total energies and free energies of activation (kcal mol^{-1})from the B3LYP/ aug-cc-pVDZ level of theory. The bimolecular rate constants were calculated using equation E 5.1 to compare to the experimentally measured values (~298 K) shown on the right side. 125

Table 5.3 Calculated orbital energies of different carbonyls in eV. The experimental rate constants are also included for the carbonyls that have reported kinetic data at room temperature. Where there were multiple reports, the average of the rate constants was taken. 127

Table 5.4 Compiled orbital energies of different CIs in eV. The experimental rate constants are also included for the CIs that have reported kinetic data at room temperature with SO_2. 134

ACKNOWLEDGMENTS

I owe a great deal of thanks to the people that have helped and supported me over the past five years.

My family for all the love and support they have given me; I wouldn't be where I am in my career without them. Mom, there are no words to accurately convey how lucky I am to be your son.

My advisor, Professor Craig Murray, for hiring me initially as a staff researcher and then taking me on as your graduate student. Your patience and passion for educating me in all aspects of being a doctoral chemistry student has not gone unnoticed. The vast expertise and knowledge you shared with me on a daily basis is something that I will benefit from for the rest of my life. Thank you for always being there for me and advocating for my success.

Marcus, Johanna, and Jonas, for letting me talk my head off and interrupt your day so I could process my thoughts and concerns about work. We have had so many laughs and fun times in and out of the lab, I never expected to make such good friends out of coworkers.

The rest of the Chemistry department and faculty for being so approachable and friendly. During my time at UC Irvine, I have forged professional relationships with some of the smartest and most talented scientists in the world.

And last but certainly not least, my beautiful and amazing wife, Ning. Thank you for listening to me vent about work and being so supportive. We became partners, we became best friends, and then we became parents to our dog, Albie. You are my anchor and I look forward to spending the rest of my life with you. I love you.

I thank American Chemical Society (ACS) Publications for permission to include the copyrighted material in Chapter Two and Four as part of my dissertation, which was published in the Journal of Physical Chemistry A. I also thank John Wiley and Sons for the permission to include the material in Chapter Three from my publication in the International Journal of Chemical Kinetics. This work was financially supported by the National Science Foundation under Grant No. ECS-1905364.

Zachary A. Cornwell

Education

Doctor of Philosophy (PhD), Physical Chemistry — 2019 – 2024
University of California, Irvine

Bachelor of Science, Chemistry — 2013 – 2016
University of California, Los Angeles

Patents

- Inventor on International Patent No. 11,534,642 — 2022

Publications

- Harrison A.W.; Ferris B.; Cornwell, Z.A.; J.J. Enders; Murray, C. Hammett Analysis and Energy Correlations of 1,3-Dipolar Cycloaddition Reactions between CH_2OO and Carbonyls: Semi-Empirical Approaches for Estimating Rate Constants (manuscript pending) — 2024
- Enders, J.J.; Cornwell, Z.A.; Harrison, A.W.; Murray, C. Temperature-Dependent Kinetics of the Reactions of CH_2OO with Aldehydes, *J. Phys. Chem. A* (manuscript pending) — 2024
- Cornwell, Z.A.; Enders, J.J.; Harrison, A.W.; Murray, C. Temperature-Dependent Kinetics of the Reactions of Criegee Intermediate CH_2OO with Hydroxyketones, *J. Phys. Chem. A* (doi.org/10.1021/acs.jpca.4c00156) — Mar. 2024
- Cornwell, Z.A.; Enders, J.J.; Harrison, A.W.; Murray, C. Temperature-Dependent Kinetics of the Reactions of CH_2OO with Acetone, Biacetyl, and Acetylacetone, *Int. J. Chem. Kin.* (doi.org/10.1002/kin.21625) — Dec. 2022
- Cornwell, Z.A.; Harrison, A.W.; Murray, C. Kinetics of the Reactions between Criegee Intermediates and Bicarbonyls, *J. Phys. Chem. A* (doi.org/10.1021/acs.jpca.1c05280) — Sept. 2021

Research Experience

Graduate: Physical Chemistry — 2019 – 2024
Department of Chemistry, University of California Irvine
Advisor: Prof. Craig Murray

- Led projects using laser flash photolysis transient absorption spectroscopy to measure the kinetics of Criegee intermediates (CIs) with functionalized ketones and other significant reacting partners.
- Designed and incorporated a custom glass-jacketed flow cell apparatus into a free-space optics setup for temperature dependent kinetics experiments.
- Developed methods and fine-tuned an optical system for the photolysis of diiodomethane to produce and monitor CI concentrations.
- Performed ab-initio calculations to characterize the potential energy surfaces of cycloaddition reactions between CIs and several types of compounds.
- Identified a structure-activity relationship between frontier molecular orbital energies and experimental rate constants for the reaction between CIs and carbonyls.

Undergraduate: Synthetic/Organometallic Chemistry 2014 – 2016

Department of Chemistry, University of California Los Angeles

Advisor: Prof. Craig A. Merlic

- Synthesized 10-membered enyne carbocycles via ring-closing metathesis required for the development of a dicobalt hexacarbonyl-mediated transannular Pauson-Khand reaction.
- Screened several copper-mediated oxidative coupling reactions with cyclonona-1,2-diene and 3-hexyne to test a novel ligand effect.
- Optimized bromination and chlorination reactions of aryl boronate esters and boronic acids in copper(II)-mediated oxidative coupling reactions.
- Organized a set of alternative strained allenes as comparable pi-ligands to cyclonona-1,2-diene.

Work Experience

Head Chemist 2018 – 2019

Extreme Fire Solutions, Garden Grove, CA

- Appointed as the sole inventor on an international patent for over sixty different formulations of a nontoxic wetting agent that is UL certified and extinguishes class A and B fires competitively.
- Ordered and inventoried all pertinent equipment to perform several tests, from aqueous solubility and miscibility to fire application testing (*Fire Types A-K*).
- Designed a project to test formulations for several factors: readily water soluble at low temperatures, effervescence and fire repression, and unique formulative utility towards different types of fires.

Analytical Chemist 2017 – 2018

Versum Materials, Carlsbad, CA

- Analyzed the quantitative and qualitative aspects of the composition, structure, and purity for numerous organosilanes, organometallic compounds, and inorganic complexes.
- Coordinated the development of analytical methods and procedures, handling and preparing of samples in a glove-box, supply ordering, and routine maintenance of instruments.

QC/QA Chemist 2016 – 2017

3M Pharmaceuticals, Northridge, CA

- Promoted and adhered to cGMP's and cGLP's in a pharmaceutical setting.
- Performed chemical assays related to drug delivery, active drug identification, particle size measurements, content, and purity on various pharmaceutical aerosol products.
- Prepared buffers and elution solvent mixtures in large scale for reverse phase HPLC.

Chemistry Tutor 2011 – 2013

OCC Student Success Center, Costa Mesa, CA

- Helped students with homework for general and organic chemistry courses.
- Led review sessions, presenting course material and key topics requested by professors.

Leadership Experience

Research Laboratory Safety Representative — 2020 – 2023

Department of Chemistry, University of California Irvine, Irvine, CA

- Cultivated a safe and comfortable working environment in the research lab.
- Led safety meetings and delegated project related safe practices to be integrated into daily routines.
- Created and modified standard operating procedures (SOPs) for a range of processes, hazards, and relevant chemicals used in the lab.

Supervisor of Undergraduate Research — 2018 – 2020

Department of Chemistry, University of California Irvine, Irvine, CA

- Instructing and monitoring the operation of a flash photolysis/transient absorbance spectroscopy experiment set up.
- Teaching students how to acquire and process kinetic data on softwares such as Labview and Igor Pro.

Presentations

Informal Symposium on Kinetis and Photochemical Processes in the Atmosphere (ISKPPA)

- Temperature-Dependent Kinetics of the Reactions of CH_2OO with — 2023
- Temperature-Dependent Kinetics of the Reactions of CH_2OO with Acetone, Biacetyl, and Acetylacetone — 2022
- Kinetics of the Reactions between Criegee Intermediates and Bicarbonyls — 2021

Honors and Awards

Raymond and Dorothy Wilson Research Fellowship — 2014

Teaching Experience

Chemistry Teaching Assistant (TA) — 2019 – 2024

Department of Chemistry, University of California Irvine, Irvine, CA

Courses

Physical Chemistry Laboratory (Head TA)

Advanced Analytical Chemistry Laboratory

General Chemistry Laboratory

General Chemistry Lecture

Responsibilities

- Delegated grading tasks and assisted professor with cascading information (Head TA)
- Maintain instruments in the lab such as startup/shutdown procedures
- Accompanied students with instrumentation and troubleshooting procedural issues
- Instructed and supervised students on proper laboratory techniques and practices
- Led and promoted discussions on general chemistry concepts

Volunteer Work

Judge: Orange County Science and Engineering Fair (OCSEF) 2020 – 2023
OCSEF Panel (remote)

- Critiqued students on the analytical and conceptual importance of the presented ideas
- Evaluated the relative impact and execution of several science and engineering projects

Chemistry Tutor/Community Service Volunteer 2014 – 2016
Alpha Chi Sigma Professional Chemistry Fraternity
Department of Chemistry, University of California Los Angeles, Los Angeles, CA

- Instructed several subjects that applied to the department's curriculum.
- Organized and led community outreach programs that teach kids more about science.

Teaching Assistant for Undergraduate Chemistry Lab 2013
Department of Chemistry, Orange Coast College, Costa Mesa, CA

- Assisted in teaching techniques for related course content.
- Kept an inventory of the equipment and chemicals being used.

Skills

Instrumentation

- Spectroscopy: Flash Photolysis Transient Absorption, FT-IR, UV-Vis, NMR
- Spectrometry: MS, GC-MS, ICP-MS
- Chromatography: HPLC, GC, IC

Software

- Editing: Microsoft office (Word, Excel, Powerpoint), Adobe (Acrobat, Photoshop, Lightroom), ChemDraw, Solidworks, Blender
- Data Acquistion/Analysis: Labview, Igor Pro, OpenLAB, Chromeleon, Empower 3, Xcalibur, MassHunter, Bruker TopSpin, MestReNova
- Chemical Computation: GAMESS, MOLPRO, NWChem

Manufacturing

- Machinist: Qualified in several machine shop applications including but not limited to: mill, lathe, table saw, band saw, and other instruments related to modifying and fabricating parts for laboratory applications.
- 3D Printing: Design and fabrication with filament-based materials for custom adapters and supports.

Laboratory Techniques

- High proficiency with chemical synthesis and related purification techniques, including flash chromatography, recrystallization, Schlenk line operation, and distillation.

ABSTRACT OF THE DISSERTATION

The Kinetics of Reactions of Criegee Intermediates with Functionalized Ketones

by

Zachary A. Cornwell

Doctor of Philosophy in Chemistry

University of California, Irvine, 2024

Professor Craig Murray, Chair

This thesis is focused on exploring different variables that affect the kinetics of the reactions between CH_2OO and several carbonyls. By using flash photolysis transient absorption spectroscopy and complementary ab-initio calculations, the bimolecular rate constants and thermochemical parameters such as activation energies and the enthalpic barriers for the reactions are discussed.

We initially measured bimolecular rate constants for the reactions of CH_2OO with acetone (Ac), the α-diketones biacetyl (BiAc) and acetylpropionyl (AcPr), and the β-diketones acetylacetone (AcAc) and 3,3,-dimethyl-2,4-pentanedione (dMAcAc) at 295 K. The bimolecular rate constant for the CH_2OO + acetone reaction was measured to be $(4.1\pm0.4)\times10^{-13}$ cm^3 s^{-1}, which is consistent with previous measurements from other groups. The reactions of CH_2OO with AcAc was found to be almost twice as fast as the reaction with dMAcAc, with rate constants of $(6.6\pm0.7)\times10^{-13}$ cm^3 s^{-1} and $(3.5\pm0.8)\times10^{-13}$ cm^3 s^{-1}, respectively. The α-diketones, BiAc and AcPr, reacted significantly faster with rate constants of $(1.45\pm0.18)\times10^{-11}$ cm^3 s^{-1} and $(1.29\pm0.15)\times10^{-11}$ cm^3 s^{-1}. The increased reactivity of the α-diketones was rationalized using concepts from frontier molecular orbital (FMO) theory, where an

inverse relationship between the log of the rate constant and the difference in energy between the interacting orbitals of the CI and carbonyl was found.

With an improved experimental setup and a new glass-jacketed flow cell, we were able to measure the temperature dependence of the reactions between CH_2OO and Ac, BiAc, and AcAc. In the range of 275–335 K, the reactions of the ketones with CH_2OO had different sensitivities to temperature in the following order with listed activation energies: AcAc < BiAc < Ac (E_a /R values of –1830±170 K, –1260±170 K, and –460±180 K, respectively). The different functionalities of the enolone structure of AcAc was also investigated computationally to reveal the cycloaddition reaction at the carbonyl (C=O) and alkene (C=C) site were competitive with nearly identical free energies of activation. The negative temperature dependence for the reaction of Ac and BiAc with CH_2OO suggests that the Criegee intermediate could be a viable atmospheric sink for some carbonyls at night under cold conditions.

The temperature-dependent kinetics of the reactions between CH_2OO and the hydroxyketones, hydroxyacetone (AcOH) and 4-hydroxy-2-butanone (4H2B). The temperature-dependent bimolecular rate constants were reported: $k_{AcOH}(T)$ = (4.3±1.7)×10^{-15}exp[(1630±120)/T] and $k_{4H2B}(T)$ = (3.5±2.6)×10^{-15}exp[(1700±200)/T]. The bifunctionality of the hydroxyketones were explored computationally, and the 1,2-addition reaction at the OH site was found to have a negligible contribution to the rate constants. The relative reactivity of the hydroxyketones was understood using the FMO theory approach, where the hydroxyalkyl substituents were found to be neither electron donating groups (EDG) or electron withdrawing groups (EWG). The CH_2OO + hydroxyketone reactions are likely too slow to be of significance in the atmosphere, except at very low temperatures.

The final chapter discusses ongoing work that is focused on developing structure activity relationships (SARs) based on calculated orbital energies that are involved in the cycloaddition reactions between CIs and their reacting partners. For the reaction between CH_2OO and a test set of

carbonyls, a SAR was based on the carbonyl π^* orbital energies which are involved in the dominant orbital interaction with the $n_{pc\text{-}po}$ orbital on CH_2OO. The following equation was developed from the SAR to predict the rate constants for the reaction of $COCl_2$ and $CO(CN)_2$ with CH_2OO at room temperature, $\ln k = (-1.53 \pm 0.14)E_{\pi^*} - (29.91 \pm 0.29)$. The effect of the substituents on the CI was then investigated by plotting experimental rate constants for the reaction between CIs and SO_2 as a function of the $n_{pc\text{-}po}$ orbital energies of the CIs. A second SAR was developed, and equation was used to predict the rate constants of the reactions of ClCHOO and CH_3OCHOO with SO_2 at room temperature: $\ln k = (1.66 \pm 0.51)E_{n_{pc-po}} - (12.03 \pm 3.39)$.

1 Introduction

1.1 Atmospheric Ozone

Ozone (O_3) is a highly reactive gas that is known to be produced naturally and anthropogenically.[1] There are two distinct mechanisms that ozone is generated, each of which correspond to the troposphere and stratosphere separately. The chemistry that is involved with each type is significantly different in the corresponding regions. The stratosphere is between ~10–50 km in altitude with temperatures ranging from ~210–270 K. The troposphere (≤ 10–15 km) is the lowest layer of the atmosphere, which contains most of the mass of the planetary atmosphere.[2] With a larger temperature range (~215–300 K) and several different chemical and physical processes occurring on the Earth's surface, tropospheric chemistry not only has an impact on biological life but also the chemistry that occurs in the other atmospheric strata.

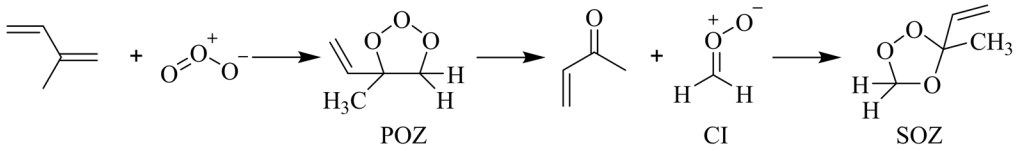
Stratospheric ozone is produced naturally when molecular oxygen (O_2) is photolytically dissociated by UV radiation (200–240 nm).[3] The excited oxygen atoms then react with O_2 to produce ozone, which is an important source for OH in the atmosphere.[1] More notably, ozone has a critical role in functioning as an effective screen for UV radiation. Ozone absorbs high frequency UV light in the stratosphere, preventing diseases such as skin cancer by keeping ~95% of UVB (280–315 nm) from reaching the surface.[4] Ozone in the stratosphere is best known for its absence, when the stratospheric ozone hole was noticed to form over Antarctica. The use and emissions of chlorofluorocarbons (CFC's), prior to the Montreal Protocol, were acknowledged to be the source of heterogeneous chemistry with polar stratospheric clouds. In what had taken countless millennia to form, human life caused the partial destruction of stratospheric ozone in less than a century.[5]

Tropospheric ozone is known to be mainly produced from the photolysis of nitrogen dioxide (NO_2). NO_2 absorbs in the 300–600 nm range, which overlaps with the solar actinic spectral region. NO_2

photolysis produces NO radicals, which can react with HO_2 to produce tropospheric ozone. Tropospheric ozone reacts readily with unsaturated hydrocarbons in the atmosphere, which are a type of volatile organic compounds (VOCs). VOCs such as isoprene and α-pinene are emitted from plants, which make up ~90% of global VOC emissions.[1] VOCs primarily react with OH radical or O_3 to produce a variety of oxygenated organic molecules. More highly oxygenated organics are less volatile, which leads to secondary organic aerosol (SOA) formation.[6] The formation of SOAs from chemical processes such as ozonolysis has a large impact on the oxidative capacity of the atmosphere, which significantly affects radiative forcing and air quality.[7–9] SOAs are found in particulate matter ($PM_{2.5}$) which is linked to adverse human health effects, such as cardiovascular and respiratory diseases.[10,11]

1.2 Alkene Ozonolysis

Ozonolysis is the overall reaction between ozone and alkenes, which ultimately leads to the breaking of the olefinic C=C bond. The Criegee mechanism for ozonolysis is outlined in Scheme 1.1, where the oxidation of isoprene is used as an example. A [3+2] cycloaddition reaction initially occurs when ozone adds across the alkene to form a 1,2,3-trioxolane intermediate species or a primary ozonide (POZ). The initial cycloaddition between ozone and isoprene is slow (~1×10^{-17} cm^3s^{-1}), and the reaction is highly exothermic.[12] The chemically activated POZ is unstable, which leads to a very rapid decomposition.[13] One of the peroxy O–O bonds is cleaved simultaneously with the C–C bond to produce a carbonyl compound and a carbonyl oxide, which is better known as a Criegee intermediate



Scheme 1.1 Cycloaddition mechanism associated to the ozonolysis of alkenes, where a Criegee intermediate (CI) and carbonyl compound are produced before forming the secondary ozonide (SOZ).

(CI).[14,15] The CI and carbonyl can further react to form a 1,2,4-trioxolane exothermically, which is also known as a secondary ozonide (SOZ). The mechanism was originally proposed by Rudolph Criegee in 1975, which was based on condensed phase chemistry.[14] The formation of the SOZ was to proceed after the POZ decomposition because it was assumed the reactants would be in close proximity to each other due to solvent effects.[16] In the gas phase the recombination of the POZ decomposition products is only one of several processes that is known to take place. A large amount of vibrational energy is initially stored in the CI, which enables further unimolecular decay. CIs can only undergo bimolecular reactions with trace atmospheric gases after collisional stabilization in ambient air.[17] The chemical fate of different CIs and the mechanisms associated will be discussed in later sections.

Isoprene is the most abundant unsaturated hydrocarbon in the atmosphere,[1] and ozonolysis consumes ~10% of isoprene globally.[18] Isoprene-derived CIs are formaldehyde oxide (CH_2OO), *syn*- and *anti*- methylvinylketone oxide (MVKO), and *syn*-methacrolein oxide (MACRO).[19–21] CH_2OO is the most abundant CI, having significantly higher yield in isoprene ozonolysis than the 4-carbon CIs (MVKO and MACRO). The overall branching of isoprene ozonolysis favors 58% of CH_2OO, MACRO and MVKO are produced less at 19% and 23% respectively.[19,22] Due to instability in the POZ, exothermic decomposition results in stored vibrational and rotational energy in CIs,[23] which gives rise to unimolecular decomposition for larger CIs.[13] CH_2OO is known to have a longer lifetime, which allows it to react with atmospheric gases.

CIs have not been detected in the atmosphere because of their short lifetimes, although Mauldin *et al.* claims to have detected them indirectly.[24] Low steady-state concentrations result from slow formation and rapid loss due to reaction with gases and unimolecular decomposition. Low concentrations of ~2.0×10^6 cm^{-3} of CH_2OO have been estimated from modelling studies, which would make detection in the troposphere not feasible.[25,26] CIs were initially proposed to contribute to SO_2 oxidation or the removal of certain VOCs, but Vereecken *et al.* suggests that stabilized CIs exist in

concentrations that are too low in the troposphere to have an atmospheric impact ($\leq 1\times10^5$ cm^{-3}).[27] Such processes could only be affected in equatorial, urban, and biomass burning regions. Initially the types of studies that could infer the existence and behavior of CIs involved monitoring the products of alkene ozonolysis reactions with techniques such as infrared and microwave spectroscopy.[16,28–31] These types of studies are useful in exploring processes such as collisional stabilization and unimolecular decomposition of CIs. Reports help in understanding how CI yields are affected in ozonolysis.[32] Understanding CIs through alkene ozonolysis can also be problematic, as there are several major obstacles that interfere with the interpretation and analysis of CIs. When alkene ozonolysis experiments are conducted in the presence of O_2 the balance of reactants and conversion of alkenes is significantly larger than the amount of generated ozone. Furthermore, the amount of unidentified products and decomposition of intermediates that lead to numerous stable molecules and radicals can lead to ambiguous mechanistic evaluations.[33,34] Horie and Moortgat considered ozonolysis experiments to be substantially difficult because CIs thermally decompose before stabilization can occur, they said it "was the source of all problems which studies on the gas-phase ozonolysis must suffer".[35]

1.3 Laboratory Production and Detection

Sander reviewed the isolation and characterization of stable CIs in solution in 1990,[36] but direct detection in the gas phase eluded researchers for a further 20 years. The first direct detection of CH_2OO was motivated by Asatryan and Bozzelli who showed the chlorine assisted oxidation of dimethylsulfoxide (DMSO) could lead to the formation of CH_2OO.[37] Taatjes et al. quickly responded by using photoionization mass spectrometry (PIMS) with tunable vacuum ultraviolet synchrotron radiation to probe and identify CH_2OO through DMSO oxidation, however concentrations were still too low for kinetics experiments.[38] An alternative method was reported by Eskola et al., who studies of the temperature dependent kinetics of the reaction between halo methyl radicals and oxygen

(CH_2X + O_2), inadvertently supplied a much more efficient route to producing CH_2OO photochemically.[39] Subsequently Welz et al. were able to use this approach to generate CH_2OO in sufficiently high concentrations to report the first bimolecular kinetics of CH_2OO in the presence of nitric oxide (NO), nitrogen dioxide (NO_2), and sulfur dioxide (SO_2).[40] As shown in Table 1.1, similar photochemical approaches involving the photolysis of *gem*-dihaloalkane precursors in the presence of excess O_2 have been used to generate a large number of different types of CIs. While diiodoalkanes were the most common, more exotic CIs have been synthesized with an approach originally shown by Sander, which is based on matrix-assisted photolysis of substituted diazomethanes to produce a carbene in the presence of oxygen.[41,42] This thesis will mainly focus on the kinetics of the simplest CI, CH_2OO, larger CIs that are atmospherically relevant will be briefly discussed, such as acetaldehyde oxide (CH_3CHOO), acetone oxide ($(CH_3)_2COO$), MVKO, and MACRO.

1.3.1 Electronic Structure

The electronic structure of CH_2OO is shown in Scheme 1.1: a zwitterionic carbonyl oxide that is isoelectronic with ozone. Although Rudolph Criegee originally postulated CIs as zwitterionic species in liquid phase synthesis, he mentioned CIs could be biradical in the gas phase.[14,43] There was an initial debate in the literature on the structure and electronic properties of CIs. With ab initio results combined with thermochemical data, Wadt and Goddard initially suggested that CIs are singlet biradicals because the zwitterionic state is too energetic to be populated (3.5 eV above the ground state).[44] Cremer et al. discussed CIs as a superposition of both zwitterionic and biradical character in the gas phase, whereas solvent and substituent effects could stabilize the zwitterionic state in the condensed phase. Sander reviewed early theoretical and experimental methods that disputed the electronic structure of CIs, agreeing with Cremer that substituents such as methyl groups can stabilize the zwitterionic state of CIs as π-donors.[36] Higher levels of theory such as CASSCF and CASPT2 allowed Aplincourt et al. to computationally explore the lowest singlet electronic states

above the X(^{1}A′) ground state of CH_2OO and the B(^{1}A′) [π*←π] transition was predicted to have the strongest oscillator strength. The ground state was seen to have substantial π-character and a planar geometry.[45] With similar approaches, multiple groups calculated the geometries, electronic configurations, as well as the vertical and adiabatic excitation energies for low lying electronic states of CH_2OO.[46,47] Along with confirming that the ground state is a planar zwitterionic structure, they concluded that the first triplet excited state is purely biradical, associated with a shorter angle of the COO component and an elongated O–O bond.

Table 1.1 Several different CIs produced in the presence of oxygen, with their corresponding photolytic precursors.

Common Name	Formula	Precursor
formaldehyde oxide	CH_2OO	CH_2I_2
		CH_2SOCH_3
acetaldehyde oxide	$(CH_3)CHOO$	CH_3CHI_2
acetone oxide [a]	$(CH_3)_2COO$	$(CH_3)_2CI_2$
propionaldehyde oxide	CH_3CH_2CHOO	$CH_3CH_2CHI_2$
methylvinylketone oxide	$CH_2=CHC(CH_3)OO$	$ICH_2CHClCH_3$
methacrolein oxide	$CH_2=C(CH_3)CHOO$	$ICH_2C(CH_3)CHI$
choroformaldehyde oxide	$ClCHOO$	$ClCHI_2$
dibenzophenone oxide	Ph_2COO	$Ph_2C=N_2$
trifluoroacetaldehyde oxide	CF_3CHOO	$CF_3CH=N_2$

a.) For some CIs like acetone oxide, the precursors in subsequent studies have different halogens attached, such as chlorine.[52,63]

1.3.2 Electronic spectroscopy (UV-Vis)

The first spectroscopic detection of CH_2OO involved the $B(^1A')$ $[\pi^* \leftarrow \pi]$ electronic transition mentioned previously. Shown in Figure 1.1 are the absolute absorption cross sections of CH_2OO. The strong UV-Vis absorption band of CH_2OO was first experimentally identified by Beames et al. using an action spectroscopy approach.[48] An accurate quantification of the absorption spectrum is difficult with this method, so it does not reflect an accurate spectrum. Various other groups have used different types of absorption spectroscopy to measure the spectra shown in Figure 1.1. The cross sections from Sheps and Beames are significantly larger than the other absorption measurements. The structure on the red side of the spectrum was attributed to the vibrational progression of the $B(^1A')$ state, which is associated to the $[\pi^* \leftarrow \pi]$ transition.[49] Ting et al. used transient absorption spectroscopy (TAS) to measure the absolute absorption cross-section that peaks at ~340 nm (~1 $\times 10^{-17}$ cm^2), which is the recommended cross section in the Jet Propulsion Laboratory (JPL)

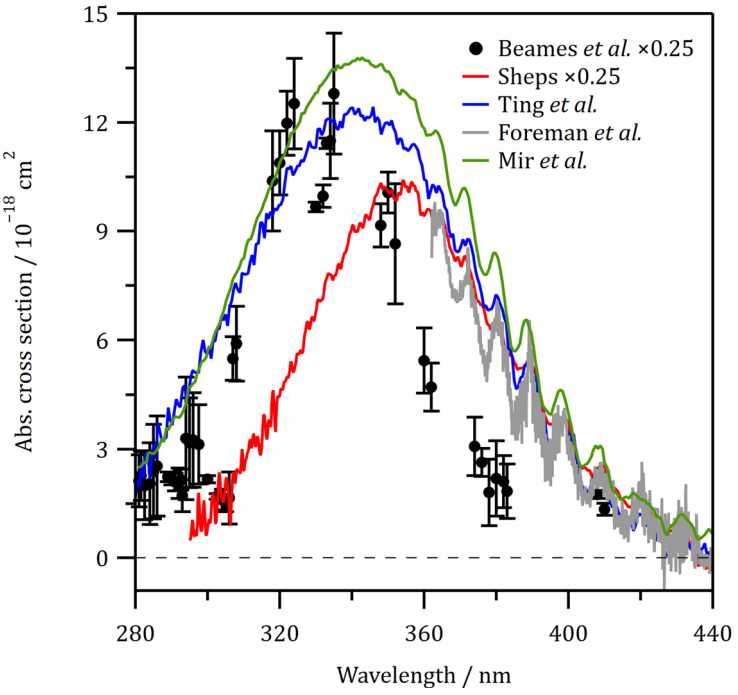


Figure 1.1 UV-Vis absorption spectra of CH_2OO. Sheps (red) and Beames (black) were scaled to the spectrum of Ting et al. (blue). The more recently measured spectra by Foreman and Mir are shown in grey and green respectively.

evaluation. The reported cross section values shown in Figure 1.1 are in good agreement on the longer wavelength side of the spectrum, but there are discrepancies at lower wavelengths.[50,51]

The same vibronic structure on the red side of the spectrum was observed but there was some discrepancy on the short wavelength side.[52] With modest levels of theory, the absorption cross section of CH_2OO was reproduced by Sršeň *et al.* with a newly formulated composite approach, which had an excellent match to the experimental work in the spectrum. Foreman *et al.* postulated the vibronic structure to be attributed to the OO stretch and COO bend due to Franck-Condon arguments.[50] Ting *et al.* later argued that the nuclear motions with respect to the C-H bonds (CH_2 wag/twist) were responsible for the characteristic structure for the long-wavelength side of the UV spectrum by tying an isotope effect to the shifted peak positions in the corresponding spectrum of CD_2OO.[53] A recent review by Karsili et al. compares the vibronic structure of the CH_2OO to the Chappuis bands in UV spectrum of ozone as well as larger aromatic CIs such as benzoquinone-oxide. They show the peak separations that support the oscillating characteristic of the spectrum to be due to excited state OO stretch and COO bending motions.[54]

The absolute UV absorption spectra for several different CIs are shown in Figure 1.2. The UV spectra of methyl and ethyl substituted CIs such as CH_3CHOO, $(CH_3)_2COO$, and propionaldehyde oxide have also been measured. They were found to have a blue-shifted spectrum relative to CH_2OO, which is most likely due to the intramolecular interaction between the α-hydrogen and the terminal oxygen of the CIs.[55,56] Unsaturated isoprene-derived CIs that such as MACRO and MVKO have been studied more recently. Vansco et al. experimentally investigated the UV-Vis spectrum of MVKO with an induced depletion method of the VUV photoionization signal.[57] With supporting computational results, they found the strong [$\pi^* \leftarrow \pi$] transition to be more distinctive than previously measured CH_2OO due to delocalized electron density across the CI. Conjugation across the molecule for MACRO and MVKO allows for an absorption spectrum at longer wavelengths.[54,58,59]

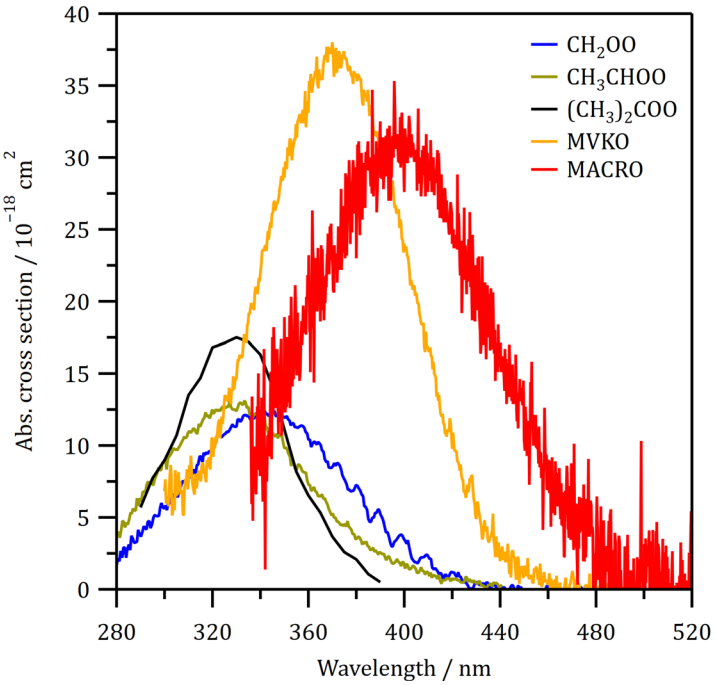


Figure 1.2 Absolute UV-Vis absorption spectra of several different CIs: CH_2OO (blue)[51], CH_3CHOO (green)[59], $(CH_3)_2COO$ (black)[54], MVKO (yellow)[58], and MACRO (red)[58].

1.3.3 Rovibrational Spectroscopy (IR)

Rovibrational (IR) spectroscopy provides information about molecular vibrations for species-specific identification via the characteristic modes found in CIs. This technique is also useful because it allows the ability to distinguish between different conformers. A substantial amount of research has been done by Lee and coworkers with the use of transient infrared absorption spectroscopy to study CIs as well as the associated formation and decomposition processes.[60–65] A step-scan FTIR spectrometer is coupled with a multireflection White cell to measure rovibrational bands that provide a detailed description of CH_2OO with the support of matching theoretical predictions.[60] The comparison of CIs to peroxy radicals in early literature supported the argument that CIs are indeed a zwitterionic species.[61,62,66] Huang et al. improved the experimental technique and achieved better resolution to identify rotational parameters for the bands assigned to the different stretching modes

on CH_2OO.[63] Chang et al. later combined UV and IR spectroscopy methods to obtain the absolute IR absorption cross section of the ν_4 fundamental of CH_2OO, which corresponds to the motions of CO stretching coupled with the CH_2 scissoring.[67] The methyl-substituted CI, CH_3CHOO, exists as both a *syn*- and *anti*- conformer with respect to the side of the terminal oxygen. The conformational analysis of *syn*- and *anti*-CH_3CHOO is more feasible with the transient IR technique due to the OO-stretching modes being separated by ~10 cm^{-1}. Although there is a good amount of overlap, the *syn*- conformer has one distinctive band assigned to CH modes that is absent in the other, which is attributed to the intramolecular bound H-bond between the methyl group and the CI terminal oxygen.[64] Various other CIs have been detected with an IR action spectroscopy approach as well as the transient IR detection method mentioned previously.[68,69]

1.3.4 Rotational Spectroscopy (Microwave)

Rotational spectroscopy allows measurements of moments of inertia which depend on molecular geometry and structure. This technique provides very high resolution and accuracy compared to other techniques. McCarthy and coworkers were involved in the early detection of CIs with Fourier Transform Microwave Spectroscopy (FTMW) through the ozonolysis of alkenes.[30] Aside from reporting the first detection of CH_2OO in the gas -phase ozonolysis of ethylene, the mechanistic pathway and production of CIs was confirmed. With the combined works from Nakajima and Endo, McCarthy et al. have differentiated isomers for CH_2OO as well as several isotopologues.[70,71] Geometric parameters such as the bond lengths and angles separating the atoms of CH_2OO have been identified.[31,71] The CO and OO bond lengths were determined, as well as the CCO bond angle. A resulting planar geometry and longer OO bond length confirmed the zwitterionic structure. Along with the structural information from these studies, investigations of *syn*- and *anti*-CH_3CHOO evidently supported the existence of CIs as zwitterionic ground state molecules, as opposed to a

diradical species.[23] This technique is especially useful for the alkyl substituted CIs, where rotational constants and the barrier heights of each methyl group rotation has been precisely determined.[72,73]

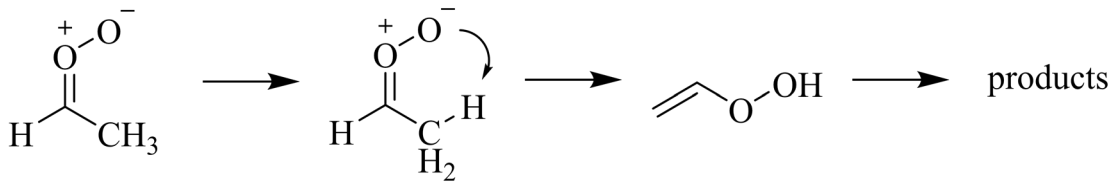
1.4 Reaction kinetics

Recent years have seen a lot of work to understand the fate of CIs in the atmosphere. There are two main loss processes: unimolecular decomposition and bimolecular reaction with trace gases. There have been numerous studies on both.[17,26,33] This work has shown that CIs participate in several different classes of reactions, which will be described below.

1.4.1 Unimolecular Decomposition

In general, CIs are known to thermally decompose via two mechanisms: 1,3-ring closure forming a dioxirane or a 1,4-hydrogen transfer across the CI. Although it is slow and only apparent at higher temperatures, the 1,3-ring closure is the only decomposition pathway for CIs lacking the α-hydrogen, such as CH_2OO.[17,74] Unimolecular decay is a major atmospheric sink for larger CIs, such as CH_3CHOO, $(CH_3)_2COO$, MACRO, and MVKO.[20] As alluded in the previous sections, the *syn*- conformers of CIs are more prone to unimolecular decomposition because of the ability to undergo an intramolecular H-shift.[17,55–57,59,68] Unimolecular decomposition rate coefficients of 166, 369, and 33 s^{-1} at 298 K have been estimated for *syn*- CH_3CHOO, $(CH_3)_2COO$, *syn*-MVKO.[23] Shown in Scheme 1.2, the terminal oxygen on the CI abstracts the H-atom from the nearby alkyl substituent in a 5-membered ring transition state, where a vinyl hydroperoxide is formed and ultimately leads to OH radical production.[13] The *syn*- conformer of CH_3CHOO is known to produce OH radical while the longer living *anti*- conformer follows the dioxirane mechanism, like CH_2OO.[75] Taatjes et al. suggested that hydroxyacetone can be produced from $(CH_3)_2COO$ decomposition after the 1,4-H shift produces a vinyl hydroperoxide, the OH can migrate to the adjacent methyl group.[76] Caravan et al. used the UV-Vis depletion method to explore the conformer dependent reactivity and unimolecular decay of MVKO, concluding the

bimolecular reactions were only viable for the *syn*- conformer, while *anti*-MVKO undergoes rapid decomposition.[77] Lee et al. recently used a master equation to study the unimolecular decay of thermalized MACRO. Besides H-atom transfer, decomposition to dioxole and dioxirane structures and conformational changes are highly dependent on the atmospheric conditions.[78]



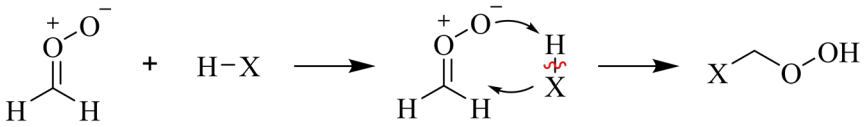
Scheme 1.2 The most common unimolecular decomposition pathway for CIs, which proceeds as a 1,4-hydrogen shift to form a vinyl hydrogenperoxide. Shown above, *syn*-CH_3CHOO was used as an example.

1.4.2 1,2-Addition Reactions

The 1,2-addition reaction mechanism is outlined in Scheme 1.3, where CH_2OO adds across a compound denoted X-H. This reaction applies to water, alcohols, amines, and mercaptans, which will be discussed below. In a strained 5-membered ring transition state, the terminal oxygen on CH_2OO abstracts a hydrogen, simultaneously the resultant electronegative atom attacks the carbonyl carbon of the CI.[79–81] The reaction sacrifices a polar covalent bond to produce a substituted hydroperoxide and is strongly exothermic (~40-50 kcal mol^{-1}). In the literature, this mechanism is also referred to as an insertion mechanism, implying the CI inserts into the polar covalent H-bond.[80] Overall a 1,2-addition to CIs are atmospherically relevant and significant because hydroperoxide compounds are produced, which further decompose and contribute to OH radical production.[17,26]

The main atmospheric sink for CH_2OO is via reaction with water.[26,82–89] The exothermic reaction between CH_2OO and water vapor produces hydroxymethyl hydroperoxide with a strong negative

temperature dependence.[86,90] Chao et al. was the first to measure the reaction kinetics between CH_2OO and water vapor. They noticed that the decay rate of CH_2OO was proportional to the square of the concentration of water, which indicated there were two water molecules participating.[83] This implied that not only was CH_2OO reacting with water monomer, but water dimer was involved as well. In fact, CH_2OO was barely reacting with water monomer because the reaction was dominated by water dimer. The reaction with water monomer is slow, $\sim 10^{-16}$ $cm^3 s^{-1}$ at 298 K, while reaction with the dimer is fast ($\sim 10^{-12}$ $cm^3 s^{-1}$).[18,90,91] With loss rates of ~ 2000 s^{-1} at a relative humidity of 50%, reaction with water dimer is 4 orders of magnitude faster than the total first order loss of CH_2OO.[26,88] Ryzhkov and Ariya used coupled cluster calculations to show the reaction with water monomer has a barrier of ~ 3 kcal mol^{-1} while reaction with the dimer has a submerged barrier of ~ 10 kcal mol^{-1}.[92] The mechanism in Scheme 1.3 involves a five-membered cyclic transition state, and the mechanism with water dimer is described by forming a 7-membered ring, which facilitates a submerged barrier and overall faster reaction.[92] The extra water molecule is catalyzing the reaction through a hydrogen atom relay mechanism, known as double hydrogen atom transfer (DHAT).[93]



Scheme 1.3 The 1,2-addition mechanism of a CH_2OO adding across X-H, where X represents a saturated or substituted -O, -S, or -N atom. X can also be a halogen such as a -Cl atom.

Alcohols also react with CH_2OO via the 1,2-addition reaction mechanism.[79,94–96] The exothermic reaction produces alkoxymethyl hydroperoxides with bimolecular rate constants on the order of $\sim 10^{-13}$ cm^3 s^{-1}. In general, alcohols tend to react more rapidly than water monomer, with submerged enthalpic barrier heights of ~ 4 kcal mol^{-1}.The reactivity of aliphatic alcohols was found to depend on the size of the alkyl group (methanol>isopropyl alcohol>ethanol).[79,95] Amines react similarly to

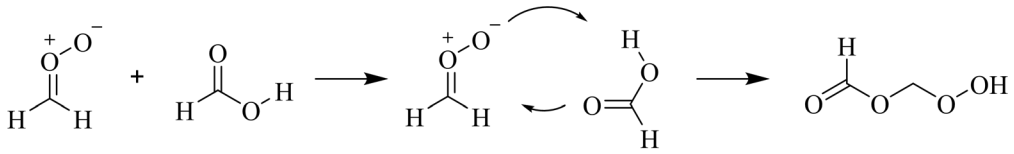
alcohols, lacking any alkyl substituents ammonia (~8×10^{-14} cm^3 s^{-1}) reacts with CH_2OO two orders of magnitude slower than methylamine (~6×10^{-12} cm^3 s^{-1}).[97–99]

Reaction of CH_2OO with hydrogen halides, specifically hydrochloric acid, is fast. Foreman *et al.* used flash photolysis transient absorption spectroscopy measure a rate constant of 4.6×10^{-11} cm^3 s^{-1} at 298 K.[100] Cabezas and Endo used FTMW spectroscopy to confirm the reaction proceeds through an entrance channel complex before producing chloromethyl hydroperoxide with a submerged reaction barrier.[101] They compared the reaction to water, as the longer H–Cl bond could reduce ring strain at the transition state, affording a faster reaction due to gas phase acidity. Taatjes et al. used PIMS to compare the relative rates of the reaction of CH_2OO with HCl and DCl separately. There was a possibility of the H-atom tunneling when they observed substantially larger kinetic isotope effect than theory predicted.[80] Although difficult to distinguish between the conformers of CH_3CHOO with LIF, Liu et al. monitored the OH signal to report a rate constant for the *syn*- conformer with HCl (4.7×10^{-11} cm^3 s^{-1}).[102] In a FTIR product analysis study, Su et al. reported an overall rate constant of 2.7×10^{-10} cm^3 s^{-1}, which could imply the *anti*- conformer is ~4 times faster than the *syn*- conformer.[103] Cabezas and Endo later reported the product analysis of the reaction between CH_3CHOO and HCl, while the results implied both conformers were present, HCl reacted much faster with the *anti*-conformer.[104]

1.4.3 1,4-Addition Reactions

The similarity between the 1,4-addition and 1,2-addition reaction mechanism, is that they both lead to substituted hydroperoxides. Reactants that take place in a 1,4-addition with CH_2OO are carboxylic acids and nitric acid. In Scheme 1.4 the reaction between CH_2OO and formic acid is used as an example, where the acidic hydrogen on the OH group is transferred to the terminal oxygen of the CI, and the carbonyl oxygen from the formic acid bonds with the carbon of the CI, producing hydroperoxy methylformate. The transition state is isoenergetic with the pre-reactive complex,

which is most likely due to a more geometrically favored 7-membered ring structure compared to the 5-membered ring formed in 1,2-additions.[81] The exoergic reaction with organic acids are negatively temperature dependent and have rate constants on the order of ~10^{-11} cm^3 s^{-1}. Chhantyal-Pun et al. measured the rate constants of CH_2OO and $(CH_3)_2COO$ with five different organic acids in a multiplexed photoionization mass spectrometry (MPIMS) experiment.[105] The large rate constants for the reactions between CIs and organic acids make them near the hard-sphere collision limit, so they are explained by long-range capture models.[106] By developing a structure activity relationship based on a dipole-dipole capture model, the rate constants for numerous CIs with nine different carboxylic acids were predicted. The model works relatively well except for the case of pyruvic acid, where there are other dipole-dipole interactions involved. It was concluded the intramolecular H-bond in pyruvic acid could be hindering the H-transfer to the CI in the transition state.



Scheme 1.4 The 1,4-addition mechanism of CH_2OO reacting with formic acid as an example, producing hydroperoxymethylformate. Larger organic acids or nitric acid are also possible reactants for this mechanism to occur.

The reaction between CH_2OO and nitric acid was measured by multiple groups. In a transient absorption experiment, Foreman et al. reported a rate constant of 5.4×10^{-10} cm^3 s^{-1}, which was twice as fast as the results from Chung et al.[100,107] Yang et al. more recently investigated the reaction kinetics of HNO_3 with four different CIs including CH_2OO, to explore the substituent effects of the CIs in this reaction.[108] The order of reactivity followed the following trend: *syn*-MVKO>$(CH_3)_2COO$>*anti*-MVKO>CH_2OO. Although they reported a rate constant for CH_2OO that was ~4 times slower than Foreman et al., both studies concluded that nitric acid was likely to be a competitive sink for $(CH_3)_2COO$ and possibly for CH_2OO.

The reactivity of compounds towards CH_2OO in 1,2- and 1,4-addition mechanisms can be described by the correlation first proposed by Tobias and Ziemann, which was based on gas-phase acidities (ΔH_{acid}) and X–H bond strengths.[109] Murray and coworkers showed a strong inverse correlation between the log of the rate constants and the geometric mean of the bond enthalpy/gas phase acidity.[79,100] The linear relationship suggests the mechanisms involve a relatively polar transition state and the reaction rates rely on the ability of the reactant to donate the H-atom to the terminal oxygen on the CI. Kumar and Francisco used high-level quantum chemical calculations to tune the barrier of the reaction between CH_2OO and H_2X (X=O, S, Se, Te), and they concluded there was an inverse correlation between the reaction barrier and the X-H bond length, alternatively a direct correlation with the pKa, or acidity of H_2X.[110]

1.4.4 Cycloaddition Reactions

Cycloaddition reactions are one of the most important reaction mechanisms involved with CI production and consumption in the atmosphere. As shown in Scheme 1.1, CH_2OO and O_3 are isoelectronic, and as the first cycloaddition is alkene ozonolysis, once CH_2OO is formed it can undergo a 1,3-dipolar cycloaddition reaction. The CI adds across a double bond with reactants such as alkenes, carbonyls, and SO_2.[17] With carbonyls as an example, the cycloaddition mechanism is initiated by the formation of a van der Waals entrance channel complex before passing over the cycloaddition transition state that leads to the production of a SOZ.[33,111–113] Cycloaddition reactions between CIs and π-bonded compounds have rate constants that are negatively temperature dependent. Reactions with alkenes are slow ($\sim 10^{-15}$ cm^3 s^{-1}) and they have been shown to have a negligible influence on CI chemistry in the atmosphere.[114,115]

Reaction with SO_2 has earned considerable attention in the Criegee chemistry community from the beginning because the formation of SO_3 can react with water to produce H_2SO_4 rapidly, which can impact aerosol and cloud formation.[26,116] Because of this, the cycloaddition reaction between CH_2OO

with SO_2 has been well characterized by several groups.[40,49,82,84,85,117–121] The barrierless formation of a cyclic SOZ favorably decomposes to produce formaldehyde and SO_3.[17,122] Although the major atmospheric sink for CH_2OO is through reaction with water vapor, SO_2 may be competitive in certain environments. In regions that have higher SO_2 concentrations (~100 ppb), the loss rate of CH_2OO is ~100 s^{-1} at room temperature. At low relative humidity (<10% RH) reaction with SO_2 would start to dominate over water dimer.[26,121] Alongside organic acids, SO_2 is a secondary sink to unimolecular decomposition for larger CIs, such as $(CH_3)_2COO$, MVKO, and MACRO.[20,123] The longer living conformers, *anti*-MACRO and *syn*-MVKO were confirmed to have fast removal with SO_2.[58,77]

1.5 Research Goals

This dissertation focuses on the bimolecular reaction kinetics of CH_2OO with different types of functionalized and substituted carbonyl compounds. CH_2OO reacts with carbonyls in a 1,3-dipolar cycloaddition mechanism, where the CI is a 1,3-dipole and the carbonyl compound is referred to as the dipolaraphile.[124,125] Substituents on the carbonyl have been shown to significantly affect reaction rate, as a range of rate constants from ~10^{-14}–10^{-10} cm^3 s^{-1} have been observed. The presence of adjacent functional groups can also have a competitive effect that may slow down or increase the rate of reaction.[17,126–130] A summarized table of the experimental rate constants between carbonyls and CH_2OO is shown in Table 1.2. In the following chapters, the reactivity of different carbonyl compounds will be assessed with direct experimental measurements with supporting quantum-chemical calculations. In Chapter 2 we will explore the kinetics of the reaction of CH_2OO with α- and β- substituted dicarbonyls at room temperature. With an improved experimental set up and custom made glass-jacketed flow cell, Chapter 3 re-investigates dicarbonyls and their behavior across the temperature range 275–335 K. In Chapter 4, the reactivity of hydroxyketones with CH_2OO is considered by the proximity of the -OH group to the carbonyl. We look at functionality of the -OH group as a competing 1,2-addition mechanism as well as a contributing substituent in the

cycloaddition reaction. Finally, Chapter 5 discusses our most current work, which explores the overall reactivity trends of different substituted carbonyls. Correlations of experimental rate constants to molecular properties such as orbital energies and the electronic characteristics of the substituents can provide a low-cost computational tool to predict reactivity.

Table 1.2 Compiled rate constants of CH_2OO with different carbonyl compounds and the substituents separated as R_1 and R_2. This is a summarized version of Table 4.4, where the references are shown along with the corresponding rate constants. For simplicity, only the weighted means are shown here.

R_1R_2CO	R_1, R_2	$k_{R_1R_2CO}$ / 10^{-13} cm^3 s^{-1}
formaldehyde (HCHO)	H, H	38.5±1.9
acetaldehyde (MeCHO)	H, CH_3	15.1±1.1
acetone (Ac)	CH_3, CH_3	4.5±0.1
methyl ethyl ketone (MEK)	CH_3, C_2H_5	6.4±0.2
hexafluoroacetone (HFA)	CF_3, CF_3	306±27
biacetyl (BiAc)	CH_3, CH_3CO	129±18
acetylpropionyl (AcPr)	CH_3, C_2H_5CO	109±13
acrolein (ACR)	H, $CH=CH_2$	16.3±1.9
methacrolein (MACR)	H, $C(CH_3)=CH_2$	4.4±0.1
methyl vinyl ketone (MVK)	CH_3, $CH=CH_2$	5.0±0.4
acetylacetone (AcAc)	CH_3, $CH=C(OH)CH_3$	8.0±0.7
hydroxyacetone (AcOH)	CH_3, CH_2OH	10.9±1.5
4-hydroxy-2-butanone (4H2B)	CH_3, CH_2CH_2OH	11.1±2.6

2 Kinetics of the reactions of CH_2OO with Acetone, α-diketones, and β-diketones

Portions of this chapter were reproduced with permission from Cornwell, Z. A.; Harrison, A. W.; Murray, C. Kinetics of the Reactions of CH_2OO with Acetone, α-Diketones, and β-Diketones. *J. Phys. Chem. A* **2021**, *125* (39), 8557–8571. https://doi.org/10.1021/acs.jpca.1c05280.

2.1 Abstract

Rate constants for the reactions between the simplest Criegee intermediate, CH_2OO, with acetone, the α-diketones biacetyl and acetylpropionyl, and the β-diketones acetylacetone and 3,3,-dimethyl-2,4-pentanedione were measured at 295 K. CH_2OO was produced photochemically in a flow reactor by 355 nm laser flash photolysis of diiodomethane in the presence of excess oxygen. Time-dependent concentrations were measured using broadband transient absorption spectroscopy and the reaction kinetics were characterized under pseudo-first order conditions. The bimolecular rate constant for the CH_2OO + acetone reaction is measured to be $(4.1\pm0.4)\times10^{-13}$ cm^3 s^{-1} consistent with previous measurements. The reactions of CH_2OO with the β-diketones acetylacetone and 3,3-dimethyl-2,5-pentanedione are found to have broadly similar rate constants of $(6.6\pm0.7)\times10^{-13}$ cm^3 s^{-1} and $(3.5\pm0.8)\times10^{-13}$ cm^3 s^{-1}, respectively; these values may be cautiously considered as upper limits. In contrast, α-diketones react significantly faster, with rate constants of $(1.45\pm0.18)\times10^{-11}$ cm^3 s^{-1} and $(1.29\pm0.15)\times10^{-11}$ cm^3 s^{-1} measured for biacetyl and acetylpropionyl. The potential energy surfaces for these 1,3-dipolar cycloaddition reactions are characterized at the M06-2X/aug-cc-pVTZ and CBS-QB3 levels of theory and provide additional support to the observed experimental trends. The reactivity of carbonyl compounds with CH_2OO is also interpreted by application of frontier molecular orbital theory and predicted using Hammett substituent constants. Finally, the results are compared with other kinetics studies of Criegee intermediate reactions with carbonyl compounds and discussed within the context of their atmospheric relevance.

2.2 Introduction

Carbonyl oxides, known as Criegee intermediates (CIs), are formed by alkene ozonolysis reactions and are important reactive species in the troposphere.[15,16,26,131,132] It is now well-established that ozonolysis of alkenes proceeds in the gas-phase via the cycloaddition mechanism originally proposed by Rudolph Criegee,[14] after whom the intermediates are named. Initial cycloaddition forms a five-membered cyclic primary ozonide, which rapidly decomposes into a carbonyl and a carbonyl oxide. The energized CI subsequently either decomposes or is collisionally relaxed to form a stabilized CI. A broad range of alkenes are found in the troposphere, and consequently a great variety of CIs are thought to be formed in the atmosphere.[26] Depending on the substituents and the particular stereoisomer formed, CIs can themselves undergo thermal unimolecular decomposition or react with trace atmospheric gases. For larger CIs, unimolecular decomposition is thought to be the dominant sink.[27] For the simplest CI, formaldehyde oxide (CH_2OO), unimolecular decomposition is slow, and secondary reactions are more significant. Globally, reaction with water dimer is the dominant mechanism for removing CH_2OO,[133] although other trace species, such as organic or inorganic acids, with large CI reaction rate constants, can be locally competitive.[100,105,134,135]

Previous work has examined gas-phase reactions between CIs and carbonyl compounds produced in alkene ozonolysis reactions,[28,88,109,136–140] and using photochemical production.[82,111,128,141] In the Criegee mechanism for ozonolysis, decomposition of the primary ozonide yields a carbonyl oxide and an aldehyde or ketone, which can subsequently react to form a secondary ozonide (SOZ, a 1,2,4-trioxolane). Moortgat and co-workers demonstrated that the presence of additional carbonyls led to formation of the expected SOZs in the gas phase ozonolysis of ethene of using Fourier transform infrared spectroscopy (FTIR) for product detection.[137–139] A subsequent study found that hexafluoroacetone (HFA) reacted ~13 times faster with CH_2OO than does acetaldehyde at 730 Torr and 295 K.[140] Fenske *et al.* also used FTIR to monitor SOZ production from acetone oxide (CH_3CHOO),

produced by ozonolysis of *trans*-2-butene, reacting with acetaldehyde and estimated a rate constant of 1.1×10^{-12} cm^3 s^{-1} (with a factor of six accuracy).[28] Tobias and Ziemann determined reactivity trends for reactions of the C13 CI formed from ozonolysis of 1-tetradecene using real-time thermal desorption particle beam mass spectrometry.[109] The observed reactivity trends indicated that HCHO reacted with the C13 CI around 50–100 times faster than alcohols such as methanol and isopropanol,[79,94] implying rate constants on the order 10^{-11} cm^3 s^{-1}. In addition, Berndt *et al.* used ozonolysis to form CH_2OO in a flow reactor and monitored concentrations by titrating with SO_2 and detecting the H_2SO_4 product by chemical ionization mass spectrometry (CIMS).[88] Rate constants of $(1.7\pm0.5)\times10^{-12}$ cm^3 s^{-1} and $(3.4\pm0.9)\times10^{-13}$ cm^3 s^{-1} were measured at 1 atm and 297 K for the reactions of CH_2OO with acetaldehyde and acetone, respectively.

Recently, photochemical routes involving reactions of α-iodoalkyl radicals with oxygen have been used to generate higher yields of carbonyl oxides and facilitate direct detection using absorption spectroscopy and photoionization techniques.[23,33] Several groups have used direct methods to investigate the kinetics of reactions of CH_2OO with carbonyl compounds. Taatjes *et al*. used tunable synchrotron photoionization mass spectrometry (PIMS) to directly measure CH_2OO loss rates in the reactions of CH_2OO with acetone, acetaldehyde, and HFA to be $(2.3\pm0.3)\times10^{-13}$ cm^3 s^{-1}, $(9.5\pm0.7)\times10^{-13}$ cm^3 s^{-1}, $(3.0\pm0.3)\times10^{-11}$ cm^3 s^{-1}, respectively, at a pressure of 4 Torr and a temperature of 295 K.[128] Secondary ozonides were observed in the mass spectra as products of the ketone reactions, although not of the acetaldehyde reaction. Subsequently, Elsamra *et al*. determined rate constants for acetone and acetaldehyde as $(3.0\pm0.6)\times10^{-13}$ cm^3 s^{-1} and $(1.2\pm0.2)\times10^{-12}$ cm^3 s^{-1} at 25 Torr and 298 K using multi-pass absorption spectroscopy.[111] Weak negative temperature and positive pressure dependences were observed. Stone *et al*. also examined the kinetics of the CH_2OO + acetaldehyde reaction.[82] In that study, CH_2OO was generated photochemically, but the reaction was probed indirectly by monitoring the HCHO products of SOZ decomposition using laser-induced fluorescence (LIF). The HCHO yield was found to decrease significantly with increasing pressure (from 88% at 4

Torr to only 4% at 730 Torr) due to stabilization of the SOZ, explaining the absence of SOZ signal in the low-pressure PIMS measurements.[128] The rate constant for the acetaldehyde reaction in the high-pressure limit was estimated to be $\sim 1.7\times10^{-12}$ cm^3 s^{-1}, consistent with the direct measurements. Recently, Eskola *et al*. have used PIMS to explore the kinetics and mechanism of the CH_2OO reactions with methyl vinyl ketone (MVK) and methacrolein (MACR).[141] These unsaturated carbonyls are, along with CH_2OO, important products of isoprene ozonolysis. The rate constants at 300 K and 4 Torr were found to be $(5.0\pm0.2)\times10^{-13}$ cm^3 s^{-1} for MVK and $(4.4\pm0.5)\times10^{-13}$ cm^3 s^{-1} for MACR. SOZ products were observed in the mass spectra and confirmed that the addition occurs primarily via 1,3-dipolar cycloaddition at the carbonyl site rather than the olefinic site, consistent with measurements of much smaller rate constants ($\sim10^{-15}$ cm^3 s^{-1}) for reactions of CH_2OO with various alkenes.[115]

Theoretical studies have also explored CI reactions with carbonyl compounds, particularly the CH_2OO + HCHO reaction. Cremer *et al*.[142] identified a dipole-dipole complex in the reaction of formaldehyde and formaldehyde oxide, which suggested the reactants would orient to promote cycloaddition to form the SOZ. The complex and transition states were subsequently characterized at various levels of theory by Aplincourt and Ruiz-López,[143,144] who performed calculations to explore mechanisms that led to formic acid anhydride and carboxylic acid formation in the atmosphere. For the reaction of CH_2OO with formaldehyde, calculations at the CCSD(T) level found the entrance channel van der Waals (vdW) complex to lie 5.8 kcal mol^{-1} lower in energy than the reactants, with a small, submerged barrier of $\sim$1.2 kcal mol^{-1} leading to formation of the SOZ in a process that is exothermic by –49.0 kcal mol^{-1}. Elsamra *et al.* described the steps leading to the formation of the SOZ as two transition states: a loose outer transition state (TS_{outer}) for the formation of the vdW complex and an inner 1,3-cycloaddition transition state (TS_{inner}) to form the SOZ. It was shown that either of the transition states could be rate-limiting depending on the temperature.[111] Jalan *et al.* found SOZ formation to increase in the order HCHO < CH_3CHO < CH_3COCH_3.[112]

In this work, we describe the results of flash photolysis broadband transient absorption spectroscopy experiments exploring the kinetics of gas phase reactions of CH_2OO with acetone, the α-diketones 2,3-butanedione (biacetyl, BiAC) and 2,3-pentanedione (acetylpropionyl, AcPr), and the β-diketones 2,4-pentanedione (acetylacetone, AcAc,) and 3,3-dimethyl-2,4-pentanedione (dMAcAc) (see Figure 2.1). The α-diketone reactions are found to be 20–40 times faster than those of acetone and β-diketones. Complementary *ab initio* calculations are used to elucidate the detailed reaction mechanisms and identify a correlation between frontier orbital energy gaps and the experimental rate constants. A strong correlation is also demonstrated between rate constants for CH_2OO + carbonyl reactions and Hammett substituent constants.

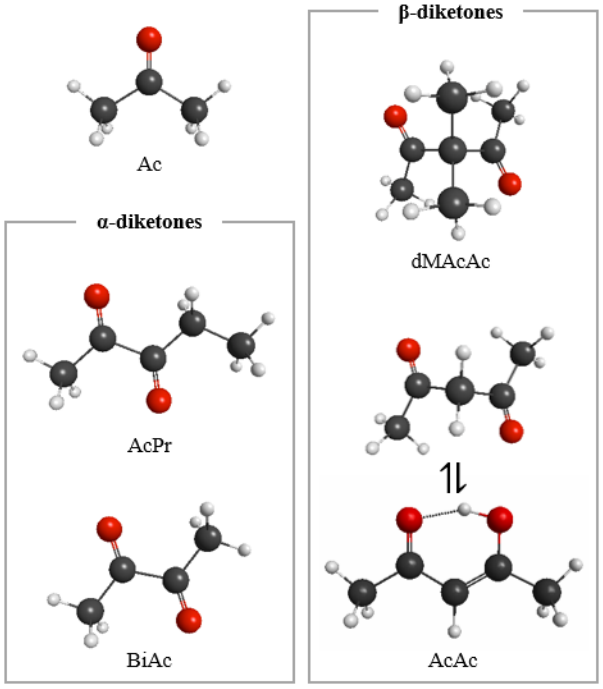


Figure 2.1 Acetone (2-propanone, Ac), the α-diketones acetylpropionyl (2,3-pentanedione, AcPr) and biacetyl (2,3-butanedione, BiAc); and the β-diketones acetylacetone (2,4-pentanedione, AcAc) and 3,3-dimethyl-2,4-pentanedione (dMAcAc). The enolone and diketone tautomers of AcAc are both shown but the former is predominant in the gas phase.

2.3 Experimental and computational methods

The flow reactor apparatus used to study the kinetics of Criegee intermediate reactions has been described in detail previously.[50,79,100] Briefly, CH_2OO was produced in a 100 cm long stainless steel flow reactor by photolysis of CH_2I_2 in the presence of excess O_2 and its time-dependent concentration was measured using broadband transient absorption spectroscopy. The 355 nm output of a Nd:YAG laser (Continuum Surelite II-10, 10 Hz repetition rate) was attenuated to provide ~8 mJ photolysis pulses (fluences of approximately ~30 mJ cm^{-2}). Transient absorption spectra were recorded in the wavelength range 360–400 nm using 500 ns duration pulses from a broadband UV LED (LightSpeed Technologies), which were dispersed in a spectrograph (Andor Shamrock 303i with iDus 420 CCD camera). Transient spectra were typically recorded at fifteen delay times ($\Delta t = t_{\mathrm{LED}} - t_{\mathrm{photolysis}}$), each derived from the average of 300 reference and signal spectra. Reference spectra were recorded with Δt = –10 μs (i.e. the LED pulse passes through the cell 10 μs before the photolysis laser). Custom data acquisition software (National Instruments LabVIEW) controls a digital delay generator (Quantum Composers 9528), which provides triggers for the laser, the LED driver, and the CCD camera, and processes raw data to generate the transient absorption spectra.

Gas flow rates into the reactor were controlled using choked-flow orifices (O'Keefe). N_2 (Praxair, 5.0 UHP) and O_2 (Airgas, 4.4 UHP) were passed through drying filters to ensure removal of residual water vapor before entering the cell. The Criegee intermediate precursor, CH_2I_2, and the carbonyl reactants are liquids at room temperature and were kept in smog bubblers (Ace Glass), which were immersed in a water bath maintained at 295 K in order to stabilize the vapor pressure and prevent evaporative cooling of the liquid. The equilibrium vapor of each reactant [Ac: 200 Torr; BiAc: 48 Torr; AcPr: 21 Torr; AcAc: 5 Torr; dMAcAc: 3 Torr (all Sigma-Aldrich, reagent grade)][145] was carried into the reactor by a flow of N_2 at a total pressure of 5 psig (1020 Torr). Experiments using BiAc were performed with the smog bubbler immersed in an ice bath at 273 K, which reduces the vapor pressure to 13 Torr. A

range of choked-flow orifices were used to control reactant concentrations, which were quantified by absorbance measurements as described below. All kinetics measurements were performed under pseudo-first order conditions of excess carbonyl compound. A small flow of nitrogen (30 sccm) was used to purge the windows and minimize formation of residue on the surfaces. An independent flow of N_2 was controlled via an adjustable tap to maintain constant total pressure. Typical total flow rates were ~3.2 sLpm, which resulted in a static pressure of ~67 Torr (~2.2×10^{18} cm^3) in the flow reactor, the majority of which was N_2 (~1.9×10^{18} cm^3). Identical CH_2I_2 and O_2 flow rates were used for all kinetics measurements and led to estimated concentrations of ~5.5×10^{14} cm^{-3} and ~2.1×10^{17} cm^{-3}, respectively. At least four independent measurements of the reaction kinetics were made for each carbonyl; the choked-flow orifices that controlled the reactant concentration were used in random order for each run to minimize systematic errors, such as deterioration of the windows.

UV/visible absorption spectra of the carbonyls were measured over the range 200–700 nm in a commercial spectrophotometer (Agilent, Cary 60 UV-Vis). A few drops of the liquids were placed in a capped quartz cuvette and the liquid/vapor mixture was allowed to reach equilibrium, which was confirmed by repeated measurements showing that the absorbance was constant with time. Absorption spectra of the carbonyl compounds were recorded in the flow reactor using LEDs centered at 420 nm and at 280 nm over the same range of reactant/N_2 flow rates used for the kinetics measurements.

Electronic structure calculations of the unimolecular reaction intermediates and energies involved were performed with the Gaussian 16[146] and GAMESS[147–149] programs. Equilibrium and transition state structures were optimized with the M06-2X hybrid functional[150] using the Dunning-type cc-pVTZ basis set augmented with diffuse functions (aug-cc-pVTZ). Minima and transition states were confirmed by frequency analysis and by following the intrinsic reaction coordinate (IRC). The structures obtained at the M06-2X/aug-cc-pVTZ level of theory were then used as input for

calculations with the CBS-QB3 compound method.[151] These levels of theory were chosen as they have been shown to provide reliable thermochemistry and geometries for reactions involving the main group elements at modest computational cost.[152–154]

2.4 Results

2.4.1 Reactant absorption spectroscopy and calibration

In contrast to the acids and alcohols studied previously,[79,100] the carbonyl species have absorption features that overlap with available UV LEDs and the concentrations obtained under typical experimental conditions can be directly quantified. Figure 2.2 shows gas phase absorption spectra for all the reactants measured in a Cary-60 spectrometer over the wavelength range 225–475 nm at 295 K. Absolute absorption cross sections were determined from application of the Beer-Lambert law, assuming equilibrium vapor pressures for each compound.[145] The measured cross sections were found to be in excellent agreement with previously reported values, where available.[155] The α-diketones AcPr and BiAc have similar absorption spectra, featuring bands in the visible and UV. The visible bands are almost identical for BiAc and AcPr, with peak absorption cross sections $\sim 7\times10^{-20}$ cm^2 and irregular vibrational structure. The UV band of BiAc is weaker than the visible band with a peak absorption of $\sim 5\times10^{-20}$ cm^2 at 271 nm. Diffuse, regular vibrational structure can be seen across the UV band. The equivalent band in the AcPr spectrum appears as a shoulder, overlapping a stronger band at 251 nm that can be assigned to the enolone tautomer that is estimated with the aid of TDDFT calculations to be present at ~0.03%. In contrast, the absorption spectra of the β-diketone absorption spectra have no bands in the visible. AcAc absorption is primarily due to the predominant enolone tautomer. The exceptionally large peak absorption cross section for AcAc (Messaadia *et al*.[156] report 4.6×10^{-17} cm^2 at 262 nm) precludes measurement at the equilibrium vapor pressure ($A > 4$). The dMAcAc spectrum appears to be qualitatively the same shape as the UV band of AcPr, albeit the maximum cross section is larger (5×10^{-19} cm^2) and the absorption peak at 268 nm is shifted ~15 nm

to longer wavelength. The lack of H-atoms on the central carbon atom in dMAcAc should prevent tautomerization.

In our previous kinetics studies,[79,100] the reactant concentrations, in cm^{-3}, were estimated using

$$[\mathrm{X}]_{\mathrm{est}} = \chi F P_{\mathrm{tot}} \frac{N_{\mathrm{A}}}{10^3 RT} \qquad \text{(E 2.1)}$$

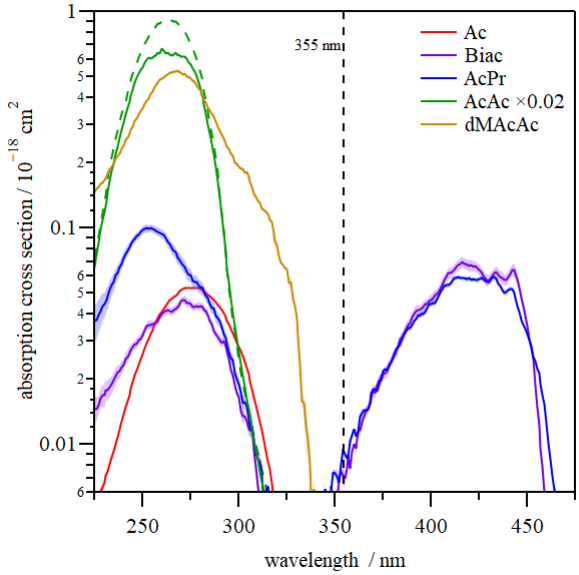


Figure 2.2 Gas phase absorption spectra at 295 K of acetone, BiAc, AcPr, AcAc, and dMAcAc. The AcAc absorption cross section values have been reduced by a factor of fifty; the dashed line is the measurement of Messaadia *et al.*,[46] which captures the peak absorption. Shaded areas are 1σ uncertainties from repeated measurements.

where χ is the mole fraction of carbonyl compound X in the X/N_2 flow, F is the fractional contribution of the X/N_2 to the total gas flow as determined from the choked-flow orifice specifications, and P_{tot} is the total pressure in the reactor, which was maintained at a constant value of 67±1 Torr for all experiments. N_A is the Avogadro constant in mol^{-1}, R = 62.364 L $Torr^{-1}$ mol^{-1} K^{-1} is the gas constant, and T is the temperature in K. Calibration measurements for each reactant were made by recording absorption spectra in the flow reactor using the same collections of choked-flow orifices to vary the concentration as in the kinetics measurements (see below). Experimental concentrations $[X]_{exp}$ were determined using the absorption cross sections shown in Figure 2.2 and used to construct calibration plots. Absorption measurements were repeated at least four times for each reactant to ensure repeatability and quantify uncertainties.

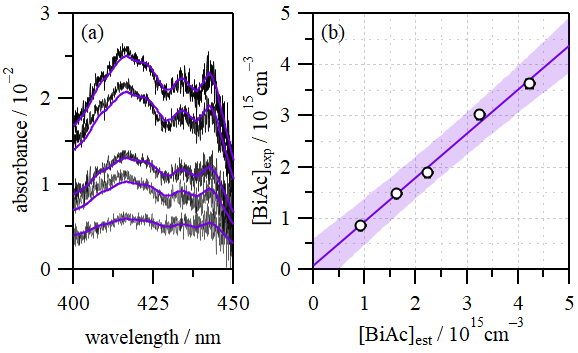


Figure 2.3 (a) Typical experimental absorbances (black) due to BiAc measured using the same selection of choked-flow orifice as in the kinetics experiments. Best-fit scaled BiAc absorption spectra are also shown (purple). (b) Calibration plot of measured concentrations, $[BiAc]_{exp}$, determined from the spectra plotted against estimated concentrations, $[BiAc]_{est}$. The gradient, $[BiAc]_{exp}/[BiAc]_{est}$ <1, indicates that reactant concentrations are slightly over-estimated. The shaded area is a 2σ prediction band.

Table 2.1 Reactant vapor pressures ($P_{vap,X}$), bimolecular rate constants derived using experimental ($k_{X,exp}$) reactant number densities, and ratio of experimentally measured reactant concentrations to those estimated ($[X]_{exp}/[X]_{est}$). The asterisk on the value of $P_{vap,BiAc}$ indicates that the liquid sample was held at 273 K rather than 295 K. All reported rate constants were derived from the *overall* fits of the experimental data (see text). Uncertainties are 1σ.

	$P_{vap,X}$ / torr	$k_{X,exp}$ / 10^{-13} cm^3 s^{-1}	$[X]_{exp}/[X]_{est}$
Ac	200.5	4.07±0.43	0.87±0.05
BiAc	13.4*	145±18	0.94±0.12
AcPr	21.2	129±15	0.84±0.10
AcAc	5.4	6.59±0.68	0.94±0.10
dMAcAc	3.4	3.54±0.79	0.97±0.09

As an example, Figure 2.3(a) shows BiAc absorption spectra recorded in the flow reactor using a visible LED centered at 420 nm. Equivalent measurements were made for AcPr, also using the 420 nm LED, while an LED centered at 280 nm was used for Ac, AcAc, and dMAcAc. The relationship between the measured and estimated concentrations is linear, as shown in Figure 2.3(b). In general, the use of equation (E 2.1) was found to systematically *over*-estimate the reactant concentrations: $[X]_{exp}/[X]_{est} < 1$ with an average value of 0.91±0.10. The origin of the discrepancy is not clear, but presumably results from surface losses as the reactant/N_2 gas mixture passes through the gas manifold into the flow reactor. The calibration factors $[X]_{exp}/[X]_{est}$ for each reactant are compiled in Table 2.1 and used to scale the estimated reactant concentrations in the kinetics measurements.

2.4.2 Transient absorption spectroscopy

CH_2OO was produced following the 355 nm photolysis of CH_2I_2 in the presence of excess O_2 and its time dependent concentration determined from analysis of transient absorption spectra recorded at various time delays after photolysis. In the absence of any additional reactants, CH_2OO is thought to be formed and removed in reactions R2a–R2c shown in Table 2.2, which is based on the model described by Ting *et al*.[157]

In the presence of excess O_2, the $CH_2I + O_2$ reaction is fast (1.4×10^{-12} cm^3 s^{-1}) and rapidly converts photolytically generated iodomethyl radicals to CH_2OO.[39] At a total pressure of 67 Torr, the fractional yield of CH_2OO via reaction (R2a) is estimated to be approximately 0.69.[157,158] Typically, maximum CH_2OO concentrations of $\sim2.5\times10^{13}$ cm^{-3} are reached approximately 10 μs after photolysis. Formation of the iodomethylperoxy adduct CH_2IO_2 via reaction (R2c) accounts for most of the remaining products, while reaction (R2b) is a minor channel.[159] The self-reaction (R4) is fast and is primarily responsible for loss of CH_2OO in the absence of other reacants.[65,118,157,160] In the analysis that follows, we hold the rate constant for CH_2OO self-reaction fixed. Under the current experimental conditions, diffusion and wall losses of CH_2OO are negligible and thermal unimolecular decomposition is too slow to significantly contribute to its loss rate.[27,118]

Figure 2.4(a) shows representative transient absorption spectra recorded at three delays (10 μs, 70 μs, and 300 μs) in the absence of any additional reactant. Absorbance in the 362–395 nm spectral region is due to CH_2OO and IO. A small fraction of the IO is formed directly by reaction (R2b), while the majority is due to the secondary reaction (R3).[157,159] The characteristic vibronic band progression[50,49,52] of CH_2OO is evident at the shortest delay but becomes increasingly indistinct at longer delays at which time the spectra increasingly resemble that of IO.[161] The transient absorption spectra shown in Figure 2.4(b) were recorded at the same time delays but with $[Ac]_{exp} \approx 2.5\times10^{16}$ cm^{-3}. The spectrum recorded at a delay of 10 μs is almost identical to that in Figure 2.4(a), indicating that

the presence of Ac has no significant effect on the CH_2OO formation kinetics. The 70 μs and 300 μs spectra in Figure 2.4(a) and (b) are distinctly different, however, and show that CH_2OO is removed more rapidly in the presence of Ac. The transient absorption spectra are decomposed by fitting to a linear combination of wavelength-dependent CH_2OO and IO absorption cross sections, $\sigma(\lambda)$,[35,54] to yield time-dependent concentrations for each absorber:

$$\frac{A(\lambda)}{l} = [CH_2OO]\sigma_{CH_2OO}(\lambda) + [IO]\sigma_{IO}(\lambda) \qquad \text{(E 2.2)}$$

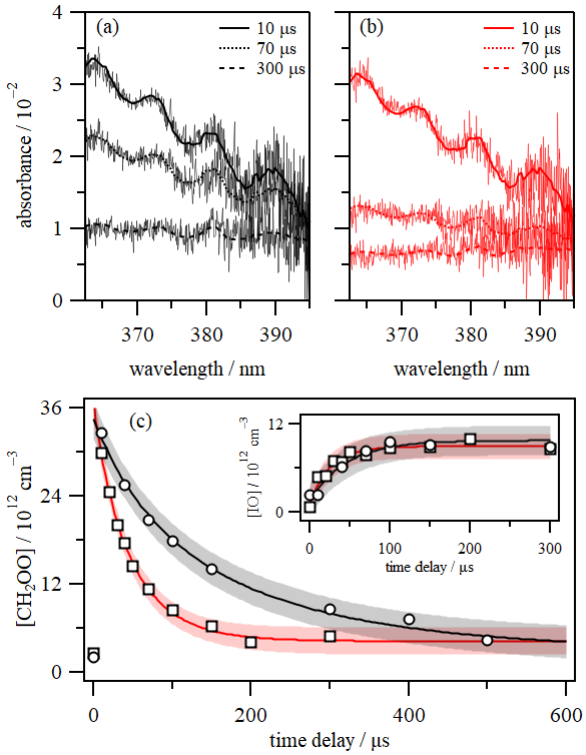


Figure 2.4 Broadband transient absorption spectra, recorded over the range 365–390 nm at the indicated time delays after photolysis (a) in the absence of any reactant and (b) in the presence of $[Ac]_{exp}$ = 2.47×10^{16} cm^{-3}. (c): Time-dependent concentration profiles for CH_2OO and IO (inset) derived from the transient absorption spectra.

Here, l is the 100 cm path length of the flow reactor. The concentration profiles of both CH_2OO and IO derived from the transient absorption spectra are shown in Figure 2.4(c). The $[CH_2OO]_t$ profile shows an increased loss rate in the presence of Ac but the peak concentrations observed at short delays are unaffected, indicating that the carbonyl reactant does not noticeably affect the chemistry leading to CH_2OO production. The $[IO]_t$ profiles are not affected by the presence of Ac; both the rise time and maximum concentration reached before slow removal by self-reaction are indistinguishable. These observations hold for all reactants (and reactant concentrations) used in the experiments.

CH_2OO loss rates are quantified using a simplified kinetic model that includes second order loss due to self-reaction (with rate constant k_{self}) and other processes that are assumed to follow first order (or pseudo-first order) kinetics (rate constant k_{loss}). The differential rate equation for the CH_2OO concentration is written as

$$\frac{d[CH_2OO]}{dt} = -2k_{self}[CH_2OO]^2 - k_{loss}[CH_2OO] \quad \text{(E 2.3)}$$

where

$$k_{loss} = k_{bgd} + k_X[X] \quad \text{(E 2.4)}$$

is the observed loss rate, which is partitioned between pseudo-first order loss due to reaction with carbonyl species X with rate constant k_X and the phenomenological background loss rate, k_{bgd}, that is observed in the absence of any carbonyl compound. Equation (E 2.3) can be solved analytically to yield the integrated rate equation:

$$[CH_2OO]_t = \frac{k_{loss}[CH_2OO]_0}{k_{loss}\exp(k_{loss}t) - 2k_{self}[CH_2OO]_0[1 - \exp(k_{loss}t)\,]} \quad \text{(E 2.5)}$$

Experimental concentration-time profiles are fit to Equation (E5) to extract k_{loss} with k_{self} constrained to the value of 7.4×10^{-11} cm^3 s^{-1} reported by Chhantyal-Pun *et al.*[118] The values of k_{loss} obtained from

the fits are insensitive to the precise value of k_{self} chosen. A re-analysis of a subset of the experimental data using the JPL recommended value[91] of 7.12×10^{-11} cm^3 s^{-1} had only a very modest effect on the values of k_{loss}, and a negligible effect on the bimolecular rate constants. Examples of the typical quality of the fits to the experimental data obtained using Equation (E 2.5) can be seen in Figure 2.4(c).

Rate constants were measured under pseudo-first order conditions of excess carbonyl reactant. Each experimental run involved measurements at five concentrations that spanned the range 10^{14}–10^{17} cm^{-3}. With the exception of Ac, discussed in detail below, the loss rates were observed to increase linearly with the reactant concentration. The concentration range was constrained somewhat by the reaction rates, the available choked-flow orifices, the reactant vapor pressures, and the need to maintain constant total pressure in the flow reactor. Measurements were repeated at least four times for each reaction to ensure repeatability and to quantify the experimental uncertainties. Rate constants were obtained by simultaneously fitting the *overall* data sets to equation (E 2.4) to extract values of k_{bgd} and k_X. In addition to fitting the *overall* data sets, two other approaches were also adopted. First, independent linear fits were performed for each *individual* experimental run, and the results averaged. Second, after noting that in most experiments, the variance in k_x was typically much smaller than that in k_{bgd}, individual kinetics runs were fit simultaneously, allowing k_{bgd} to vary independently, but returning a single *global* value of k_X. All three fitting approaches (*overall*, *individual*, and *global*) yielded consistent values for k_{bgd} and k_X. Only the values obtained from the *overall* fits are discussed in the text and summarized in Table 2.1.

The $[X]_{exp}/[X]_{est}$ ratios determined from repeated measurements for each reactant are also compiled in Table 2.1, alongside rate constants, $k_{X,exp}$. While the uncertainties in $[X]_{exp}/[X]_{est}$ are relatively small, they are typically larger than the statistical uncertainties resulting from either data fitting or among the individual measurements of k_1. For each reaction rate constant, the reported uncertainty (1σ) is

based on the larger of the relative uncertainties arising from the fitting or the concentration calibration factor (~10–20%).

The pseudo-first order loss rates observed for the CH_2OO + Ac reaction are plotted as a function of the estimated Ac concentrations in Figure 2.5. Fitting the *overall* data set, which comprises five individual kinetic runs, to Equation (E 2.4) yields $k_{Ac} = (5.6\pm0.3)\times10^{-13}$ cm^3 s^{-1}, which is ~40% larger than previous measurements.[88,128,111] While equation (E 2.4) provides a plausible fit to the data the relatively high concentrations of [Ac] and slight curvature evident in Figure 2.5, suggests an additional contribution to the loss rate from acetone dimer, Ac_2. Using data from Anderson *et al.*,[162] the equilibrium constant for formation of acetone dimer at 295 K is $K_p = 0.098$ atm^{-1} ($K_c = 4.2\times10^{-21}$ cm^3), leading to dimer concentrations [Ac_2] =4.1×10^{10} cm^{-3} to 7.5×10^{12} cm^{-3} (or 13–177 ppm). While these concentrations are low, acetone dimer may contribute to CH_2OO loss if the reaction rate

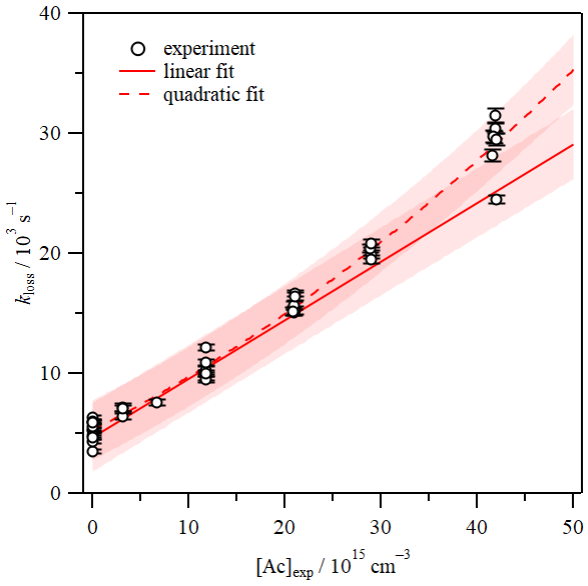


Figure 2.5 Observed pseudo-first order loss rates (symbols), and linear (solid line) and quadratic fits (dashed line) for the reaction of CH_2OO with Ac at 295 K and 67 Torr. The shaded areas represent 2σ prediction bands.

constant is sufficiently large relative to that of the monomer reaction. Consequently, we include an additional term $k_{\mathrm{Ac_2}}[\mathrm{Ac_2}]$ to equation (E4), leading to

$$k_{\mathrm{loss}} = k_{\mathrm{bgd}} + k_{\mathrm{Ac}}[\mathrm{Ac}] + k_{\mathrm{Ac_2}}K_{\mathrm{c}}[\mathrm{Ac}]^2 \qquad \text{(E 2.6)}$$

where

$$[\mathrm{Ac_2}] = K_{\mathrm{c}}[\mathrm{Ac}]^2 \qquad \text{(E 2.7)}$$

Fitting to the quadratic equation (E 2.6) yields an improved fit (shown in Figure 2.5) with k_{Ac} = (4.1±0.4)×10^{-13} cm^3 s^{-1} and $k_{\mathrm{Ac_2}}K_{\mathrm{c}}$ = (3.9±1.0)×10^{-30} cm^6 s^{-1}, with the former rate constant agreeing well with previous measurements for the CH_2OO + Ac reaction.[88,128,111] At the upper end of the [Ac] range, the dimer reaction is responsible for up to 30% of the total CH_2OO loss while at the lower end of the range (specifically [Ac] < 10^{16} cm^{-3}, i.e. the range of concentrations used for the other reactions discussed below) the dimer contribution is at most a few %.

Although imprecisely determined, the value obtained for $k_{\mathrm{Ac_2}}K_{\mathrm{c}}$ suggests an extremely large rate constant of (9.2±2.4)×10^{-10} cm^3 s^{-1} for the CH_2OO + Ac_2 reaction. By comparison, reaction of CH_2OO with water dimer is indeed much faster than the monomer. However, the reaction mechanism involves direct participation of both water molecules in the transition state resulting in a much higher rate via an autocatalytic mechanism. In the case of acetone dimer, there is less reason to expect the dimer to react much more rapidly than the monomer. It is possible that the presence of the second acetone molecule could stabilize the cycloaddition transition state to some extent resulting in an increased reaction rate.

Figure 2.6 shows the analogous pseudo-first order loss rates observed for the CH_2OO + BiAc, AcPr, AcAc, and dMAcAc reactions, alongside linear fits to equation (E 2.4). The α-diketone reactions have rate constants that are far larger than acetone. Based on the *overall* fits to the complete data sets we

find for the α-diketones that k_{BiAc} = (1.45±0.18)×10^{-11} cm^3 s^{-1} and k_{AcPr} = (1.29±0.15)×10^{-11} cm^3 s^{-1}. In contrast, the rate constants for the β-diketones are similar in magnitude to that of acetone with values of k_{AcAc} = (6.2±0.5)×10^{-13} cm^3 s^{-1} and k_{dMAcAc} = (3.4±0.8)×10^{-13} cm^3 s^{-1}. For the β-diketone reactions, the limited range of reactant concentrations restricted the maximum observed loss rates to only ~1.5–2 × k_{bgd} and the rate constants may be better considered cautiously as upper limits. The range of reactant concentrations used are much smaller, with [X] < 8×10^{15} cm^{-3}. Under these conditions, any contributions to the observed CH_2OO loss from dimers are expected to be negligible and no curvature is observed in the pseudo-first order plots.

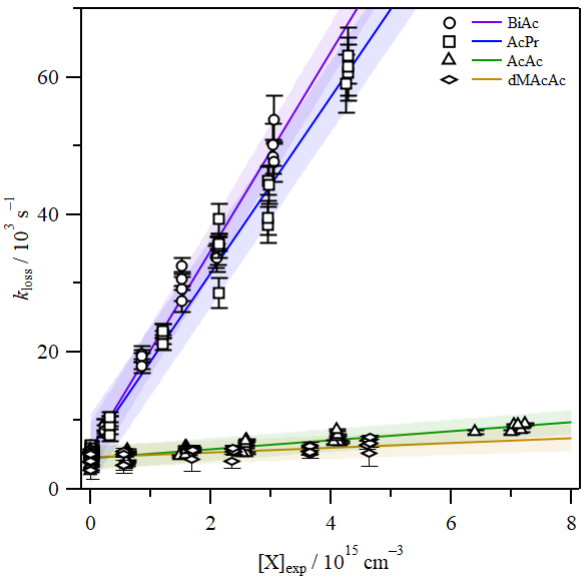


Figure 2.6 Observed pseudo-first order loss rates (symbols) and fits (lines) for the reaction of CH_2OO with BiAc (circle, purple), AcPr (square, blue), AcAc (triangle, green) and dMAcAc (diamond, yellow) at 295 K and 67 Torr. The shaded areas represent 2σ prediction bands.

2.4.3 Modeling and systematic uncertainties in k_{loss}

To explore the robustness of determining k_{loss} by fitting $[CH_2OO]_t$ profiles to equation (E 2.4) and to identify any systematic uncertainties, we have performed simulations of the reaction kinetics. The simulations use the detailed mechanism for the $CH_2I + O_2$ system described by Ting *et al*.,[157] implemented in the stochastic kinetics simulation program *Kinetiscope* (version 1.1.956.x64).[163] The complete mechanism and the rate constants for each reaction appropriate for our experimental conditions are compiled in Table 2.2, and the key reactions are summarized here. The initial reaction between $CH_2I + O_2$ displays pressure-dependent branching as outlined in reactions (R2a), (R2b), and (R2c), with relative quantum yields of 0.69, 0.04, and 0.27, respectively, at 67 Torr. Ting *et al*. do not directly assign the products of reaction 2b as HCHO + IO, but we chose to do so here based on previous work that found it necessary to describe the early-time IO concentrations. CH_2OO is removed via several reactions. The reverse of reaction (R2a), shown as reaction (R3a), regenerates CH_2I, although cycling is effectively over in the first ~10 μs following photolysis, beyond which the CH_2OO concentration declines. There are two major loss processes for CH_2OO: self-reaction (R4) and reaction with I atoms, which can lead either to HCHO + IO via reaction (R3b) or to the CH_2IO_2 adduct via reaction (R3c). IO is formed predominantly by the reactions of I atoms with either CH_2OO via reaction (R3b) or with the adduct CH_2IO_2 in reaction R5. In turn, IO loss is driven by its self-reaction. shows simulated $[CH_2OO]_t$ and $[IO]_t$ profiles where initial concentrations of $[CH_2I]_0 = [I]_0 = 4.0\times10^{13}$ cm^{-3} and $[O_2]_0 = 2.1\times10^{17}$ cm^{-3} were used. The simulations are compared to average experimental concentration profiles measured in the absence of any carbonyl reactant. The experimental data shown in Figure 2.7 correspond to background measurements made in the course of BiAc and Ac experiments. While the simulation reproduces the peak $[CH_2OO]$ concentration reasonably well the loss is slower than the experiment: analysis of the simulated $[CH_2OO]_t$ profile using equation (E 2.5) yielded $k_{bgd} \approx$

3000 s^{-1}. The simulated and experimental $[IO]_t$ profiles show similar discrepancies; maximum IO concentrations are in good agreement, but experimentally IO is observed to form much more quickly. Fitting the simulated data to equation (E 2.4) returned bimolecular rate constants that were systematically lower than the values used in the model. For the faster BiAc reaction, analysis of the simulated $[CH_2OO]_t$ profiles returned a value of $k_{BiAc,sim}$ = $(1.18\pm0.03)\times10^{-11}$ cm^3 s^{-1}, which is 86% of the input value used in the model. The discrepancy for the slower Ac reaction was smaller, with $k_{Ac,sim}$ = $(3.8\pm0.2)\times10^{-13}$ cm^3 s^{-1} being 93% of the input value. These results could imply that the analysis results in a modest systematic and *k*-dependent underestimation of the true bimolecular rate constants. Although, the simulations show several qualitative discrepancies from the experiments as will be discussed further below.

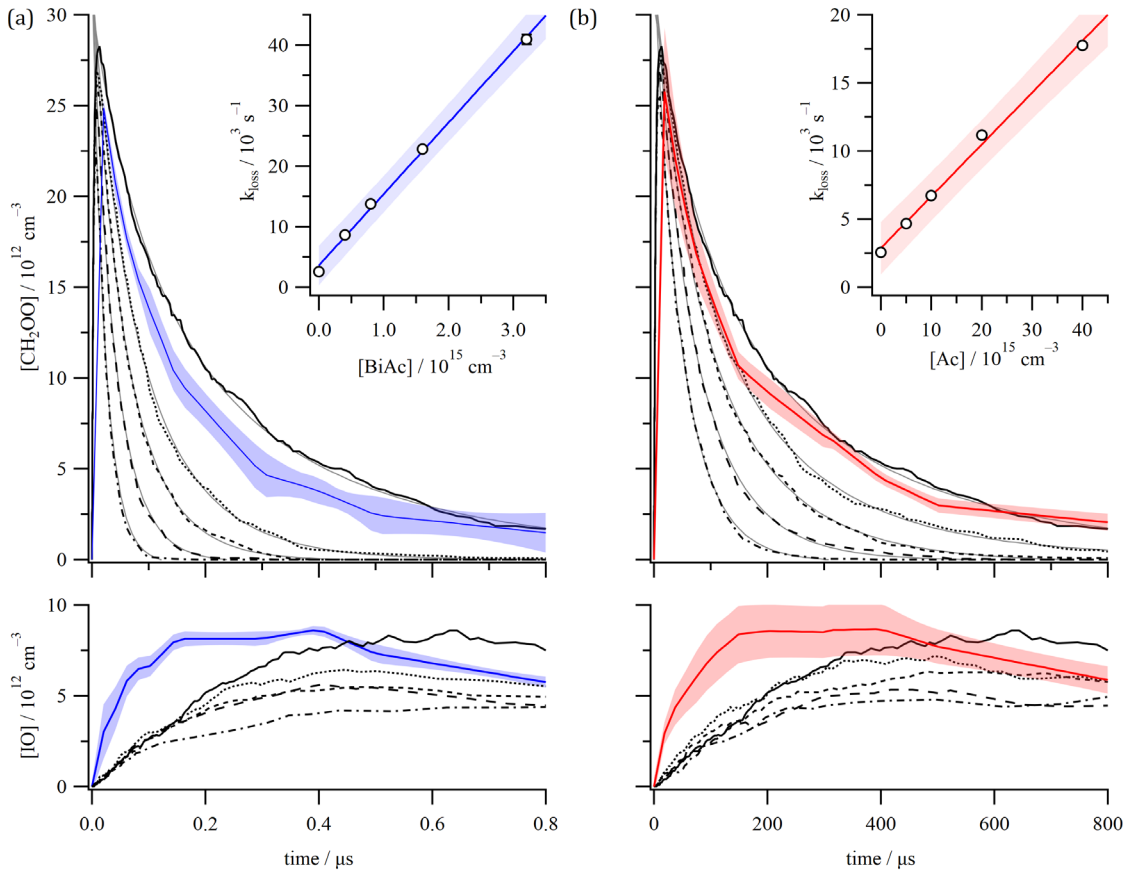


Figure 2.7 Simulated $[CH_2OO]_t$ and $[IO]_t$ profiles at various concentrations of BiAc and Ac. In panel (a) [BiAc] / 10^{15} cm^{-3} = 0 (solid), 0.4 (dotted), 0.8 (short dash), 1.6, long dash), 3.2 (dash-dot). In panel (b) [Ac] / 10^{16} cm^{-3} = 0 (solid), 0.5 (dotted), 1.0 (short dash), 2.0, long dash), 4.0 (dash-dot). Average experimental profiles in the absence of BiAc and Ac are shown as blue and red lines respectively, with 1σ uncertainties shaded. Inset: pseudo-first order loss rates plotted as a function of the reactant determined from analysis of simulated $[CH_2OO]_t$ profiles. Linear fit is shown with shaded area representing 2σ prediction band.

Table 2.2 Mechanism and reaction rate constants used to simulate $CH_2I + O_2$ reaction from Ting *et al*. following the photolysis of diiodomethane (R1).[164]

#	reaction	k / $cm^3\ s^{-1}$ or s^{-1}	comments
1	$CH_2I_2 \rightarrow CH_2I + I$		
2	$CH_2I + O_2 \rightarrow$ products	1.5×10^{-12}	Average of previous measurements.
2a	$CH_2I + O_2 \rightarrow CH_2OO + I$	1.2×10^{-12}	Φ = 0.69 at 67 Torr.
2b	$CH_2I + O_2 \rightarrow HCHO + IO$	7.1×10^{-14}	Φ= 0.06 at 67 Torr, products identified based on Foreman and Murray.[159]
2c	$CH_2I + O_2 + M \rightarrow CH_2IO_2 + M$	2.9×10^{-13}	Φ = 0.27 at 67 Torr.
3	$CH_2OO + I \rightarrow$ products		$k_3 = k_{3a} + k_{3b} + k_{3c}$
3a	$CH_2OO + I \rightarrow CH_2I + O_2$	6.6×10^{-11}	Reverse of 2a, based on equilibrium constant, adjusted .
3b	$CH_2OO + I \rightarrow HCHO + IO$	9.0×10^{-12}	Theory predicts 5.5×10^{-14} $cm^3\ s^{-1}$, adjustment needed to reproduce early time IO.
3c	$CH_2OO + I + M \rightarrow CH_2IO_2 + M$	1.6×10^{-11}	Estimated based on equilibrium considerations.
4	$CH_2OO + CH_2OO \rightarrow 2\ HCHO + O_2$	8.0×10^{-11}	Determined by Ting *et al.* [164] Value consistent with subsequent JPL recommended value 7.1×10^{-11} $cm^3\ s^{-1}$
5	$CH_2IO_2 + I \rightarrow ICH_2O + IO$	3.5×10^{-11}	Gravestock *et al.*[165] Value taken from Table 1, although text suggests range (1–2)$\times10^{-11}$ $cm^3\ s^{-1}$
6	$CH_2IO_2 + CH_2IO_2 \rightarrow 2\ ICH_2O + O_2$	9.0×10^{-11}	Gravestock et al.[165] citing Sehested et al.[166] Text suggests range of (6–12)$\times10^{-11}$ $cm^3\ s^{-1}$
7	$ICH_2O \rightarrow HCHO + I$	10^5	Gravestock *et al.*[165] Value in footnote to Table 1 is 10^6 s^{-1}
8	$IO + IO \rightarrow$ products	9.9×10^{-11}	IUPAC[18] recommended value
	$CH_2OO + Ac \rightarrow$ products	4.1×10^{-13}	This work
	$CH_2OO + BiAc \rightarrow$ products	1.4×10^{-11}	This work

2.4.4 Computational results

Reaction Energetics: The reactions of CIs with carbonyl compounds primarily occur through 1,3-cycloaddition across the carbonyl double bond leading to the formation of a cyclic secondary ozonide (SOZ).[112] Stationary points on this reaction pathway were identified at the M06-2X/aug-cc-pVTZ and CBS-QB3 levels of theory for reaction of CH_2OO with Ac (an aliphatic ketone), BiAc (a model α-diketone), and both the diketone (β-diketone) and enolone tautomers of AcAc. The energies calculated for reaction of CH_2OO with these chosen carbonyls are shown in Table 2.3 at the M06-2X/aug-cc-pVTZ and CBS-QB3 levels of theory. The reaction pathways are also illustrated in Figure 2.8 in terms of the changes in free energy (ΔG) at 298 K and the electronic energies at 0 K with zero-

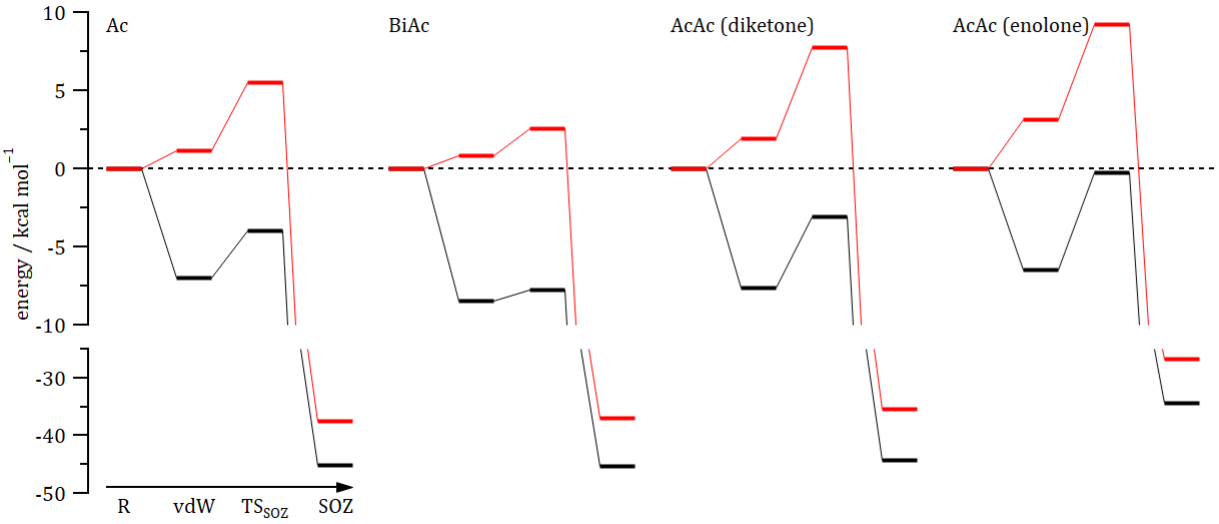


Figure 2.8 Stationary points on the potential energy surfaces for reactions of CH_2OO with representative carbonyls acetone (Ac), biacetyl (BiAc) and both diketone and enolone tautomers of acetylacetone (AcAc). Energies of reactants (R), entrance channel van der Waals complex (vdW), cycloaddition transition state (TS_{SOZ}), and secondary ozonide products (SOZ) are shown for each reaction. Energies were calculated at the CBS-QB3 level of theory (see Table 2.3) as described in the text. Free energies (ΔG; 298 K) and zero-point corrected electronic energies (ΔE + ZPE; 0 K) are shown in red and black, respectively.

point energy (ZPE) correction (ΔE + ZPE) calculated at the CBS-QB3 level of theory. Thermal corrections are calculated within the rigid rotor, harmonic oscillator (RRHO) approximation and inaccuracies due to incomplete treatment of low-frequency vibrations and hindered internal rotations are expected.

As can be seen in Figure 2.8, the cycloaddition reaction is initiated by the formation of a van der Waals entrance channel complex (vdW), typically stabilized at the zero-point level by ~7–12 kcal mol^{-1} with respect to the reactants. From the vdW minimum, the cycloaddition transition state (TS_{SOZ}) that leads to SOZ formation is higher in energy, but in all cases submerged relative to the separated reactants in terms of the zero-point corrected electronic energies. The TS_{SOZ} complex is lower in energy by ~0–10 kcal mol^{-1} with respect to reactants depending on the carbonyl species and level of theory used. However, the entropic contribution to the free energy moves the relative energies of both the entrance channel complex and the transition state structure above the reactants by ~0–3 kcal mol^{-1} and ~3–10 kcal mol^{-1}, respectively (see Table 2.3). The formation of the SOZ is highly exoergic (ΔG ranges from –27 kcal mol^{-1} to –41 kcal mol^{-1}), and this energized intermediate can undergo several further isomerization and decomposition reactions.[112] However, we do not characterize these subsequent reactions in detail as the cycloaddition reaction to form the SOZ will be most important in dictating the overall reaction kinetics, and the experimental technique used here is insensitive to the products formed.

Overall, both the M06-2X/aug-cc-pVTZ and CBS-QB3 levels of theory provide a similar picture of the energetics for the cycloaddition reaction pathway of CH_2OO to the carbonyls studied here. For acetone, the free energy of the transition state is ~5 kcal mol^{-1} above the separated reactants. The reaction of CH_2OO with acetone has been studied previously by Jalan *et al.*,[112] however, only the ΔE+ZPE; 0 K energies were reported. Using B3LYP geometries and electronic energies refined with RCCSD(T)-F12a, the electronic energies of the vdW and TS_{SOZ} complexes were calculated to be –7.6

Table 2.3 Relative energies (ΔE+ZPE at 0 K), including zero-point contributions, and free energies (ΔG at 298 K), evaluated using RRHO partition functions, calculated at the M06-2X/aug-cc-pVTZ and CBS-QB3 levels for the SOZ pathway (see Figure 2.8) for reactions of CH_2OO with acetone (Ac), biacetyl (BiAc), and the enolone and diketone tautomers of acetylacetone (AcAc). All energies are reported in kcal mol^{-1}.

M06-2X/aVTZ	ΔE+ZPE ($\Delta G_{298\,K}$)		
	vdW	TS_{SOZ}	SOZ
Ac	–9.7 (0.7)	–6.8 (5.3)	–54.3 (–41.0)
BiAc	–10.7 (0.2)	–9.5 (2.7)	–54.1 (–41.4)
AcAc (keto)	–11.7 (0.2)	–5.7 (7.2)	–53.2 (–39.2)
AcAc (enol)	–8.1 (2.7)	–2.3 (9.5)	–41.6 (–28.9)
CBS-QB3	ΔE+ZPE ($\Delta G_{298\,K}$)		
	vdW	TS_{SOZ}	SOZ
Ac	–7.0 (1.2)	–4.0 (5.5)	–45.1 (–37.5)
BiAc	–8.4 (0.8)	–7.8 (2.5)	–45.3 (–37.0)
AcAc (keto)	–7.7 (1.9)	–3.1 (7.8)	–44.3 (–35.4)
AcAc (enol)	–6.5 (3.1)	–0.3 (9.2)	–34.4 (–26.8)

kcal mol^{-1} and –4.9 kcal mol^{-1}, respectively. These values are nearer to the CBS-QB3 values reported here. This should be expected though, as the CBS-QB3 composite method also utilizes B3LYP optimized geometries for subsequent coupled cluster calculations.[151]

For BiAc, both levels of theory predict a significantly lower free energy barrier of TS_{SOZ} of ~2.5 kcal mol^{-1} compared to an aliphatic ketone such as Ac. This is qualitatively consistent with the experimental results where α-diketones (BiAc and AcPr) have measured rate constants an order of magnitude larger than the other carbonyl species (see Table 1). This suggests that α-diketones in general undergo rapid cycloaddition reactions with CIs. By contrast, both the enolone and diketone tautomers of AcAc have higher barriers to cycloaddition compared to acetone and BiAc. In fact, TS_{SOZ} of the enolone tautomer, the dominant tautomer in the gas phase, has a calculated free energy of nearly 10 kcal mol^{-1} above the separated reactants. This would indicate that the reaction rate for SOZ formation would be significantly slower for AcAc by comparison to Ac and BiAc.

In addition to the cycloaddition pathway characterized here, it is also possible for α,β-unsaturated carbonyls such as methacrolein (MACR) and methyl vinyl ketone (MVK) to undergo another cycloaddition reaction involving the carbonyl oxygen and the β-vinylic carbon leading to a seven-membered, cyclic adduct.[141] However, previous study of the reaction of CH_2OO with MACR and MVK using PIMS saw no evidence for the formation of these species and concluded that the reaction proceeds near exclusively through addition to the carbonyl C-O bond leading to the five-membered, cyclic SOZ.[141] Though this reaction is also possible for the enolone tautomer of AcAc, we do not calculate this alternative cycloaddition pathway given these previous observations.

With the results from Table 2.3, we can provide an estimate of the relative magnitudes for the rate constants of CH_2OO with carbonyls using a simplified, two-step model for the overall reaction rate.[79,95,96]

$$CH_2OO + R(CO)R' \rightleftharpoons [vdW] \rightarrow SOZ \qquad \text{(R 2.1)}$$

For this model, it is assumed that the vdW complex formation is in an established equilibrium such that the rate constant for the reaction for a given carbonyl can be expressed as

$$k_{\mathrm{C=O}} = K_{\mathrm{eq}} k_{\mathrm{SOZ}} \quad \text{(E 2.8)}$$

where K_{eq} is the equilibrium constant for vdW complex formation and k_{SOZ} is the rate of passage over the cycloaddition transition state (TS_{SOZ}). Canonical transition state theory (CTST) can then be used to calculate this rate constant:

$$k_{\mathrm{SOZ}} = \kappa \frac{k_{\mathrm{B}} T}{h} \exp\left(-\frac{\Delta G^{\circ}}{RT}\right) \quad \text{(E 2.9)}$$

Table 2.4 Rate constants at 298 K calculated using the two-step model (E 2.8 – E 2.9) and the values of ΔG at the M06-2X/aug-cc-pVTZ and CBS-QB3 levels of theory (see Table 2.3).

M06-2X/aVTZ	K_{eq} / 10^{-20} cm^3	k_{SOZ} / 10^{7} s^{-1}	$k_{\mathrm{C=O}}$ / 10^{-11} cm^3 s^{-1}
Ac	1.3	190	2.4
BiAc	2.8	8200	230
AcAc (keto)	3.1	2.5	0.076
AcAc (enol)	0.044	3.5	0.0015
CBS-QB3	K_{eq} / 10^{-20} cm^3	k_{SOZ} / 10^{7} s^{-1}	$k_{\mathrm{C=O}}$ / 10^{-11} cm^3 s^{-1}
Ac	0.55	300	1.6
BiAc	1.0	30000	300
AcAc (keto)	0.15	21	0.031
AcAc (enol)	0.02	13	0.0027

where κ is the transmission coefficient (assumed to be unity here); k_B is the Boltzmann constant; T is temperature; h is Planck's constant. The rate constants calculated with this method are included in Table 2.4. While the absolute values of the calculated rate constants using this simplified model differ from the experimental values, there is general agreement with observed experimental trends. Applying this model at both the M06-2X/aug-cc-pVTZ and CBS-QB3 levels of theory, BiAc is predicted to react two orders of magnitude faster than acetone but ~10^3–10^4 times faster than the keto- and enolone tautomers of AcAc deviating more from the relative rates measured experimentally.

The rate constants are extremely sensitive to the transition state barrier height, so it is likely that further refinement of these energies would improve the theoretical rate constants as well as a more

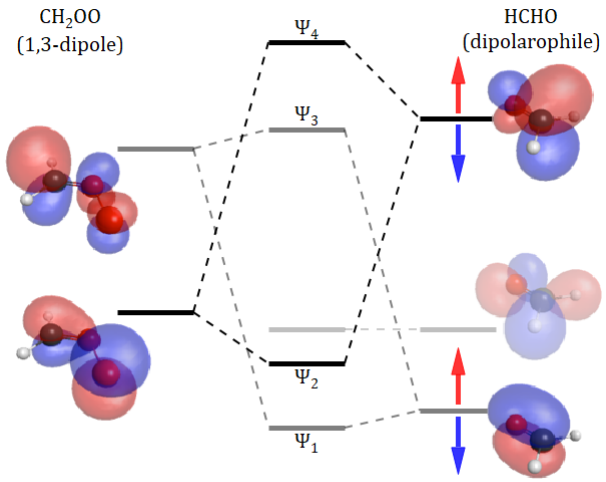


Figure 2.9 Schematic molecular orbital diagram, for the 1,3-dipolar cycloaddition reaction between CH_2OO and HCHO. Relative orbital energies are based on M06-2X/aug-cc-VTZ calculations. The "antisymmetric" combination (gray) has a large energy gap ΔE_A and gives rise to the Ψ_1, Ψ_3 bonding and anti-bonding molecular orbitals. The "symmetric" combination (black) has a smaller energy gap ΔE_S and gives rise to the Ψ_2, Ψ_4 pair. Red arrows: effect of electron-donating substituents; blue arrows: effect of electron-withdrawing substituents.

accurate treatment of the electronic structure, along with a careful evaluation of the molecular partition functions, including hindered internal rotors and tunneling corrections that go beyond the RRHO approximation.

Frontier Molecular Orbitals: The reactions of CIs with carbonyl compounds are typically viewed as 1,3-dipolar cycloaddition reactions,[167] where the CI is the 1,3-dipole and the carbonyl compound is the dipolarophile. The mechanism is analogous to a Diels-Alder reaction, which is achieved primarily through an interaction between the highest occupied molecular orbital (HOMO) of the electron rich species and the lowest unoccupied molecular orbital (LUMO) of the electron deficient species. In the case of forming the SOZ, the more electron rich carbonyl oxide would initiate bond formation via interaction of its HOMO with the π* LUMO of the carbonyl.[124,125]

The effects of carbonyl substituents on reactivity can be understood qualitatively using a model initially described by Sustmann,[168,169] which considers the symmetry-allowed interactions of the molecular orbitals on each reactant and quantitatively using concepts from frontier molecular orbital theory.[124,125] Figure 2.9 shows schematically the orbitals involved for the model CH_2OO + HCHO reaction, based on Figure 1 from Sustmann.[168] Based on loose symmetry considerations, the CI nonbonding orbital (HOMO) interacts with the π* orbital (LUMO) of the carbonyl ("symmetric", $\Delta E_S = |n_{CI} - \pi^*_{C=O}|$), while the CI π* orbital (LUMO) interacts with the π orbital (HOMO–1) of the carbonyls ("antisymmetric", $\Delta E_A = |\pi^*_{CI} - \pi_{C=O}|$). The former energy gap ΔE_S is smaller than ΔE_A and this interaction makes the greater contribution to stabilizing the TS. Electron-withdrawing substituents on the carbonyl (dipolarophile) will lower the energies of the π* and π orbitals, decreasing ΔE_S (stabilizing the TS) at the expense of increasing the already larger value ΔE_A. In contrast, electron-donating substituents will raise the energies of the π* and π orbitals, increasing ΔE_S and de-stabilizing the TS. Therefore, it would be expected that carbonyls with electron-withdrawing substituents would undergo more rapid cycloaddition with a given CI due to the smaller ΔE_S energy gap.

Table 2.5 Frontier orbital energies calculated at the M06-2X/aVTZ level.

	E_{π} / eV	E_{π^*} / eV	ΔE_S / eV	ΔE_A / eV
CH_2OO	–8.77[a]	–1.65		
acetaldehyde (AcA)	–11.95	0.32	9.09	10.29
acetone (Ac)	–11.51	0.87	9.64	9.85
hexafluoroacetone (HFA)	–14.56	–1.86	6.91	12.91
biacetyl (BiAC)	–12.11	–1.30	7.47	10.46
acetylpropionyl (AcPr)	–12.09	–1.24	7.53	10.44
acetylacetone (AcAc, diketone)	–11.92	–0.42	8.35	10.27
acetylacetone (AcAc, enolone)	–11.72	–0.40	8.37	10.06
3,3-dimethyl-2,4-pentanedione (dMAcAc)	–11.60	–0.49	8.28	9.95
methylvinylketone (MVK)	–11.96	–0.78	7.99	10.31
methacrolein (MACR)	–12.65	–0.82	7.95	11.00

To explore these trends in more detail, the frontier orbital energies for the n_0 and the π^* orbitals of the simplest CI (CH_2OO) and a range of carbonyls with known CI reaction rate constants were calculated at the M06-2X/aVTZ level of theory. These values are shown in Table 2.5 along with the corresponding values for ΔE_S and ΔE_A. For this analysis, only the π orbitals are considered; we neglect any contribution from the non-bonding n_O (HOMO) of the carbonyls. These results will be discussed further below with detailed comparison to the known CI reaction rate constants of each carbonyl.

2.5 Discussion

2.5.1 Systematic uncertainties in k_{loss}

Analysis of $[CH_2OO]_t$ profiles obtained from simulations using the detailed mechanism and rate constants for the $CH_2I + O_2$ reaction reported by Ting et al.[157] suggested that fitting to equation (E 2.5) may lead to a possible systematic and k-dependent underestimation of the true bimolecular rate constants for the CH_2OO + X reactions. For the faster reaction CH_2OO + BiAc, the rate constant was ~84% of the value used in the simulation, while a smaller discrepancy of ~93% was found for the slower CH_2OO + Ac reaction. We note that the value of k_{Ac} (discussed below) is in good agreement with previous measurements although a correction for the systematic error implied by the modeling would increase it by only 7%, which is within the reported uncertainty. A greater increase of ~19% would be implied for the BiAc reaction rate constant. However, the model has sufficient deficiencies, which would suggest that any such correction is unjustified.

As has already been noted, the decay rate of CH_2OO and formation rate of IO in the absence of an additional reactant are both underpredicted when compared to the experimental data, although the peak concentrations are well-reproduced. Inclusion of BiAc or Ac reactions in the simulation leads to increased loss rates of CH_2OO, which were observed experimentally, but also decreased yields of IO, which were not. Within the reaction model, IO is formed by the reactions of I atoms with CH_2OO via reaction (R3b) or with CH_2IO_2 via reaction (R5). Increasing BiAc or Ac concentrations compete with I atoms for CH_2OO and reduce the contribution of reaction (R3b) to the IO yield. At the highest simulated reactant concentrations, maximum [IO] is reduced by around a factor of two relative to the background conditions, in contrast to the experiments, which show no noticeable effect on the $[IO]_t$ profiles.

Neither rate constant for IO production used in the model has been measured directly. Ting *et al*.[157] report a value of 9.0×10^{-12} cm^3 s^{-1} for reaction (R3b), although this value was adjusted significantly from a much smaller theoretical value of 5.5×10^{-14} cm^3 s^{-1} to better describe early time IO formation. Similarly, the rate constant for reaction (R5) of 3.5×10^{-11} cm^3 s^{-1} is taken directly from earlier estimates based on mechanisms that explicitly did not include the CI.[166,165] Adjustment of these rate constants, or alternatively exclusion of existing reactions or inclusion of additional reactions could be used to bring the simulations into better agreement with the experimental observations across the range of reactant concentrations. However, it is unclear that such revisions would necessarily provide greater confidence that implied systematic uncertainties in the rate constants for the reactions of CH_2OO with additional reactants are real. The current experimental results do, however, suggest that IO production is effectively decoupled from CH_2OO loss. The initial branching fraction for reaction (R2a) appears to be in accord with the experimental observations and the maximum observed [IO] is consistent with the expected yield of the CH_2IO_2 adduct via reaction (R2b). A parsimonious explanation is that IO is formed near exclusively from conversion of the CH_2IO_2 adduct, likely via reaction (R5), although a significantly larger rate constant for this reaction would be necessary to account for the early time kinetics.

2.5.2 Previous measurements

Only the CH_2OO + Ac reaction has been studied previously. The rate constant determined in this work (k_{Ac} = 4.1×10^{-13} cm^3 s^{-1} at 295 K and 67 Torr) is in reasonably good agreement with previous measurements made at similar temperatures and pressures. Two previous measurements have used the same photochemical method to produce CH_2OO. A value of 2.3×10^{-13} cm^3 s^{-1} was measured by Taatjes *et al*. at 293 K and 4 Torr while Elsamra *et al*. found a positive pressure dependence over 4–50 Torr and a rate constant of 3.5×10^{-13} cm^3 s^{-1} at the upper end of the range at 298 K.[111,128] The value determined in the current work at 67 Torr lies on the trend suggested by the pressure-dependent

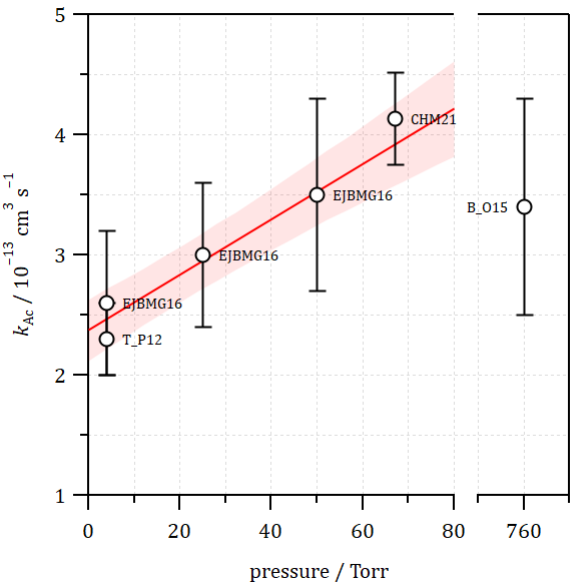


Figure 2.10 Pressure dependence of rate constants for the CH_2OO + acetone reaction. Previous results from Taatjes *et al*. [T_P12],[4] Berndt *et al*. [B_O15],[5] and Elsamra *et al*. [EJBMG16J[6] are compared to the current results [CHM21]. A linear fit to the data of Elsamra *et al*. is shown in red, with the shaded area representing a 1σ prediction band.

measurements in Figure 2.10, which is consistent with the conclusion of Elsamra et al. that their experimental conditions corresponded to the low pressure limit. The value of 3.4×10^{-13} cm^3 s^{-1} reported by Berndt *et al*. was determined using ethene ozonolysis to produce CH_2OO in synthetic air at atmospheric pressure,[88] and agrees (within the mutual uncertainties) with the low-pressure measurements.

2.5.3 Mechanism and reactivity trends

The α-diketones BiAc and AcPr react much more rapidly with CH_2OO than acetone, with rate constants that are approximately 25 times larger (k_{BiAc} = 1.45×10^{-11} cm^3 s^{-1} and k_{AcPr} = 1.29×10^{-11} cm^3 s^{-1}). The larger rate constants for the α-diketone reactions relative to that for acetone can be rationalized, at least qualitatively, by the results of the *ab initio* calculations. The free energy profiles

calculated using the CBS-Q3 method are shown in Figure 2.8 for the Ac and BiAc reactions (see also Table 2.3) and indicate that the cycloaddition transition state (TS_{SOZ}) is 3.0 kcal mol^{-1} lower for the latter reaction.

In contrast to the α-diketone reactions, the rate constants obtained for the reactions of the β-diketones AcAc and dMAcAc with CH_2OO are similar in magnitude ($k_{AcAc} = 6.6\times10^{-13}$ cm^3 s^{-1} and $k_{dMAcAc} = 3.5\times10^{-13}$ cm^3 s^{-1}) to k_{Ac}. The picture is more complicated for the β-diketones due to tautomerization. For AcAc, the enolone form is strongly favored (~97%) in the gas phase at room temperature[170,171] and the absorption spectrum of dMAcAc shows features that may indicate some degree of tautomerization. Focusing first on AcAc, Figure 2.8 shows the free energy profiles for SOZ production via the cycloaddition reaction for both diketone and enolone forms. The free energy barriers are higher than that for the benchmark Ac reaction for both tautomers (by 2.3 kcal mol^{-1} higher for the minor diketone and 3.7 kcal mol^{-1} for the major enolone form). Application of the Eyring equation would predict rate constants for the diketone that is ~50 and ~500 times smaller than Ac reaction (Table 2.4). Weighting for the relative abundances, the minor diketone tautomer accounts for one in four reactive encounters and an overall rate constant that is ~400 times smaller than that for Ac, while the experiment finds k_{Ac} to be ~20% larger than k_{dMAcAc}. The qualitative disagreement suggests that additional reaction pathways via the other functional groups (C=C and OH) in the enolone form may be available.

By comparison, rate constants for reactions of CH_2OO with alcohols are similar in magnitude ($k_{ROH} \approx 10^{-13}$ cm^3 s^{-1}),[79,94] while reactions with alkenes are significantly slower ($k_{C=C} \approx 10^{-15}$ cm^3 s^{-1}).[115] The conjugated enone functionality is shared with methylvinylketone, which reacts with CH_2OO with a rate constant of $k_{MVK} = (5.0\pm0.2)\times10^{-13}$ cm^3 s^{-1},[141] although the reaction occurs predominantly via cycloaddition at the carbonyl group to form the SOZ, rather than reacting at the C=C double bond. Detection of the products of the CH_2OO + AcAc reaction using techniques such as PIMS or FTIR would

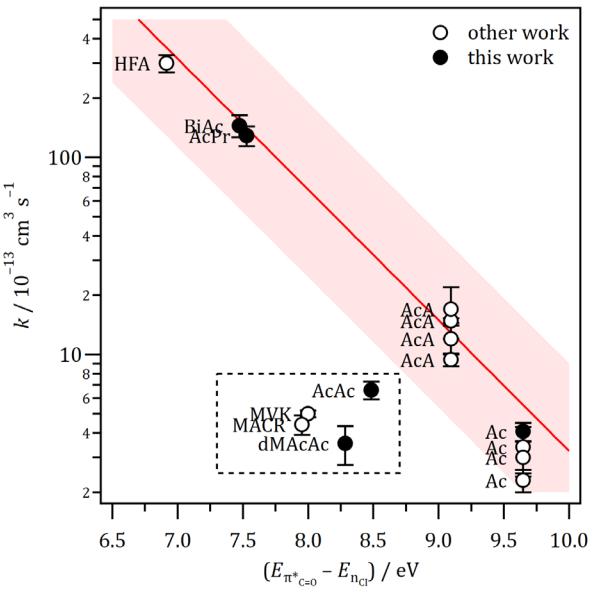


Figure 2.11 Inverse correlation between ln k and the energy gap between the carbonyl π* orbital (LUMO) and the n_0 orbital (HOMO) of CH_2OO. Orbital energies were calculated at the M06-2X/aVTZ level. Filled circles are measurements from this work, open circles are results of previous work. A linear fit with 2σ prediction band is shown (R^2 = 0.83). Reactions indicated in the dashed box were not included in the fit.

be valuable. For the CH_2OO + dMAcAc reaction, the smaller rate constant relative to CH_2OO + Ac is qualitatively consistent with the *ab initio* prediction of higher energy transition state barrier for the diketone, although steric hindrance due to the presence of methyl groups at the C3 position may also contribute. The equilibrium constant for dMAcAc tautomerization is unknown, but since it would have to involve a terminal C=C bond, it is likely to be disfavored in the absence of additional stabilization through conjugation and intramolecular H-bond formation as in AcAc.

Previously, Taatjes et al.[128] used PIMS to study the reactions of CH_2OO with acetone (Ac), acetaldehyde (AcA), and hexafluoracetone (HFA), confirming the formation of SOZ products (for the Ac and HFA reactions). The observed rate constant trend kAc < kAcA ≪ kHFA mirrored the trend in

the electron-withdrawing character of the carbonyl substituents CH_3 < H ≪ CF_3, which increasingly stabilize the transition state. Here, we demonstrate that reactivity trends can be predicted and explained by considering the influence of the substituents on the energies of the frontier orbitals of the dipolarophiles. Figure 2.11 shows a plot of ln k against ΔE_S (see Table 2.5) for a range of CH_2OO reactions with carbonyl and dicarbonyls. In general, we find a strong inverse correlation (the linear fit shown in Figure 2.11 has R^2 = 0.83) for CI reactions involving monocarbonyls (AcA, Ac, HFA) or α-diketones (BiAc, AcPr), however, the conjugated enones (MACR, MVK, AcAc) and the β-diketone dMAcAc deviate from the trend and react more slowly than would be predicted. The relationship between ln k and ΔE_S can be used to estimate the rate constant for the simplest reaction of a Criegee intermediate with a given carbonyl. For instance, in the reaction of CH_2OO and HCHO, the orbital energy gap for this reaction is ΔE_{FMO} = 8.436 eV (see Table 2.5), and based upon the linear fit and prediction bands shown in Figure 2.11, we estimate a rate constant of $(3.5^{+2.9}_{-1.6})\times10^{-12}$ cm^3 s^{-1}.

An alternative approach to predict rate constants for the 1,3-dipolar cycloaddition reactions between CH_2OO and carbonyl compounds uses Hammett substituent constants which can be viewed as proxy measures of the degree of electron-withdrawing/electron-donating character of the substituents on the carbonyl.[172,173] Here, we do not perform a standard Hammett analysis but rather observe a strong positive correlation between the bimolecular rate constants and the sum of the *para* position Hammett substituent constant (σ_p) values for the substituents on the carbonyls. Figure 2.12 shows that a plot of k versus $\Sigma\sigma_p$ is linear with correlation coefficient R^2 = 0.93 – an equally large value is obtained using the *meta* position constants, σ_m. Substituent constants are taken from the work of Hansch *et al*.[173] for the carbonyls Ac, AcA, MVK, MACR, BiAc, AcPr, and HFA and are compiled in Table 2.6. It is important to note, a standard Hammett analysis uses the relationship $\ln\left(\frac{k}{k_0}\right) = \sigma\rho$ where σ and ρ are the substituent and reaction constants, respectively, and k_0 is the rate constant for a reference reaction with σ = 0. For the current data set, a standard Hammett plot is non-linear. While

there is an apparent ambiguity in the choice of substituents on the asymmetric α-diketone AcPr, which can be viewed as either CH_3 and $C(O)C_2H_5$ or alternatively as C_2H_5 and $C(O)CH_3$, the sums $\Sigma\sigma_p$ values are nearly the same in either case, and the correlation is largely unaffected. As with the frontier orbital analysis, this empirical correlation can be used to predict the gas phase rate constant for other reactions. For example, using the upper and lower prediction bounds in Figure 2.12 the rate constant for the CH_2OO + HCHO reaction, for which $\Sigma\sigma_p = 0$, is estimated to be $(5.7\pm0.7)\times10^{-12}$ cm^3 s^{-1} (1σ uncertainty), which is in good agreement with the FMO prediction.

The use of tabulated Hammett substituent constants may provide a quantitative means to predict rate constants for CH_2OO + carbonyl reactions; where unavailable, relatively low-cost *ab initio* calculations of the relevant orbital energies may also provide a suitable substitute without the need to apply a full TST treatment. For instance, the rate constant for the reaction of the atmospherically

Table 2.6 Hammett substituent constants for carbonyl compounds. Data taken from Table 1 of Hansch *et al*.[7]

substituent	#	σ_m	σ_p
H	43	0.00	0.00
CF_3	70	0.43	0.54
CH_3	133	–0.07	–0.17
C_2H_5	219	–0.07	–0.15
$CH=CH_2$	193	0.06	–0.04
$C(O)CH_3$	200	0.38	0.55
$C(O)C_2H_5$	276	0.38	0.48
$C(CH_3)=CH_2$	271	0.09	0.05

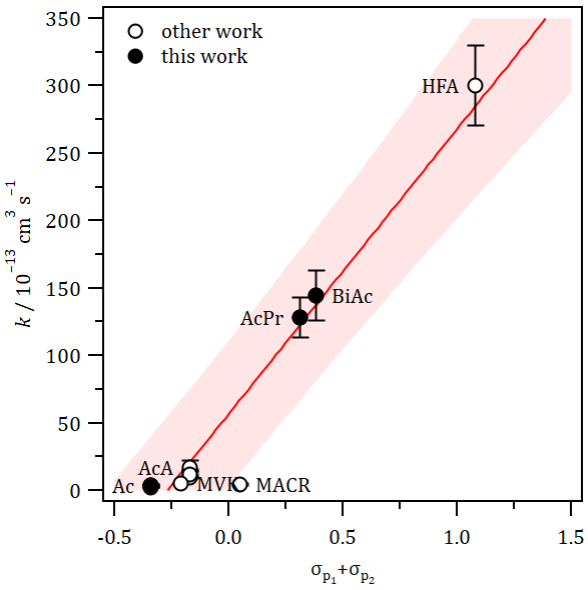


Figure 2.12 Plot showing correlation between observed rate constants and the sum of the *para* position Hammett constants, σ_p, for each substituent on the carbonyl. Closed circles are from this work, open circles are results of previous work. A linear fit with 2σ prediction band is shown (R^2 = 0.93).

important α-dicarbonyl glyoxal (Gly) with CH_2OO is predicted to be (1.5±0.2)×10^{-11} cm^3 s^{-1}. For the related species methylglyoxal (MGly), we estimate rate constants of (1.1±0.2)×10^{-11} cm^3 s^{-1} for reaction at the ketone and (1.7±0.2)×10^{-11} cm^3 s^{-1} for reaction at the aldehyde group. Experimental work to measure the rate constants for the CH_2OO + Gly and MGly reactions and test these predictions is underway.

2.5.4 Atmospheric implications

Acetone is typically found in the troposphere in low concentrations with mixing ratios of <2 ppb.[174] Dicarbonyls (BiAc, AcAc, Gly) have been detected at similar or even lower mixing ratios.[175–178] Using 2 ppb as an upper limit, the rate constants measured (or estimated) in the current work indicate CH_2OO loss rates of <0.03 s^{-1} for reaction with Ac or AcAc, and <0.6 s^{-1} for reaction with BiAc or Gly.

Consequently, reactions with acetone and dicarbonyl species are in general a negligible sink for CH_2OO in the troposphere where reaction with water vapor contributes a loss rate of ~2000 s^{-1} at 50% RH.[133] Reaction with CH_2OO (or other CIs) is also likely a very minor sink for the carbonyl/dicarbonyl compounds when compared to reaction with OH or photolysis. For example, Ac reacts slightly more slowly with OH (1.8×10^{-13} cm^3 s^{-1})[18,91] than with CH_2OO, but the much larger concentration of OH (~10^6 cm^{-3}) compared to CH_2OO (~10^4 cm^{-3})[4] leads to the former reaction being around 30 times faster. For dicarbonyls too, reaction with OH is generally faster than reaction with CH_2OO. The rate constant for the OH + AcAc reaction is significantly larger (~9×10^{-11} cm^3 s^{-1}),[156,177,179] while that for the OH + Gly reaction of is similar in magnitude (1.1×10^{-11} cm^3 s^{-1}),[18] to the measured (or estimated) rate constants for the reactions with CH_2OO. Despite the reported rate constant for the OH + BiAc reaction being small (2.2×10^{-13} cm^3 s^{-1}),[180] reaction with OH is still twice as fast as reaction with CH_2OO. For dicarbonyls in particular, photolysis is the dominant loss process in the troposphere. Photolysis rates of ~10^4 s^{-1} for the dicarbonyls (AcAc, BiAc, Gly) have been reported, which result in atmospheric lifetimes of only a few hours.[156,175,181] The rate of photolysis of Ac is much slower (4×10^{-7} s^{-1}),[182] but is still faster than reaction with either OH or CH_2OO. Considering all three processes, we estimate that reaction with CIs could be responsible for <1% of the loss of Ac and <0.1% for BiAc, AcAc, or Gly in the troposphere.

2.6 Conclusions

The rate constants for the 1,3-dipolar cycloaddition reactions of the Criegee intermediate CH_2OO with acetone (Ac), two α-diketones (BiAc and AcPr), and two β-diketones (AcAc and dMAcAc) have been measured at a temperature of 295 K and a pressure of 67 Torr. The rate constant measured for the Ac reaction in this work [k_{Ac} = $(4.1\pm0.4)\times10^{-13}$ cm^3 s^{-1}] is in good agreement with previous measurements; acetone dimers may also contribute to reactivity at higher reactant concentrations. The α-diketones are significantly (~30–35 times) more reactive towards CH_2OO [k_{BiAc} =

$(1.29\pm0.15)\times10^{-11}$ cm^3 s^{-1} and k_{AcPr} = $(1.45\pm0.18)\times10^{-11}$ cm^3 s^{-1}] than Ac. The reactivity trends of carbonyl and dicarbonyl species towards CH_2OO can be explained using concepts from frontier molecular orbital theory – rate constants inversely correlate with the energy gap between the "symmetric" LUMO of the carbonyl and the HOMO of CH_2OO. The presence of electron-withdrawing groups lowers the energy of the carbonyl LUMO, leading to a smaller energy gap, while electron-donating substituents increase the energy gap. More simply, the rate constants correlate strongly with the electron-withdrawing/donating character of substituents quantified by Hammett parameters, which may provide a simple predictive approach for rate constants. The β-diketones show reactivity towards CH_2OO that is similar to that of acetone [k_{AcAc} = $(6.59\pm0.68)\times10^{-13}$ cm^3 s^{-1} and k_{dMAcAc} = $(3.54\pm0.79)\times10^{-13}$ cm^3 s^{-1}], although the presence of enolone tautomers clouds the picture due to the presence of additional functional groups and the limited range of loss rates suggest that these rate constants may be better considered as upper limits. For the more atmospherically relevant carbonyl species, the rate constants are too small for these reactions to have a significant impact in the troposphere.

3 Temperature-Dependent Kinetics of the Reactions of CH_2OO with Acetone, Biacetyl, and Acetylacetone

Portions of this chapter were reproduced with permission from Cornwell, Z. A.; Enders, J. J.; Harrison, A. W.; Murray, C. Temperature-Dependent Kinetics of the Reactions of CH_2OO with Acetone, Biacetyl, and Acetylacetone. *Int. J. Chem. Kinet.* **2023**, *55* (3), 154–166. https://doi.org/10.1002/kin.21625.

3.1 Abstract

Temperature-dependent rate constants for the reactions of CH_2OO with acetone (Ac), biacetyl (BiAc), and acetylacetone (AcAc) have been measured over the range 275–335 K using a flash photolysis, transient absorption spectroscopy technique. The measurements were performed at a total pressure of ~80 Torr in N_2 bath gas, which corresponds to the high-pressure limit for these reactions. All three reactions show linear Arrhenius plots with negative temperature dependences. Rate constants increase in the order Ac < AcAc ≪ BiAc across the temperature range; at 295 K the rate constants are k_{Ac} = (4.8±0.4)×10^{-13} cm^3 s^{-1}, k_{AcAc} = (8.0±0.7)×10^{-13} cm^3 s^{-1}, and k_{BiAc} = (1.10±0.09)×10^{-11} cm^3 s^{-1}. Sensitivity to temperature, characterized by the magnitude of the negative activation energy, increases in the order AcAc < BiAc < Ac (E_a /R values of –1830±170 K, –1260±170 K, and –460±180 K, respectively). CBS-QB3 calculations show that the Ac and BiAc reactions proceed via formation of an entrance channel complex followed by 1,3-dipolar cycloaddition to form secondary ozonide products via a submerged transition state. For the BiAc reaction, the rate limiting step appears to be rearrangement of a long-range van der Waals complex into the short-range complex that subsequently leads directly to the cycloaddition transition state with a very low energy barrier. The calculations show that two reaction pathways are competitive for AcAc with nearly identical transition state free energies ($\Delta G°$ = +10.1 kcal mol^{-1} at 298 K) found for cycloaddition at the C=O and at the C=C site of the dominant enolone tautomer. The weak temperature dependence observed is likely due to competition between these pathways.

3.2 Introduction

Gas phase alkene ozonolysis proceeds via the well-established Criegee mechanism of 1,3-cycloaddition across the olefinic bond to form a cyclic primary ozonide (POZ), which promptly decomposes into a carbonyl oxide, known as a Criegee intermediate, and a carbonyl compound.[14] In the troposphere, energized Criegee intermediates (CIs) formed in the ozonolysis of volatile organic compounds (VOCs) either undergo unimolecular decomposition, typically generating OH radicals, or are stabilized by collisions and subsequently removed by reaction with trace atmospheric gases.[13,15,16] Over the last decade, the development of more efficient photochemical production methods has stimulated a surge of interest in the properties and chemistry of a range of CIs.[131,23,33,26,31,17,132] The single most important reactive sink in the troposphere for the simplest CI (formaldehyde oxide, CH_2OO), which is a major product in the ozonolysis of isoprene and other terminal or exocyclic alkenes,[19] is water vapor, overwhelmingly in the form of water dimer.[132] Reactions with other trace species such as organic acids, SO_2, and carbonyl compounds may be important in some environments, as well as for substituted CIs.[17,132]

Table 3.1 Compiled rate constants for CH_2OO + acetone reaction at or near room temperature. Uncertainties are 1σ.

k_{Ac} / 10^{-13} cm^3 s^{-1}	T / K	P / Torr	Bath gas	Reference
2.3±0.3	293	4	He	Taatjes et al.[21]
3.0±0.6	298	25	He	Elsamra et al.[23]
3.4±0.9	297	760	air	Berndt et al.[22]
4.7±0.1	295	30–100	N_2	Chhantyal-Pun et al.[25]
4.1±0.1	295	67	N_2	Cornwell et al.[26]

Carbonyl compounds are an important class of VOCs that directly influence the oxidative capacity of the atmosphere through production of O_3 and formation of secondary organic aerosols (SOAs).[174,183,184] CIs have been shown in ozonolysis experiments to react with aldehydes and ketones through a 1,3-dipolar cycloaddition across the carbonyl to form a cyclic 1,2,4-trioxolane secondary ozonide (SOZ).[136–140] More recent experiments have quantified the rate constants of the reactions of CH_2OO with acetone and other carbonyls.[128,88,111,141,130,126] Table 3.1 summarizes measurements near room temperature of the rate constant for the reaction of CH_2OO with acetone, one of the most abundant carbonyl compounds in the atmosphere.[174] The experimental measurements are in reasonably good agreement, with rate constants of $\sim 10^{-13}$ cm^3 s^{-1}. Photoionization mass spectrometry (PIMS) measurements also identified the formation of SOZ products.[128] Kinetics measurements performed across the range 250–500 K find a marked negative temperature dependence.[111,130] Pressure-dependent measurements in N_2 bath gas find that the rate constant increases with pressure and that the high-pressure limit is reached by ~30 Torr;[130] the smaller rate constants observed in He bath gas at similar pressures[111] suggest that the identity of the bath gas affects the high-pressure limit. The temperature and pressure dependences are consistent with computational work for CI + carbonyl reactions that has suggested the reaction proceeds by the formation of an entrance-channel van der Waals (vdW) complex followed by passage over the cycloaddition transition state (TS) that leads directly to the SOZ product.[111,112,142–144] More recently, Wang *et al.* have identified longer range vdW complexes and rearrangement TSs in the reactions of CH_2OO with acetaldehyde and acetone.[185] In the case of acetaldehyde, the novel rearrangement TS that separates the outer and inner vdW complexes was found to be rate-limiting.

Rate constants for CI + aldehyde and ketone cycloaddition reactions strongly depend on the identity of the carbonyl substituents.[126,128,141,186] Acetaldehyde has a rate constant approximately three times larger than acetone,[111,128] while for hexafluoroacetone (HFA) the rate constant is two orders of magnitude larger.[128] Increased rate constants relative to acetone were also found in our previous

work on the reactions of CH_2OO with α-diketones for which rate constants were ~30 times larger than that of acetone, while β-diketones react with similar rate constants.[126] The difference in rate constants can be attributed to a stabilization of the TS, which can be understood from frontier molecular orbital theory considerations.[168,124,125] The presence of electron-withdrawing substituents lowers the energy of the lowest unoccupied molecular orbital (LUMO) of the carbonyl (the dipolarophile), reducing the energy mismatch with highest occupied molecular orbital (HOMO) of the CI (the 1,3-dipole). Correlations (or anti-correlations) identified between the experimental rate constants and either the orbital energy gap or compiled σ_p Hammett substituent parameters[173] may prove useful in the development of structure-activity relationships (SARs). The effect of conjugation on reactivity when unsaturated vinyl or allyl substituents are present is less clear.[141,186] PIMS measurements confirmed that the methyl vinyl ketone (MVK) and methacrolein (MACR) reactions occurred at the carbonyl rather than the alkene site, for which much slower rate constants have been measured.[115] Despite being an enone and enal respectively, rate constants for MVK and MACR are similar to that of acetone,[141] while acrolein (ACR) reacts with a rate constant similar to that of acetaldehyde.[186]

Here, we describe the results of experimental and computational work that explores the temperature-dependent kinetics of the reactions of CH_2OO with acetone (Ac), biacetyl (BiAc), and acetylacetone (AcAc), extending our previous study.[126] Ac and BiAc are prototypical ketone and α-diketone species, respectively, while AcAc exists primarily as its enolone tautomer. The reaction kinetics are studied over the temperature range of 275–335 K at a pressure of 80 Torr using laser flash photolysis transient absorption spectroscopy. Complementary *ab initio* calculations characterize stationary points on the reaction potential energy surfaces, suggesting that the loose outer TS is rate-limiting in the BiAc reaction and identifying several new reaction pathways in the AcAc reaction.

3.3 Experimental and theoretical methods

Laser flash photolysis transient absorption spectroscopy measurements of the reaction kinetics were performed in a recently upgraded apparatus. The stainless steel flow reactor used in our previous Criegee intermediate kinetics studies[79,100,126] has been replaced by a jacketed glass reactor. The total reactor length is 132 cm, with an internal diameter of 2.5 cm. The central 90 cm between the gas inlet and outlet ports are jacketed and can be temperature controlled. The cell temperature is controlled using a unistat (Huber Tango) and can be varied from 228–523 K. Two Type K thermocouples positioned at each end of the flow reactor measure the temperature; the measurements agree to within < 1 K and are stable within the same range over the course of experimental kinetics runs. The reactant gas mixture inlet and outlet are positioned within the temperature-controlled region of the apparatus (20 cm from the windows). The windows are purged with a flow of N_2 to reduce build-up of residue. The pressure inside the apparatus is measured with a capacitance manometer (MKS, 902B) situated centrally.

The flow reactor is evacuated to a base pressure of < 10 mTorr by a rotary vane pump (Leybold Oerlikon D16B), throttled by a variable flow valve. Gas flow rates into the reactor are controlled using choked flow orifices (O'Keefe), selected to achieve a total flow rate of ~3.8 sLpm. The cell is operated at a static pressure of ~80 Torr (stable to within < 1 Torr). The total gas flow comprises a mixture of CH_2I_2, O_2, N_2, and reactant X (where X = Ac, BiAc, or AcAc). Gases O_2 (Airgas, UHP 4.4) and N_2 (Airgas, HP 4.8) are used directly from the cylinders. Liquids are placed in smog bubblers (Ace Glass) and carried into the reactor by a flow of N_2. The smog bubblers are maintained at either 273 K in a water/ice slush or 295 K in a temperature-controlled water bath to ensure stability of the liquid vapor pressure. Concentrations are estimated based on the fractional contributions to the total flow and the mole fraction present. Typically, we use $[CH_2I_2] = 1\times10^{15}$ cm^{-3}, $[O_2] = 2.1\times10^{17}$ cm^{-3}, [X] = 0–2.4×10^{16} cm^{-3}, with N_2 balance. Calibration measurements, in which the carbonyl spectrum is

recorded using LEDs centered at 280 nm (Ac, AcAc) or 420 nm (BiAc) using identical flow and static conditions, confirm that the effective path length is 90±7 cm and that the ratios of estimated to experimentally measured concentrations are not significantly different from one.

A Nd:YAG laser (Continuum, Surelite II-10) operating at 355 nm is used to initiate CH_2OO production by photolysis of precursor CH_2I_2 in the presence of excess O_2. The photolysis laser is steered through the flow reactor using long-pass dichroics (Semrock, RazorEdge LPD01-335RS). Additional long-pass filters (Semrock, EdgeBasic BLP01-355R) prevent any scattered laser light from reaching either the spectrograph or pulsed LED driver (described below). Typical pulse energies are ~10 mJ in a 7 mm diameter beam, resulting in fluences of ~26 mJ cm^{-2}. The CH_2I_2 absorption cross section at 355 nm ($\sigma_{355} = 5.0\times10^{-19}$ cm^2) is effectively independent of temperature,[187,188] and we estimate that <2% of the CH_2I_2 molecules are photolyzed. Peak concentrations of $[CH_2OO] \approx 1\times10^{13}$ cm^{-3} (measured as described below) are observed approximately 20 μs after photolysis, consistent with the expected pressure-dependent yield and rate of the $CH_2I + O_2$ reaction.[39,157,158]

Transient absorption spectra are recorded in the wavelength range 360–390 nm as a function of delay time between photolysis and probe ($\Delta t = t_{LED} - t_{355}$). Broadband probe light pulses (200 ns duration) are generated using a pulsed LED driver (LightSpeed Technologies, HPLS-36) fitted with a UV LED centered at 365 nm (approximate FWHM of ~10 nm, maximum output 800 mW). The LED output is highly divergent and is collected using a 2" diameter condenser lens before being focused into 200 μm core multi-mode fiber (NA = 0.22) using a f = 6 cm plano-convex lens. The fiber delivers the LED pulses to the flow reactor where they are approximately collimated using f = 3.5 cm and f = 20 cm lenses and counter-propagated through the flow reactor. The transmitted light is recoupled into an identical fiber and ultimately dispersed in a spectrograph (Andor Shamrock 33i with iDus 420 CCD camera, operated with resolution of 2.5 nm). Synchronization of the photolysis laser, LED,

and spectrograph CCD camera) is performed using a digital delay generator (Quantum Composers, 9528) controlled by custom data acquisition software (National Instruments, LabVIEW).

Transient spectra were derived from the average of 400 reference and signal spectra, after subtracting the detector baseline from each. Reference spectra were recorded with delay $\Delta t = t_{LED} - t_{355} = -10$ μs (i.e. the LED probe pulse is before the laser photolysis pulse), and signal spectra obtained at various (typically ~15) delays spread across the range Δt = 2–2000 μs. Kinetics measurements were performed under pseudo-1st order conditions of excess reactant ([X] at least 30 times greater than $[CH_2OO]_0$) by recording transient blanks ([X] = 0) and using five choked-flow orifices to vary [X]. The choked-flow orifices were selected randomly in each run to minimize the effects of any systematic changes in experimental conditions (e.g. drift in photolysis laser pulse energy or degradation of the reactor windows).

Electronic structure calculations on CH_2OO reaction pathways for acetone (Ac), biacetyl (BiAc), and the enolone tautomer of acetylacetone (AcAc) were performed with *Gaussian 16*.[146] Equilibrium and transition state structures were optimized within the CBS-QB3 compound method that utilizes the B3LYP functional for geometry optimization.[151] The structures obtained are then used for complete basis limit extrapolation based on coupled cluster calculations in CBS-QB3. Minima and transition states were confirmed by harmonic frequency analysis. This level of theory was chosen as it has been shown to provide reliable thermochemistry for reactions involving the main group elements at modest computational cost.[152–154]

3.4 Results

3.4.1 Experimental kinetics measurements

The kinetics of the reactions of CH_2OO with acetone, biacetyl, and acetylacetone were studied at a total pressure of 80 Torr and at the temperatures 275 K, 295 K, 315 K, and 335 K.

$$CH_2OO + Ac \rightarrow SOZ \qquad k_{Ac} \qquad \text{(R 3.1)}$$

$$CH_2OO + BiAc \rightarrow SOZ \qquad k_{BiAc} \qquad \text{(R 3.2)}$$

$$CH_2OO + AcAc \rightarrow products \qquad k_{AcAc} \qquad \text{(R 3.3)}$$

All kinetics measurements were performed under pseudo-1st order conditions of excess carbonyl ([X] $\gg$ $[CH_2OO]_0$, by factors of 30–3000). Transient absorption spectra in the range 362–395 nm are decomposed by fitting to a linear combination of reference CH_2OO and IO absorption spectra to obtain time-dependent concentrations $[CH_2OO]_t$ (and $[IO]_t$), as described in our previous work.[79,100,126] Maximum concentrations of $[CH_2OO]_0 \approx (6–8)\times10^{12}$ cm^{-3} are typically observed around 20 μs after photolysis and the increased loss rate due to the presence of the carbonyl compound is evident. The time required to reach the maximum concentration is minimally affected by the presence of Ac, BiAc, or AcAc reactants, although CH_2OO yields are generally lower at higher temperatures.

The analysis for the time dependent loss of CH_2OO concentrations was described previously. The equations and their use in the kinetic model will be reiterated and summarized here. The model includes the bimolecular self-reaction, characterized by a rate constant k_{self}, and pseudo-1st order loss, with rate constant k_{loss}. The differential rate equation for CH_2OO loss is described in E 2.3 from

the previous chapter, which can be solved to yield the integrated rate equation, E 2.5 that can be used to fit the $[CH_2OO]_t$ data. Unconstrained fits of the experimental data to Equation E 2.5 are not generally reliable, however, particularly when the self-reaction makes comparatively small contribution to CH_2OO loss, which tends to be the case at lower $[CH_2OO]_0$. Neglect of the self-reaction reduces the integrated rate equation for $[CH_2OO]_t$ to a simple exponential decay. Consequently, curvature in plots of $\ln[CH_2OO]_t$ against Δt is evidence of non-negligible contribution from the self-reaction.

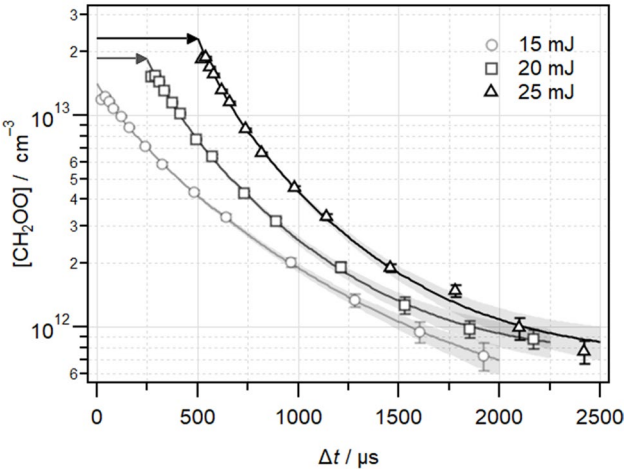


Figure 3.1 Laser fluence dependence of $[CH_2OO]_t$ at 335 K to show increasing $[CH_2OO]_0$ and increasing curvature at 15 mJ (light gray circles), 20 mJ (gray squares), and 25 mJ (black triangles). Fits to determine k_{loss} and k_{self} are also shown, with shading representing 1σ prediction bands. Data and fits are sequentially offset horizontally for clarity (+250 μs), indicated by the horizontal arrows.

In our previous work, we have fixed k_{self} to a previously reported value during fitting. The NASA-JPL evaluation[91] recommends a value of k_{self} = 7.12×10^{-11} cm^3 s^{-1}, which is the average of several measurements all made near room temperature.[157,160,118] In order to explore any possible temperature dependence of k_{self}, we measured transient absorption spectra in the absence of any CI scavenger at 275 K and 335 K. Increasing the laser fluence increases $[CH_2OO]_0$ and consequently

leads to a larger contribution of the self-reaction to the CH_2OO loss. At photolysis pulse energies > 10 mJ, plots of $\ln[CH_2OO]_t$ against Δt become increasingly curved (see Figure 3.1) and fitting to Equation E 2.5 is able to reliably return values for both k_{loss} and k_{self}. The value of k_{loss} increases with laser fluence, consistent with the suggestion that a photochemical product contributes to reactive CH_2OO loss and is generally lower at the higher temperature, for the equivalent laser fluence. In contrast, the values of k_{self} are independent of laser fluence and temperature. We find a value of $k_{self} = (7.6\pm0.8)\times10^{-11}$ cm^3 s^{-1} at 275 K and $(8.2\pm0.5)\times10^{-11}$ cm^3 s^{-1} at 335 K. Combining this value with previous measurements[157,160,118] gives a temperature-independent weighted average value of $k_{self} = (7.8\pm0.4)\times10^{-11}$ cm^3 s^{-1}. This value is used in all subsequent fits of experimental $[CH_2OO]_t$ time profiles using Equation E 2.5.

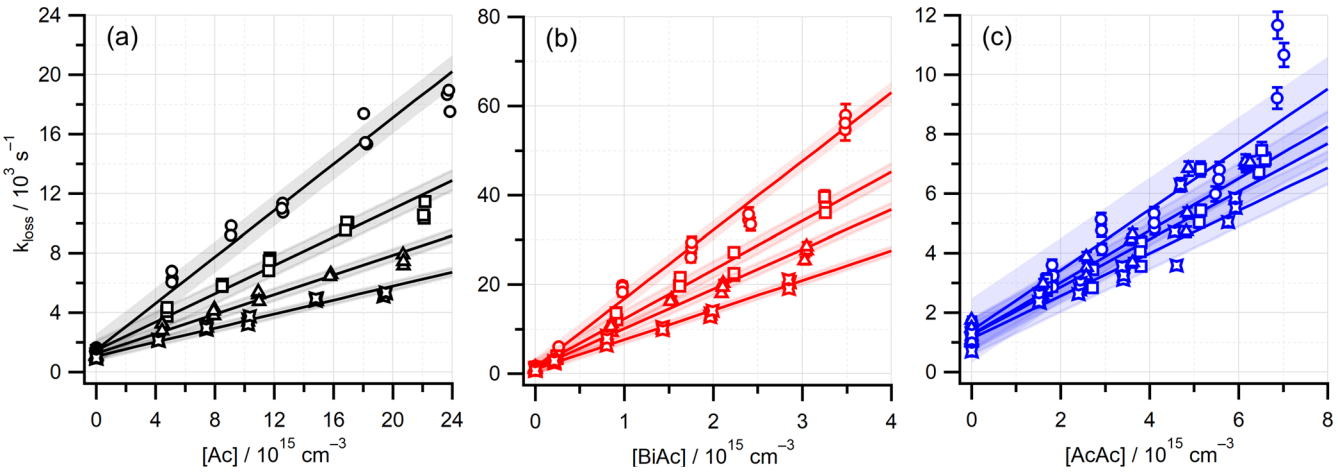


Figure 3.2 Complete data set of pseudo-first order kinetics for the CH_2OO + X reactions over the experimental temperature range, 275 K (circles), 295 K (squares), 315 (triangles), and 335 K (stars). X = (a) Ac (black), (b) BiAc (red), and (c) AcAc (blue).Solid lines are linear fits with shaded areas representing 1σ prediction bands.

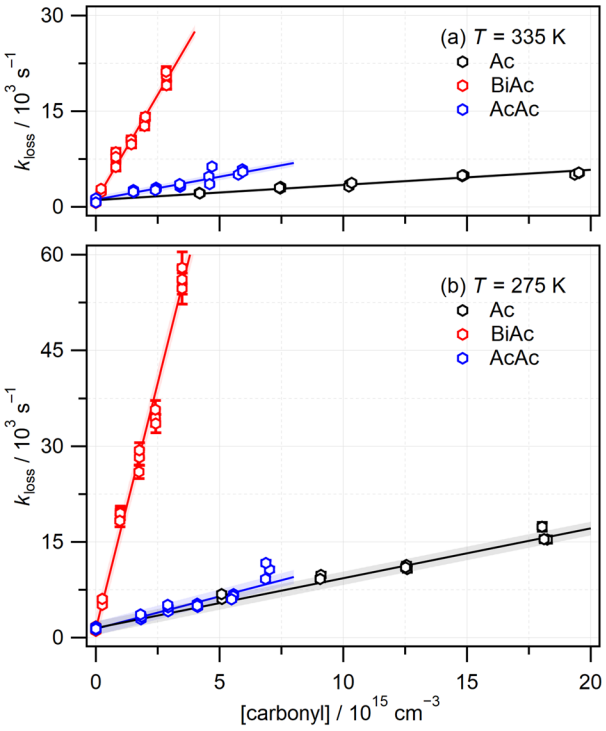


Figure 3.3 Pseudo-1st order plots of observed k_{loss} against reactant concentration at (a) 335 K and (b) 275 K for the reactions of CH_2OO with Ac (black), BiAc (red), and AcAc (blue).

The complete pseudo-first order kinetics data set for all three carbonyls across the experimental temperature range is shown in Figure 3.2. To show a sense of scale between the kinetics of the corresponding carbonyls, Figure 3.3 shows CH_2OO loss rates obtained on either end of the temperature range at 275 K and 335 K. The data in Figure 3.2 and Figure 3.3 confirm the linear increase of k_{loss} with increasing carbonyl concentration [X], as expected for pseudo-1st order conditions. Linear fits of the experimental k_{loss} data as a function of [X] return the bimolecular rate constants, k_X, and a background loss rate, k_{bgd} according to Equation E 2.4

$$k_{loss} = k_{bgd} + k_X[X] \qquad \text{E 2.4}$$

The T-dependent bimolecular rate constants obtained from an overall fit to three independent kinetics runs are summarized in Table 3.2, where the reported error bars (1σ) combine the statistical

from the linear fits and an estimated 8% uncertainty in the reactant concentrations derived from calibration measurements. The T-dependent rate constants for the CH_2OO + BiAc reaction ($\sim 10^{-11}$ cm^3 s^{-1}) are markedly larger than those for the CH_2OO + Ac and CH_2OO + AcAc reactions ($\sim 10^{-13}$–10^{-12} cm^3 s^{-1}) across the temperature range and all three reactions show a negative temperature dependence. The background CH_2OO loss rates also decrease with increasing temperature (k_{bgd} is approximately 1500s^{-1} at 275 K and 1000 s^{-1} at 335 K). Arrhenius plots, shown in Figure 3.4, are linear over the experimental temperature range. The pre-exponential factors and activation energies derived from linear fits are summarized in Table 3.3. The sensitivity of $k(T)$ to changes in temperature decreases in the order Ac > BiAc > AcAc, as indicated by the smaller magnitude of E_a. The pre-exponential factors suffer from significant statistical uncertainty, particularly for the Ac and BiAc reactions.

Table 3.2 Temperature-dependent bimolecular rate constants ($\times 10^{-13}$ cm^3 s^{-1}) for the reactions of CH_2OO with Ac, BiAc, and AcAc at 80 Torr. Reported errors are 1σ based on estimated 8% uncertainties in the reactant concentration and statistical uncertainties from the fits.

T / K	k_{Ac}	k_{BiAc}	k_{AcAc}
275	7.8±0.6	154±12	10.2±0.8
295	4.8±0.4	110±9	8.0±0.7
315	3.3±0.3	89±7	8.7±0.7
335	2.4±0.2	66±5	7.2±0.6

The kinetics of the CH_2OO + Ac reaction has been studied by several groups previously and the results are summarized in Table 3.1.[88,111,126,128,130] The value of $k_{Ac} = (4.8\pm0.4)\times10^{-13}$ cm^3 s^{-1} at 295 K obtained in this work agrees well with our previous measurement[126] and, where temperature ranges overlap, the agreement with the values reported Chhantyal-Pun et al.[130] across the range 251–311 K is excellent. In contrast, Taatjes et al.[128] at 296 K and Elsamra et al.,[111] across the range 298-494 K, found rate constants that are around a factor of two smaller. As argued by Chhantyal-Pun et al., the discrepancy is likely attributable to the different bath gas and pressure conditions used in the earlier experiments. As in the current experiments, Chhantyal-Pun et al. used N_2 bath gas and furthermore they showed that the high-*P* limit had been reached by ~30 Torr. A series of experiments performed to measure CH_2OO loss rates in the presence of a fixed concentration of Ac showed no pressure dependence across the range 50–100 Torr. Consequently, we conclude that the results of the current experiments at 80 Torr N_2 are also performed under conditions that correspond to the high-*P* limit and are directly comparable to the results of Chhantyal-Pun et al. The earlier measurements by Taatjes et al. and Elsamra et al. used He and were performed at lower pressures (4 Torr and < 25 Torr, respectively);[111,128] a weak positive pressure dependence was observed by the latter group,

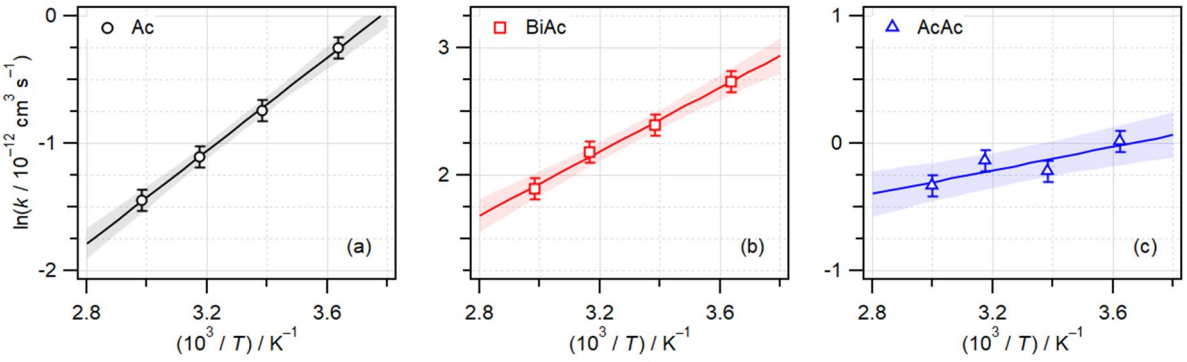


Figure 3.4 Arrhenius plots for the reactions of CH_2OO with (a) Ac (black circles), (b) BiAc (red squares), and (c) AcAc (blue triangles) over the temperature range 275–335 K. Shaded areas represent 1σ prediction bands for the linear fits. Fit parameters are summarized in Table 3.3.

suggesting the high-*P* limit may not have been reached. The rate constant measured at 297 K and in 1 atm air by ae high-*P* limit. The value reported is slightly smaller than more recent values,[126,130] but agrees within the mutual experimental uncertainties.

Table 3.3 Arrhenius and thermodynamic parameters for rate-limiting TS.

	Ac	BiAc	AcAc
A / cm^3 s^{-1}	(1.0±0.5)×10^{-15}	(1.6±0.9)×10^{-13}	(1.8±1.1)×10^{-13}
E_a / kcal mol^{-1}	–3.6±0.3	–2.5±0.3	–0.9±0.3
(E_a / R) / K	–1830±170	–1260±170	–460±180
$\Delta S°$ / cal K^{-1} mol^{-1}	–42.5±1.1	–32.1±1.2	–32.4±1.1
$\Delta H°$ / kcal mol^{-1}	–4.8±0.3	–2.1±0.4	–3.7±0.3

To the best of our knowledge, the only previous report of the kinetics of the reactions of CH_2OO with BiAc and AcAc is our recent study at 295 K.[126] For the BiAc reaction, the value of the rate constant at 295 K of (1.10±0.09)×10^{-11} cm^3 s^{-1} is smaller than the previous value of (1.45±0.18)×10^{-11} cm^3 s^{-1} (1σ uncertainties). In contrast, the current value of the rate constant for the AcAc reaction of (8.0±0.7)×10^{-13} cm^3 s^{-1} is larger than our previous measurement of (6.6±0.6)×10^{-13} cm^3 s^{-1}. Although there is an apparent disagreement, we note that the measurements agree within 2σ uncertainty. We consider the current results to be more reliable. Background CH_2OO loss rates in the current work were significantly slower (~1300 s^{-1} at 295 K in the current work compared to ~4000–6000 s^{-1} in Cornwell et al.[126]) and the pseudo-1st order plots span a greater range of k_{loss}. As with the CH_2OO + Ac reaction, a series of measurements of CH_2OO loss rates with known concentrations of BiAc and Ac were performed at total pressures in the range 50–100 Torr (see Figure 3.5). No pressure dependence was observed, and we conclude that these reactions are either pressure-independent or, more likely, also taking place at the high-*P* limit.

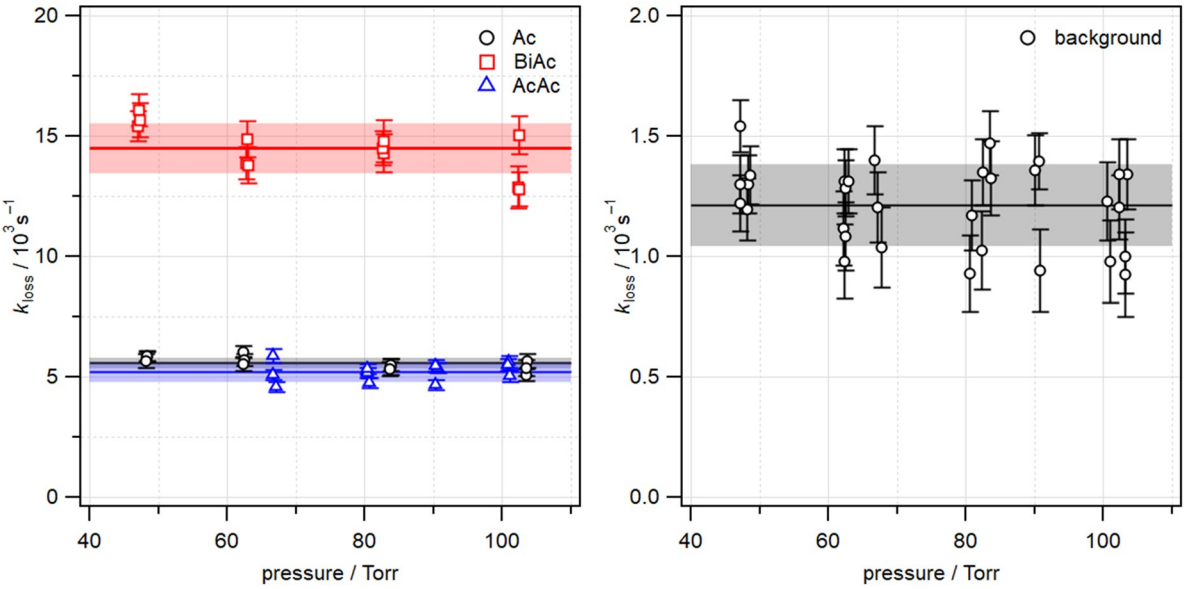


Figure 3.5 Left: Observed CH_2OO loss rates for the reactions with Ac, BiAc, and AcAc at 295 K over the total pressure range 50–100 Torr. Reactant concentrations: [Ac] = 8.60×10^{15} cm^{-3}, [BiAc] = 9.36×10^{14} cm^{-3}, [AcAc] = 4.33×10^{15} cm^{-3}. Horizontal lines are average values of $\langle k_{loss}\rangle$ across the pressure range, with shaded areas representing the 1σ standard deviation. Right: Observed background loss rates in the absence of reactant. Horizontal lines are average values of $\langle k_{loss}\rangle$ across the pressure range, with shaded areas representing the 1σ standard deviation.

3.4.2 Computational Results

3.4.2.1 Cycloaddition at the carbonyl group

The cycloaddition reactions between CH_2OO and Ac, BiAc, and AcAc at the carbonyl group were characterized in our previous work.[126] Here, we expand on those results and correct a minor error in the 0 K energies reported in that publication. The reaction pathway for cycloaddition at the carbonyl group consists of an entrance channel van der Waals complex before reaching a transition state barrier that leads to the secondary ozonide. However, recent work has shown that another complex and transition state pair at further reactant separation can also play an important role in these

reactions.[185] Therefore, we have also characterized what will be referred to as the *outer* complex (vdW_{outer})and transition state (TS_{outer}) in addition to the *inner* complex (vdW_{SOZ}) and transition state (TS_{SOZ}) that lead to SOZ products that were characterized previously. The reaction pathways with 0 K energies (ΔE+ ZPE) and standard Gibbs free energies (Δ*G*°) at 298 K are shown in Figure 3.6 and tabulated in Table 3.4. The 0 K Δ*E*+ZPE results presented here for the CH_2OO + Ac reaction are identical to the CBS-QB3 values reported by Wang et al.[185]

The 0 K energy profiles in Figure 3.6 (a) show that the long-range complex vdW_{outer} lies around 4 kcal mol^{-1} lower than the reactants for all three reactions. TS_{outer} presents only a modest energy barrier

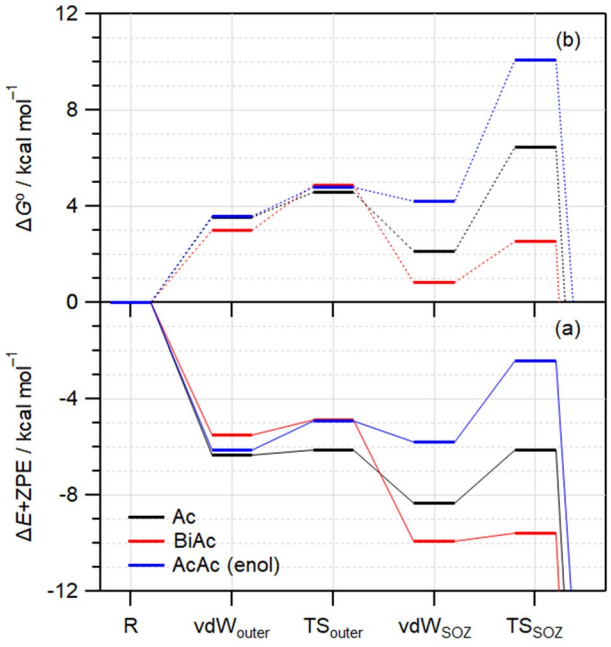


Figure 3.6 Stationary point (a) energies at 0 K (Δ*E*+ZPE, solid lines) and (b) free energies at 298 K (Δ*G*°, dotted lines) cycloaddition reactions of CH_2OO with acetone (Ac, black), biacetyl (BiAc, red), and the enol tautomer of acetylacetone (AcAc, blue) to form a secondary ozonide (SOZ).

Table 3.4 Relative energies (ΔE+ZPE at 0 K), including zero-point contributions, and free energies ($\Delta G°$ at 298 K), calculated at the CBS-QB3 levels for the SOZ pathway (see Figure 3.6) for reactions of CH_2OO with acetone (Ac), biacetyl (BiAc), and the enolone tautomer of acetylacetone (AcAc). All energies are reported in kcal mol^{-1}.

	Ac	BiAc	AcAc
vdW_{outer}	–6.3 (+3.5)	–5.5 (+3.0)	–6.1 (+3.6)
TS_{outer}	–6.1 (+4.6)	–4.9 (+4.9)	–4.9 (+4.8)
vdW_{SOZ}	–8.3 (+2.1)	–9.9 (+0.8)	–7.5 (+2.9)
TS_{SOZ}	–6.1 (+6.5)	–9.6 (+2.5)	–2.4 (+10.1)
SOZ	–50.3 (–36.6)	–50.1 (–37.0)	–39.2 (–25.9)

<2 kcal mol^{-1} to rearrangement to vdW_{SOZ}, which lies to lower energy than vdW_{outer} for the Ac and BiAc reactions. For the Ac and AcAc reactions the five-membered cyclic transition state for SOZ formation, TS_{SOZ} is ∼+4kcal mol^{-1} higher in energy relative to vdW_{SOZ}, but only +0.3 kcal mol^{-1} for the BiAc reaction. On the 0 K energy surfaces, TS_{SOZ} presents the largest barrier (relative to the previous complex) for the Ac and AcAc reactions, while TS_{outer} is the largest barrier for the BiAc reaction. The equivalent $\Delta G°$ reaction profiles are shown in Figure 3.6 (b). The reaction profiles are similar for the three reactions up to TS_{outer}, at around +5 kcal mol^{-1} but diverge beyond. For the BiAc reaction, TS_{outer} is the highest point on the free energy surface, and is likely rate-limiting, while TS_{SOZ} is significantly higher in energy for the Ac and AcAc reactions.

3.4.2.2 Alternate pathways for the enolone tautomer of AcAc

The enolone tautomer of AcAc has more possible reaction sites than Ac and BiAc given the presence of the C=C double bond and the O–H functional group. Therefore, it is of interest to identify if other reaction pathways are contributing to the measured reaction rate in addition to cycloaddition at the carbonyl group. We have identified four additional transition states that are representative of the major reaction pathways but neglect subtle conformational differences that would lead to TSs with very similar energies. These new transition states correspond to two cycloadditions at the C=C group involving different orientations of CH_2OO (O atom of the CI adding either to the α–C or β–C atom, labelled as C_α=C and C_β=C, respectively), a cycloaddition via a seven-membered transition state that involves the carbonyl O atom and the β–C atom(labelled C_β=C–C=O), and a 1,2-addition (1,2-insertion, labelled OH) of the CI across the CH_2OO, typical of reactions with simple alcohols.[79,95,96] These transition state structures are shown in Figure 3.7 and the ΔE+ZPE at 0 K and $\Delta G°$ at 298 K values for

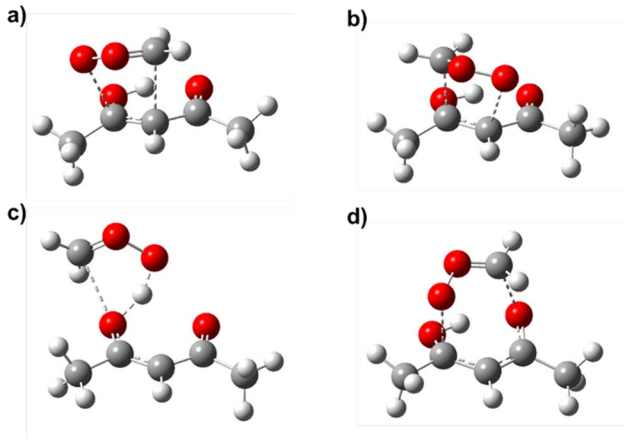


Figure 3.7 Transition state structures for reactions of the enolone tautomer of AcAc. (a) Cycloaddition at the C=C bond with O atom attack at the β-C atom; (b) cycloaddition at the C=C bond with O atom attack at the α-C atom; (c) 1,2-addition at the OH group; and (d) cycloaddition via a seven-membered cyclic adduct involving the carbonyl O atom and β-C atom.

Table 3.5 Relative energies (ΔE+ZPE at 0 K), including zero-point contributions, and free energies ($\Delta G°$ at 298 K) calculated at the CBS-QB3 levels for all reaction pathways for the enolone tautomer of acetylacetone (AcAc). TS energies are for the inner transition states (see Figure 3.7). All energies are reported in kcal mol^{-1}.

Reaction Site	ΔE+ZPE ($\Delta G°$)	
	TS	Products
C=O	–2.4 (+10.1)	–39.2 (–25.9)
C_β=C	–2.3 (+10.1)	–53.1 (–39.9)
C_α=C	+3.3 (+16.1)	–46.6 (–33.6)
OH	+9.8 (+20.9)	–36.0 (–24.0)
C_β= C_α–C=O	+10.4 (+23.4)	–39.8 (–26.1)

the TSs and the direct products that result are compiled in Table 3.5. In comparison to reaction at the carbonyl group, reaction at the C=C double bond would be expected to be the most competitive. In fact, reaction in the C_β=C orientation has a free energy barrier that is equivalent to that for reaction at the C=O group (discussed further below). However, reaction at the OH group and the cycloaddition reactions involving the C_α=C orientation and the seven-membered TS are likely minor channels given that their free energies barriers are significantly higher.

It is interesting that the C_α=C and C_β=C isomeric reaction pathways differ so much in relative energy (> 5 kcal mol^{-1}). The difference between the isomers is likely due to two effects. Firstly, there is more steric hinderance between the CH_2 group of CH_2OO and the terminal methyl group of AcAc that is not present in the C_β=C transition state. In addition to the steric effects, natural bond orbital (NBO) analysis on the enolone tautomer of AcAc reveals that the β–C atom is more electropositive than the α–C atom which can result in a more favorable interaction with the electronegative terminal oxygen atom in CH_2OO.

3.5 Discussion

The major experimental result is the clear negative temperature dependences of all three reactions studied over the range 275–315 K. The linear Arrhenius plots shown in Figure 3.4 and activation energies collated in Table 3.3 indicate that the sensitivity to temperature decreases in order Ac > BiAc > AcAc. The CH_2OO + Ac reaction is independent of the pressure of N_2 bath gas over the range 50–100 Torr, consistent with earlier work that found the high-pressure limit had been reached by 30 Torr.[130] The rates of the BiAc and AcAc reactions also appear to be independent of pressure over the same range and consequently are assumed to also be taking place in the high-*P* limit regime. In the gas phase, AcAc exists as a mixture of diketone and enolone tautomers, with the latter being strongly favored. [170,171,189] Using the enthalpy and entropy changes from the van't Hoff analysis reported by Antonov et al.,[171] the mole fraction of the dominant enolone tautomer decreases only slightly from 0.983 to 0.941 across the experimental temperature range. Since the *ab initio* results described above do not suggest any reason to expect the minor diketone to react significantly more rapidly than the enolone, we assume in the following discussion that all reactivity is due to the latter.

While previous work on the cycloaddition of CIs to carbonyls has largely focused on the inner vdW complex and TS as the rate-determining step in this reaction, recent work by Wang et al. has shown that the long-range outer vdW complex and TS can be rate-limiting in some cases.[185] For instance, in the reaction of CH_2OO and CH_3CHO, the energy barriers for the outer complex and TS are higher energy and were shown to determine the overall rate. Here, the reaction profile for BiAc (Figure 3.6) is like that of acetaldehyde, suggesting that the overall reaction rate is dictated by TS_{outer}. For Ac and AcAc, the rate limiting step is expected to be passage over the inner TS_{SOZ}, although for the latter, other reaction pathways may be competitive.

Reactions between CIs and carbonyls are thought to proceed via the following two-step mechanism in the high-*P* limit:[111,130]

$CH_2OO + X \rightleftharpoons vdW$ k_1/k_{-1} (R 3.4)

$vdW \rightarrow product$ k_2 (R 3.5)

The highly exothermic second step (R 3.5) is a 1,3-cycloaddition reaction that forms the cyclic 1,2,4-trioxolane SOZ product. The notation vdW refers to the complex prior to the rate-limiting TS, viz. the *inner* complex for Ac and AcAc, and the *outer* complex for BiAc. Application of the steady state approximation to the vdW complex leads to an expression for the overall reaction rate wherein the observed second order rate constant is

$$k_{\text{obs}} = \frac{k_2 k_1}{k_{-1} + k_2} \quad \text{E 3.1}$$

If the second step is rate limiting (i.e. in the limit that $k_{-1} \gg k_2$), a fast equilibrium between the reactants and the entrance channel vdW complex is established and the expression for the observed rate constant will be reduced to

$$k_{\text{obs}} = k_2 \frac{k_1}{k_{-1}} = k_2 K_1 \quad \text{E 3.2}$$

While this limit seems reasonable for the Ac and AcAc reactions, for which TS_{in} lies at a significantly higher energy than the most stable complex, vdW_{in}, the same cannot be said for the BiAc reaction, where the small barriers suggest that k_2 is likely to be large (see Figure 3.6 and Table 3.4). However, in the alternative limit that $k_2 \gg k_{-1}$, the expression for the observed rate constant reduces to that of formation of the relevant vdW complex and

$$k_{\text{obs}} = k_1 \quad \text{E 3.3}$$

The value of k_2 can be readily calculated using the results of the CBS-QB3 calculations and applying canonical transition state theory (CTST). Similarly, we can estimate the value of k_{-1} using the theoretical value for K_1 and estimating k_1. Upper limits for k_1 (and hence lower limits for k_{-1}) can be estimated using a simple hard-sphere collision rate, k_{hs}. Using $k_1 \approx k_{hs}$, we estimate that the ratio k_{-1}/k_2 has values of order 10^5, 10^2, and 10 for AcAc, Ac, and BiAc, respectively, with the values increasing with temperature. Consequently, based on the two-step high-P limit model and the discussion above, we assume that the observed experimental rate constant represents the product of k_2 and the equilibrium constant K_1. Applying CTST to k_2 leads to the expression[130]

$$k_{obs}(T) = \frac{k_B^2}{hp^\circ} \exp\left(\frac{\Delta S^\circ}{R}\right) T^2 \exp\left(-\frac{\Delta H^\circ}{RT}\right) \qquad \text{E 3.4}$$

where the values of ΔS° and ΔH° correspond to the change from the reactants to the highest point on the free energy surface (ΔG°). For the Ac and AcAc reactions, that corresponds to TS_{SOZ}, while for the BiAc reaction it is TS_{outer} (see Figure 3.6 and Table 3.4). The factor k_B^2/hp° is evaluated to be 2.84×10^{-12} cm^3 s^{-1} K^{-2} using p° = 101325 Pa. We fit the experimental T-dependent rate constants to the expression

$$k_{obs}(T) = AT^2 \exp(-B/T) \qquad \text{E 3.5}$$

where the parameters A and B can be related to the entropy and enthalpy via Equation E 3.4. The fits are shown in Figure 3.8 and the thermodynamic variables obtained are compiled in Table 3.3.

Comparing the experimental values of ΔS° and ΔH° obtained from this analysis to the theoretical values calculated at the CBS-QB3 level of theory, we find a qualitative trend with the theoretical ΔH° values being slightly more negative by ~1.0 – 2.2 kcal mol^{-1}. For ΔS°, there is excellent agreement for the experimental and theoretical values for Ac and BiAc with Ac exhibiting a significantly more negative value. This is consistent with the expected rate-determining steps for Ac and BiAc based on

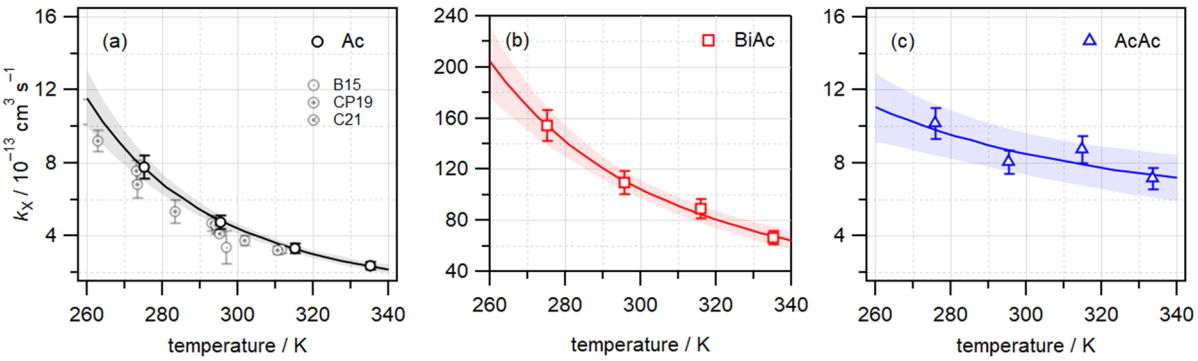


Figure 3.8 Plots of k_X against T for the reactions of CH_2OO with (a) Ac (black circles), (b) BiAc (red squares), and (c) AcAc (blue triangles). The solid lines are fits to Equation E 3.5 (see text), used to extract thermodynamic parameters for the rate-limiting TS. Shaded areas represent 1σ prediction bands. Previous high-P limit measurements in this temperature range from Berndt et al.[22] (B15, gray circle with dot), Chhantyal-Pun et al.[25] (CP19, gray circle with plus), Cornwell et al.[26] (C21, gray circle with cross) are also shown.

the reaction profiles in Figure 3.6. For Ac, formation of the TS_{SOZ} is the rate determining step which is a tighter (more ordered, higher vibrational frequencies) structure than the TS_{outer} that occurs at larger reactant separation. The opposite is true of BiAc where the rate-determining step is passage over the looser, higher entropy TS. In contrast, the experimental value of $\Delta S°$ for AcAc differs substantially from the theoretical value. Given that the rate-determining step for AcAc is the formation of TS_{SOZ}, it would be expected to have a more negative $\Delta S°$ similar to that of Ac. However, the $\Delta S°$ is much closer to the value for BiAc. The higher-than-expected entropy for AcAc may be due to the contributions of multiple available reaction pathways (Figure 3.7), discussed below.

Multiple reaction pathways are possible for the reaction of CH_2OO with the dominant enolone tautomer of AcAc, which shows the weakest T dependence of the reactions studied. The CBS-QB3 calculations find the smallest, and equivalent, free energy barriers at 298 K for cycloaddition at both the C=O and C_β=C sites (Table 3.5), while reaction at the OH group or other sites is uncompetitive.

Previously, reactions of CH_2OO with alkenes have been shown to have rate constants that are significantly smaller than acetone but with a positive temperature dependence.[115] The overall weak T dependence observed for the AcAc reaction may reflect the balance between the expected positive and negative T dependences of the rate constants for reaction at the C=C and C=O sites, respectively. This interpretation would imply that reactivity at the C_β=C site is significantly enhanced over that of simple alkenes, perhaps enhanced by the presence of the OH group in the enolone tautomer of AcAc. Previous work with the ozonolysis of alkenes, which proceeds via a similar cycloaddition mechanism, has shown that nearby OH groups enhance the rate of reaction.[190] We note that the conjugated π-system in AcAc is akin to the α,β-unsaturated carbonyl moiety found in species such as MVK, MACR, and ACR for which the kinetics of reactions with CH_2OO have also been studied.[141,186] PIMS measurements from Eskola *et al.*[141] confirmed the formation of the 1,2,4-trioxolane SOZ species in the MVK and MACR reactions, and it was concluded that the reactions proceed near exclusively through cycloaddition at the C=O at room temperature. Further experimental work identifying the products of the CH_2OO + AcAc reaction would be required to confirm that both reaction mechanisms are indeed competitive given that the theoretical $\Delta G°$ values indicate that both pathways will occur.

In the troposphere, the major daytime removal process for BiAc and AcAc is photolysis, which dominates over reaction with atmospheric oxidants such as OH or CH_2OO, and results in lifetimes of only a few hours.[175,156] Photolysis is far slower for Ac,[182] but still the most important sink. Consequently, reactive sinks primarily contribute at nighttime when temperatures are also lower. For AcAc, the rate constant for reaction with OH is significantly larger than that for CH_2OO, and also shows a stronger negative temperature dependence (E_a/R = –980 K for OH + AcAc).[177] Consequently, reaction with OH becomes increasingly important relative to CH_2OO as temperature decreases. In contrast, the reactions of OH with Ac (E_a/R = +1320 K)[18] and BiAc (E_a/R = +450 K)[180] both have positive temperature dependences. Loss due to reaction with CH_2OO may become relatively more important at nighttime, when both the temperature and the OH concentration are lower. Figure 3.9

shows the ratio of Ac and BiAc loss rates due to reaction with OH and CH_2OO as a function of temperature for day and night. Atmpospheric concentrations of CH_2OO have been estimated to span the range $(1–10)\times10^4$ cm^{-3};[25,26] the calculations use a estimated value of 2×10^4 cm^{-3}, while the value of [OH] is estimated to be 5×10^6 cm^{-3} during the day and 2×10^5 cm^{-3} at night.[1,2] OH is a more important reactive sink than CH_2OO in the daytime for both Ac and BiAc across the 220–320 K temperature range. Nighttime loss rates due to reaction with CH_2OO are larger at all temperatures for BiAc, and at T < 260 K for Ac.

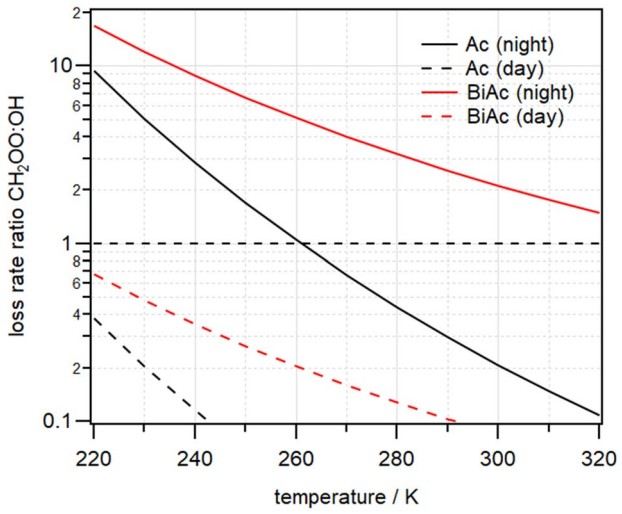


Figure 3.9 Temperature dependence of the ratio of Ac (black) and BiAc (red) loss rates due to reaction with CH_2OO and OH. Calculated ratios based on estimated approximate daytime (dashed lines) and nighttime (solid lines) concentrations of CH_2OO and OH are shown.

3.6 Conclusions

The *T*-dependent kinetics of the reactions of CH_2OO with Ac, BiAc, and AcAc have been measured over the range 275–335 K at total pressure of 80 Torr, which corresponds to the high-*P* limit. The measured rate constants are in good agreement with previous measurements performed under similar conditions.[130] All three reactions show a negative temperature dependence, with rate constants increasing at lower temperature. Characterization of the key stationary points on the reaction potential energy (and free energy) surfaces, suggests that the rate limiting step for the fast BiAc reaction is a long-range re-orientation TS, akin to that identified in the CH_2OO + acetaldehyde reaction.[185] In contrast, the short-range cycloaddition TS is rate-limiting for the slower Ac and AcAc reactions. Four new reaction pathways have been identified computationally for the AcAc reaction, with cycloaddition at the C_β=C site being competitive with the analogous reaction at the C=O site. Work is underway to expand the available experimental kinetic data set to include other multifunctional VOCs, with a goal of developing SARs with predictive power, analogous to those that have been used for alkene ozonolysis.[190–195] For Ac and BiAc, the negative temperature dependence suggests that CH_2OO could be a more significant reactive sink than OH at night, when concentrations of the latter are lower and photolysis is absent.

4 Temperature-Dependent Kinetics of the Reactions of the Criegee Intermediate CH_2OO with Hydroxyketones

Portions of this chapter were reproduced with permission from Cornwell, Z. A.; Enders, J. J.; Harrison, A. W.; Murray, C. Temperature-Dependent Kinetics of the Reactions of the Criegee Intermediate CH_2OO with Hydroxyketones. *J. Phys. Chem. A* **2024**, *128* (10), 1880–1891. https://doi.org/10.1021/acs.jpca.4c00156.

4.1 Abstract

Though there is a growing body of literature on the kinetics of CIs with simple carbonyls, CI reactions with functionalized carbonyls such as hydroxyketones remain unexplored. In this work, the temperature-dependent kinetics of the reactions of CH_2OO with two hydroxyketones, hydroxyacetone (AcOH) and 4-hydroxy-2-butanone (4H2B), have been studied using a laser flash photolysis transient absorption spectroscopy technique and complementary quantum chemistry calculations. Bimolecular rate constants were determined from CH_2OO loss rates observed under pseudo-1st order conditions across the temperature range 275–335 K. Arrhenius plots were linear and yielded T-dependent bimolecular rate constants: $k_{AcOH}(T) = (4.3\pm1.7)\times10^{-15}\exp[(1630\pm120)/T]$ and $k_{4H2B}(T) = (3.5\pm2.6)\times10^{-15}\exp[(1700\pm200)/T]$. Both reactions show negative temperature dependences and overall very similar rate constants. Stationary points on the reaction energy surfaces were characterized using the composite CBS-QB3 method. Transition states were identified for both 1,3-dipolar cycloaddition reactions across the carbonyl and 1,2-insertion/addition at the hydroxyl group. The free energy barriers for the latter reaction pathways are higher by ~4–5 kcal mol^{-1}, and their contributions are presumed to be negligible for both AcOH and 4H2B. The cycloaddition reactions are highly exothermic and form cyclic secondary ozonides (SOZs) that are the typical primary products of Criegee intermediate reactions with carbonyl compounds. The reactivity of the hydroxyketones towards CH_2OO appears to be similar to that of acetaldehyde, which can be rationalized by consideration of the energies of the frontier molecular orbitals involved in the cycloaddition. The CH_2OO + hydroxyketone reactions are likely too slow to be of significance in the atmosphere, except at very low temperatures.

4.2 Introduction

Criegee intermediates (CIs) are a zwitterionic species formed in alkene ozonolysis that can impact the oxidizing capacity of the troposphere.[131,23,26,132] Alkene ozonolysis proceeds via a 1,3-dipolar cycloaddition reaction to produce a cyclic 1,2,3-trioxolane, or primary ozonide (POZ), that promptly decomposes to form a CI and a carbonyl compound.[14,131] While larger CIs tend to undergo unimolecular decomposition,[27,196] generating OH radicals, the smallest CI, CH_2OO, has a longer lifetime and may undergo bimolecular reaction with trace atmospheric gases after collisional stabilization.[74,197] Reaction with water vapor, primarily in the form of water dimer, is the major reactive sink for CH_2OO,[132] although bimolecular reactions with other trace atmospheric gases, such as SO_2 and organic acids, are occasionally competitive in specific environments and under favorable conditions.[17,132]

CIs react with carbonyl species in a concerted 1,3-dipolar cycloaddition reaction to form a cyclic 1,2,4-trioxolane, or secondary ozonide (SOZ). Recently, work in our laboratory has explored the effect of varying the carbonyl substituents (R_1R_2CO, where R_1, R_2 are alkyl or acyl groups) on the gas-phase reactivity of a series of ketones and diketones with CH_2OO.[126,127] Reactivity trends can be rationalized using concepts from frontier molecular orbital (FMO) theory.[169,198,124,125] The cycloaddition mechanism arises primarily from π–π^* interactions between the occupied $n(p_C–p_O)$ orbital of the electron rich species (CH_2OO) and the unoccupied π^* orbital of the electron deficient species (R_1R_2CO). Electron withdrawing groups (EWGs) on the carbonyl lower the energy of the carbonyl π^* orbital, which reduces the energy gap with the CI orbital, stabilizes the transition state (TS), and increases reactivity. Electron donating groups (EDGs) have the opposite effect, and ultimately decrease reactivity. Hammett substituent constants provide a useful qualitative proxy for the electron-donating or withdrawing-character of the substituents on the carbonyl.[172,173]

The kinetics of the reaction of acetone (Ac, $R_1 = R_2 = CH_3$), a representative model ketone, with CH_2OO has been thoroughly investigated experimentally,[88,111,126–128,130] with recent measurements converging on a 298 K rate constant of $\sim 5\times10^{-13}$ cm^3 s^{-1}. Aldehydes (R_1 = H, R_2 = H or alkyl) react faster, with rate constants in the range $(1–4)\times10^{-12}$ cm^3 s^{-1}.[82,111,128,199,200] The presence of strongly electron withdrawing groups increases rate constants further. For example, hexafluoroacetone (HFA, $R_1 = R_2 = CF_3$) has a rate constant of $\sim 3\times10^{-11}$ cm^3 s^{-1}.[117,128] The α-diketones, biacetyl (BiAc, R_1=CH_3, R_2 = CH_3CO) and acetyl propionyl (AcPr, R_1 = CH_3/C_2H_5), have both electron-donating alkyl and electron-withdrawing acyl substituents, and the reactions $\sim 1\times10^{-11}$ cm^3 s^{-1}.[126,127] Where examined, all reactions of carbonyls with CH_2OO show a negative temperature dependence.

Our focus in this study is the reactions of CH_2OO with two hydroxyketones: hydroxyacetone (acetol, AcOH, R_1 = CH_3, R_2 = CH_2OH) and 4-hydroxy-2-butanone (4H2B, R_1 = CH_3, R_2 = CH_2CH_2OH). Hydroxyketones are multifunctional VOCs, which present multiple reactive sites and may exhibit cooperative effects.[93] The reactions of AcOH and 4H2B with CH_2OO can occur at the carbonyl or the hydroxyl moieties. The latter pathway is expected to be minor, as aliphatic alcohols react with CH_2OO to form alkoxymethyl hydroperoxides, with rate constants in the range $(1–2)\times10^{-13}$ cm^3 s^{-1} at 298 K,[79,94] smaller than those of most carbonyls. The hydroxymethyl (CH_2OH) group has Hammett substituent constants of zero, and is neither electron-donating nor withdrawing. Consequently, the rate constant for the cycloaddition reaction is anticipated to be comparable to that of acetaldehyde.

AcOH and 4H2B have also been identified as trace gases in the troposphere,[201,202] where they are formed as secondary oxidation products of isoprene and other atmospheric hydrocarbons.[203–205,76] AcOH is also produced directly from biomass burning.[206,207] The major reactive sink for hydroxyketones is reaction with OH radicals, which results in lifetimes of a few days. Kinetics studies of the OH + AcOH reaction have produced surprisingly inconsistent results; the IUPAC recommendation for the 298 K rate constant is 5.9×10^{-12} cm^3 s^{-1}.[208–217] The OH + 4H2B kinetics

measurements show similar inconsistencies, but the 298 K rate constant appears to be similar.[210,218–222] Photolysis of both species is far slower than reaction with OH, particularly for AcOH where the presence of the α-hydroxyl group causes a ~10 nm blue shift of the first absorption band that reduces the absorption at actinic wavelengths (see Figure 4.2).[155]

The results of laser flash photolysis transient absorption spectroscopy measurements quantifying the temperature-dependent kinetics of the reactions of CH_2OO with AcOH and 4H2B across the range 275–335 K are reported here. Complementary *ab initio* calculations map out the reaction energy profiles and provide a basis for explaining reactivity trends using frontier molecular orbital theory. The potential implications of the title reactions in the atmosphere are briefly discussed.

4.3 Methods

The temperature-controlled flash photolysis, transient absorption spectroscopy apparatus has been described in detail previously,[127] and will be summarized briefly here.

CH_2OO was produced in the flow reactor by the photolysis of diiodomethane (CH_2I_2) in the presence of excess O_2 using the 355 nm output of an Nd:YAG laser (Continuum Surelite II-10). Typical pulse energies were ~10 mJ, resulting in fluences of ~28 mJ cm^{-2}. Absorption spectra were obtained by dispersing the output of pulsed LEDs (LightSpeed Technologies) in a spectrograph (Andor Shamrock 303i with iDus 420 CCD camera). Kinetics measurements used an LED nominally centered at 365 nm to obtain transient absorption spectra of CH_2OO (and IO) in the range 360–395 nm at various time delays after photolysis. Independent absorption measurements were performed in the range 270–295 nm using an LED centered at 280 nm to quantify reactant concentrations. A digital delay generator (Quantum Composers, 9528) synchronized the photolysis laser, LED driver, and CCD camera.

The flow reactor itself comprises a jacketed quartz tube, with an effective path length of 90 cm. A unistat (Huber Tango) precisely controlled the reactor temperature (within < 1 K) over the range 275–335 K. Gas flows into the reactor were controlled using a range of choked-flow orifices (O'Keefe). Gases (O_2 and N_2) were used directly from the cylinders, while liquids (CH_2I_2, AcOH, and 4H2B) were placed in smog bubblers and carried into the cell by a flow of N_2. The smog bubblers were held in a water bath maintained at 295 K to prevent evaporative cooling and vapor pressure drop off. Measurements with AcOH used a total flow rate of 3.8 sLpm, resulting in a pressure of 78 Torr in the reactor. The lower vapor pressure of 4H2B (1.2 Torr versus 3.5 Torr at 295 K)[219,223] required a larger total flow rate of 4.9 sLpm and a reactor pressure of 100 Torr. Typically, the concentrations in the reactor were $[CH_2I_2] = 1.1\times10^{15}$ cm^{-3}, $[O_2] = 2.1\times10^{17}$ cm^{-3}, [AcOH] = (1–5)×10^{15} cm^{-3}, [4H2B] = (0.5–1.5)×10^{15} cm^{-3}, with N_2 balance. All chemicals were used as supplied: O_2 (Airgas, UHP 4.4), N_2 (Airgas, industrial grade), CH_2I_2 (Sigma Aldrich, 99%), AcOH (Acros Organics, 90%), and 4H2B (Tokyo Chemical Industry, 95%). FT-IR spectra of the headspace above samples of liquid AcOH and 4H2B were recorded (see Figure 4.1) using a JASCO 4700 spectrometer to identify any impurities. No bands associated with any other organic species were identified, consistent with previous suggestions that the likely impurity in AcOH is residual H_2O,[224] although at levels too low to affect the kinetics measurements.

Electronic structure calculations were performed with the GAMESS and Gaussian 16 programs.[146–149] Geometries of reactants, products, entrance channel complexes, and transition state structures were initially optimized using the B3LYP functional with the Dunning-type cc-pVDZ basis set and the harmonic frequencies subsequently calculated. The presence of zero or one imaginary frequency confirmed that the optimized geometries were true minima or transition states (TSs), respectively. Intrinsic reaction coordinate (IRC) calculations were performed to verify that the expected reactants and products were reached on either side of the TS. Reaction thermochemistry was determined using rigid-rotor harmonic-oscillator (RRHO) partition functions. Additional calculations were performed

using the composite CBS-QB3 method to refine the calculated energies.[151] The CBS-QB3 method provides reliable thermochemistry at modest computational cost.[152–154] In addition, the frontier molecular orbital energies are obtained from the optimization output at the B3LYP/cc-pVDZ level of theory. Previous work has shown the frontier orbital energies calculated at a similar level of theory to provide linear correlation with molecular properties such ionization potential, electron affinity, and excitation energy.[225]

4.4 Results

4.4.1 Reactant Concentration Measurements

The AcOH and 4H2B samples were used as provided by the manufacturers, with reported purities of 90% and 95%, respectively. IR spectra of the headspace above liquid samples of both hydroxyketones were recorded in a 10 cm cell with ZnSe windows in a JASCO 4700 FT-IR spectrometer to identify any impurities present. The spectra are Figure 4.1. The AcOH spectrum is

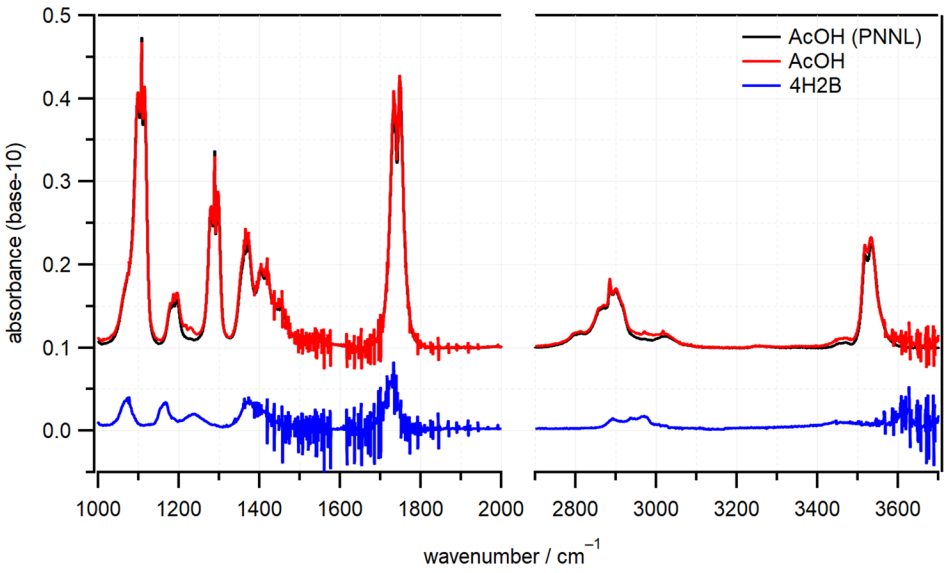


Figure 4.1 Headspace FT-IR spectra of AcOH (red) and 4H2B (blue). Also shown is the AcOH spectrum (black) obtained from the PNNL IR spectral database.[1]

the same as the that obtained from the PNNL database,[206] with no obvious features present that could be attributed to impurities. To the best of our knowledge, the gas-phase spectrum of 4H2B has not been reported in the literature. The differences in the major features of the corresponding spectra for 4H2B and AcOH are most likely attributed to the different number of carbons and hydrogens. The C–H modes at ~1300 and ~2900 cm^{-1} do not agree. The O–H band on 4H2B is blue-shifted, which implies it is less hydrogen bonded to the carbonyl oxygen. The carbonyl stretching bands look similar, although the absorbance is weaker as a result of the lower vapor pressure of 4H2B.

As in our previous work,[79,126,127] concentrations of the hydroxyketone reactants in the flow cell during kinetics measurements can be estimated using reported vapor pressures (3.50±0.17 Torr for AcOH, and 1.24±0.04 Torr for 4H2B)[219,223] and fractional flow rates. Since the first UV absorption bands of both hydroxyketones can be observed using an LED centered at 280 nm,[155] their concentrations can also be measured directly. Absorption spectra of the hydroxyketones are recorded in the wavelength range 275–290 nm under conditions that are otherwise identical to those used in the kinetics measurements across the 275–335 K temperature range. Absolute hydroxyketone number densities are determined using previously reported absorption cross sections. The first UV absorption bands of AcOH and 4H2B have peak cross sections of ~6×10^{-20} cm^2 at ~270 nm and 280 nm respectively, as is typical of the excitation to the $S_1(n\pi^*)$ state in carbonyls.[155] The only reported measurement for 4H2B is by Messaadia et al,[226] while various measurements exist for AcOH.[155,209,212,226] There is a discrepancy between the AcOH cross sections recommended by the IUPAC Task Group on Atmospheric Chemical Kinetic Data Evaluation and JPL Chemical Kinetics and Photochemical Data for Use in Atmospheric Studies Evaluation.[91,217] While IUPAC prefers the values of Orlando et al,[209] JPL uses an average of that and lower values measured by Butkovskaya et al.[209,212] Since the other reported measurements agree well with the JPL recommendation,[155,226] we elect to use it to quantify $[AcOH]_{exp}$ and determine a concentration scale factor. The UV absorption spectra of both hydroxyketones are shown in Figure 4.2.

The gradients of plots of measured against estimated concentrations ($[X]_{exp}$ vs. $[X]_{est}$) (Figure 4.3) provide a scaling factor that can be used to correct the estimated hydroxyketone concentrations. Previously,[126,127] we have found concentration scaling factor values within 10% of unity for acetone and diketones, indicating that the estimates give values close to the actual concentrations in the flow cell. The hydroxyketone concentration scaling factors deviate from unity, however, as can be seen from Figure 4.4. For AcOH, the scale factor is independent of temperature with an average value of 1.23±0.07, indicating that the actual concentration is slightly higher than estimated. In contrast, the values determined for 4H2B suggest that its concentration is overestimated, with an average 0.59±0.08. The overall uncertainties are estimated from the spread in values obtained in multiple measurements across the temperature range.

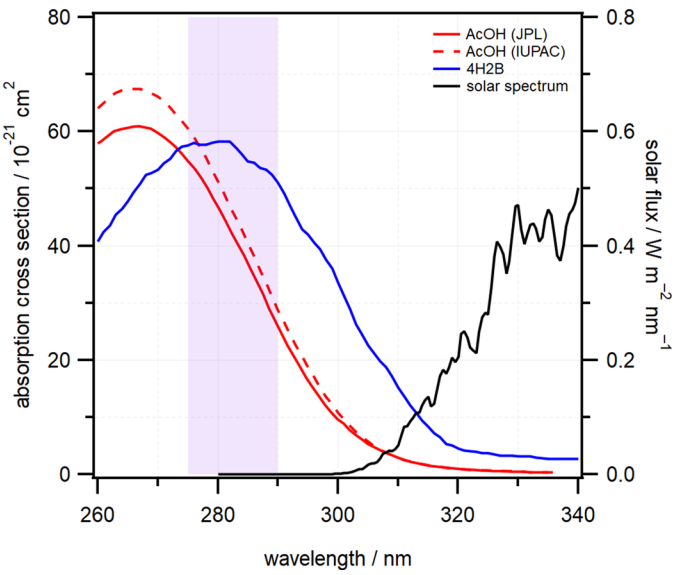


Figure 4.2 UV absorption spectra of AcOH (red) and 4H2B (blue). The shaded area indicates the wavelength range covered by the 280 nm LED used for concentration measurements. Solar flux (black) is also shown.

Deviations from unity for the concentration scaling factors derive primarily from systematic errors in $[X]_{est}$ and/or $[X]_{exp}$, which depend respectively on the hydroxyketone vapor pressures $P_{vap,X}$ and absorption cross sections $\sigma_X(\lambda)$. The T-dependent vapor pressures of AcOH and 4H2B have been measured to a high degree of precision,[219,223] although several groups have discussed evidence of hydroxyketone "stickiness" in the course of kinetics measurements.[213,214,226] Wall losses between the bubbler and the flow reactor would lead to concentration overestimates and scaling factors <1, which is consistent with the observed value for 4H2B but not for AcOH. Based on the FT-IR spectrum of AcOH shown in and reported band intensities,[206] we estimate a vapor pressure of 3.9±0.4 Torr. If the C=O stretch bands of AcOH and 4H2B are assumed to have the same intensity (as supported by *ab initio* calculations) we estimate the vapor pressure of 4H2B to be 0.76±0.11 Torr. The ratios of these

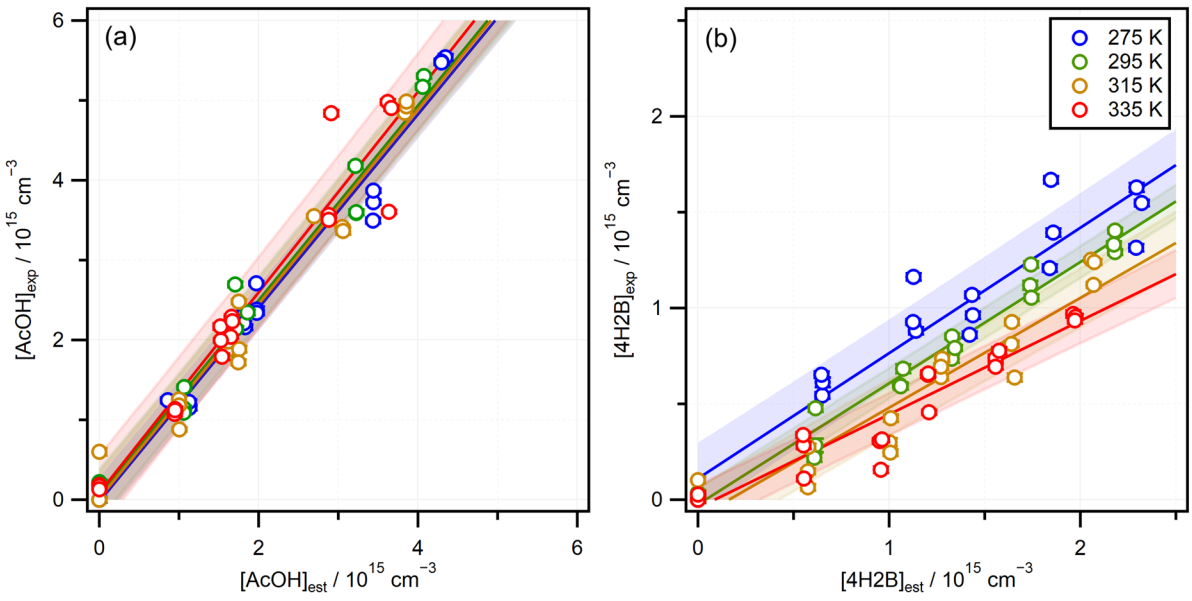


Figure 4.3 Calibration plots of experimental versus estimated concentrations of (a) AcOH on the left and (b) 4H2B on the right in the range 275–335 K, blue to red respectively.

estimated vapor pressures to the literature values[219,223] are 1.11±0.12 for AcOH and 0.61±0.09, in good agreement with the measured scaling factors and suggesting that the systematic error originates in the reported values of $P_{vap,X}$. Another possibility for values <1 is that the smog bubbler headspace is not saturated with the organic vapor, although the use of the experimental scale factor corrects for this effect.

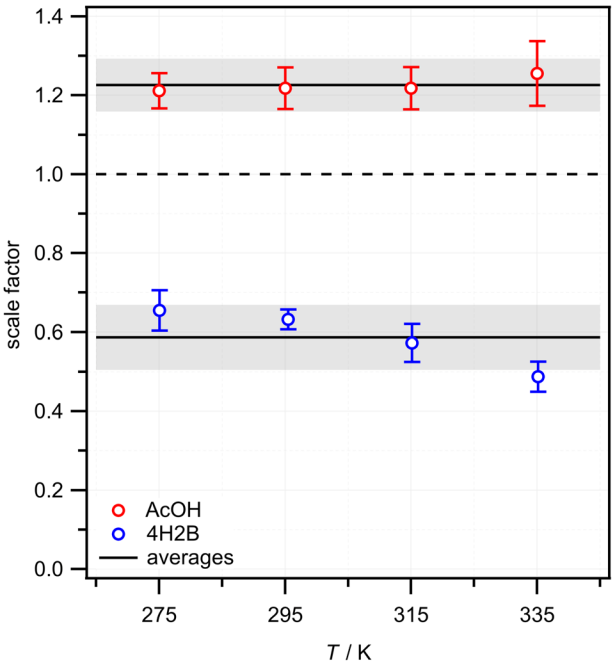


Figure 4.4 Scale factors determined from gradient of $[X]_{exp}$ versus $[X]_{est}$ calibration plots as a function of temperature. Solid lines are the *T*-independent average, while shaded areas represent the estimated experimental uncertainty, based on the variability of the measurements. Values >1 or <1 indicate that reactant concentration is underestimated (AcOH) or overestimated (4H2B), respectively.

For the purposes of the kinetics measurements, the absorption cross sections are ultimately of most significance as they are used to determine $[X]_{exp}$ directly. As noted above, $\sigma_{AcOH}(\lambda)$ values recommended by IUPAC are 10% greater than the JPL values, which would produce lower values of

$[AcOH]_{exp}$ and bring the concentration scaling factor value closer to unity (1.12±0.06) and closer to the vapor pressure ratio estimated from the FT-IR spectra. Such a change would also require an increase in the bimolecular rate constant for reaction with CH_2OO proportionally. We proceed on the basis that the $\sigma_X(\lambda)$ values used are accurate. The rate constants determined in the experiments discussed below are inversely proportional to $\sigma_X(\lambda)$ and can be adjusted appropriately if improved values become available in the future.

4.4.2 Kinetics Measurements

The kinetics of the reactions of CH_2OO with AcOH and 4H2B were studied under pseudo-1st order conditions of excess hydroxyketone at four temperatures in the range 275–335 K. The lowest hydroxyketone concentrations were approximately two orders of magnitude greater than $[CH_2OO]_0$. Transient absorption spectra obtained in the range 363–395 nm at various photolysis-probe delay

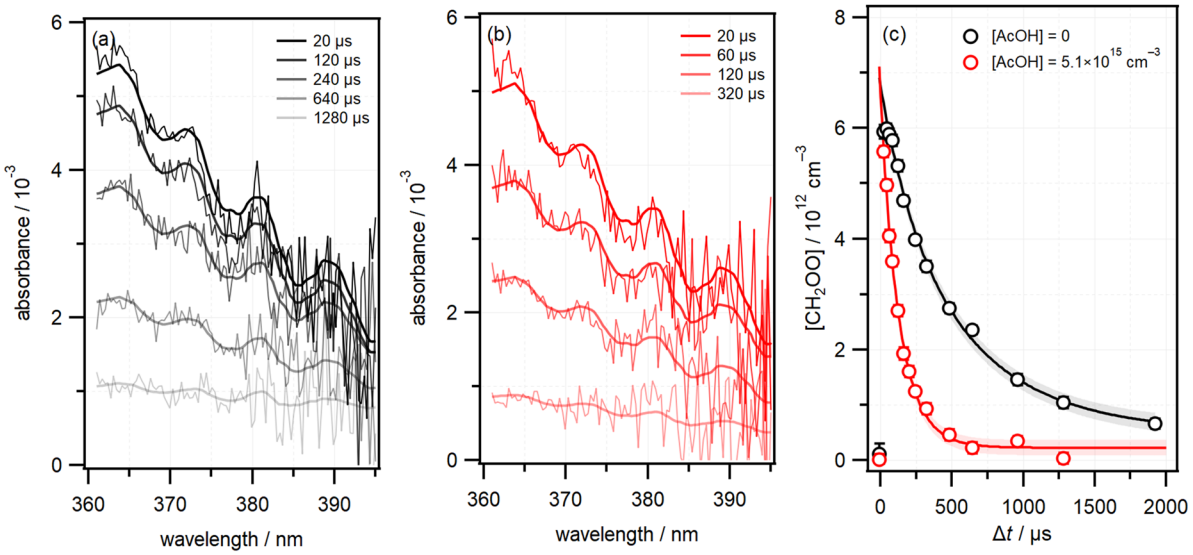


Figure 4.5 Broadband transient absorption spectra recorded at various time delays after photolysis at 295 K. (a) Spectra recorded in the absence of any additional reactive species, (b) spectra recorded with [AcOH = 5.1×10^{15} cm^{-3}. (c) $[CH_2OO]$ time profiles resulting from fitting the experimental transient spectra.

times were decomposed into contributions from CH_2OO and IO using known absorption spectra[50,161] to generate $[CH_2OO]_t$ and $[IO]_t$ concentration-time profiles. Examples of typical experimental transient spectra recorded with and without AcOH and the resulting $[CH_2OO]_t$ profiles are shown in Figure 4.5. As expected, the CH_2OO concentrations are observed to decrease more rapidly with increasing hydroxyketone concentration, while the IO concentration profiles remain unaffected. Peak Criegee intermediate concentrations of $[CH_2OO]_0$ = (6–8)×10^{12} cm^{-3} are significantly smaller than those of the hydroxyketone reactants, ensuring pseudo-1st order conditions.

Analysis of the $[CH_2OO]_t$ profiles used the same kinetic model as described previously and will be summarized here.[126,127] The differential rate law for CH_2OO loss includes a quadratic term for bimolecular self-reaction with rate constant k_{self} and a linear term for pseudo-1st order reactions with rate constant k_{loss}. The pseudo-1st order rate constants k_{loss} at each hydroxyketone concentration are derived from fits of the $[CH_2OO]_t$ profiles to the integrated rate law, with k_{self} fixed to a T-independent value of 7.8×10^{-11} cm^3 s^{-1}.[127] Plots of k_{loss} against [hydroxyketone] are linear and a least-squares fit (weighted by the uncertainties in both k_{loss} and [hydroxyketone]) returns a background loss rate k_{bgd} and the bimolecular rate constant $k_{hydroxyketone}$ as the gradient. Examples are shown in Figure 4.6 for the reactions of CH_2OO with AcOH and 4H2B from 275–335 K. At room temperature, the bimolecular rate constants for the CH_2OO + AcOH and CH_2OO + 4H2B reactions are the same within the statistical uncertainties of the fits: k_{AcOH} = (1.09±0.15)×10^{-12} cm^3 s^{-1} and k_{4H2B} = (1.11±0.26)×10^{-12} cm^3 s^{-1}. As has been observed for other reactions of CH_2OO with carbonyl species,[111,127,130,200] the rate constants for the AcOH and 4H2B reactions also decrease with increasing temperature. The complete set of measured T-dependent rate constants are summarized in Table 4.1. Background loss rates, attributed to reaction with I atoms or other species present in the flow reactor, are typically between ~1000–1500 s^{-1} and decrease slightly with increasing temperature. The bimolecular rate constants for the CH_2OO + hydroxyketone reactions were obtained by averaging three individual kinetic runs at each temperature, with errors representing the statistical uncertainty (1σ) in the fit. The same values,

although with smaller uncertainties, are obtained from global fits to the complete data sets at each temperature.

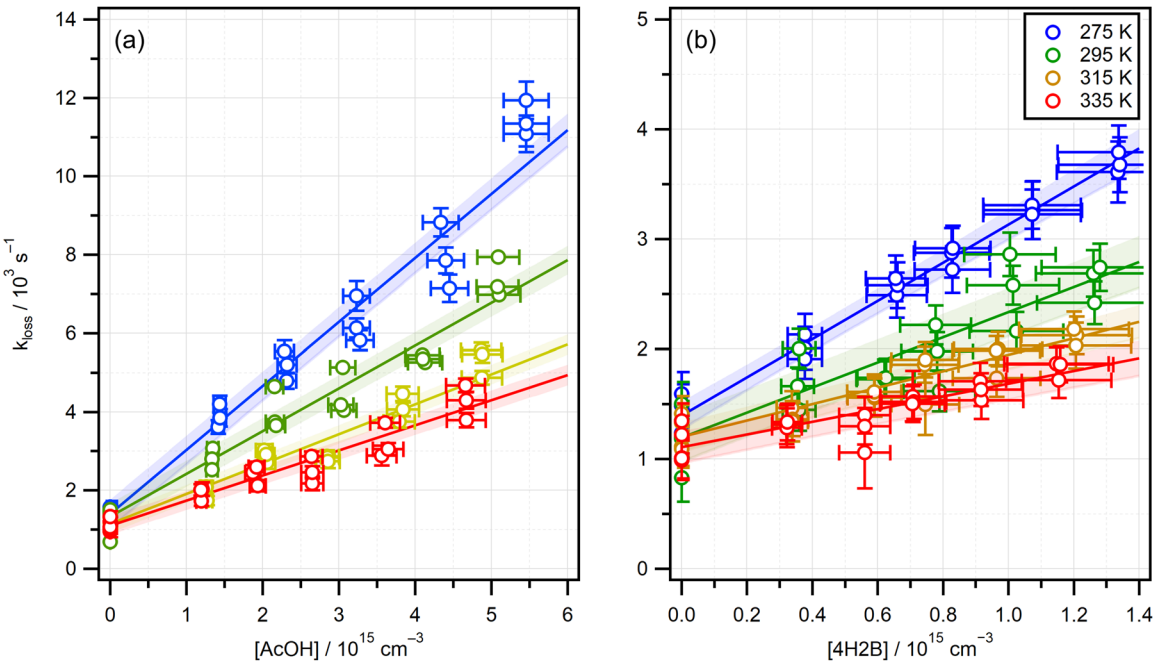


Figure 4.6 Pseudo-1st order plots for the reactions of CH_2OO with (a) AcOH and (b) 4H2B across the experimental temperature range 275–335 K, blue to red respectively. Vertical and horizontal error bars represent statistical uncertainties (1σ) in the loss rates determined from fitting [CH_2OO] time profiles and uncertainties in the hydroxyketone concentration calibration measurements, respectively. Weighted linear fits to the experimental data are also shown, with shaded area representing 1σ prediction bands.

Arrhenius plots for both reactions are shown in Figure 4.7. The plots are linear over the temperature range explored in the experiments and the T-dependent bimolecular rate constants can be expressed in Arrhenius form as $k_{AcOH}(T)$ = (4.3±1.7)×10^{-15}exp[(1630±120)/T] and $k_{4H2B}(T)$ = (3.5±2.6)×10^{-15}exp[(1700±200)/T]. The similarity of the $-E_a/R$ values indicates both reactions are equally

Table 4.1 T-dependent bimolecular rate constants, Arrhenius parameters, and standard enthalpies, entropies, and Gibbs energies of activation at 298 K for the reactions of CH_2OO with hydroxyacetone and 4H2B. Uncertainties are 1σ statistical uncertainties from the fits.

T / K	k_{AcOH} /10^{-12} cm^3 s^{-1}	k_{4H2B} / 10^{-12} cm^3 s^{-1}
275	1.63±0.07	1.70±0.04
295	1.09±0.15	1.11±0.26
315	0.75±0.03	0.75±0.09
335	0.62±0.09	0.60±0.12
A / 10^{-15} cm^3 s^{-1}	4.3±1.7	3.5±2.6
E_a/R / K	–1630±120	–1700±200
E_a / kcal mol^{-1}	–3.24±0.23	–3.38±0.40
$\Delta^{\ddagger}H°$ / kcal mol^{-1}	–4.43±0.23	–4.56±0.40
$\Delta^{\ddagger}S°$ / cal K^{-1} mol^{-1}	–39.5±0.4	–39.9±0.7
$\Delta^{\ddagger}G°$ / kcal mol^{-1}	+7.36±0.26	+7.34±0.46

sensitive to temperature, within the 1σ experimental uncertainties, with negative energies of activation of $E_a \approx -3.3$ kcal mol^{-1}.

The thermodynamic formulation of canonical transition state theory (CTST) for a bimolecular gas-phase reaction can be used to extract the standard entropy, enthalpy, free energy of activation:

$$k = \frac{k_B^2}{hp°} \exp\left(\frac{\Delta^{\ddagger}S°}{R}\right) T^2 \exp\left(-\frac{\Delta^{\ddagger}H°}{RT}\right) \qquad \text{E 4.1}$$

The factor $k_B^2/hp°$ is evaluated to be 2.87×10^{-12} cm^3 s^{-1} K^{-2} using $p° = 10^5$ Pa. $\Delta^{\ddagger}S°$ and $\Delta^{\ddagger}H°$ are the standard entropy and enthalpy of activation, respectively. The latter is related to the activation

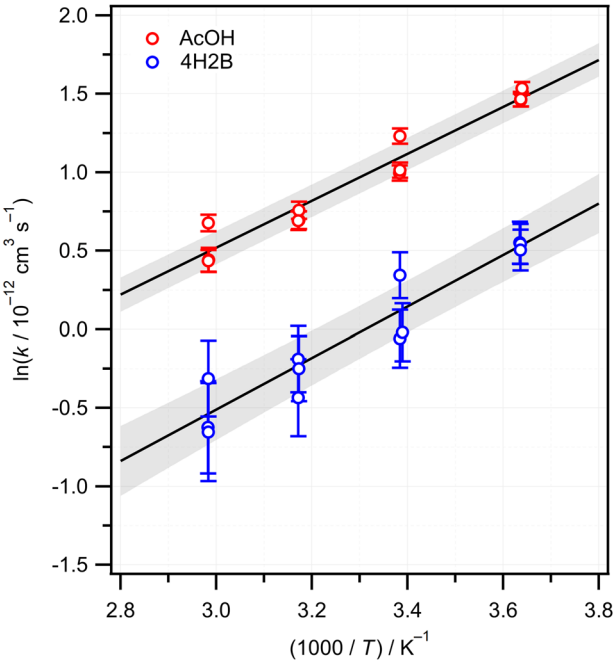


Figure 4.7 Arrhenius plots for the reaction of CH_2OO with AcOH (red) and 4H2B (blue), with 1σ statistical uncertainties. The AcOH data has been offset vertically for clarity. Solid black lines are linear fits with shaded areas representing 1σ prediction bands.

energy by $\Delta^{\ddagger}H^{\circ} = E_a - 2RT$ for a bimolecular reaction.[227] Unsurprisingly, given the similarities in the T-dependent rate constants, the thermodynamic parameters derived for the AcOH and 4H2B reactions are also similar, with $\Delta^{\ddagger}S^{\circ} \approx -40$ cal K^{-1} mol^{-1}, $\Delta^{\ddagger}H^{\circ} \approx -4.5$ kcal mol^{-1}, and $\Delta^{\ddagger}G^{\circ} \approx +7.3$ kcal mol^{-1} at 298 K. The pre-exponential factors, activation energies, and thermodynamics of activation for AcOH and 4H2B are compiled in Table 4.1.

The pressure dependence of the CH_2OO + hydroxyketone reactions was also investigated by measuring k_{loss} across the range 80–120 Torr range at 295 K and using a single concentration of each hydroxyketone ([AcOH] = (5.1±0.3)×10^{15} cm^{-3} and [4H2B] = (8.0±1.1)×10^{14} cm^{-3}). The total pressure was changed by varying the flow rate of the N_2 buffer gas, while leaving all other flow rates unchanged. The average k_{loss} values as a function of total pressure are shown in Figure 4.8. No change

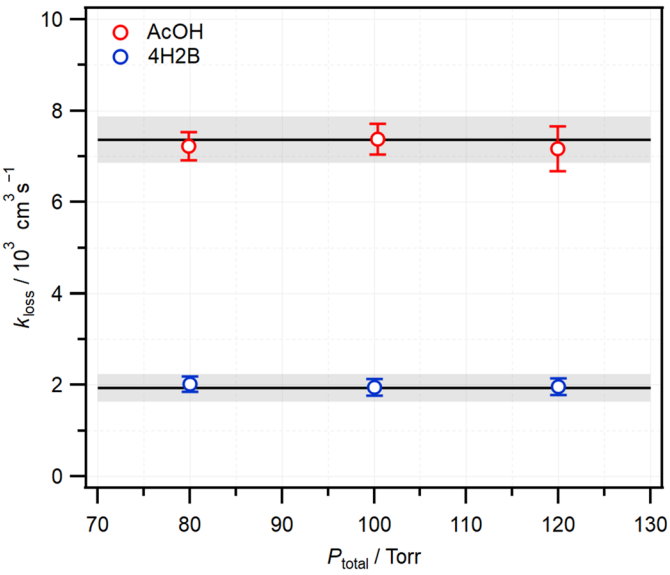


Figure 4.8 Pressure dependence of CH_2OO loss rates in the presence of AcOH (red, [AcOH] = (5.1±0.3)×10^{15} cm^{-3}) and 4H2B (blue, [4H2B] = (8.0±1.1)×10^{14} cm^{-3}) at 295 K. Total pressure was varied by changing only the flow rate of the N_2 buffer, with all other gas flows held constant. The solid lines indicate the average loss rates determined from the kinetics measurements. Shaded areas represent 1σ uncertainties.

in k_{loss} is observed as the total pressure is varied and the average values are the same as those obtained in the kinetics measurements. Based on similar measurements for the CH_2OO + Ac reaction,[127,130] we conclude that the rate constants measured in 80–100 Torr of N_2 likely represent the high-pressure limit.

4.4.3 Computational Results

We have performed ab initio calculations to characterize the reactions of CH_2OO with AcOH and 4H2B. Geometries of the reactants, entrance channel complexes, transition states (TSs), and primary products were optimized, initially at the B3LYP/cc-pVDZ level of theory, and harmonic frequency analysis performed to confirm minima and saddle points. Intrinsic reaction coordinate calculations

were performed to ensure that the TSs connected the reactant and product minima. Subsequent calculations were performed at the CBS-QB3 level of theory to provide improved thermochemistry. The CBS-QB3 thermochemistry data, $\Delta(E+\text{ZPE})$ at 0 K and $\Delta H°$, $\Delta G°$ at 298 K, is summarized in Table 4.2.

Preliminary calculations at the B3LYP/cc-pVDZ level of theory were performed to assess the possible relevance of different hydroxyketone conformers. Four low-energy conformers were identified for each molecule, distinguished primarily by rotations about the α C–C bond and the C–O bond. The optimized geometries are shown in Figure 4.9. The most stable hydroxyketone conformers are distinguished by the presence of an intramolecular hydrogen bond, resulting in a cyclic five and six membered structures for AcOH and 4H2B, respectively. For both hydroxyketones, the Boltzmann population distribution is dominated at all temperatures (>98%) by the intramolecular H-bonded conformers, which are at least 3 kcal mol^{-1} lower in energy than the next lowest conformer. Higher energy conformers were assumed to play no significant role in the reactions with CH_2OO and were neglected in subsequent calculations.

Table 4.2 CBS-QB3 thermochemistry for the reactions of CH_2OO with AcOH and 4H2B: $\Delta E+\text{ZPE}$ @ 0K ($\Delta H°$ @298 K) [$\Delta G°$@ 298 K] in kcal mol^{-1}.

		cycloaddition A	cycloaddition B	1,2-addition
AcOH	vdW	–8.7 (–8.3) [+1.3]	–8.7 (–8.5) [+2.1]	–4.0 (–3.7) [+5.1]
	TS	–5.6 (–6.5) [+6.9]	–6.2 (–7.2) [+6.7]	+2.2 (+1.4) [+13.6]
	product	–48.1 (–49.5) [–34.9]	–48.3 (–49.8) [–34.8]	–48.0 (–48.9) [–35.9]
4H2B	vdW	–8.3 (–8.0) [+1.8]	–8.9 (–8.6) [+1.3]	–4.9(–4.6) [+4.1]
	TS	–5.7 (–6.5) [+6.4]	–6.7 (–7.6) [+5.6]	–0.5 (–1.1) [+10.3]
	product	–49.2 (–50.6) [–35.8]	–49.6 (–51.0) [–36.2]	–46.6 (–46.9) [–36.1]
Ac	TS	–6.1 (–6.4) [+5.5]		–
MeOH	TS	–	–	–2.0 (–3.1) [+9.1]

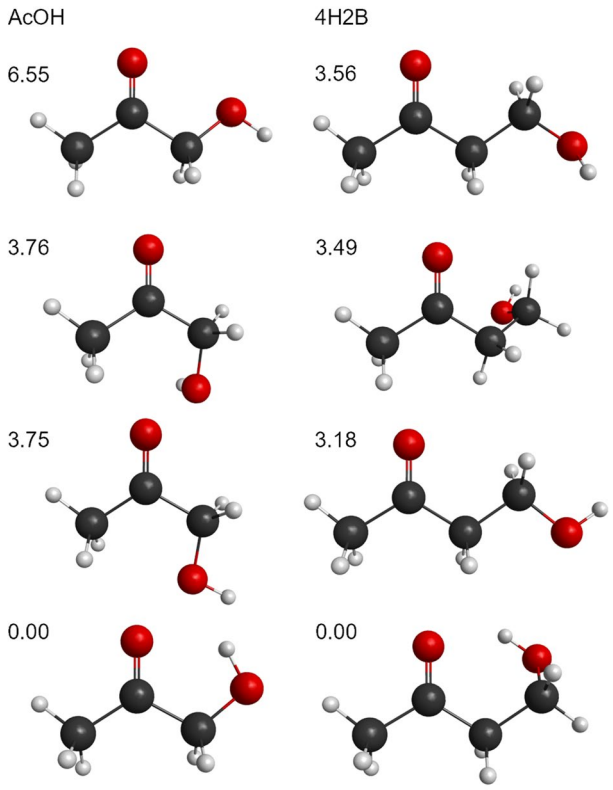


Figure 4.9 Low-energy conformers of AcOH (left) and 4H2B (right), calculated at the B3LYP/cc-pVDZ level. The zero-point corrected energy (kcal mol^{-1}) of each conformer relative to the most stable cyclic H-bonded structures is indicated.

Hydroxyketones can react with CH_2OO as either carbonyls or alcohols. Reaction at the carbonyl site occurs via a 1,3-dipolar cycloaddition, leading to the formation of a five membered cyclic trioxolane, or secondary ozonide (SOZ). Reaction at the hydroxyl group can occur via a 1,2-addition (or insertion) mechanism, leading to a substituted hydroperoxide. The overall zero-point corrected energy [$\Delta(E$+ZPE) at 0 K] and Gibbs free energy ($\Delta G°$ at 298 K) profiles are shown in Figure 4.10. The reactions are similarly exoergic with products lying at values of $\Delta(E$+ZPE) ≈ –50 kcal mol^{-1} ($\Delta G°$ ≈ –35 kcal mol^{-1}). The entrance channels of both reactions support van der Waals complexes that are bound by 4–9 kcal mol^{-1}, while the TSs have energies that are generally below the separated

reactants. On the free energy surface, all entrance channel complexes and TSs are higher in energy than the reactants.

Cycloaddition at the carbonyl site of each hydroxyketone can occur via two near-equivalent pathways that differ in the orientation of the CH_2OO with respect to the OH group of the hydroxyketone. In pathway A, the central O atom of CH_2OO is oriented toward the hydroxyalkyl side at TS_A, while pathway B has the central O oriented towards the methyl side of the hydroxyketone at TS_B. The optimized TS_A and TS_B geometries are shown in Figure 4.11. Unsurprisingly, the energies and free energies are similar. The free energy barriers for the A and B pathways of the AcOH reaction differ by only 0.2 kcal mol^{-1}, while a difference of 0. 8 kcal is found for the 4H2B reaction, slightly favoring

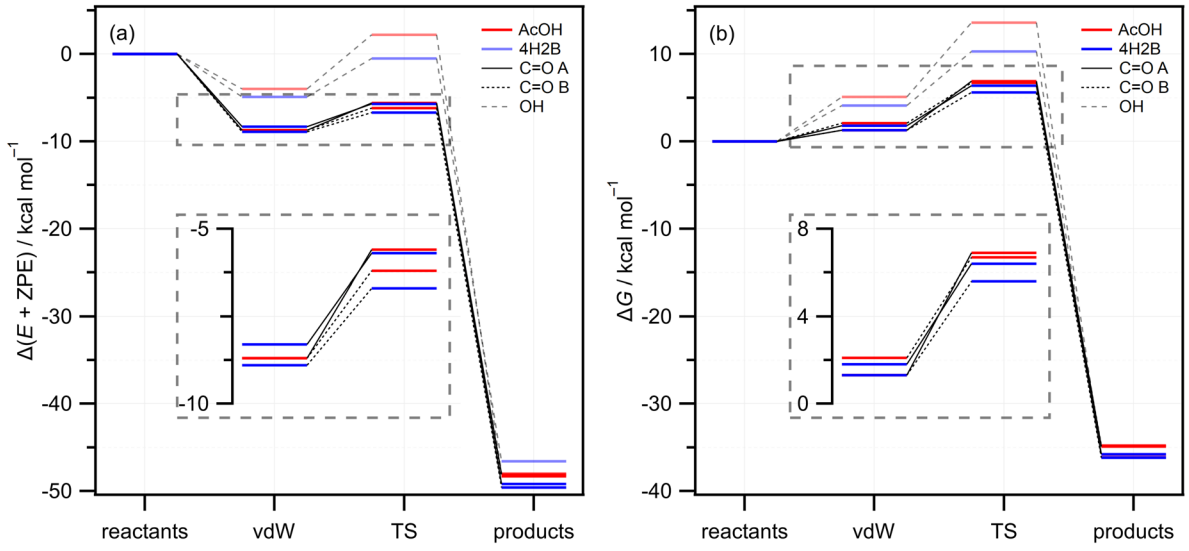


Figure 4.10 CBS-QB3 energy and free energy profiles for the CH_2OO + AcOH (red) and 4H2B (blue). Panel (a) shows $\Delta(E$+ZPE) at 0 K and panel (b) shows ΔG at 298 K for both reactions. Solid lines connect stationary points for cycloaddition A, dotted lines for cycloaddition B, and dashed lines for 1,2-addition at the OH group. The inset shows a magnified view of the entrance channel van der Waals complex (vdW) and the transition state (TS) for the cycloaddition pathways.

TS_B. The larger energy difference for 4H2B arises because of a geometrical distortion of the hydroxyethyl group out of the plane, away from the attacking CH_2OO, in TS_A while the carbon backbone maintains planarity in TS_B. The TS free energies for reaction at the OH site of the hydroxyketones are significantly higher than those for the cycloaddition reactions (almost 7 kcal mol^{-1} for the AcOH reaction and ~4 kcal mol^{-1} higher for the 4H2B reaction), as shown in Figure 4.10 and Table 4.2.

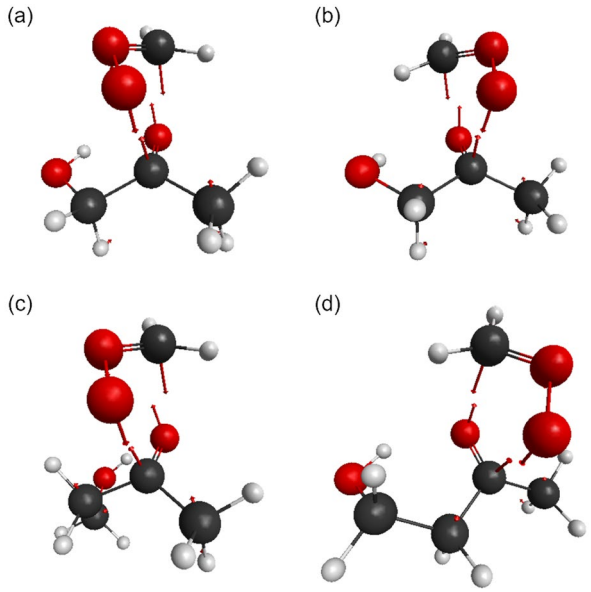


Figure 4.11 Optimized transition state geometries for the 1,3-dipolar cycloaddition reactions of CH_2OO with AcOH (a, b) and 4H2B (c, d). The orientation of the central O atom of CH_2OO oriented towards (a,c) or away (b,d) from the hydroxyl group of the hydroxyketone identifies cycloaddition A or B, respectively. Red arrows indicate displacement vectors along the reaction coordinate.

4.5 Discussion

The CH_2OO + AcOH and CH_2OO + 4H2B reactions are found to have almost identical rate constants across the 275–335 K temperature range studied experimentally, as summarized in Table 4.1. At room temperature (~295 K), the rate constants for both reactions are 1.1×10^{-12} cm^3 s^{-1}, which is greater than the reactions of simple ketones by around a factor of two. The rate constant for the CH_2OO + acetone (Ac) reaction has been measured by various groups, with values in the range k_{Ac} = $(2.3–4.8)\times10^{-13}$ cm^3 s^{-1} reported,[88,111,126–128,130] where the range is likely a consequence of the reaction pressure dependence. Measurements at the high-*P* limit have a weighted average value k_{Ac} = 4.3×10^{-13} cm^3 s^{-1}.[88,126,127,130] The rate constant for the CH_2OO + methylethylketone (MEK) reaction is slightly larger than that of Ac with a value k_{MEK} = 6.4×10^{-13} cm^3 s^{-1}.[228] The room temperature rate constants

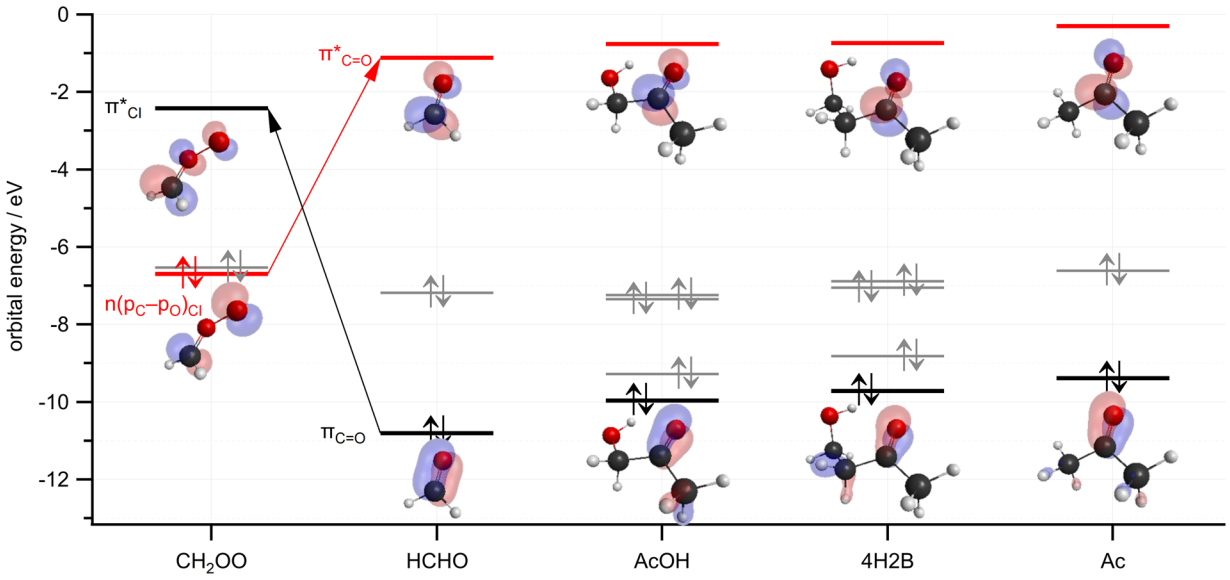


Figure 4.12 Frontier orbital energies calculated at B3LYP/cc-pVDZ level for CH_2OO and the carbonyls formaldehyde, acetone, and the hydroxyketones AcOH and 4H2B. Red: S orbitals (non-bonding $n(p_C–p_O)$ for CH_2OO, π* LUMO for carbonyls), black: A orbitals (π bonding orbitals of carbonyls, π* antibonding for CH_2OO), gray: non-bonding (n_O orbitals).

for the hydroxyketone reactions are much closer to that of acetaldehyde (MeCHO), for which rate constants in the range k_{MeCHO} = (1.0–1.7)×10^{-12} cm^3 s^{-1} have been reported.[82,128,111] The CH_2OO + R_1R_2CO reactions also all show similar negative temperature dependences.

The reactivity of the hydroxyketones towards CH_2OO is increased relative to aliphatic ketones, although the effect is largely insensitive to whether the OH is at the α or β position. The OH group provides an additional site for reaction via the 1,2-addition mechanism that has been characterized for alcohols.[79,94–96] In general, alcohols tend to react with CH_2OO much more slowly than carbonyls. For example, the rate constant for the CH_2OO + methanol (MeOH) reaction at room temperature is k_{MeOH} = 1.2×10^{-13} cm^3 s^{-1}.[79,94] The increased rate constant for the hydroxyketones relative to acetone is likely due to enhancement of the 1,3-dipolar cycloaddition mechanism rather than being due to the presence of an additional reaction pathway. We note that synergistic rate constant increases arising from the presence of different functional groups have been demonstrated in other Criegee intermediate reactions. For example, 3-aminopropanol reacts with acetaldehyde oxide, CH_3CHOO, in a concerted double hydrogen atom transfer (DHAT) step, where both the amine and hydroxyl functional groups interact with the CI simultaneously, significantly faster than simple amines or alcohols.[93,229] Additionally, acetylacetone (AcAc), which exists predominantly as its enolone tautomer, has C=O, OH, and C=C sites for reaction with CH_2OO. The CH_2OO + AcAc reaction is twice as fast as CH_2OO + Ac at room temperature (k_{AcAc} = 8.0×10^{-13} cm^3 s^{-1}) and shows a weak temperature dependence ($-E_a/R$ = 460 K) which can be explained in part by the existence of competitive pathways for reaction at both the C=O and C=C sites, where *ab initio* calculations find similar $\Delta^{\ddagger}G°$ values at 298 K.[126,127] Rate constants for CH_2OO + alkene reactions are generally much smaller than for carbonyls,[115] and show a positive temperature dependence. For the AcAc reaction, it appears that the adjacent carbonyl group may enhance the reactivity at the C=C site.

The experimental kinetics observations are supported by the *ab initio* calculations, which show the presence of relatively stable entrance channel complexes followed by TS barriers that are in most cases submerged relative to the reactants, consistent with the negative temperature dependences. Additionally, no dependence on total pressure was observed in the range 80–120 Torr of N_2. A two-step mechanism for either the cycloaddition or 1,2-addition reactions can be written as

$$CH_2OO + R_1R_2C{=}O \rightleftharpoons \text{complex} \quad \text{(R 4.1)}$$

$$\text{complex} \rightarrow \text{products} \quad \text{(R 4.2)}$$

where the products are either SOZs or hydroperoxide species. In the high-P limit, equilibrium is established for reaction R1 and the overall rate constant can be represented as $k = k_2K_1$, where $K_1 = k_1/k_{-1}$. From the perspective of transition-state theory, the magnitude of the overall experimental rate constant is largely determined by the standard free energy of activation $\Delta^{\ddagger}G°$ at the TS. The results of the CBS-QB3 ab initio calculations are summarized in Table 4.2 and Figure 4.10. Free energy barriers for the cycloaddition reactions at the carbonyl are calculated to be broadly similar (~+6 kcal mol^{-1}) and analysis of the temperature dependence of the rate constants results in values that are in good agreement (see Table 4.1). In contrast, the calculated free energy barriers for reaction at the hydroxyl group are significantly higher (>10 kcal mol^{-1}). For comparison, the free energy of activation for CH_2OO reacting with methanol is calculated to be $\Delta G°$ = +9.1 kcal mol^{-1} at the same CBS-QB3 level of theory (see Table 4.2). That is, the energy barrier for reaction at the OH position is even higher in the hydroxyketones than in a simple alcohol like methanol, for which the observed rate constant is an order of magnitude lower. The higher energy barrier is consistent with the disruption of the intramolecular H-bond in the minimum energy structure of hydroxyketones required for reaction at the hydroxyl group. It is only the slightly higher-energy conformers shown in Figure 4.9 that can take part in the 1,2-addition with CH_2OO. Consequently, we conclude that the dominant reaction between CH_2OO and the hydroxyketones is the 1,3-dipolar cycloaddition at the C=O reaction

site. The presence of the hydroxyl group on either the α or β carbon appears to have no significant effect on the observed rate constants, consistent with the similarity of the calculated free energy barriers.

Table 4.3 B3LYP/cc-pVDZ calculated orbital energies (eV) of HCHO, AcOH, 4H2B, and Ac. CH_2OO π* E = –2.422 eV, n(pC–pO) E = –6.694 eV. $|\Delta E_A|$ is the magnitude of the energy difference between the occupied π orbital of CH_2OO and unoccupied π*of the carbonyl (dominant). $|\Delta E_S|$ is the magnitude of the difference between the unoccupied π* orbital of CH_2OO and the occupied π orbital of the carbonyl. The $|\Delta E_A|$ interaction is always smaller.

	HCHO	AcOH	4H2B	Ac
π*	–1.116	–0.762	–0.735	–0.299
$\|\Delta E_A\|$	5.578	5.932	5.959	6.395
π	–10.803	–9.959	–9.714	–9.388
$\|\Delta E_S\|$	6.980	7.538	7.293	6.966

Previously,[126] we have attempted to rationalize the reactivity trends in 1,3-dipolar cycloaddition reactions between CH_2OO and carbonyl compounds (R_1R_2CO, where R1, R2 are alkyl or acyl substituents) using a frontier molecular orbital (FMO) theory approach.[124,125,169,198] Starting with the model of symmetry-allowed orbital interactions developed by Sustmann,[169] the cycloaddition between carbonyl compounds and CH_2OO primarily involves interactions between the out-of-plane π and π* orbitals of CH_2OO and R_1R_2CO. The dominant interaction is between the occupied non-bonding $n(p_C–p_O)$ molecular orbital of the electron rich species CH_2OO (the 1,3-dipole) and the lowest unoccupied π* molecular orbital of the electron deficient carbonyl, R_1R_2CO (the dipolarophile), with energy gap $|\Delta E_S|$. The energy gap $|\Delta E_A|$ between the occupied carbonyl π orbital and the unoccupied π* orbital of CH_2OO is, in general, larger and makes a smaller contribution to the reactivity. The

energies of the carbonyl FMOs are affected by the electron-donating or electron-withdrawing nature of the substituents R_1 and R_2. Electron-donating groups (EDGs) on the carbonyl raise the energy of the orbitals, increasing the magnitude of $|\Delta E_S|$, leading to a decreased reactivity. In contrast, electron-withdrawing groups (EWGs) lower the orbital energies and have the opposite effect on reactivity. The orbital interactions are illustrated in Figure 4.12, which shows the FMOs of CH_2OO, and the carbonyls formaldehyde (HCHO), AcOH, 4H2B, and acetone (Ac), calculated at the B3LYP/cc-pVDZ level of theory.

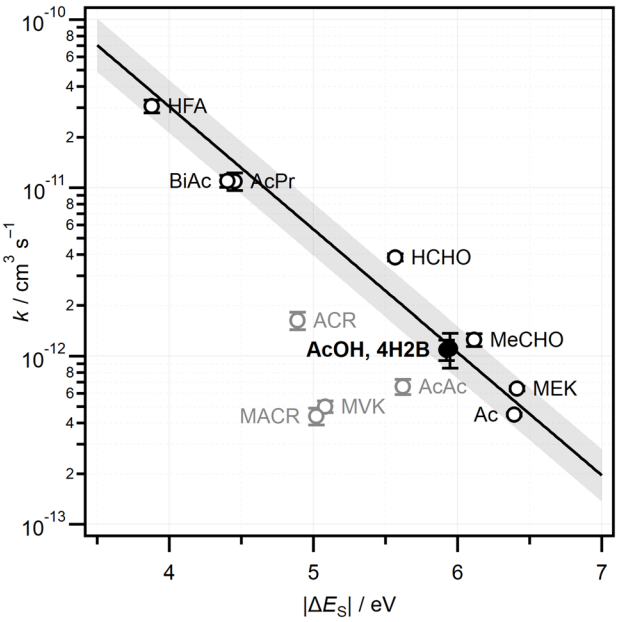


Figure 4.13 Inverse correlation between reported experimental rate constants at room temperature for the reactions of CH_2OO with a series of carbonyl compounds and the energy gap $|\Delta E_S|$ between the π^* orbital of the carbonyl and the $n(p_C–p_O)$ orbital of CH_2OO. Orbital energies were calculated at the B3LYP/cc-pVDZ level. A linear fit is shown, where the shaded area represents 1σ prediction bands. Experimental rate constants are drawn from various sources – see text for details. Reactions involving α,β-unsaturated carbonyls (gray) were excluded from the fit.

The EWG or EDG character of the R_1, R_2 substituents can be represented by Hammett substituent constants, σ_m and σ_p, where the subscripts refer to substitution at the meta/para position of benzoic acid.[173] Positive values indicate EWG character and increased reactivity, while negative values indicate EDG character, and reduced reactivity. Among the carbonyls HCHO, AcOH, 4H2B, and Ac, the substituents and their Hammett constants are: H ($\sigma_m = \sigma_p = 0$); CH_3 ($\sigma_m = -0.07$, $\sigma_p = -0.17$), CH_2OH ($\sigma_m = \sigma_p = 0$), while values for CH_2CH_2OH are unknown. Methyl is electron-donating, raising the energies of the frontier orbitals while the others are neither. The effect of the electron-donating methyl groups on the calculated FMO energies is evident in Figure 4.12 and Table 4.3. Relative to H, each methyl group substituent increases the carbonyl FMO energies by ~0.4 eV. Based on the calculated orbital energies in Table 4.3 it is likely that CH_2CH_2OH is marginally more electron-donating than CH_2OH, due to the presence of the additional methylene group between the hydroxyl and the carbonyl. Although the experimental rate constants were found to be indistinguishable, accounting for the possible systematic error in the UV absorption cross section of AcOH described above would lead to a 10% increase in k_{AcOH}, in line with the expectations of the orbital analysis.

Previously, we showed that the relationship between observed rate constants and calculated orbital energy gaps could be used quantitatively.[126] Figure 4.13 shows an updated plot of ln k against the magnitude of the orbital energy gap $|\Delta E_S|$, for a range of CH_2OO + R_1R_2CO reactions. Experimental rate constants at room temperature have been obtained from various sources, and are compiled in Table 4.4. The data set includes reactions of CH_2OO with ketones, α-diketones, aldehydes, and α,β-unsaturated enones and enals. Where more than one experimental value is available, the weighted average rate constant is used. Orbital energies have been calculated at the B3LYP/cc-pVDZ level, rather than M06-2X/aug-cc-pVTZ as previously.[126] The effect of the electron-donating or electron-withdrawing character of the R_1, R_2 substituents on the orbital energy gaps and rate constants leads to a strong negative linear correlation. The fastest reaction is with hexafluoroacetone (HFA), which has strongly electron-withdrawing substituents ($R_1 = R_2 = CF_3$, $\sigma_m = 0.43$, $\sigma_p = 0.54$) while the slowest

reaction is with acetone, which has electron-donating substituents ($R_1 = R_2 = CH_3$). For species with $R_1 \neq R_2$, such as acetaldehyde ($R_1 = H$, $R_2 = CH_3$) or the hydroxyketones, the effect is additive. The α,β-unsaturated carbonyls such as MVK, MACR, ACR, and the enolone form of AcAc are shown in Figure 4.13 but clearly deviate from the trend and are not included in the fit. The $|\Delta E_S|$ values for these species imply that the reactions with CH_2OO should be much faster than observed experimentally,[126,127,141,186] suggesting that delocalization of the π system reduces the reactivity of the carbonyl. Further work is required to explain the reactivity of α,β-unsaturated carbonyls towards CH_2OO, which deviate from the trend.

4.6 Atmospheric Implications

The major reactive sink for hydroxyketones in the atmosphere is reaction with OH radicals. Rate constants for reaction with OH are $2.0\times10^{-12}\exp(-320/T)$ cm^3 s^{-1} and $1.3\times10^{-12}\exp(-400/T)$ cm^3 s^{-1} for AcOH and 4H2B respectively.[217,221] Typical lifetimes for both hydroxyketones reacting with OH radical are ~3 days in the troposphere.[208,209,213,214,219,221] Comparatively, photolysis has a minor contribution with lifetimes of ~12-14 days for AcOH and 26 days for 4H2B.[213,221] Temperature-dependent lifetimes for AcOH and 4H2B were estimated using typical average tropospheric concentrations for CH_2OO and OH. The average CH_2OO concentration was assumed to be 2×10^4 cm^{-3}, although concentrations as high as 1×10^5 cm^{-3} have been reported.[25,26] The average concentration of OH was estimated to be 5×10^6 cm^{-3} during the day and 2×10^5 cm^{-3} at night.[1,2] At 295 K, the hydroxyketone reactions with CH_2OO are insignificant, with estimated lifetimes >500 days. However, the CH_2OO reactions show a strong negative T dependence and may become relatively more important at lower temperatures. While the hydroxyketone loss rates due to CH_2OO increase at lower temperature, with lifetimes of ~80 days at 220 K, OH remains the most important reactive sink for both hydroxyketones across the temperature range, even at night when OH concentrations are markedly lower.

4.7 Conclusions

The kinetics of the CH_2OO + AcOH and CH_2OO + 4H2B reactions were measured across the temperature range 275–335 K using a flash photolysis, transient absorption spectroscopy technique. The temperature dependent bimolecular rate constants are k_{AcOH} = (4.3±1.7)×10^{-15}exp[(1630±120)/T] and k_{4H2B} = (3.5±2.6)×10^{-15}exp[(1700±200)/T]. Complementary *ab initio* calculations confirm that both reactions proceed via 1,3-dipolar cycloaddition at the carbonyl to form cyclic secondary ozonides, while reaction at the hydroxyl group via 1,2-addition is insignificant. The increased reactivity of hydroxyketones relative to acetone can be understood from a frontier molecular orbital theory approach, wherein the cycloaddition involves an interaction between the occupied n(p_C–p_O) orbital of the CH_2OO and the unoccupied π* orbital of the carbonyl. Electron-donating or electron-withdrawing substituents increase or decrease the π* orbital energy. Alkyl substituents are electron-donating, which decreases reactivity, while hydroxyalkyl substituents are, like H, neither electron-donating nor electron-withdrawing. A strong inverse correlation is found between the logarithm of the rate constants and the orbital energy gap for a range of R_1R_2CO species. The reactions of CH_2OO with AcOH and 4H2B are unlikely to be significant in the troposphere, where reaction with hydroxyl radicals and photolysis control the hydroxyketone lifetimes.

Table 4.4 Experimental rate constants for CH_2OO + R_1R_2CO reactions at room temperature.

R_1R_2CO	R_1, R_2	$k_{R_1R_2CO}$ / 10^{-13} cm^3 s^{-1}	Reference
formaldehyde (HCHO)	H, H	41.1±2.5	Luo et al.[9]
		35.0±2.9	unpublished results
		38.5±1.9	**weighted mean**
acetaldehyde (MeCHO)	H, CH_3	17	Stone et al.[10]
		9.5±0.7*	Taatjes et al.[11]
		13±2	Elsamra et al.[12]
		16.1±1.4	unpublished results
		15.1±1.1	**weighted mean**
acetone (Ac)	CH_3, CH_3	2.3±0.3	Taatjes et al.[11]
		3.5±0.8	Elsamra et al.[12]
		3.4±0.9	Berndt et al.[13]
		4.7±0.1	Chhantyal-Pun et al.[14]
		4.8±0.4	Cornwell et al.[8]
		4.5±0.1	**weighted mean**
methyl ethyl ketone (MEK)	CH_3, C_2H_5	6.4±0.2	Debnath & Rajakumar[15]
hexafluoroacetone (HFA)	CF_3, CF_3	306±27	Taatjes et al.[11]
		333±63	Liu et al.[16]
		306±27	**weighted mean**
biacetyl (BiAc)	CH_3, CH_3CO	129±18	Cornwell et al.[8]
acetylpropionyl (AcPr)	CH_3, C_2H_5CO C_2H_5, CH_3CO	109±13	Cornwell et al.[17]
acrolein (ACR)	H, $CH=CH_2$	16.3±1.9	Eskola et al.[18]
methacrolein (MACR)	H, $C(CH_3)=CH_2$	4.4±0.1	Eskola et al.[18]
methyl vinyl ketone (MVK)	CH_3, $CH=CH_2$	5.0±0.4	Zhou et al.[19]
acetylacetone (AcAc)	CH_3, $CH=C(OH)CH_3$	8.0±0.7	Cornwell et al.[8]
hydroxyacetone (AcOH)	CH_3, CH_2OH	10.9±1.5	this work
4-hydroxy-2-butanone (4H2B)	CH_3, CH_2CH_2OH	11.1±2.6	this work

5 Structure Activity Relationships for Cycloaddition Reactions with Criegee Intermediates: A Computational Study

5.1 Abstract

The bimolecular rate constants for the reactions of Criegee intermediates (CIs) with carbonyls is dependent on the identity of the substituents on both reactants. It is our goal to construct a relatively low-cost computational tool to predict rate constants based on structure activity relationships (SARs) for the cycloaddition reaction between CIs and carbonyls. We calculated optimized geometries for several different carbonyls and CIs with a B3LYP/aug-cc-pVDZ level of theory. The calculated rate constants from computed free energies of activation are shown to be significantly inaccurate. Comparison to experimental rate constants has proven standard transition state theory (TST) to be inadequate for predicting rate constants for a number of reasons. With the use of frontier molecular orbital (FMO) theory a SAR was developed from a test set of carbonyls: $(CH_3)_2CO$, CH_3CHO, HCHO, $(COCH_3)_2$, $(CF_3)_2CO$. We observed an inverse correlation between $\ln k$ and the carbonyl π^* orbital energies from comparing orbital energies of the substituted carbonyls with experimentally determined rate constants. The SAR can be used to predict rate constants for the reaction of $COCl_2$ and $CO(CN)_2$ with CH_2OO with the following equation, $\ln k = (-1.53 \pm 0.14)E_{\pi^*} - (29.21 \pm 0.29)$. The effect that different substituents have on the reaction between CIs and SO_2 was then explored with the same approach, using FMO theory. A positive linear correlation was observed between the $n_{pc\text{-}po}$ orbital energies on the CI and experimentally determined rate constants for the reactions of SO_2 with CH_2OO, CH_3CHOO, and $(CH_3)_2COO$. The following equation can be used to predict the rate constants for the reaction of different CIs with SO_2: $\ln k = (1.66 \pm 0.51)E_{n_{pC-pO}} - (12.03 \pm 3.39)$.

5.2 Introduction

The reaction of Criegee intermediates (CIs) with carbonyl compounds has been shown to be sensitive to the substituents present on the carbonyl reactants. The identity of substituents R_1 and R_2 can either increase or decrease the reactivity of the carbonyl towards CH_2OO, depending on the electronegativity. The bimolecular rate constant for the reaction of CH_2OO with hexafluoroacetone ($(CF_3)_2CO$) is ~300 times larger than with acetone ($(CH_3)_2CO$).[117,128] It was apparent that the electronegative trifluoromethyl (CF_3) groups attached to the carbonyl had a significant impact on the reaction rate. We have previously shown a difference in reactivity between α- and β- substituted diketones.[126,127] The proximity of the adjacent carbonyl has an influence on how fast the cycloaddition reaction with CH_2OO occurred, with the α- diketones reacting ~30 times faster than acetone. The β-diketones showed a very minor difference in rate constants compared to acetone. We also showed hydroxyketones react twice as fast as acetone, while the proximity of the hydroxyl group from the carbonyl had a minimal effect on the rate constant between hydroxyketones.[129] Most recently we have measured the kinetics of CH_2OO with aliphatic aldehydes.[230] While the kinetics of other aldehydes have been investigated,[82,111,128] the bimolecular rate constant for the reaction between formaldehyde (HCHO) and CH_2OO has only been reported by one other group recently. The single methyl (CH_3) group on acetaldehyde (CH_3CHO) has an influence on rate constant to be less than half of the average rate constant reported for HCHO at 298 K.

The substituent effects on carbonyls in a cycloaddition reaction with CH_2OO has been rationalized with concepts from frontier molecular orbital (FMO) theory.[124,125] We have adapted the qualitative understanding of symmetry-allowed orbital interactions from Sustmann, which was based on Diels Alder cycloaddition reactions.[168,169] A 1,3-dipolar cycloaddition reaction occurs where the electron rich 1,3-dipole (CI) initiates bond formation via interaction with the electron-deficient dipolarphile

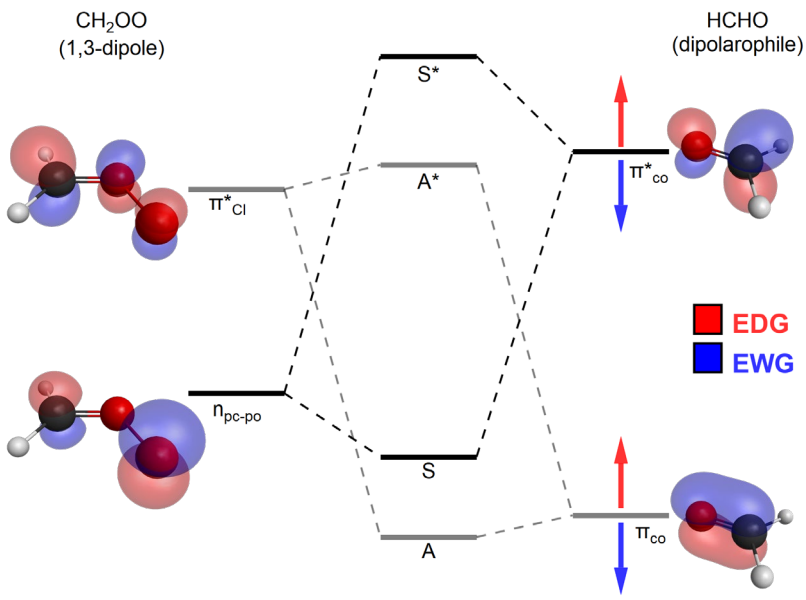


Figure 5.1 Molecular orbital diagram for the cycloaddition reaction between CH_2OO (left) and formaldehyde (right). The "symmetric" orbitals interact to form the molecular orbitals (S, S*) in the black trace, and the "antisymmetric" orbitals form the molecular orbitals (A, A*) in the grey trace. The effect of EDGs in red and EWGs in blue are shown by the corresponding arrows on the carbonyl π and π^* orbital energies.

(carbonyl). The electronic properties of a substituent can inductively affect the electron density of the carbonyl. The different types of substituents are classified as electron donating groups (EDG) and electron withdrawing groups (EWG). The FMO theory approach can be used to understand how the orbital energies on the carbonyl change with different substituents, as they interact with the orbitals of CH_2OO in the 1,3-dipolar cycloaddition transition state (TS). A molecular orbital (MO) diagram between CH_2OO and formaldehyde (HCHO, R_1=R_2=H) is shown Figure 5.1. The orbital interactions are labeled based on loose symmetry considerations. The occupied non-bonding ($n_{pc\text{-}po}$) orbital on CH_2OO and the unoccupied π^* orbital of HCHO are symmetric about a center of inversion, and they interact to form the molecular orbitals S and S*. The anti-symmetric orbitals are the occupied π orbital on HCHO and the unoccupied π^* orbital of CH_2OO, which form molecular orbitals A and A*.

The interaction with the smaller gap in orbital energies has a larger contribution to stabilizing the 1,3-dipolar cycloaddition TS. The dominant interaction is shown in black forming S and S*. The effect of substituents as EDGs or EWGs on the carbonyl is shown as red and blue arrows respectively. As the EWG character of the substituent is increased, the orbital energies on the carbonyl are decreased and the S-interaction has a smaller orbital energy gap, making the cycloaddition reaction more favorable. The effect of EDGs would increase the orbital energies, which increase the orbital energy gap for the S-interaction and effectively slow down the reaction.

Hammett parameters are a useful tool to gauge how a strong an EDG or EWG substituent may be, which can give insight on physical parameters discussed in the text, such as orbital energies. The values are measured dissociation constants for substituted benzoic acids. Hansch et al. organized the Hammett parameter coefficients for over 200 substituents that have several different electronic and steric properties.[173] Table 5.1 shows a range of substituents and the corresponding of Hammett parameters for both the *meta*- and *para*- substituted benzyl positions. The value for the hydrogen atom (H) is zero because it is not an EWG or EDG. H is emphasized in the table because it is a reference point for where the substituents change from having donating to withdrawing characteristics. Above H, the methyl group (CH_3) has a negative value and is an EDG, which can be understood as deactivating. EWGs are below H and have positive values, which are effectively activating the reaction. Chlorine (Cl) atoms are slightly electron withdrawing, whereas acetyl (CH_3CO) and trifluoromethyl (CF_3) groups have more electronegative characteristics and therefore have larger Hammett coefficients. The cyano group (CN) is the most effective EWG and largest value that will be considered in this study.

In this chapter we are computationally exploring the reaction of CH_2OO with a test set of carbonyls, and we will be initially focusing on substituent effects on the carbonyl. With the concepts from FMO theory and using DFT calculations, we develop a structure activity relationship (SAR) based on the

π^* orbital energies of the carbonyl. We also explore the effect of substituents on the CI using the cycloaddition reaction between CH_2OO and SO_2 to build a separate SAR that is based on the $n_{pc\text{-}po}$ orbital energies of the CIs. By developing SARs based on the orbital energies on the carbonyls and CIs separately, we can predict the rate constants of the reactions between CIs and the cycloaddition reaction partners.

Table 5.1 Hammett parameters for a range of different substituents that are EDGs or EWGs, represented as the *para*- (σ_p) and *meta*- (σ_m) substituted coefficients.

Substituent (R_n)	σ_p	σ_m
CH_3	-0.17	-0.07
H	0.00	0.00
Cl	0.23	0.37
CH_3CO	0.5	0.38
CF_3	0.54	0.43
CN	0.66	0.56

5.3 Methods

All electronic structure calculations were performed using GAMESS.[148,149] The geometries of the reactants, entrance channel complexes, transition state structures, and products were optimized using the B3LYP functional with the Dunning's correlation-consistent polarized valence double zeta bases, augmented with diffuse functions (aug-cc-pVDZ).[231] The harmonic frequencies of all species were calculated and the presence of zero or one imaginary frequency confirmed a true minima or transition state was located. Free energies of activation were calculated using rigid-rotor harmonic oscillator (RRHO) partition functions. Intrinsic reaction coordinate (IRC) calculations confirmed the transition state structures led to the correctly anticipated local and global minima along the potential energy surface.

5.4 Results and Discussion

This computational project is focused on a test set of molecules with different substituents (R_1 and R_2) that have either EWG or EDG characteristics. To investigate the relationship between substituent effects and the bimolecular rate of reaction between carbonyls and CH_2OO, we will explore different physical parameters from the DFT calculations such as free energy of activation and orbital energies to build a SAR. Experimental rate constants are only available for acetone (CH_3, CH_3),[88,111,126–128,130] acetaldehyde (H, CH_3),[82,111,128,230] formaldehyde (H, H),[200,230] biacetyl (CH_3, $COCH_3$),[126,127] and hexafluoroacetone (CF_3, CF_3).[117,128] The experimental rate constants shown in the following sections are the weighted mean from the multiple reports in the literature. The reactions of CH_2OO with carbonyl dichloride and carbonyl dicyanide have not been explored experimentally or computationally. They were chosen to probe the EWG character the Cl and CN groups. The first few sections will be comparing the reactivity of different carbonyls with CH_2OO before considering substituent effects on different CIs.

5.4.1 Standard Transition State Theory (TST)

The general cycloaddition reaction mechanism has been outlined previously, so it will be briefly mentioned here.[126,127,129] After the reactants pass through a vdW entrance channel complex they undergo a 1,3-dipolar cycloaddition transition state before producing a secondary ozonide (SOZ). The partition functions, with the rigid-rotor harmonic oscillator (RRHO) approximation, were computed to provide thermochemical parameters for the reactions of CH_2OO with the test set of carbonyls. Shown in Table 5.2, the calculated overall zero-point corrected energies at 0 K and Gibbs free energies (kcal mol^{-1}) at the transition state (TS) for the test set of carbonyls. With conventional canonical transition state theory (TST), we can calculate the rate constant using the Gibbs free energy in Equation 5.1,

$$k_{\text{calc}} = \kappa \frac{k_{\text{B}} T}{h} \exp\left(-\frac{\Delta G^{\circ}}{RT}\right) \quad \text{(E 5.1)}$$

where κ is the transmission coefficient, k_B is the Boltzmann constant, h is Planck's constant, and T is the temperature. Here we assume κ to be equal to 1 and a standard concentration value at 1 bar and 298 K.

At the B3LYP/aug cc-PVDZ level of theory, a saddle point did not converge for the reaction between HFA and CH_2OO, which is the initial drawback of relying on DFT to quantify kinetic information. Depending on the method and basis set, a TS may not exist on the specified surface. The comparison of the calculated rate constants for the successfully computed reactions shows a significant disagreement, which highlights the limitation of the level of theory that was used. We have not applied a more appropriate way to approach using calculated Gibbs free energy values to predict rate constants. Reliably quantifying thermochemical data from ab-initio calculations requires an accurate treatment of the electronic structure along with careful evaluation of the molecular partition functions such as including hindered rotors, or improved treatment of anharmonicity as well as

Table 5.2 Calculated zero point corrected total energies and free energies of activation (kcal mol^{-1})from the B3LYP/ aug-cc-pVDZ level of theory. The bimolecular rate constants were calculated using equation E 5.1 to compare to the experimentally measured values (~298 K) shown on the right side.

Common Name	$\Delta(E+\text{ZPE})$	$\Delta G^{\ddagger}$	k_{calc} / 10^{-13} cm^3 s^{-1}	k_{exp} / 10^{-13} cm^3 s^{-1}
Acetone	–1.53	+11.93	0.01	4.5±0.1
Acetaldehyde	–3.06	+10.62	0.05	12.5±1.1
Formaldehyde	–5.02	+7.55	9.77	38.5±1.9
Biacetyl	–4.49	+8.74	1.31	110±9.0

taking into account tunneling contributions.[96] The predicted rate constants from the calculated free energies of activation result in values that are orders of magnitude lower than the experimentally measured values. The calculated rate constant is very sensitive to the free energy of activation, which causes inconsistencies such as the reaction of CH_2OO with biacetyl being predicted as slower than formaldehyde. Aside from a TS calculation already being costly, larger levels of theory would also be needed. This was not the goal of this study, we want a convenient low-cost predictive tool that can be used in place of experimental methods.

5.4.2 FMO Theory: Carbonyl Substituents R_1 & R_2

The orbital energies for the test set of carbonyls are shown in Table 5.3 with the π and π^* orbital energies (eV) shown beside the experimental rate constants. HCHO is emphasized in Table 5.3 as a reference to distinguish where the "origin" is for orbital energies on the carbonyl because the hydrogen atom is a baseline for substituent effects, just as Hammett parameters predict. Above HCHO is acetone (R_1=R_2=CH_3) and acetaldehyde (R_1=H, R_2=CH_3), where the donating effect of adding one or two methyl groups on either side of the carbonyl increases the orbital energies accordingly. Below HCHO are carbonyls with a range of different substituents that have increasing EWG character in the following order: Cl < $COCH_3$ < CF_3 < CN. Overall the rate constants increase as π and π^* orbitals of the carbonyls become increasingly negative.

The MO diagram for all the carbonyls in the test set is shown in Figure 5.2. In panel (a) the orbitals of CH_2OO are shown on the left with the non-bonding ($n_{pc\text{-}po}$) and π^* orbital, interacting with the π and π^* orbitals of the carbonyls. The occupied non-bonding orbitals on the carbonyls are shown in grey, and a shaded box is shown for the compounds that have multiple occupied non-bonding orbitals present. The bottom axis shows HCHO in bold, as emphasized in Table 5.3 and Figure 5.4, to show the effect of EWGs and EDGs decreasing or increasing the orbital energies respectively. It is worthy to not that $(COCH_3)_2$ is a dicarbonyl, which pushes the two π orbitals higher in energy than they

Table 5.3 Calculated orbital energies of different carbonyls in eV. The experimental rate constants are also included for the carbonyls that have reported kinetic data at room temperature. Where there were multiple reports, the average of the rate constants was taken.

R_1	R_2	$k_{X,exp}$ / 10^{-13} cm^3 s^{-1}	$\pi_{C=O}$	$\pi^*_{C=O}$
CH_3	CH_3	4.5±0.1	–9.7	–0.7
H	CH_3	12.5±1.1	–10.1	–1.1
H	H	38.5±1.9	–11.1	–1.7
Cl	Cl	N/A	–13.3	–2.0
CH_3	$COCH_3$	110±9.0	–10.3	–2.7
CF_3	CF_3	306.1±27	–12.3	–3.3
CN	CN	N/A	–13.9	–4.6

typically would be as separate π-systems. In panel (b), the difference in energy (eV) between the A or S orbitals was plotted on the common axis labeled by the different carbonyls shown in panel (a). The energy gap between the S orbitals is smaller than the A orbital gap for all the carbonyls, which implies the S-interaction has more orbital overlap and a larger contribution to controlling the energy of the cycloaddition TS with CH_2OO. The S-interaction is weaker, and has a larger orbital energy gap, because the methyl substituents on acetone (CH_3, CH_3) are EDGs relative to HCHO (H, H). While the A-interaction becomes stronger with a smaller energy gap, it is still less overall. Further analysis with substituents that have more EDG character than methyl groups could cause the A-interaction to have a smaller energy gap than the S orbitals, therefore a competition could arise for which interaction contributes more to the cycloaddition TS.

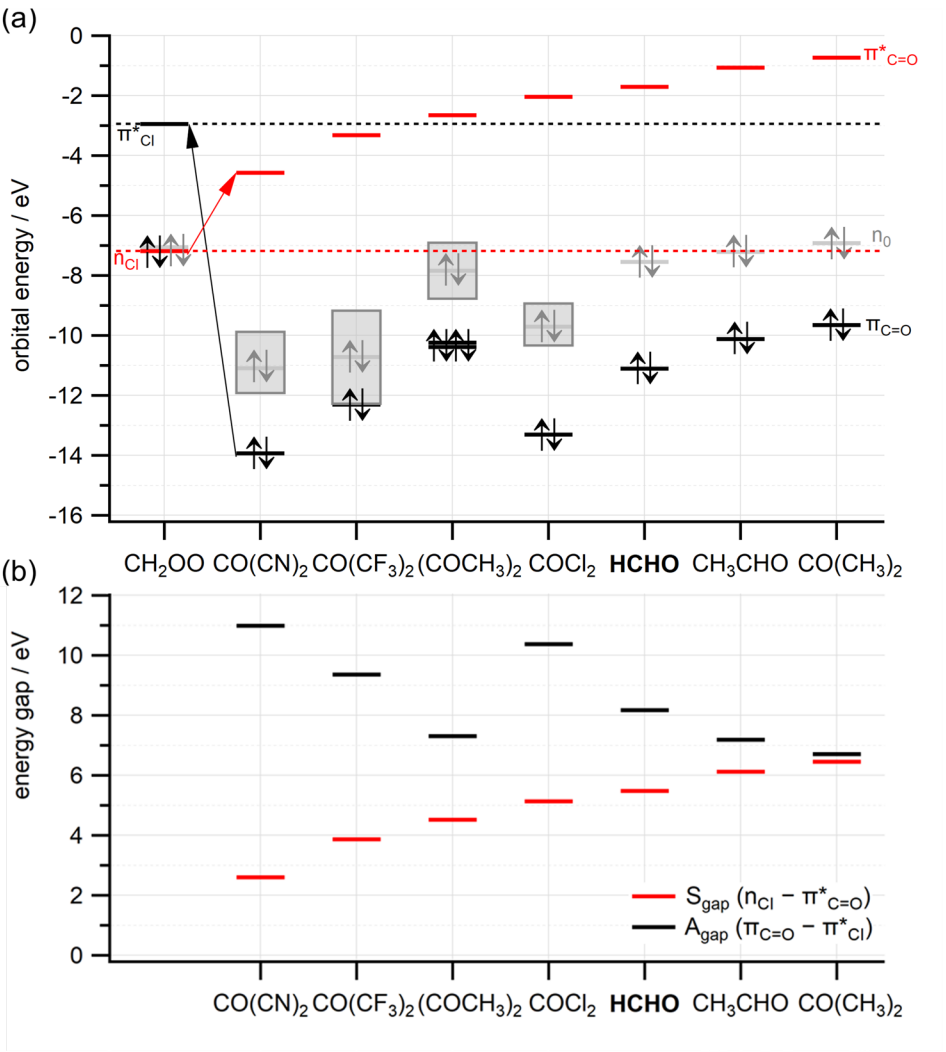


Figure 5.2 Panel (a) MO diagram for the cycloaddition reaction between CH_2OO and the seven carbonyls listed in Table 5.3. The A and S energy gaps between the orbitals are shown in panel (b) (red or black) with the same common bottom axis.

To develop a SAR for the reaction between CH_2OO and substituted carbonyls, we need to quantify the correlation between the orbital energies and bimolecular rate constants. In Figure 5.3 the experimental rate constants are plotted as a function of the π and π^* orbital energies on the carbonyl separately in panel (a) and (b). The fitted lines show a direct correlation between ln k and the orbital energies of the carbonyl. The orbital energies of $CO(CN)_2$ and $COCl_2$ are shown as blue and green arrows leading to the fits to indicate their approximate reactivity with respect to the other carbonyls.

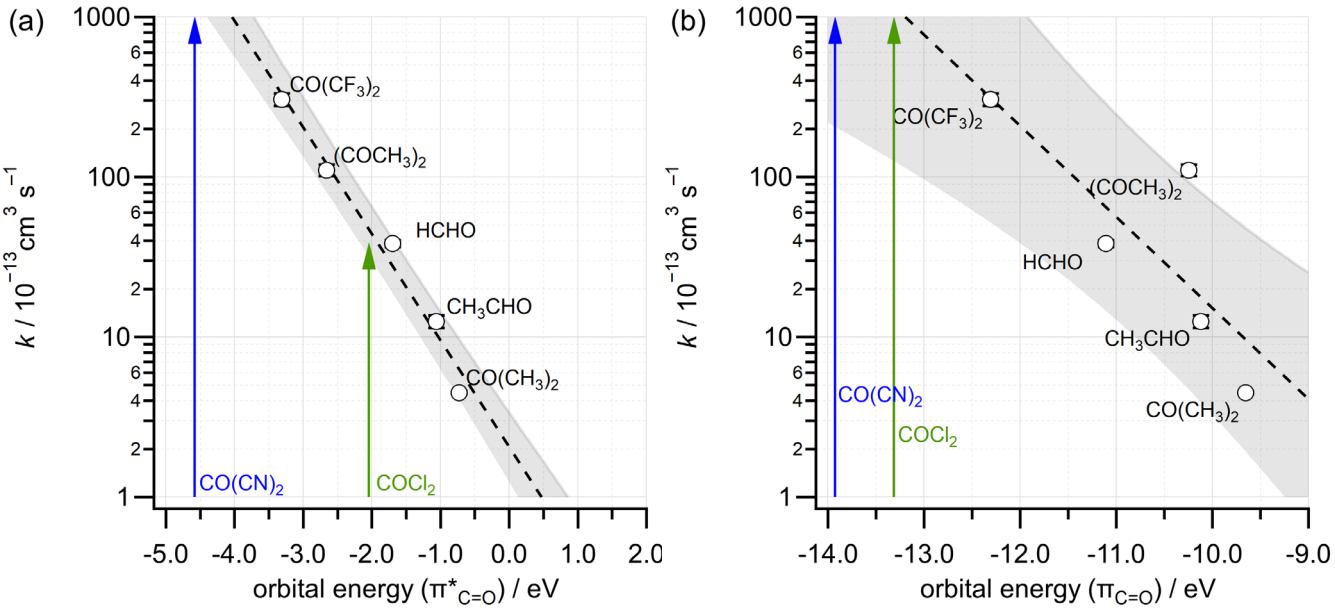


Figure 5.3 The energies of the carbonyl π^* (a) and π (b) orbitals plotted against the experimental rate constants for the bimolecular cycloaddition reaction of the specified carbonyls with CH_2OO.

A linear regression returns an R^2 value of 0.98 for the fit in panel (a) and 0.67 in panel (b). Panel (a) shows a clear representation of a SAR between the bimolecular rate constant of the cycloaddition reaction with CH_2OO and the π^* orbital energy of the carbonyl. Although it was suggested that both orbital interactions A and S contribute to the energy of the cycloaddition TS, Figure 5.3 indicates the reactivity is primarily controlled by energy of the π^* orbitals on the carbonyl. The SAR can be used to predict rate constant values with the trendline equation (E 5.2),

$$\ln k = (-1.53 \pm 0.14)E_{\pi^*} - (29.21 \pm 0.29) \qquad \text{(E 5.2)}$$

where E_{π^*} is the orbital energy of the unoccupied anti-bonding π^* orbital on the carbonyl. Considering the Hammett parameters in Table 5.1 and the trend in panel (a) of Figure 5.3, the chlorines on $COCl_2$ have a slight EWG character relative to H, which results in a predicted rate constant of $(4.68\pm0.42)\times10^{-12}$ cm^{3}s^{-1}, which is marginally faster than the reaction of HCHO with

CH_2OO. The cyano groups on $CO(CN)_2$ have the greatest relative EWG character in this study, resulting in a predicted rate constant of $(2.29\pm0.20)\times10^{-10}$ cm^3s^{-1}.

5.4.3 Hammett Parameters: Carbonyl Substituents R_1 & R_2

Hammett parameters were previously mentioned as a useful reference to understand the electronic character of substituents relative to hydrogen as a baseline. Table 5.1 shows the increasing order of individual substituents with the corresponding Hammett coefficients. Including the test set of carbonyls from the previous section, the geometries of eleven carbonyls were optimized and the π^* orbital energies were plotted as a function of the summed Hammett coefficients in Figure 5.4. Panel (a) and (b) show the fitted trends based on the summed σ_p and σ_m values. A dotted zero line is shown on the horizontal axis to illustrate hydrogens as neutral substituents, represented by the π^* orbital energy of HCHO. The points on the right (positive) of HCHO are associated as activating EWGs and to

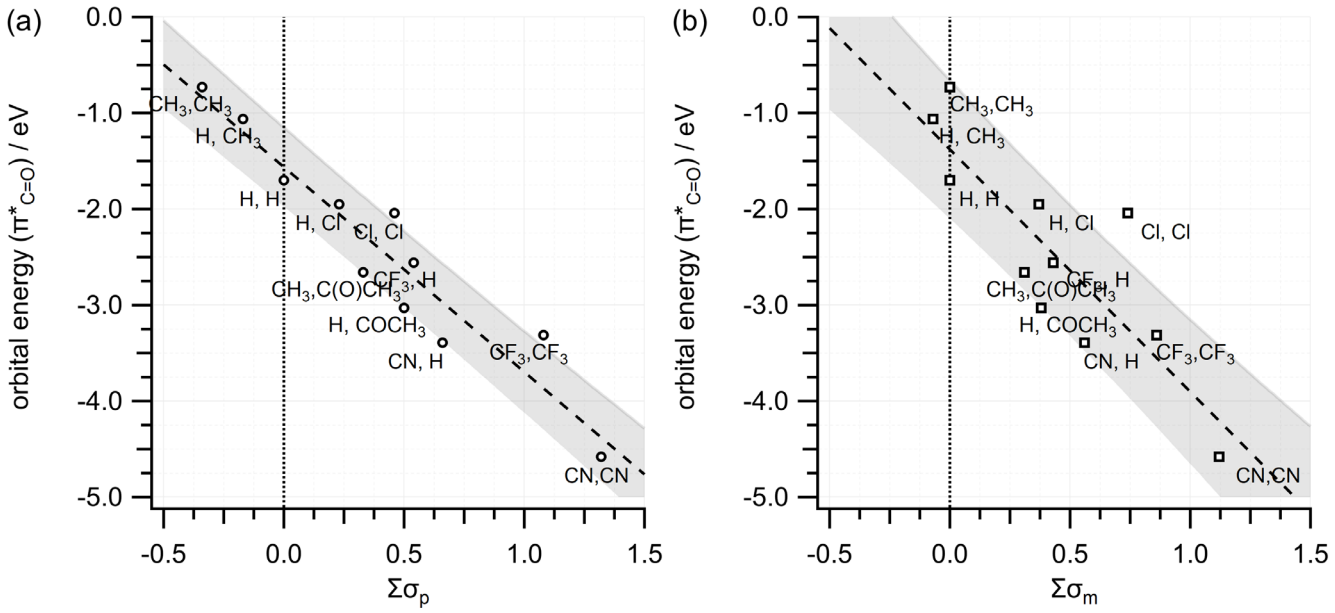


Figure 5.4 The carbonyl π^* orbital energies are plotted as a function of Hammett parameters. Panel (a) and (b) show the relationship based on the *para*- (σ_p) and *meta*- (σ_m) substituted positions on benzoic acid. The substituents (R_1, R_2) that correspond to the summed σ_p and σ_m values are indicated with text adjacent to the points on the plot.

the left (negative) are the deactivating EDGs for the carbonyl compound. The linear regression for the fits in panel (a) and (b) returns R^2 values of 0.91 and 0.72, which suggests the sum of the σ_p values correlate more with the calculated π^* orbital energies. By considering σ_p values and π^* orbital energies as comparable proxies this correlation is a useful guide for understanding the relative effects carbonyl substituents in a cycloaddition reaction with CH_2OO.

5.4.4 FMO Theory: Criegee Substituents R_1 & R_2

We can also consider the effect of substituents on the CI (R_1R_2COO) to further explore reactivity trends of the 1,3-dipolar cycloaddition reactions. To the best of our knowledge there are no experimental kinetics experiments for a range of CIs that have a common carbonyl reactant. Fortunately, there are numerous kinetic studies on the reaction of SO_2 with different CIs at room temperature, which also proceed through a 1,3-dipolar cycloaddition reaction. A MO diagram is shown in Figure 5.5 to qualitatively show the orbital interactions that contribute to the 1,3-dipolar cycloaddition reaction between CH_2OO and SO_2. The effect of changing the substituents on the CI (left side) suggests an opposite trend from what was discussed when considering substituent effects on the carbonyl in Figure 5.1. The $n_{pc\text{-}po}$ and π^* orbital energies on the CI are now changing as substituents with different electronic characteristics are added in place of the hydrogens on CH_2OO. The addition of EWGs (blue arrows) lower the orbital energies, causing the energy gap of the dominant S-interaction to increase, which would allow less orbital overlap. Alternatively, the addition of EDGs (red arrows) to the CI would increase the energy of the orbitals and the S-interaction between the $n_{pc\text{-}po}$ orbital on the CI and π^* orbital of SO_2 would become more favorable.

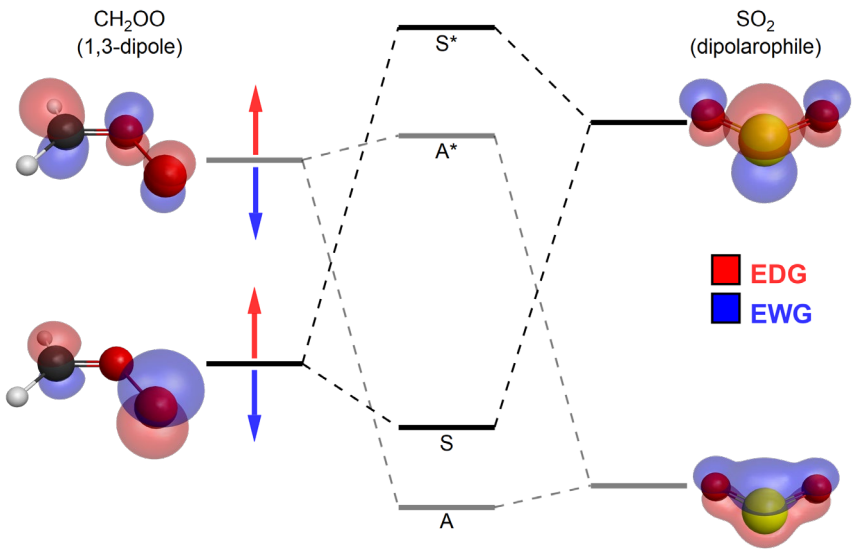


Figure 5.5 Molecular orbital diagram for the cycloaddition reaction between CH_2OO (left) and sulfur dioxide (right). The "symmetric" orbitals interact to form the molecular orbitals (S_1, S_2) in the black trace, and the "antisymmetric" orbitals form the molecular orbitals (A_1, A_2) in the grey trace. The effect of EDGs in red and EWGs in blue are shown by the corresponding arrows on the carbonyl π and π^* orbital energies.

The substituents that were considered are CH_3, H, Cl, and CH_3O. The CIs that have experimental rate constants for reaction with SO_2 are formaldehyde oxide (CH_2OO),[40,49,82,84,85,117–119,121] acetaldehyde oxide (CH_3CHOO),[119,232–234] and acetone oxide ($(CH_3)_2COO$).[84,123] We have not considered the α,β-unsaturated CIs such as methylvinylketone oxide and methacrolein oxide, because the conjugated π-systems have been previously shown to disrupt the correlation between the *lnk* and π^* orbital energies on carbonyls.[126] The rate constants for the reactions of different CIs with SO_2 at room temperature are listed in Table 5.4. The reaction of CH_2OO and SO_2 has been well-determined by several groups and the reproduced values all agree within the reported uncertainties.[40,49,82,84,85,117–119,121] The *syn*- and *anti*- conformers of acetaldehyde oxide (CH_3CHOO) have a large discrepancy between the bimolecular rate constants with SO_2. The bimolecular rate constant for the reaction of

syn-CH_3CHOO with SO_2 has been reported by four different groups and they all agree within ~20% relative uncertainty of each other.[119,232–234] The *anti*- conformer of CH_3CHOO has only two reported values and they do not agree. Taatjes et al. reported a rate constant of $(6.7\pm1)\times10^{-11}$ cm^3s^{-1} and Sheps et al. showed a rate constant ~3 times larger ($(22\pm2)\times10^{-11}$ cm^3s^{-1}).[232,233] The large difference between the rate constants for the *anti*- conformer could be due to a pressure-dependence, but an upper limit for this reaction has not been reported. Distinguishing the isomers is the main challenge with measuring conformer-dependent bimolecular rate constants between the two isomers of CH_3CHOO. Taatjes et al. argues the mass signal (m/z=60) is almost entirely due to the presence of *syn*-CH_3CHOO, but the ionization energies for the *syn*- and *anti*- conformers are 9.4 and 9.3 eV respectively.[233] The rate constant for the reaction between $(CH_3)_2COO$ and SO_2 was measured by two different groups. The unweighted average from results reported by Chhantyal-Pun and Huang et al. was taken as the high-pressure limit rate constant.[84,123]

The orbital energies of the different CIs compared in this study are shown in Table 5.4, with CH_2OO (R_1=R_2=H) outlined as our baseline case with no substituent effects present. The orbital energies for the two conformers of CH_3CHOO are relatively the same, and the addition of an extra methyl group results in slightly larger values for $(CH_3)_2COO$. The two CIs that do not have experimental rate constants with SO_2 are methylformate oxide (CH_3OCHOO) and formylchloride oxide (ClCHOO). The methoxy (CH_3O) group is more electron donating than a simple methyl group and the chlorine (Cl) is slightly withdrawing. The separate test case CIs were chosen to have either an EWG and EDG to compare to the baseline case of CH_2OO.

Table 5.4 Compiled orbital energies of different CIs in eV. The experimental rate constants are also included for the CIs that have reported kinetic data at room temperature with SO_2.

	$k_{X,exp}$ / 10^{-11} cm^3 s^{-1}	$n_{pc\text{-}po}$	π^*_{CI}
CH_3OCHOO	N/A	−6.03	-2.00
$(CH_3)_2COO$	14.3±0.8	−6.31	-1.83
a-CH_3CHOO	14.4±1.5	−6.57	-2.37
s-CH_3CHOO	2.3±0.3	−6.76	-2.32
CH_2OO	3.7±0.3	−7.18	-2.94
$ClCHOO$	N/A	−7.18	-2.87

Overall, the S-interaction is dominant over the A-interaction for the reactions of SO_2 and the CIs listed in Table 5.4. The S-interaction between the CIs and SO_2 has smaller energy gaps with the substituents that have increasing EDG character above CH_2OO, from bottom to top. The log of the rate constants were plotted as a function of the non-bonding ($n_{pc\text{-}po}$) orbital energies of the CIs in Figure 5.6. The linear relationship suggests there is a correlation between the *lnk* and the CI orbital energies, with an R^2 value of 0.91. The value for *syn*-CH_3CHOO was masked from the fit, and although the *syn*-conformer doesn't work with the correlation, it matters least because the dominant loss process for *syn*-CH_3CHOO is unimolecular decomposition.[23,196] The trendline equation corresponding to the fit in Figure 5.6 was rearranged as Equation 5.3 (E 5.3), to provide a rate constant in the form of *lnk*.

$$\ln k = (1.66 \pm 0.51)E_{n_{pc-po}} - (12.03 \pm 3.39) \quad \text{(E 5.3)}$$

The impact of a single chlorine as a substituent, having slight EWG character, has been previously discussed to have little effect on the reactivity on carbonyls and the same can be seen for CIs. The resultant calculated rate constant for ClCHOO ($(4.0\pm1.2)\times10^{-11}$ cm^3s^{-1}) implies it would react with SO_2 similarly to CH_2OO. The significant EDG character of the methoxy group on CH_3OCHOO causes the smallest energy gap for the S-interaction between the $n_{pc\text{-}po}$ orbital and the π^* orbital of SO_2, which causes the calculated rate constant to be $(2.7\pm0.8)\times10^{-10}$ cm^3s^{-1}.

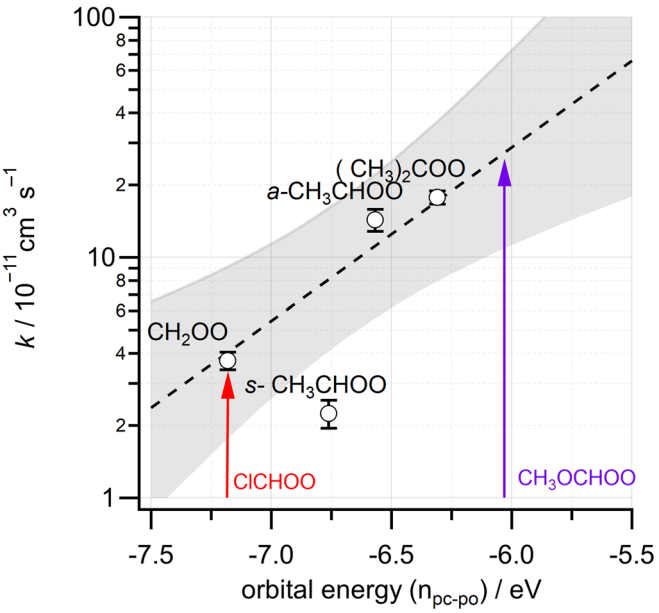


Figure 5.6 The log of the rate constant of the CIs for the reaction with SO_2 plotted as a function of the $n_{pc\text{-}po}$ orbital energies. The reported experimental values are shown in black, and the *syn*- conformer of CH_3CHOO was masked from the fit. ClCHOO (red) and CH_3OCHOO (purple) are shown with the corresponding arrows to indicate where they would end up on the trend.

5.5 Conclusion

The concepts from FMO theory have been used to construct SARs that are based on a correlation between calculated orbital energies and experimental rate constants. The reaction between CH_2OO and HCHO was used as a baseline case to explain how substituent effects of EWGs and EDGs on the carbonyl can influence the rate of the reaction. An inverse correlation was found between the π^* orbital energy of the carbonyls and the bimolecular rate constants for the reaction with CH_2OO. The strong linear correlation provides a SAR to predict rate constants for the reaction of CH_2OO with carbonyls. A separate SAR was developed for the reaction of different CIs with SO_2. CH_2OO is the baseline case and the reaction with SO_2 is faster with EDGs on the CIs. There is not a large body of research that explores the experimental rate constants of the reaction of SO_2 with various CIs. Aside from having a large discrepancy in the measured rate constants for the two isomers of acetaldehyde oxide, there are only three rate constants that were used to develop the SAR for substituted CIs. More work is needed to predict rate constants for substituted CIs. The utility of the developed SARs has potential in predicting rate constants for more atmospherically relevant reactions.

6 Dissertation Summary

The kinetics of the reactions of CH_2OO with various functionalized ketones were explored in this dissertation. The bimolecular rate constants were measured using a laser flash photolysis transient absorption spectroscopy technique in a glass-jacketed flow cell apparatus. The kinetics measurements spanned across the experimental temperature range of 275–335 K at relatively low pressures (~60–100 Torr). All the reactions showed linear Arrhenius plots with varying temperature sensitivities. Complementary quantum calculations were used to characterize the potential energy surface of the 1,3-dipolar cycloaddition reactions. The reactants proceed through a weakly bound van der Waals entrance channel complex before passing over the cycloaddition transition state (TS). The collection of reactions of CH_2OO with various ketones pass over a relatively low energy barrier before producing a secondary ozonide (SOZ) exothermically.

The kinetics of the reactions of CH_2OO with acetone (Ac), α-diketones biacetyl (BiAc) and acetylpropionyl (AcPr), and β-diketones acetylacetone (AcAc) and 3,3-dimethyl-2,4-pentanedione (dMAcAc) at 295 K were measured. The bimolecular rate constant for the CH_2OO+Ac reaction was measured to be $(4.1\pm0.4)\times10^{-13}$ cm^3 s^{-1}, which is consistent with previous measurements. The reactions of CH_2OO with AcAc and dMAcAc have broadly similar with rate constants of $(6.6\pm0.7)\times10^{-13}$ cm^3 s^{-1} and $(3.5\pm0.8)\times10^{-13}$ cm^3 s^{-1}, respectively. The α-diketones react significantly faster with rate constants of $(1.45\pm0.18)\times10^{-11}$ cm^3 s^{-1} and $(1.29\pm0.15)\times10^{-11}$ cm^3 s^{-1} for BiAc and AcPr. Although it was found that ketones are a negligible atmospheric sink, CH_2OO could be a viable sink for ketones such as Ac and BiAc in some environments.

Temperature-dependent bimolecular rate constants for the reactions of CH_2OO with Ac, BiAc, and AcAc were measured across the experimental temperature range of 275–335 K. The rate constants generally increase in the order Ac<AcAc<<BiAc across the temperature range. All of the reactions are negatively temperature-dependent and have the following bimolecular rate constants: $k_{Ac}(T)$ =

$(1.0\pm0.5)\times10^{-15}\exp[(1830\pm170)/T]$, $k_{BiAc}(T)$ = $(1.6\pm0.9)\times10^{-13}\exp[(1260\pm170)/T]$, and $k_{AcAc}(T)$ = $(1.8\pm1.1)\times10^{-13}\exp[(460\pm180)/T]$. The reaction of CH_2OO with AcAc is the least sensitive to temperature comparatively, which was explained computationally at the CBS-QB3 level of theory. Among the five possible different reaction pathways that were identified for AcAc, the cycloaddition of CH_2OO at the carbonyl (C=O) and alkene (C=C) site have nearly identical free energies of activation ($\Delta G°$ = +10.1 kcal mol^{-1} at 298 K). The small magnitude of the negative activation energy for AcAc can be understood as a result of the positive temperature dependence of alkene cycloaddition pathway competing with the negative temperature dependence of the reaction at the carbonyl site.

The temperature-dependent kinetics of the reactions of CH_2OO with hydroxyacetone (AcOH) and 4-hydroxy-2-butanone (4H2B) were measured separately across the experimental temperature range. The Arrhenius plots were linear and the following temperature-dependent bimolecular rate constants were determined: $k_{AcOH}(T)$ = $(4.3\pm1.7)\times10^{-15}\exp[(1630\pm120)/T]$ and $k_{4H2B}(T)$ = $(3.5\pm2.6)\times10^{-15}\exp[(1700\pm200)/T]$. Both reactions overall have similar rate constants and are negatively temperature dependent. The stationary points along the potential energy surfaces were calculated using the CBS-QB3 level of theory. The free-energy barriers for the reaction of CH_2OO at the OH site were ~4–5 kcal mol^{-1}, so the contribution to the bimolecular rate constants are presumed to be negligible for both AcOH and 4H2B.

The reactivity of substituted carbonyls was rationalized using concepts from frontier molecular orbital (FMO) theory. Substituents on the carbonyl were classified into two types: electron donating groups (EDGs) and electron withdrawing groups (EWGs). The magnitude at which a substituent affects the reactivity is understood relative to hydrogen (H), which is neither an EWG or EDG. The cycloaddition transition state is sensitive to the electronic character of the substituents, where EWGs decrease the orbital energies on the carbonyl and therefore increase the reactivity. The dominant interaction that stabilizes the TS is between the occupied non-bonding $n_{pc\text{-}po}$ orbital energy on CH_2OO

and the unoccupied π^* orbital energies of the substituted carbonyl. The dominant interaction was initially labeled as the energy gap between the corresponding orbitals, or ΔE_S. The rate constants were found to correlate strongly with the EWG/EDG character of substituents quantified by Hammett parameters. In the final chapter of this dissertation, a structure activity relationship (SAR) was developed from this correlation. The π^* orbital energies and log of the experimental rate constants for the reactions of CH_2OO with several carbonyls at room temperature were shown to have a linear relationship. The SAR provides the ability to predict the rate constants for carbonyls in the cycloaddition reaction with CH_2OO by using the following equation, $\ln k = (-1.53 \pm 0.14)E_{\pi^*} - (29.21 \pm 0.29)$. This work is not finished, as the predictive power of this SAR needs to be demonstrated for compounds that are particularly problematic to be investigated experimentally.

Future kinetics experiments for the reactions of CH_2OO with substituted ketones could answer open questions that this research is focused on. The understanding of the SAR we have developed could be strengthened by measuring bimolecular rate constants for more ketones with different types and varieties of EWGs and EDGs. Substituents such as haloalkyl, phenyl, alkoxy, or alkylamine groups would translate to perhaloketones, phenones, esters, or amides respectively. The current SAR is based on room temperature kinetics experiments, so incorporating a temperature-dependence with the correlations could offer more potential in supporting the atmospheric implications of the reactions involving CIs with ketones. The α,β-unsaturated compounds, such as AcAc, did not correlate well with the SAR because of lower π^* orbital energies. The current prediction for α,β-unsaturated carbonyls gives larger rate constants than what was confirmed experimentally. More computational work on how delocalized π-systems affect the orbital energies of carbonyls could offer new directions in this work.

7 References

(1) Finlayson-Pitts, B. J.; Pitts, J. N. *Chemistry of the Upper and Lower Atmosphere: Theory, Experiments, and Applications*; Academic Press: San Diego, 2000.

(2) Seinfeld, J. H.; Pandis, S. N. *Atmospheric Chemistry and Physics: From Air Pollution to Climate Change*; Wiley, 2012.

(3) Yung, Y. L.; Demore, W. B. *Photochemistry of Planetary Atmospheres*; Oxford University Press, 1998.

(4) Calvert, J. G.; Orlando, J. J.; Stockwell, W. R.; Wallington, T. J. *The Mechanisms of Reactions Influencing Atmospheric Ozone*; Oxford University Press, 2015.

(5) McElroy, C. T.; Fogal, P. F. Ozone: From Discovery to Protection. *Atmosphere-Ocean* **2008**, *46* (1), 1–13. https://doi.org/10.3137/ao.460101.

(6) Kroll, J. H.; Seinfeld, J. H. Chemistry of Secondary Organic Aerosol: Formation and Evolution of Low-Volatility Organics in the Atmosphere. *Atmospheric Environment* **2008**, *42* (16), 3593–3624. https://doi.org/10.1016/j.atmosenv.2008.01.003.

(7) Nguyen, D.-H.; Lin, C.; Vu, C.-T.; Cheruiyot, N. K.; Nguyen, M. K.; Le, T. H.; Lukkhasorn, W.; Vo, T.-D.-H.; Bui, X.-T. Tropospheric Ozone and NO X : A Review of Worldwide Variation and Meteorological Influences. *Environmental Technology & Innovation* **2022**, *28*, 102809. https://doi.org/10.1016/j.eti.2022.102809.

(8) Lu, X.; Zhang, L.; Shen, L. Meteorology and Climate Influences on Tropospheric Ozone: A Review of Natural Sources, Chemistry, and Transport Patterns. *Curr Pollution Rep* **2019**, *5* (4), 238–260. https://doi.org/10.1007/s40726-019-00118-3.

(9) Pöschl, U. Atmospheric Aerosols: Composition, Transformation, Climate and Health Effects. *Angew Chem Int Ed* **2005**, *44* (46), 7520–7540. https://doi.org/10.1002/anie.200501122.

(10) De Marco, A.; Garcia-Gomez, H.; Collalti, A.; Khaniabadi, Y. O.; Feng, Z.; Proietti, C.; Sicard, P.; Vitale, M.; Anav, A.; Paoletti, E. Ozone Modelling and Mapping for Risk Assessment: An Overview of Different Approaches for Human and Ecosystems Health. *Environmental Research* **2022**, *211*, 113048. https://doi.org/10.1016/j.envres.2022.113048.

(11) Sicard, P. Ground-Level Ozone over Time: An Observation-Based Global Overview. *Current Opinion in Environmental Science & Health* **2021**, *19*, 100226. https://doi.org/10.1016/j.coesh.2020.100226.

(12) Gutbrod, R.; Kraka, E.; Schindler, R. N.; Cremer, D. Kinetic and Theoretical Investigation of the Gas-Phase Ozonolysis of Isoprene: Carbonyl Oxides as an Important Source for OH Radicals in the Atmosphere. *J. Am. Chem. Soc.* **1997**, *119* (31), 7330–7342. https://doi.org/10.1021/ja970050c.

(13) Donahue, N. M.; Drozd, G. T.; Epstein, S. A.; Presto, A. A.; Kroll, J. H. Adventures in Ozoneland: Down the Rabbit-Hole. *Phys. Chem. Chem. Phys.* **2011**, *13* (23), 10848–10857. https://doi.org/10.1039/C0CP02564J.

(14) Criegee, R. Mechanism of Ozonolysis. *Angew. Chem. Int. Ed. Engl.* **1975**, *14* (11), 745–752. https://doi.org/10.1002/anie.197507451.

(15) Hatakeyama, S.; Akimoto, H. Reactions of Criegee Intermediates in the Gas Phase. *Res. Chem. Intermed.* **1994**, *20* (3–5), 503–524. https://doi.org/10.1163/156856794X00432.

(16) Johnson, D.; Marston, G. The Gas-Phase Ozonolysis of Unsaturated Volatile Organic Compounds in the Troposphere. *Chem. Soc. Rev.* **2008**, *37* (4), 699–716. https://doi.org/10.1039/B704260B.

(17) Chhantyal-Pun, R.; Khan, M. A. H.; Taatjes, C. A.; Percival, C. J.; Orr-Ewing, A. J.; Shallcross, D. E. Criegee Intermediates: Production, Detection and Reactivity. *Int. Rev. Phys. Chem.* **2020**, *39* (3), 385–424. https://doi.org/10.1080/0144235X.2020.1792104.

(18) Atkinson, R.; Baulch, D. L.; Cox, R. A.; Crowley, J. N.; Hampson, R. F.; Hynes, R. G.; Jenkin, M. E.; Rossi, M. J.; Troe, J.; IUPAC Subcommittee. Evaluated Kinetic and Photochemical Data for Atmospheric Chemistry: Volume II – Gas Phase Reactions of Organic Species. *Atmos. Chem. Phys.* **2006**, *6* (11), 3625–4055. https://doi.org/10.5194/acp-6-3625-2006.
(19) Nguyen, T. B.; Tyndall, G. S.; Crounse, J. D.; Teng, A. P.; Bates, K. H.; Schwantes, R. H.; Coggon, M. M.; Zhang, L.; Feiner, P.; Milller, D. O.; Skog, K. M.; Rivera-Rios, J. C.; Dorris, M.; Olson, K. F.; Koss, A.; Wild, R. J.; Brown, S. S.; Goldstein, A. H.; de Gouw, J. A.; Brune, W. H.; Keutsch, F. N.; Seinfeld, J. H.; Wennberg, P. O. Atmospheric Fates of Criegee Intermediates in the Ozonolysis of Isoprene. *Phys. Chem. Chem. Phys.* **2016**, *18* (15), 10241–10254. https://doi.org/10.1039/C6CP00053C.
(20) Caravan, R. L.; Vansco, M. F.; Lester, M. I. Open Questions on the Reactivity of Criegee Intermediates. *Commun Chem* **2021**, *4* (1), 44. https://doi.org/10.1038/s42004-021-00483-5.
(21) Wennberg, P. O.; Bates, K. H.; Crounse, J. D.; Dodson, L. G.; McVay, R. C.; Mertens, L. A.; Nguyen, T. B.; Praske, E.; Schwantes, R. H.; Smarte, M. D.; St Clair, J. M.; Teng, A. P.; Zhang, X.; Seinfeld, J. H. Gas-Phase Reactions of Isoprene and Its Major Oxidation Products. *Chem. Rev.* **2018**, *118* (7), 3337–3390. https://doi.org/10.1021/acs.chemrev.7b00439.
(22) Atkinson, R. Atmospheric Chemistry of VOCs and NOx. *Atmos. Environ.* **2000**, *34* (12–14), 2063–2101. https://doi.org/10.1016/S1352-2310(99)00460-4.
(23) Osborn, D. L.; Taatjes, C. A. The Physical Chemistry of Criegee Intermediates in the Gas Phase. *Int. Rev. Phys. Chem.* **2015**, *34* (3), 309–360. https://doi.org/10.1080/0144235X.2015.1055676.
(24) Mauldin III, R. L.; Berndt, T.; Sipilä, M.; Paasonen, P.; Petäjä, T.; Kim, S.; Kurtén, T.; Stratmann, F.; Kerminen, V.-M.; Kulmala, M. A New Atmospherically Relevant Oxidant of Sulphur Dioxide. *Nature* **2012**, *488* (7410), 193–196. https://doi.org/10.1038/nature11278.
(25) Novelli, A.; Hens, K.; Tatum Ernest, C.; Martinez, M.; Nölscher, A. C.; Sinha, V.; Paasonen, P.; Petäjä, T.; Sipilä, M.; Elste, T.; Plass-Dülmer, C.; Phillips, G. J.; Kubistin, D.; Williams, J.; Vereecken, L.; Lelieveld, J.; Harder, H. Estimating the Atmospheric Concentration of Criegee Intermediates and Their Possible Interference in a FAGE-LIF Instrument. *Atmos. Chem. Phys.* **2017**, *17* (12), 7807–7826. https://doi.org/10.5194/acp-17-7807-2017.
(26) Khan, M. A. H.; Percival, C. J.; Caravan, R. L.; Taatjes, C. A.; Shallcross, D. E. Criegee Intermediates and Their Impacts on the Troposphere. *Environ. Sci.: Processes Impacts* **2018**, *20* (3), 437–453. https://doi.org/10.1039/C7EM00585G.
(27) Vereecken, L.; Novelli, A.; Taraborrelli, D. Unimolecular Decay Strongly Limits the Atmospheric Impact of Criegee Intermediates. *Phys. Chem. Chem. Phys.* **2017**, *19* (47), 31599–31612. https://doi.org/10.1039/C7CP05541B.
(28) Fenske, J. D.; Hasson, A. S.; Ho, A. W.; Paulson, S. E. Measurement of Absolute Unimolecular and Bimolecular Rate Constants for CH_3CHOO Generated by the *Trans*-2-Butene Reaction with Ozone in the Gas Phase. *J. Phys. Chem. A* **2000**, *104* (44), 9921–9932. https://doi.org/10.1021/jp0016636.
(29) Sipilä, M.; Jokinen, T.; Berndt, T.; Richters, S.; Makkonen, R.; Donahue, N. M.; Mauldin III, R. L.; Kurtén, T.; Paasonen, P.; Sarnela, N.; Ehn, M.; Junninen, H.; Rissanen, M. P.; Thornton, J.; Stratmann, F.; Herrmann, H.; Worsnop, D. R.; Kulmala, M.; Kerminen, V.-M.; Petäjä, T. Reactivity of Stabilized Criegee Intermediates (sCIs) from Isoprene and Monoterpene Ozonolysis toward SO_2 and Organic Acids. *Atmos. Chem. Phys.* **2014**, *14* (22), 12143–12153. https://doi.org/10.5194/acp-14-12143-2014.
(30) Womack, C. C.; Martin-Drumel, M.-A.; Brown, G. G.; Field, R. W.; McCarthy, M. C. Observation of the Simplest Criegee Intermediate CH_2OO in the Gas-Phase Ozonolysis of Ethylene. *Sci. Adv.* **2015**, *1* (2), e1400105–e1400105. https://doi.org/10.1126/sciadv.1400105.
(31) Cabezas, C.; Nakajima, M.; Endo, Y. Criegee Intermediates Meet Rotational Spectroscopy. *Int. Rev. Phys. Chem.* **2020**, *39* (3), 351–384. https://doi.org/10.1080/0144235X.2020.1782651.

(32) Hakala, J.; Donahue, N. M. Carbonyl Oxide Stabilization from Trans Alkene and Terpene Ozonolysis. *J. Phys. Chem. A* **2023**, *127* (41), 8530–8543. https://doi.org/10.1021/acs.jpca.3c03650.
(33) Taatjes, C. A. Criegee Intermediates: What Direct Production and Detection Can Teach Us About Reactions of Carbonyl Oxides. *Annu. Rev. Phys. Chem.* **2017**, *68* (1), 183–207. https://doi.org/10.1146/annurev-physchem-052516-050739.
(34) Horie, O.; Neeb, P.; Moortgat, G. K. The Reactions of the Criegee Intermediate CH_3CHOO in the Gas-Phase Ozonolysis of 2-Butene Isomers. *Int. J. Chem. Kinet.* **1997**, *29* (6), 461–468. https://doi.org/10.1002/(SICI)1097-4601(1997)29:6<461::AID-KIN8>3.0.CO;2-S.
(35) Horie, O.; Moortgat, G. K. Gas-Phase Ozonolysis of Alkenes. Recent Advances in Mechanistic Investigations. *Acc. Chem. Res.* **1998**, *31* (7), 387–396. https://doi.org/10.1021/ar9702740.
(36) Sander, W. Carbonyl Oxides: Zwitterions or Diradicals? *Angew. Chem. Int. Ed. Engl.* **1990**, *29* (4), 344–354. https://doi.org/10.1002/anie.199003441.
(37) Asatryan, R.; Bozzelli, J. W. Formation of a Criegee Intermediate in the Low-Temperature Oxidation of Dimethyl Sulfoxide. *Phys. Chem. Chem. Phys.* **2008**, *10* (13), 1769. https://doi.org/10.1039/b716179d.
(38) Taatjes, C. A.; Meloni, G.; Selby, T. M.; Trevitt, A. J.; Osborn, D. L.; Percival, C. J.; Shallcross, D. E. Direct Observation of the Gas-Phase Criegee Intermediate (CH_2OO). *J. Am. Chem. Soc.* **2008**, *130* (36), 11883–11885. https://doi.org/10.1021/ja804165q.
(39) Eskola, A. J.; Wojcik-Pastuszka, D.; Ratajczak, E.; Timonen, R. S. Kinetics of the Reactions of CH_2Br and CH_2I Radicals with Molecular Oxygen at Atmospheric Temperatures. *Phys. Chem. Chem. Phys.* **2006**, *8* (12), 1416–1424. https://doi.org/10.1039/b516291b.
(40) Welz, O.; Savee, J. D.; Osborn, D. L.; Vasu, S. S.; Percival, C. J.; Shallcross, D. E.; Taatjes, C. A. Direct Kinetic Measurements of Criegee Intermediate (CH_2OO) Formed by Reaction of CH_2I with O_2. *Science* **2012**, *335* (6065), 204–207. https://doi.org/10.1126/science.1213229.
(41) Sander, W. W. Reaction of Diphenylmethylene and Phenylmethylene with Oxygen. A Matrix Isolation Study. *J. Org. Chem.* **1989**, *54* (2), 333–339. https://doi.org/10.1021/jo00263a014.
(42) Wang, L.; Wu, Z.; Lu, B.; Zeng, X. Spectroscopic Characterization and Photochemistry of the Criegee Intermediate CF3C(H)OO. *Journal of Environmental Sciences* **2022**, *114*, 160–169. https://doi.org/10.1016/j.jes.2021.08.018.
(43) Criegee, R.; Wenner, G. Die Ozonisierung des 9,10-Oktalins. *Justus Liebigs Ann. Chem.* **1949**, *564* (1), 9–15. https://doi.org/10.1002/jlac.19495640103.
(44) Wadt, W. R.; Goddard, W. A. Electronic Structure of the Criegee Intermediate. Ramifications for the Mechanism of Ozonolysis. *J. Am. Chem. Soc.* **1975**, *97* (11), 3004–3021. https://doi.org/10.1021/ja00844a016.
(45) Aplincourt, P.; Henon, E.; Bohr, F.; Ruiz-López, M. F. Theoretical Study of Photochemical Processes Involving Singlet Excited States of Formaldehyde Carbonyl Oxide in the Atmosphere. *Chemical Physics* **2002**, *285* (2–3), 221–231. https://doi.org/10.1016/S0301-0104(02)00804-2.
(46) Dawes, R.; Jiang, B.; Guo, H. UV Absorption Spectrum and Photodissociation Channels of the Simplest Criegee Intermediate (CH_2OO). *J. Am. Chem. Soc.* **2015**, *137* (1), 50–53. https://doi.org/10.1021/ja510736d.
(47) Miliordos, E.; Xantheas, S. S. The Origin of the Reactivity of the Criegee Intermediate: Implications for Atmospheric Particle Growth. *Angew. Chem. Int. Ed.* **2016**, *55* (3), 1015–1019. https://doi.org/10.1002/anie.201509685.
(48) Beames, J. M.; Liu, F.; Lu, L.; Lester, M. I. Ultraviolet Spectrum and Photochemistry of the Simplest Criegee Intermediate CH_2OO. *J. Am. Chem. Soc.* **2012**, *134* (49), 20045–20048. https://doi.org/10.1021/ja310603j.
(49) Sheps, L. Absolute Ultraviolet Absorption Spectrum of a Criegee Intermediate CH_2OO. *J. Phys. Chem. Lett.* **2013**, *4* (24), 4201–4205. https://doi.org/10.1021/jz402191w.

(50) Foreman, E. S.; Kapnas, K. M.; Jou, Y.; Kalinowski, J.; Feng, D.; Gerber, R. B.; Murray, C. High Resolution Absolute Absorption Cross Sections of the $\tilde{B}^1A'$–$\tilde{X}^1A'$ Transition of the CH_2OO Biradical. *Phys. Chem. Chem. Phys.* **2015**, *17* (48), 32539–32546. https://doi.org/10.1039/C5CP04977F.
(51) Mir, Z. S.; Lewis, T. R.; Onel, L.; Blitz, M. A.; Seakins, P. W.; Stone, D. CH_2OO Criegee Intermediate UV Absorption Cross-Sections and Kinetics of CH_2OO + CH_2OO and CH_2OO + I as a Function of Pressure. *Phys. Chem. Chem. Phys.* **2020**, *22* (17), 9448–9459. https://doi.org/10.1039/D0CP00988A.
(52) Ting, W.-L.; Chen, Y.-H.; Chao, W.; Smith, M. C.; Lin, J. J.-M. The UV Absorption Spectrum of the Simplest Criegee Intermediate CH_2OO. *Phys. Chem. Chem. Phys.* **2014**, *16* (22), 10438–10443. https://doi.org/10.1039/C4CP00877D.
(53) Ting, A. W.-L.; Lin, J. J.-M. UV Spectrum of the Simplest Deuterated Criegee Intermediate CD_2OO. *J. Chin. Chem. Soc.* **2017**, *64* (4), 360–368. https://doi.org/10.1002/jccs.201700049.
(54) Karsili, T. N. V.; Marchetti, B.; Lester, M. I.; Ashfold, M. N. R. Electronic Absorption Spectroscopy and Photochemistry of Criegee Intermediates. *Photochem & Photobiology* **2023**, *99* (1), 4–18. https://doi.org/10.1111/php.13665.
(55) Chang, Y.-P.; Chang, C.-H.; Takahashi, K.; Lin, J. J.-M. Absolute UV Absorption Cross Sections of Dimethyl Substituted Criegee Intermediate $(CH_3)_2COO$. *Chem. Phys. Lett.* **2016**, *653*, 155–160. https://doi.org/10.1016/j.cplett.2016.04.082.
(56) Liu, F.; Beames, J. M.; Green, A. M.; Lester, M. I. UV Spectroscopic Characterization of Dimethyl- and Ethyl-Substituted Carbonyl Oxides. *J. Phys. Chem. A* **2014**, *118* (12), 2298–2306. https://doi.org/10.1021/jp412726z.
(57) Vansco, M. F.; Marchetti, B.; Lester, M. I. Electronic Spectroscopy of Methyl Vinyl Ketone Oxide: A Four-Carbon Unsaturated Criegee Intermediate from Isoprene Ozonolysis. *The Journal of Chemical Physics* **2018**, *149* (24), 244309. https://doi.org/10.1063/1.5064716.
(58) Lin, Y.-H.; Yin, C.; Takahashi, K.; Lin, J. J.-M. Surprisingly Long Lifetime of Methacrolein Oxide, an Isoprene Derived Criegee Intermediate, under Humid Conditions. *Commun Chem* **2021**, *4* (1), 12. https://doi.org/10.1038/s42004-021-00451-z.
(59) Lin, Y.-H.; Takahashi, K.; Lin, J. J.-M. Absolute Photodissociation Cross Sections of Thermalized Methyl Vinyl Ketone Oxide and Methacrolein Oxide. *Phys. Chem. Chem. Phys.* **2022**, *24* (17), 10439–10450. https://doi.org/10.1039/D2CP00476C.
(60) Lee, Y.-P. Perspective: Spectroscopy and Kinetics of Small Gaseous Criegee Intermediates. *The Journal of Chemical Physics* **2015**, *143* (2), 020901. https://doi.org/10.1063/1.4923165.
(61) Su, Y.-T.; Huang, Y.-H.; Witek, H. A.; Lee, Y.-P. Infrared Absorption Spectrum of the Simplest Criegee Intermediate CH_2OO. *Science* **2013**, *340* (6129), 174–176. https://doi.org/10.1126/science.1234369.
(62) Chen, S.-Y.; Lee, Y.-P. Transient Infrared Absorption of T-$CH_3C(O)OO$, c-$CH_3C(O)OO$, and α-Lactone Recorded in Gaseous Reactions of CH_3CO and O_2. *J. Chem. Phys.* **2010**, *132* (11), 114303. https://doi.org/10.1063/1.3352315.
(63) Huang, Y.-H.; Li, J.; Guo, H.; Lee, Y.-P. Infrared Spectrum of the Simplest Criegee Intermediate CH_2OO at Resolution 0.25 Cm−1 and New Assignments of Bands 2 ν 9 and ν 5. *The Journal of Chemical Physics* **2015**, *142* (21), 214301. https://doi.org/10.1063/1.4921731.
(64) Lin, H.-Y.; Huang, Y.-H.; Wang, X.; Bowman, J. M.; Nishimura, Y.; Witek, H. A.; Lee, Y.-P. Infrared Identification of the Criegee Intermediates Syn- and Anti-CH3CHOO, and Their Distinct Conformation-Dependent Reactivity. *Nat Commun* **2015**, *6* (1), 7012. https://doi.org/10.1038/ncomms8012.
(65) Su, Y.-T.; Lin, H.-Y.; Putikam, R.; Matsui, H.; Lin, M. C.; Lee, Y.-P. Extremely Rapid Self-Reaction of the Simplest Criegee Intermediate CH_2OO and Its Implications in Atmospheric Chemistry. *Nat. Chem.* **2014**, *6* (6), 477–483. https://doi.org/10.1038/nchem.1890.

(66) Golec, B.; Chen, J.-D.; Lee, Y.-P. Infrared Absorption of Gaseous Benzoylperoxy Radical $C_6H_5C(O)OO$ Recorded with a Step-Scan Fourier-Transform Spectrometer. *J. Chem. Phys.* **2011**, *135* (22), 224302. https://doi.org/10.1063/1.3664304.
(67) Chang, Y.-P.; Li, Y.-L.; Liu, M.-L.; Ou, T.-C.; Lin, J. J.-M. Absolute Infrared Absorption Cross Section of the Simplest Criegee Intermediate Near 1285.7 Cm^{-1}. *J. Phys. Chem. A* **2018**, *122* (45), 8874–8881. https://doi.org/10.1021/acs.jpca.8b06759.
(68) Barber, V. P.; Pandit, S.; Green, A. M.; Trongsiriwat, N.; Walsh, P. J.; Klippenstein, S. J.; Lester, M. I. Four-Carbon Criegee Intermediate from Isoprene Ozonolysis: Methyl Vinyl Ketone Oxide Synthesis, Infrared Spectrum, and OH Production. *J. Am. Chem. Soc.* **2018**, *140* (34), 10866–10880. https://doi.org/10.1021/jacs.8b06010.
(69) Cai, J.-R.; Su, J.-H.; Lee, Y.-P. Formation Reaction Mechanism and Infrared Spectra of Anti-Trans-Methacrolein Oxide and Its Associated Precursor and Adduct Radicals. *Commun Chem* **2022**, *5* (1), 26. https://doi.org/10.1038/s42004-022-00644-0.
(70) Nakajima, M.; Endo, Y. Communication: Determination of the Molecular Structure of the Simplest Criegee Intermediate CH_2OO. *J. Chem. Phys.* **2013**, *139* (10), 101103. https://doi.org/10.1063/1.4821165.
(71) McCarthy, M. C.; Cheng, L.; Crabtree, K. N.; Martinez, O.; Nguyen, T. L.; Womack, C. C.; Stanton, J. F. The Simplest Criegee Intermediate ($H_2C{=}O{-}O$): Isotopic Spectroscopy, Equilibrium Structure, and Possible Formation from Atmospheric Lightning. *J. Phys. Chem. Lett.* **2013**, *4* (23), 4133–4139. https://doi.org/10.1021/jz4023128.
(72) Cabezas, C.; Guillemin, J.-C.; Endo, Y. Conformational Analysis of Ethyl-Substituted Criegee Intermediate by FTMW Spectroscopy. *The Journal of Chemical Physics* **2016**, *145* (22), 224314. https://doi.org/10.1063/1.4972017.
(73) Nakajima, M.; Endo, Y. Fourier-Transform Microwave Spectroscopy of Dimethyl-Substituted Criegee Intermediate (CH3)2COO. *The Journal of Chemical Physics* **2016**, *145* (24), 244307. https://doi.org/10.1063/1.4973014.
(74) Stone, D.; Au, K.; Sime, S.; Medeiros, D. J.; Blitz, M.; Seakins, P. W.; Decker, Z.; Sheps, L. Unimolecular Decomposition Kinetics of the Stabilised Criegee Intermediates CH_2OO and CD_2OO. *Phys. Chem. Chem. Phys.* **2018**, *20* (38), 24940–24954. https://doi.org/10.1039/C8CP05332D.
(75) Liu, F.; Beames, J. M.; Petit, A. S.; McCoy, A. B.; Lester, M. I. Infrared-Driven Unimolecular Reaction of CH_3CHOO Criegee Intermediates to OH Radical Products. *Science* **2014**, *345* (6204), 1596–1598. https://doi.org/10.1126/science.1257158.
(76) Taatjes, C. A.; Liu, F.; Rotavera, B.; Kumar, M.; Caravan, R.; Osborn, D. L.; Thompson, W. H.; Lester, M. I. Hydroxyacetone Production From C_3 Criegee Intermediates. *J. Phys. Chem. A* **2017**, *121* (1), 16–23. https://doi.org/10.1021/acs.jpca.6b07712.
(77) Caravan, R. L.; Vansco, M. F.; Au, K.; Khan, M. A. H.; Li, Y.-L.; Winiberg, F. A. F.; Zuraski, K.; Lin, Y.-H.; Chao, W.; Trongsiriwat, N.; Walsh, P. J.; Osborn, D. L.; Percival, C. J.; Lin, J. J.-M.; Shallcross, D. E.; Sheps, L.; Klippenstein, S. J.; Taatjes, C. A.; Lester, M. I. Direct Kinetic Measurements and Theoretical Predictions of an Isoprene-Derived Criegee Intermediate. *Proc. Natl. Acad. Sci. U.S.A.* **2020**, *117* (18), 9733–9740. https://doi.org/10.1073/pnas.1916711117.
(78) Lee, H. K.; Chantanapongvanij, P.; Schmidt, R. R.; Stephenson, T. A. Master Equation Studies of the Unimolecular Decay of Thermalized Methacrolein Oxide: The Impact of Atmospheric Conditions. *J. Phys. Chem. A* **2023**, *127* (20), 4492–4502. https://doi.org/10.1021/acs.jpca.3c00542.
(79) Tadayon, S. V.; Foreman, E. S.; Murray, C. Kinetics of the Reactions between the Criegee Intermediate CH_2OO and Alcohols. *J. Phys. Chem. A* **2018**, *122* (1), 258–268. https://doi.org/10.1021/acs.jpca.7b09773.
(80) Taatjes, C. A.; Caravan, R. L.; Winiberg, F. A. F.; Zuraski, K.; Au, K.; Sheps, L.; Osborn, D. L.; Vereecken, L.; Percival, C. J. Insertion Products in the Reaction of Carbonyl Oxide Criegee

Intermediates with Acids: Chloro(Hydroperoxy)Methane Formation from Reaction of CH_2OO with HCl and DCl. *Mol. Phys.* **2021**, *119* (17–18), e1975199. https://doi.org/10.1080/00268976.2021.1975199.
(81) Vereecken, L. The Reaction of Criegee Intermediates with Acids and Enols. *Phys. Chem. Chem. Phys.* **2017**, *19* (42), 28630–28640. https://doi.org/10.1039/C7CP05132H.
(82) Stone, D.; Blitz, M.; Daubney, L.; Howes, N. U. M.; Seakins, P. Kinetics of CH_2OO Reactions with SO_2, NO_2, NO, H_2O and CH_3CHO as a Function of Pressure. *Phys. Chem. Chem. Phys.* **2014**, *16* (3), 1139–1149. https://doi.org/10.1039/C3CP54391A.
(83) Chao, W.; Hsieh, J.-T.; Chang, C.-H.; Lin, J. J.-M. Direct Kinetic Measurement of the Reaction of the Simplest Criegee Intermediate with Water Vapor. *Science* **2015**, *347* (6223), 751–754. https://doi.org/10.1126/science.1261549.
(84) Huang, H.-L.; Chao, W.; Lin, J. J.-M. Kinetics of a Criegee Intermediate That Would Survive High Humidity and May Oxidize Atmospheric SO_2. *Proc. Nat. Acad. Sci.* **2015**, *112* (35), 10857–10862. https://doi.org/10.1073/pnas.1513149112.
(85) Liu, Y.; Liu, F.; Liu, S.; Dai, D.; Dong, W.; Yang, X. A Kinetic Study of the CH_2OO Criegee Intermediate Reaction with SO_2, $(H_2O)_2$, CH_2I_2 and I Atoms Using OH Laser Induced Fluorescence. *Phys. Chem. Chem. Phys.* **2017**, *19* (31), 20786–20794. https://doi.org/10.1039/C7CP04336H.
(86) Smith, M. C.; Chang, C.-H.; Chao, W.; Lin, L.-C.; Takahashi, K.; Boering, K. A.; Lin, J. J.-M. Strong Negative Temperature Dependence of the Simplest Criegee Intermediate CH_2OO Reaction with Water Dimer. *J. Phys. Chem. Lett.* **2015**, *6* (14), 2708–2713. https://doi.org/10.1021/acs.jpclett.5b01109.
(87) Lewis, T. R.; Blitz, M. A.; Heard, D. E.; Seakins, P. W. Direct Evidence for a Substantive Reaction between the Criegee Intermediate, CH_2OO, and the Water Vapour Dimer. *Phys. Chem. Chem. Phys.* **2015**, *17* (7), 4859–4863. https://doi.org/10.1039/C4CP04750H.
(88) Berndt, T.; Kaethner, R.; Voigtländer, J.; Stratmann, F.; Pfeifle, M.; Reichle, P.; Sipilä, M.; Kulmala, M.; Olzmann, M. Kinetics of the Unimolecular Reaction of CH_2OO and the Bimolecular Reactions with the Water Monomer, Acetaldehyde and Acetone under Atmospheric Conditions. *Phys. Chem. Chem. Phys.* **2015**, *17* (30), 19862–19873. https://doi.org/10.1039/C5CP02224J.
(89) Sheps, L.; Rotavera, B.; Eskola, A. J.; Osborn, D. L.; Taatjes, C. A.; Au, K.; Shallcross, D. E.; Khan, M. A. H.; Percival, C. J. The Reaction of Criegee Intermediate CH_2OO with Water Dimer: Primary Products and Atmospheric Impact. *Phys. Chem. Chem. Phys.* **2017**, *19* (33), 21970–21979. https://doi.org/10.1039/C7CP03265J.
(90) Wu, Y.-J.; Takahashi, K.; Lin, J. J.-M. Kinetics of the Simplest Criegee Intermediate Reaction with Water Vapor: Revisit and Isotope Effect. *J. Phys. Chem. A* **2023**, *127* (39), 8059–8072. https://doi.org/10.1021/acs.jpca.3c03418.
(91) *J. B. Burkholder, S. P. Sander, J. Abbatt, J. R. Barker, C. Cappa, J. D. Crounse, T. S. Dibble, R. E. Huie, C. E. Kolb, M. J. Kurylo, V. L. Orkin, C. J. Percival, D. M. Wilmouth, and P. H. Wine "Chemical Kinetics and Photochemical Data for Use in Atmospheric Studies, Evaluation No. 19," JPL Publication 19-5, Jet Propulsion Laboratory, Pasadena, 2019 Http://Jpldataeval.Jpl.Nasa.Gov*; 19; 2019.
(92) Ryzhkov, A. B.; Ariya, P. A. A Theoretical Study of the Reactions of Parent and Substituted Criegee Intermediates with Water and the Water Dimer. *Phys. Chem. Chem. Phys.* **2004**, *6* (21), 5042. https://doi.org/10.1039/b408414d.
(93) Kuo, M.; Takahashi, K.; Lin, J. J. Reactions of Criegee Intermediates Are Enhanced by Hydrogen-Atom Relay Through Molecular Design. *ChemPhysChem* **2020**, *21* (18), 2056–2059. https://doi.org/10.1002/cphc.202000585.
(94) McGillen, M. R.; Curchod, B. F. E.; Chhantyal-Pun, R.; Beames, J. M.; Watson, N.; Khan, M. A. H.; McMahon, L.; Shallcross, D. E.; Orr-Ewing, A. J. Criegee Intermediate–Alcohol Reactions, A Potential Source of Functionalized Hydroperoxides in the Atmosphere. *ACS Earth Space Chem.* **2017**. https://doi.org/10.1021/acsearthspacechem.7b00108.

(95) Watson, N. A. I.; Black, J. A.; Stonelake, T. M.; Knowles, P. J.; Beames, J. M. An Extended Computational Study of Criegee Intermediate–Alcohol Reactions. *J. Phys. Chem. A* **2019**, *123* (1), 218–229. https://doi.org/10.1021/acs.jpca.8b09349.
(96) Aroeira, G. J. R.; Abbott, A. S.; Elliott, S. N.; Turney, J. M.; Schaefer, H. F. The Addition of Methanol to Criegee Intermediates. *Phys. Chem. Chem. Phys.* **2019**, *21* (32), 17760–17771. https://doi.org/10.1039/C9CP03480C.
(97) Liu, Y.; Yin, C.; Smith, M. C.; Liu, S.; Chen, M.; Zhou, X.; Xiao, C.; Dai, D.; Lin, J. J.-M.; Takahashi, K.; Dong, W.; Yang, X. Kinetics of the Reaction of the Simplest Criegee Intermediate with Ammonia: A Combination of Experiment and Theory. *Physical Chemistry Chemical Physics* **2018**, *20* (47), 29669–29676. https://doi.org/10.1039/C8CP05920A.
(98) Misiewicz, J. P.; Elliott, S. N.; Moore, K. B.; Schaefer, H. F. Re-Examining Ammonia Addition to the Criegee Intermediate: Converging to Chemical Accuracy. *Phys. Chem. Chem. Phys.* **2018**, *20* (11), 7479–7491. https://doi.org/10.1039/C7CP08582F.
(99) Chhantyal-Pun, R.; Shannon, R. J.; Tew, D. P.; Caravan, R. L.; Duchi, M.; Wong, C.; Ingham, A.; Feldman, C.; McGillen, M. R.; Khan, M. A. H.; Antonov, I. O.; Rotavera, B.; Ramasesha, K.; Osborn, D. L.; Taatjes, C. A.; Percival, C. J.; Shallcross, D. E.; Orr-Ewing, A. J. Experimental and Computational Studies of Criegee Intermediate Reactions with NH_3 and CH_3NH_2. *Phys. Chem. Chem. Phys.* **2019**, *21* (26), 14042–14052. https://doi.org/10.1039/C8CP06810K.
(100) Foreman, E. S.; Kapnas, K. M.; Murray, C. Reactions between Criegee Intermediates and the Inorganic Acids HCl and HNO_3: Kinetics and Atmospheric Implications. *Angew. Chem. Int. Ed.* **2016**, *55* (35), 10419–10422. https://doi.org/10.1002/anie.201604662.
(101) Cabezas, C.; Endo, Y. Spectroscopic Characterization of the Reaction Products between the Criegee Intermediate CH_2OO and HCl. *ChemPhysChem* **2017**, *18* (14), 1860–1863. https://doi.org/10.1002/cphc.201700446.
(102) Liu, S.; Zhou, X.; Chen, Y.; Liu, Y.; Yu, S.; Takahashi, K.; Ding, H.; Ding, Z.; Yang, X.; Dong, W. Experimental and Computational Studies of Criegee Intermediate *Syn*-CH_3CHOO Reaction with Hydrogen Chloride. *J. Phys. Chem. A* **2021**, *125* (39), 8587–8594. https://doi.org/10.1021/acs.jpca.1c05578.
(103) Su, Z.-S.; Lee, Y.-P. Infrared Characterization of the Products of the Reaction between the Criegee Intermediate CH_3CHOO and HCl. *J. Phys. Chem. A* **2023**, *127* (33), 6902–6915. https://doi.org/10.1021/acs.jpca.3c03527.
(104) Cabezas, C.; Endo, Y. The Reaction between the Methyl Criegee Intermediate and Hydrogen Chloride: An FTMW Spectroscopic Study. *Phys. Chem. Chem. Phys.* **2018**, *20* (35), 22569–22575. https://doi.org/10.1039/C8CP04171G.
(105) Chhantyal-Pun, R.; Rotavera, B.; McGillen, M. R.; Khan, M. A. H.; Eskola, A. J.; Caravan, R. L.; Blacker, L.; Tew, D. P.; Osborn, D. L.; Percival, C. J.; Taatjes, C. A.; Shallcross, D. E.; Orr-Ewing, A. J. Criegee Intermediate Reactions with Carboxylic Acids: A Potential Source of Secondary Organic Aerosol in the Atmosphere. *ACS Earth Space Chem.* **2018**, *2* (8), 833–842. https://doi.org/10.1021/acsearthspacechem.8b00069.
(106) Georgievskii, Y.; Klippenstein, S. J. Long-Range Transition State Theory. *J. Chem. Phys.* **2005**, *122* (19), 194103. https://doi.org/10.1063/1.1899603.
(107) Chung, C.-A.; Hsu, C.-W.; Lee, Y.-P. Infrared Characterization of the Products and Rate Coefficient of the Reaction between Criegee Intermediate CH_2OO and HNO_3. *J. Phys. Chem. A* **2022**, *126* (34), 5738–5750. https://doi.org/10.1021/acs.jpca.2c04557.
(108) Yang, J.-N.; Takahashi, K.; Lin, J. J.-M. Reaction Kinetics of Criegee Intermediates with Nitric Acid. *J. Phys. Chem. A* **2022**, *126* (36), 6160–6170. https://doi.org/10.1021/acs.jpca.2c04596.
(109) Tobias, H. J.; Ziemann, P. J. Kinetics of the Gas-Phase Reactions of Alcohols, Aldehydes, Carboxylic Acids, and Water with the C13 Stabilized Criegee Intermediate Formed from Ozonolysis of 1-Tetradecene. *J. Phys. Chem. A* **2001**, *105* (25), 6129–6135. https://doi.org/10.1021/jp004631r.

(110) Kumar, M.; Francisco, J. S. Heteroatom Tuning of Bimolecular Criegee Reactions and Its Implications. *Angew Chem Int Ed* **2016**, *55* (43), 13432–13435. https://doi.org/10.1002/anie.201604848.
(111) Elsamra, R. M. I.; Jalan, A.; Buras, Z. J.; Middaugh, J. E.; Green, W. H. Temperature- and Pressure-Dependent Kinetics of CH_2OO + CH_3COCH_3 and CH_2OO + CH_3CHO: Direct Measurements and Theoretical Analysis. *Int. J. Chem. Kinet.* **2016**, *48* (8), 474–488. https://doi.org/10.1002/kin.21007.
(112) Jalan, A.; Allen, J. W.; Green, W. H. Chemically Activated Formation of Organic Acids in Reactions of the Criegee Intermediate with Aldehydes and Ketones. *Phys. Chem. Chem. Phys.* **2013**, *15* (39), 16841–16852. https://doi.org/10.1039/C3CP52598H.
(113) Vereecken, L.; Francisco, J. S. Theoretical Studies of Atmospheric Reaction Mechanisms in the Troposphere. *Chem. Soc. Rev.* **2012**, *41* (19), 6259–6293. https://doi.org/10.1039/C2CS35070J.
(114) Vereecken, L.; Harder, H.; Novelli, A. The Reactions of Criegee Intermediates with Alkenes, Ozone, and Carbonyl Oxides. *Phys. Chem. Chem. Phys.* **2014**, *16* (9), 4039–4049. https://doi.org/10.1039/C3CP54514H.
(115) Buras, Z. J.; Elsamra, R. M. I.; Jalan, A.; Middaugh, J. E.; Green, W. H. Direct Kinetic Measurements of Reactions between the Simplest Criegee Intermediate CH_2OO and Alkenes. *J. Phys. Chem. A* **2014**, *118* (11), 1997–2006. https://doi.org/10.1021/jp4118985.
(116) Percival, C. J.; Welz, O.; Eskola, A. J.; Savee, J. D.; Osborn, D. L.; Topping, D. O.; Lowe, D.; Utembe, S. R.; Bacak, A.; McFiggans, G.; Cooke, M. C.; Xiao, P.; Archibald†, A. T.; Jenkin, M. E.; Derwent, R. G.; Riipinen, I.; Mok, D. W. K.; Lee, E. P. F.; Dyke, J. M.; Taatjes, C. A.; Shallcross, D. E. Regional and Global Impacts of Criegee Intermediates on Atmospheric Sulphuric Acid Concentrations and First Steps of Aerosol Formation. *Faraday Discuss.* **2013**, *165*, 45. https://doi.org/10.1039/c3fd00048f.
(117) Liu, Y.; Bayes, K. D.; Sander, S. P. Measuring Rate Constants for Reactions of the Simplest Criegee Intermediate (CH_2OO) by Monitoring the OH Radical. *J. Phys. Chem. A* **2014**, *118* (4), 741–747. https://doi.org/10.1021/jp407058b.
(118) Chhantyal-Pun, R.; Davey, A.; Shallcross, D. E.; Percival, C. J.; Orr-Ewing, A. J. A Kinetic Study of the CH_2OO Criegee Intermediate Self-Reaction, Reaction with SO_2 and Unimolecular Reaction Using Cavity Ring-down Spectroscopy. *Phys. Chem. Chem. Phys.* **2015**, *17* (5), 3617–3626. https://doi.org/10.1039/C4CP04198D.
(119) Howes, N. U. M.; Mir, Z. S.; Blitz, M. A.; Hardman, S.; Lewis, T. R.; Stone, D.; Seakins, P. W. Kinetic Studies of C_1 and C_2 Criegee Intermediates with SO_2 Using Laser Flash Photolysis Coupled with Photoionization Mass Spectrometry and Time Resolved UV Absorption Spectroscopy. *Phys. Chem. Chem. Phys.* **2018**, *20* (34), 22218–22227. https://doi.org/10.1039/C8CP03115K.
(120) Qiu, J.; Tonokura, K. Detection of the Simplest Criegee Intermediate CH_2OO in the N4 Band Using a Continuous Wave Quantum Cascade Laser and Its Kinetics with SO2 and NO2. *Chemical Physics Letters* **2019**, *737*, 100019. https://doi.org/10.1016/j.cpletx.2019.100019.
(121) Onel, L.; Lade, R.; Mortiboy, J.; Blitz, M. A.; Seakins, P. W.; Heard, D. E.; Stone, D. Kinetics of the Gas Phase Reaction of the Criegee Intermediate CH_2OO with SO_2 as a Function of Temperature. *Phys. Chem. Chem. Phys.* **2021**, *23* (35), 19415–19423. https://doi.org/10.1039/D1CP02932K.
(122) Vereecken, L.; Harder, H.; Novelli, A. The Reaction of Criegee Intermediates with NO, RO_2, and SO_2, and Their Fate in the Atmosphere. *Phys. Chem. Chem. Phys.* **2012**, *14* (42), 14682. https://doi.org/10.1039/c2cp42300f.
(123) Chhantyal-Pun, R.; Welz, O.; Savee, J. D.; Eskola, A. J.; Lee, E. P. F.; Blacker, L.; Hill, H. R.; Ashcroft, M.; Khan, M. A. H.; Lloyd-Jones, G. C.; Evans, L.; Rotavera, B.; Huang, H.; Osborn, D. L.; Mok, D. K. W.; Dyke, J. M.; Shallcross, D. E.; Percival, C. J.; Orr-Ewing, A. J.; Taatjes, C. A. Direct Measurements of Unimolecular and Bimolecular Reaction Kinetics of the Criegee Intermediate $(CH_3)_2COO$. *J. Phys. Chem. A* **2017**, *121* (1), 4–15. https://doi.org/10.1021/acs.jpca.6b07810.

(124) Houk, K. N. Frontier Molecular Orbital Theory of Cycloaddition Reactions. *Acc. Chem. Res.* **1975**, *8* (11), 361–369. https://doi.org/10.1021/ar50095a001.
(125) Fukui, K. Role of Frontier Orbitals in Chemical Reactions. *Science* **1982**, *218* (4574), 747–754. https://doi.org/10.1126/science.218.4574.747.
(126) Cornwell, Z. A.; Harrison, A. W.; Murray, C. Kinetics of the Reactions of CH_2OO with Acetone, α-Diketones, and β-Diketones. *J. Phys. Chem. A* **2021**, *125* (39), 8557–8571. https://doi.org/10.1021/acs.jpca.1c05280.
(127) Cornwell, Z. A.; Enders, J. J.; Harrison, A. W.; Murray, C. Temperature-Dependent Kinetics of the Reactions of CH_2OO with Acetone, Biacetyl, and Acetylacetone. *Int. J. Chem. Kinet.* **2023**, *55* (3), 154–166. https://doi.org/10.1002/kin.21625.
(128) Taatjes, C. A.; Welz, O.; Eskola, A. J.; Savee, J. D.; Osborn, D. L.; Lee, E. P. F.; Dyke, J. M.; Mok, D. W. K.; Shallcross, D. E.; Percival, C. J. Direct Measurement of Criegee Intermediate (CH_2OO) Reactions with Acetone, Acetaldehyde, and Hexafluoroacetone. *Phys. Chem. Chem. Phys.* **2012**, *14* (30), 10391–10400. https://doi.org/10.1039/C2CP40294G.
(129) Cornwell, Z. A.; Enders, J. J.; Harrison, A. W.; Murray, C. Temperature-Dependent Kinetics of the Reactions of the Criegee Intermediate CH_2OO with Hydroxyketones. *J. Phys. Chem. A* **2024**, *128* (10), 1880–1891. https://doi.org/10.1021/acs.jpca.4c00156.
(130) Chhantyal-Pun, R.; Khan, M. A. H.; Martin, R.; Zachhuber, N.; Buras, Z. J.; Percival, C. J.; Shallcross, D. E.; Orr-Ewing, A. J. Direct Kinetic and Atmospheric Modeling Studies of Criegee Intermediate Reactions with Acetone. *ACS Earth Space Chem.* **2019**, *3* (10), 2363–2371. https://doi.org/10.1021/acsearthspacechem.9b00213.
(131) Taatjes, C. A.; Shallcross, D. E.; Percival, C. J. Research Frontiers in the Chemistry of Criegee Intermediates and Tropospheric Ozonolysis. *Phys. Chem. Chem. Phys.* **2014**, *16* (5), 1704–1718. https://doi.org/10.1039/C3CP52842A.
(132) Cox, R. A.; Ammann, M.; Crowley, J. N.; Herrmann, H.; Jenkin, M. E.; McNeill, V. F.; Mellouki, A.; Troe, J.; Wallington, T. J. Evaluated Kinetic and Photochemical Data for Atmospheric Chemistry: Volume VII – Criegee Intermediates. *Atmos. Chem. Phys.* **2020**, *20* (21), 13497–13519. https://doi.org/10.5194/acp-20-13497-2020.
(133) Chao, W.; Hsieh, J.-T.; Chang, C.-H.; Lin, J. J.-M. Direct Kinetic Measurement of the Reaction of the Simplest Criegee Intermediate with Water Vapor. *Science* **2015**, *347* (6223), 751–754. https://doi.org/10.1126/science.1261549.
(134) Welz, O.; Eskola, A. J.; Sheps, L.; Rotavera, B.; Savee, J. D.; Scheer, A. M.; Osborn, D. L.; Lowe, D.; Murray Booth, A.; Xiao, P.; Anwar H. Khan, M.; Percival, C. J.; Shallcross, D. E.; Taatjes, C. A. Rate Coefficients of C1 and C2 Criegee Intermediate Reactions with Formic and Acetic Acid Near the Collision Limit: Direct Kinetics Measurements and Atmospheric Implications. *Angew. Chem. Int. Ed.* **2014**, *126* (18), 4635–4638. https://doi.org/10.1002/ange.201400964.
(135) Berndt, T.; Herrmann, H.; Kurtén, T. Direct Probing of Criegee Intermediates from Gas-Phase Ozonolysis Using Chemical Ionization Mass Spectrometry. *J. Am. Chem. Soc.* **2017**, *139* (38), 13387–13392. https://doi.org/10.1021/jacs.7b05849.
(136) Su, F.; Calvert, J. G.; Shaw, J. H. A FT IR Spectroscopic Study of the Ozone-Ethene Reaction Mechanism in Oxygen-Rich Mixtures. *J. Phys. Chem.* **1980**, *84* (3), 239–246. https://doi.org/10.1021/j100440a003.
(137) Neeb, P.; Horie, O.; Moortgat, G. K. The Nature of the Transitory Product in the Gas-Phase Ozonolysis of Ethene. *Chem. Phys. Lett.* **1995**, *246* (1–2), 150–156. https://doi.org/10.1016/0009-2614(95)01073-I.
(138) Neeb, P.; Horie, O.; Moortgat, G. K. Formation of Secondary Ozonides in the Gas-Phase Ozonolysis of Simple Alkenes. *Tetrahedron Lett.* **1996**, *37* (52), 9297–9300. https://doi.org/10.1016/S0040-4039(97)82946-2.
(139) Neeb, P.; Horie, O.; Moortgat, G. K. The Ethene−Ozone Reaction in the Gas Phase. *J. Phys. Chem. A* **1998**, *102* (34), 6778–6785. https://doi.org/10.1021/jp981264z.

(140) Horie, O.; Schäfer, C.; Moortgat, G. K. High Reactivity of Hexafluoro Acetone toward Criegee Intermediates in the Gas-Phase Ozonolysis of Simple Alkenes. *Int. J. Chem. Kinet.* **1999**, *31* (4), 261–269. https://doi.org/10.1002/(SICI)1097-4601(1999)31:4<261::AID-KIN3>3.0.CO;2-Z.

(141) Eskola, A. J.; Döntgen, M.; Rotavera, B.; Caravan, R. L.; Welz, O.; Savee, J. D.; Osborn, D. L.; Shallcross, D. E.; Percival, C. J.; Taatjes, C. A. Direct Kinetics Study of CH_2OO + Methyl Vinyl Ketone and CH_2OO + Methacrolein Reactions and an Upper Limit Determination for CH_2OO + CO Reaction. *Phys. Chem. Chem. Phys.* **2018**, *20* (29), 19373–19381. https://doi.org/10.1039/C8CP03606C.

(142) Cremer, D.; Kraka, E.; McKee, M. L.; Radharkrishnan, T. P. The Carbonyl Oxide-Aldehyde Complex: A New Intermediate of the Ozonolysis Reaction. *Chem. Phys. Lett.* **1991**, *187* (5), 491–493. https://doi.org/10.1016/0009-2614(91)80288-9.

(143) Aplincourt, P.; Ruiz-López, M. F. Theoretical Study of Formic Acid Anhydride Formation from Carbonyl Oxide in the Atmosphere. *J. Phys. Chem. A* **2000**, *104* (2), 380–388. https://doi.org/10.1021/jp9928208.

(144) Aplincourt, P.; Ruiz-López, M. F. Theoretical Investigation of Reaction Mechanisms for Carboxylic Acid Formation in the Atmosphere. *J. Am. Chem. Soc.* **2000**, *122* (37), 8990–8997. https://doi.org/10.1021/ja000731z.

(145) Yaws, C. L. *The Yaws Handbook of Vapor Pressure*; Elsevier, 2015. https://doi.org/10.1016/C2014-0-03590-3.

(146) Gaussian 16, Revision B.01, Frisch, M. J.; Trucks, G. W.; Schlegel, H. B.; Scuseria, G. E.; Robb, M. A.; Cheeseman, J. R.; Scalmani, G.; Barone, V.; Petersson, G. A.; Nakatsuji, H.; Li, X.; Caricato, M.; Marenich, A. V.; Bloino, J.; Janesko, B. G.; Gomperts, R.; Mennucci, B.; Hratchian, H. P.; Ortiz, J. V.; Izmaylov, A. F.; Sonnenberg, J. L.; Williams-Young, D.; Ding, F.; Lipparini, F.; Egidi, F.; Goings, J.; Peng, B.; Petrone, A.; Henderson, T.; Ranasinghe, D.; Zakrzewski, V. G.; Gao, J.; Rega, N.; Zheng, G.; Liang, W.; Hada, M.; Ehara, M.; Toyota, K.; Fukuda, R.; Hasegawa, J.; Ishida, M.; Nakajima, T.; Honda, Y.; Kitao, O.; Nakai, H.; Vreven, T.; Throssell, K.; Montgomery, J. A., Jr.; Peralta, J. E.; Ogliaro, F.; Bearpark, M. J.; Heyd, J. J.; Brothers, E. N.; Kudin, K. N.; Staroverov, V. N.; Keith, T. A.; Kobayashi, R.; Normand, J.; Raghavachari, K.; Rendell, A. P.; Burant, J. C.; Iyengar, S. S.; Tomasi, J.; Cossi, M.; Millam, J. M.; Klene, M.; Adamo, C.; Cammi, R.; Ochterski, J. W.; Martin, R. L.; Morokuma, K.; Farkas, O.; Foresman, J. B.; Fox, D. J. Gaussian, Inc., Wallingford CT, 2016.

(147) Schmidt, M. W.; Baldridge, K. K.; Boatz, J. A.; Elbert, S. T.; Gordon, M. S.; Jensen, J. H.; Koseki, S.; Matsunaga, N.; Nguyen, K. A.; Su, S.; Windus, T. L.; Dupuis, M.; Montgomery, J. A. General Atomic and Molecular Electronic Structure System. *J. Comput. Chem.* **1993**, *14* (11), 1347–1363. https://doi.org/10.1002/jcc.540141112.

(148) Gordon, M. S.; Schmidt, M. W. Advances in Electronic Structure Theory: GAMESS a Decade Later. In *Theory and Applications of Computational Chemistry, the First Forty Years*; Dykstra, C. E., Frenking, G., Kim, K. S., Scuseria, G. E., Eds.; Elsevier: Amsterdam, 2005; Vol. Chapter 41, pp 1167–1189.

(149) Barca, G. M. J.; Bertoni, C.; Carrington, L.; Datta, D.; De Silva, N.; Deustua, J. E.; Fedorov, D. G.; Gour, J. R.; Gunina, A. O.; Guidez, E.; Harville, T.; Irle, S.; Ivanic, J.; Kowalski, K.; Leang, S. S.; Li, H.; Li, W.; Lutz, J. J.; Magoulas, I.; Mato, J.; Mironov, V.; Nakata, H.; Pham, B. Q.; Piecuch, P.; Poole, D.; Pruitt, S. R.; Rendell, A. P.; Roskop, L. B.; Ruedenberg, K.; Sattasathuchana, T.; Schmidt, M. W.; Shen, J.; Slipchenko, L.; Sosonkina, M.; Sundriyal, V.; Tiwari, A.; Galvez Vallejo, J. L.; Westheimer, B.; Włoch, M.; Xu, P.; Zahariev, F.; Gordon, M. S. Recent Developments in the General Atomic and Molecular Electronic Structure System. *J. Chem. Phys.* **2020**, *152* (15), 154102. https://doi.org/10.1063/5.0005188.

(150) Zhao, Y.; Truhlar, D. G. A New Local Density Functional for Main-Group Thermochemistry, Transition Metal Bonding, Thermochemical Kinetics, and Noncovalent Interactions. *J. Chem. Phys.* **2006**, *125* (19), 194101. https://doi.org/10.1063/1.2370993.

(151) Montgomery, J. A.; Frisch, M. J.; Ochterski, J. W.; Petersson, G. A. A Complete Basis Set Model Chemistry. VI. Use of Density Functional Geometries and Frequencies. *J. Chem. Phys.* **1999**, *110* (6), 2822–2827. https://doi.org/10.1063/1.477924.
(152) Xu, X.; Alecu, I. M.; Truhlar, D. G. How Well Can Modern Density Functionals Predict Internuclear Distances at Transition States? *J. Chem. Theory Comput.* **2011**, *7* (6), 1667–1676. https://doi.org/10.1021/ct2001057.
(153) Schenker, S.; Schneider, C.; Tsogoeva, S. B.; Clark, T. Assessment of Popular DFT and Semiempirical Molecular Orbital Techniques for Calculating Relative Transition State Energies and Kinetic Product Distributions in Enantioselective Organocatalytic Reactions. *J. Chem. Theory Comput.* **2011**, *7* (11), 3586–3595. https://doi.org/10.1021/ct2002013.
(154) Simmie, J. M.; Somers, K. P. Benchmarking Compound Methods (CBS-QB3, CBS-APNO, G3, G4, W1BD) against the Active Thermochemical Tables: A Litmus Test for Cost-Effective Molecular Formation Enthalpies. *J. Phys. Chem. A* **2015**, *119* (28), 7235–7246. https://doi.org/10.1021/jp511403a.
(155) Keller-Rudek, H.; Moortgat, G. K.; Sander, R.; Sörensen, R. The MPI-Mainz UV/VIS Spectral Atlas of Gaseous Molecules of Atmospheric Interest. *Earth Syst. Sci. Data* **2013**, *5*, 365–373. https://doi.org/10.5194/essd-5-365-2013.
(156) Messaadia, L.; El Dib, G.; Ferhati, A.; Chakir, A. UV–Visible Spectra and Gas-Phase Rate Coefficients for the Reaction of 2,3-Pentanedione and 2,4-Pentanedione with OH Radicals. *Chem. Phys. Lett.* **2015**, *626*, 73–79. https://doi.org/10.1016/j.cplett.2015.02.032.
(157) Ting, W.-L.; Chang, C.-H.; Lee, Y.-F.; Matsui, H.; Lee, Y.-P.; Lin, J. J.-M. Detailed Mechanism of the $CH_2I + O_2$ Reaction: Yield and Self-Reaction of the Simplest Criegee Intermediate CH_2OO. *J. Chem. Phys.* **2014**, *141* (10), 104308. https://doi.org/10.1063/1.4894405.
(158) Huang, Y.-H.; Chen, L.-W.; Lee, Y.-P. Simultaneous Infrared Detection of the ICH_2OO Radical and Criegee Intermediate CH_2OO: The Pressure Dependence of the Yield of CH_2OO in the Reaction $CH_2I + O_2$. *J. Phys. Chem. Lett.* **2015**, *6* (22), 4610–4615. https://doi.org/10.1021/acs.jpclett.5b02298.
(159) Foreman, E. S.; Murray, C. Kinetics of IO Production in the $CH_2I + O_2$ Reaction Studied by Cavity Ring-Down Spectroscopy. *J. Phys. Chem. A* **2015**, *119* (34), 8981–8990. https://doi.org/10.1021/acs.jpca.5b05058.
(160) Buras, Z. J.; Elsamra, R. M. I.; Green, W. H. Direct Determination of the Simplest Criegee Intermediate (CH_2OO) Self Reaction Rate. *J. Phys. Chem. Lett.* **2014**, *5* (13), 2224–2228. https://doi.org/10.1021/jz5008406.
(161) Spietz, P.; Gómez Martín, J. C.; Burrows, J. P. Spectroscopic Studies of the I_2/O_3 Photochemistry: Part 2. Improved Spectra of Iodine Oxides and Analysis of the IO Absorption Spectrum. *J. Photochem. Photobio. A* **2005**, *176* (1–3), 50–67. https://doi.org/10.1016/j.jphotochem.2005.08.023.
(162) Anderson, L. N.; Kudchadker, A. P.; Eubank, P. T. Volumetric Properties of Gaseous Acetone. *J. Chem. Eng. Data* **1968**, *13* (3), 321–327. https://doi.org/10.1021/je60038a007.
(163) Hinsberg, W. D.; Houle, F. A. *Kinetiscope - A stochastic kinetics simulator*. https://hinsberg.net/kinetiscope/index.html (accessed 2021-08-12).
(164) Ting, W.-L.; Chang, C.-H.; Lee, Y.-F.; Matsui, H.; Lee, Y.-P.; Lin, J. J.-M. Detailed Mechanism of the $CH_2I + O_2$ Reaction: Yield and Self-Reaction of the Simplest Criegee Intermediate CH_2OO. *J. Chem. Phys.* **2014**, *141* (10), 104308. https://doi.org/10.1063/1.4894405.
(165) Gravestock, T. J.; Blitz, M. A.; Bloss, W. J.; Heard, D. E. A Multidimensional Study of the Reaction CH_2I+O_2: Products and Atmospheric Implications. *ChemPhysChem* **2010**, *11* (18), 3928–3941. https://doi.org/10.1002/cphc.201000575.
(166) Sehested, J.; Ellermann, T.; Nielsen, O. J. A Spectrokinetic Study of CH_2I and CH_2IO_2 Radicals. *Int. J. Chem. Kinet.* **1994**, *26* (2), 259–272. https://doi.org/10.1002/kin.550260204.

(167) Bunnelle, W. H. Preparation, Properties, and Reactions of Carbonyl Oxides. *Chem. Rev.* **1991**, *91* (3), 335–362. https://doi.org/10.1021/cr00003a003.
(168) Sustmann, R. A Simple Model for Substituent Effects in Cycloaddition Reactions. I. 1,3-Dipolar Cycloadditions. *Tetrahedron Lett.* **1971**, *12* (29), 2717–2720. https://doi.org/10.1016/S0040-4039(01)96961-8.
(169) Sustmann, R. A Simple Model for Substituent Effects in Cycloaddition Reactions. II. The Diels-Alder Reaction. *Tetrahedron Lett.* **1971**, *12* (29), 2721–2724. https://doi.org/10.1016/S0040-4039(01)96962-X.
(170) Nakanishi, H.; Morita, H.; Nagakura, S. Charge-Transfer Character in the Intramolecular Hydrogen Bond: Vacuum Ultraviolet Spectra of Acetylacetone and Its Fluoro Derivatives. *Bull. Chem. Soc. Jpn.* **1978**, *51* (6), 1723–1729. https://doi.org/10.1246/bcsj.51.1723.
(171) Antonov, I.; Voronova, K.; Chen, M.-W.; Sztáray, B.; Hemberger, P.; Bodi, A.; Osborn, D. L.; Sheps, L. To Boldly Look Where No One Has Looked Before: Identifying the Primary Photoproducts of Acetylacetone. *J. Phys. Chem. A* **2019**, *123* (26), 5472–5490. https://doi.org/10.1021/acs.jpca.9b04640.
(172) Hammett, L. P. The Effect of Structure upon the Reactions of Organic Compounds. Benzene Derivatives. *J. Am. Chem. Soc.* **1937**, *59* (1), 96–103. https://doi.org/10.1021/ja01280a022.
(173) Hansch, Corwin.; Leo, A.; Taft, R. W. A Survey of Hammett Substituent Constants and Resonance and Field Parameters. *Chem. Rev.* **1991**, *91* (2), 165–195. https://doi.org/10.1021/cr00002a004.
(174) Khan, M. A. H.; Cooke, M. C.; Utembe, S. R.; Archibald, A. T.; Maxwell, P.; Morris, W. C.; Xiao, P.; Derwent, R. G.; Jenkin, M. E.; Percival, C. J.; Walsh, R. C.; Young, T. D. S.; Simmonds, P. G.; Nickless, G.; O'Doherty, S.; Shallcross, D. E. A Study of Global Atmospheric Budget and Distribution of Acetone Using Global Atmospheric Model STOCHEM-CRI. *Atmos. Environ.* **2015**, *112*, 269–277. https://doi.org/10.1016/j.atmosenv.2015.04.056.
(175) Klotz, B.; Graedler, F.; Sørensen, S.; Barnes, I.; Becker, K.-H. A Kinetic Study of the Atmospheric Photolysis of α-Dicarbonyls. *Int. J. Chem. Kinet.* **2001**, *33* (1), 9–20. https://doi.org/10.1002/1097-4601(20010101)33:1<9::AID-KIN2>3.0.CO;2-V.
(176) Volkamer, R.; Molina, L. T.; Molina, M. J.; Shirley, T.; Brune, W. H. DOAS Measurement of Glyoxal as an Indicator for Fast VOC Chemistry in Urban Air. *Geophys. Res. Lett.* **2005**, *32* (8). https://doi.org/10.1029/2005GL022616.
(177) Zhou, S.; Barnes, I.; Zhu, T.; Bejan, I.; Albu, M.; Benter, T. Atmospheric Chemistry of Acetylacetone. *Environ. Sci. Technol.* **2008**, *42* (21), 7905–7910. https://doi.org/10.1021/es8010282.
(178) Ji, Y.; Zheng, J.; Qin, D.; Li, Y.; Gao, Y.; Yao, M.; Chen, X.; Li, G.; An, T.; Zhang, R. OH-Initiated Oxidation of Acetylacetone: Implications for Ozone and Secondary Organic Aerosol Formation. *Environ. Sci. Technol.* **2018**, *52* (19), 11169–11177. https://doi.org/10.1021/acs.est.8b03972.
(179) Holloway, A.-L.; Treacy, J.; Sidebottom, H.; Mellouki, A.; Daële, V.; Bras, G. L.; Barnes, I. Rate Coefficients for the Reactions of OH Radicals with the Keto/Enol Tautomers of 2,4-Pentanedione and 3-Methyl-2,4-Pentanedione, Allyl Alcohol and Methyl Vinyl Ketone Using the Enols and Methyl Nitrite as Photolytic Sources of OH. *J. Photochem. Photobio. A* **2005**, *176* (1–3), 183–190. https://doi.org/10.1016/j.jphotochem.2005.08.031.
(180) Dagaut, P.; Wallington, T. J.; Liu, R.; Kurylo, M. J. A Kinetic Investigation of the Gas-Phase Reactions of Hydroxyl Radicals with Cyclic Ketones and Diones: Mechanistic Insights. *J. Phys. Chem.* **1988**, *92* (15), 4375–4377. https://doi.org/10.1021/j100326a026.
(181) Tadić, J.; Moortgat, G. K.; Wirtz, K. Photolysis of Glyoxal in Air. *J. Photochem. Photobio. A* **2006**, *177* (2), 116–124. https://doi.org/10.1016/j.jphotochem.2005.10.010.
(182) Lee, K. L. K.; Nauta, K.; Kable, S. H. Photodissociation of Acetone from 266 to 312 Nm: Dynamics of CH_3 + CH_3CO Channels on the S_0 and T_1 States. *J. Chem. Phys.* **2017**, *146* (4), 044304. https://doi.org/10.1063/1.4974035.

(183) Jenkin, M. E.; Clemitshaw, K. C. Ozone and Other Secondary Photochemical Pollutants: Chemical Processes Governing Their Formation in the Planetary Boundary Layer. *Atmos. Environ.* **2000**, *34* (16), 2499–2527. https://doi.org/10.1016/S1352-2310(99)00478-1.
(184) Lary, D. J.; Shallcross, D. E. Central Role of Carbonyl Compounds in Atmospheric Chemistry. *J. Geophys. Res.* **2000**, *105* (D15), 19771–19778. https://doi.org/10.1029/1999JD901184.
(185) Wang, P.-B.; Truhlar, D. G.; Xia, Y.; Long, B. Temperature-Dependent Kinetics of the Atmospheric Reaction between CH_2OO and Acetone. *Phys. Chem. Chem. Phys.* **2022**, *24* (21), 13066–13073. https://doi.org/10.1039/D2CP01118B.
(186) Zhou, X.; Chen, Y.; Liu, Y.; Li, X.; Dong, W.; Yang, X. Kinetics of CH_2OO and Syn-CH_3CHOO Reaction with Acrolein. *Phys. Chem. Chem. Phys.* **2021**, *23* (23), 13276–13283. https://doi.org/10.1039/D1CP00492A.
(187) Roehl, C. M.; Burkholder, J. B.; Moortgat, G. K.; Ravishankara, A. R.; Crutzen, P. J. Temperature Dependence of UV Absorption Cross Sections and Atmospheric Implications of Several Alkyl Iodides. *J. Geophys. Res.* **1997**, *102* (D11), 12819–12829. https://doi.org/10.1029/97JD00530.
(188) Mössinger, J. C.; Shallcross, D. E.; Cox, R. A. UV-VIS Absorption Cross-Sections and Atmospheric Lifetimes of CH_2Br_2, CH_2I_2 and CH_2BrI. *J. Chem. Soc., Faraday Trans.* **1998**, *94* (10), 1391–1396. https://doi.org/10.1039/A709160E.
(189) Belova, N. V.; Oberhammer, H.; Trang, N. H.; Girichev, G. V. Tautomeric Properties and Gas-Phase Structure of Acetylacetone. *J. Org. Chem.* **2014**, *79* (12), 5412–5419. https://doi.org/10.1021/jo402814c.
(190) McGillen, M. R.; Archibald, A. T.; Carey, T.; Leather, K. E.; Shallcross, D. E.; Wenger, J. C.; Percival, C. J. Structure–Activity Relationship (SAR) for the Prediction of Gas-Phase Ozonolysis Rate Coefficients: An Extension towards Heteroatomic Unsaturated Species. *Phys. Chem. Chem. Phys.* **2011**, *13* (7), 2842–2849. https://doi.org/10.1039/C0CP01732A.
(191) King, M. D.; Canosa-Mas, C. E.; Wayne, R. P. Frontier Molecular Orbital Correlations for Predicting Rate Constants between Alkenes and the Tropospheric Oxidants NO_3, OH and O_3. *Phys. Chem. Chem. Phys.* **1999**, *1* (9), 2231–2238. https://doi.org/10.1039/A901192G.
(192) Pfrang, C.; King, M. D.; Canosa-Mas, C. E.; Wayne, R. P. Correlations for Gas-Phase Reactions of NO_3, OH and O_3 with Alkenes: An Update. *Atmos. Environ.* **2006**, *40* (6), 1170–1179. https://doi.org/10.1016/j.atmosenv.2005.10.019.
(193) Pfrang, C.; King, M. D.; Canosa-Mas, C. E.; Wayne, R. P. Structure–Activity Relations (SARs) for Gas-Phase Reactions of NO_3, OH and O_3 with Alkenes: An Update. *Atmos. Environ.* **2006**, *40* (6), 1180–1186. https://doi.org/10.1016/j.atmosenv.2005.09.080.
(194) McGillen, M. R.; Carey, T. J.; Archibald, A. T.; Wenger, J. C.; Shallcross, D. E.; Percival, C. J. Structure–Activity Relationship (SAR) for the Gas-Phase Ozonolysis of Aliphatic Alkenes and Dialkenes. *Phys. Chem. Chem. Phys.* **2008**, *10* (13), 1757–1768. https://doi.org/10.1039/B715394E.
(195) Jenkin, M. E.; Valorso, R.; Aumont, B.; Newland, M. J.; Rickard, A. R. Estimation of Rate Coefficients for the Reactions of O_3 with Unsaturated Organic Compounds for Use in Automated Mechanism Construction. *Atmos. Chem. Phys.* **2020**, *20* (21), 12921–12937. https://doi.org/10.5194/acp-20-12921-2020.
(196) Stephenson, T. A.; Lester, M. I. Unimolecular Decay Dynamics of Criegee Intermediates: Energy-Resolved Rates, Thermal Rates, and Their Atmospheric Impact. *Int. Rev. Phys. Chem.* **2020**, *39* (1), 1–33. https://doi.org/10.1080/0144235X.2020.1688530.
(197) Peltola, J.; Seal, P.; Inkilä, A.; Eskola, A. Time-Resolved, Broadband UV-Absorption Spectrometry Measurements of Criegee Intermediate Kinetics Using a New Photolytic Precursor: Unimolecular Decomposition of CH_2OO and Its Reaction with Formic Acid. *Phys. Chem. Chem. Phys.* **2020**, *22* (21), 11797–11808. https://doi.org/10.1039/D0CP00302F.

(198) Houk, K. N.; Sims, Joyner.; Duke, R. E.; Strozier, R. W.; George, J. K. Frontier Molecular Orbitals of 1,3 Dipoles and Dipolarophiles. *J. Am. Chem. Soc.* **1973**, *95* (22), 7287–7301. https://doi.org/10.1021/ja00803a017.
(199) Liu, S.; Chen, Y.; Jiang, H.; Shi, J.; Ding, H.; Yang, X.; Dong, W. Kinetics for the Reaction of Criegee Intermediate CH_2OO with n-Butyraldehyde and Its Atmospheric Implications. *Atmos. Environ.* **2023**, *311*, 120012. https://doi.org/10.1016/j.atmosenv.2023.120012.
(200) Luo, P.-L.; Chen, I.-Y.; Khan, M. A. H.; Shallcross, D. E. Direct Gas-Phase Formation of Formic Acid through Reaction of Criegee Intermediates with Formaldehyde. *Commun. Chem.* **2023**, *6* (1), 1–10. https://doi.org/10.1038/s42004-023-00933-2.
(201) Kawamura, K.; Okuzawa, K.; Aggarwal, S. G.; Irie, H.; Kanaya, Y.; Wang, Z. Determination of Gaseous and Particulate Carbonyls (Glycolaldehyde, Hydroxyacetone, Glyoxal, Methylglyoxal, Nonanal and Decanal) in the Atmosphere at Mt. Tai. *Atmos. Chem. Phys.* **2013**, *13* (10), 5369–5380. https://doi.org/10.5194/acp-13-5369-2013.
(202) Clair, J. M. St.; Spencer, K. M.; Beaver, M. R.; Crounse, J. D.; Paulot, F.; Wennberg, P. O. Quantification of Hydroxyacetone and Glycolaldehyde Using Chemical Ionization Mass Spectrometry. *Atmos. Chem. Phys.* **2014**, *14* (8), 4251–4262. https://doi.org/10.5194/acp-14-4251-2014.
(203) Grosjean, D.; Williams, E. L.; Grosjean, E. Atmospheric Chemistry of Isoprene and of Its Carbonyl Products. *Environ. Sci. Technol.* **1993**, *27* (5), 830–840. https://doi.org/10.1021/es00042a004.
(204) Mellouki, A.; Wallington, T. J.; Chen, J. Atmospheric Chemistry of Oxygenated Volatile Organic Compounds: Impacts on Air Quality and Climate. *Chem. Rev.* **2015**, *115* (10), 3984–4014. https://doi.org/10.1021/cr500549n.
(205) Xing, Y.; Li, H.; Huang, L.; Wu, H.; Shen, H.; Chen, Z. The Production of Formaldehyde and Hydroxyacetone in Methacrolein Photooxidation: New Insights into Mechanism and Effects of Water Vapor. *J. Environ. Sci.* **2018**, *66*, 1–11. https://doi.org/10.1016/j.jes.2017.05.037.
(206) Johnson, T. J.; Profeta, L. T. M.; Sams, R. L.; Griffith, D. W. T.; Yokelson, R. L. An Infrared Spectral Database for Detection of Gases Emitted by Biomass Burning. *Vib. Spectrosc.* **2010**, *53* (1), 97–102. https://doi.org/10.1016/j.vibspec.2010.02.010.
(207) Weise, D. R.; Johnson, T. J.; Reardon, J. Particulate and Trace Gas Emissions from Prescribed Burns in Southeastern U.S. Fuel Types: Summary of a 5-Year Project. *Fire Saf. J.* **2015**, *74*, 71–81. https://doi.org/10.1016/j.firesaf.2015.02.016.
(208) Dagaut, P.; Liu, R.; Wallington, T. J.; Kurylo, M. J. Kinetic Measurements of the Gas-Phase Reactions of Hydroxyl Radicals with Hydroxy Ethers, Hydroxy Ketones, and Keto Ethers. *J. Phys. Chem.* **1989**, *93* (23), 7838–7840. https://doi.org/10.1021/j100360a022.
(209) Orlando, J. J.; Tyndall, G. S.; Fracheboud, J.-M.; Estupiñan, E. G.; Haberkorn, S.; Zimmer, A. The Rate and Mechanism of the Gas-Phase Oxidation of Hydroxyacetone. *Atmos. Environ.* **1999**, *33* (10), 1621–1629. https://doi.org/10.1016/S1352-2310(98)00386-0.
(210) Aschmann, S. M.; Arey, J.; Atkinson, R. Atmospheric Chemistry of Selected Hydroxycarbonyls. *J. Phys. Chem. A* **2000**, *104* (17), 3998–4003. https://doi.org/10.1021/jp9939874.
(211) Chowdhury, P. K.; Upadhyaya, H. P.; Naik, P. D.; Mittal, J. P. ArF Laser Photodissociation Dynamics of Hydroxyacetone: LIF Observation of OH and Its Reaction Rate with the Parent. *Chem. Phys. Lett.* **2002**, *351* (3), 201–207. https://doi.org/10.1016/S0009-2614(01)01377-X.
(212) Butkovskaya, N. I.; Pouvesle, N.; Kukui, A.; Mu, Y.; Le Bras, G. Mechanism of the OH-Initiated Oxidation of Hydroxyacetone over the Temperature Range 236–298 K. *J. Phys. Chem. A* **2006**, *110* (21), 6833–6843. https://doi.org/10.1021/jp056345r.
(213) Dillon, T. J.; Horowitz, A.; Hölscher, D.; Crowley, J. N.; Vereecken, L.; Peeters, J. Reaction of HO with Hydroxyacetone ($HOCH_2C(O)CH_3$): Rate Coefficients (233–363 K) and Mechanism. *Phys. Chem. Chem. Phys.* **2006**, *8* (2), 236–246. https://doi.org/10.1039/B513056E.

(214) Baasandorj, M.; Griffith, S.; Dusanter, S.; Stevens, P. S. Experimental and Theoretical Studies of the Kinetics of the OH + Hydroxyacetone Reaction As a Function of Temperature. *J. Phys. Chem. A* **2009**, *113* (39), 10495–10502. https://doi.org/10.1021/jp904238w.
(215) Bedjanian, Y. Temperature-Dependent Kinetic Study of the Reaction of Hydroxyl Radicals with Hydroxyacetone. *J. Phys. Chem. A* **2020**, *124* (14), 2863–2870. https://doi.org/10.1021/acs.jpca.0c00429.
(216) Vu, N. D.; Khamaganov, V.; Nguyen, V. S.; Carl, S. A.; Peeters, J. Absolute Rate Coefficient of the Gas-Phase Reaction between Hydroxyl Radical (OH) and Hydroxyacetone: Investigating the Effects of Temperature and Pressure. *J. Phys. Chem. A* **2013**, *117* (47), 12208–12215. https://doi.org/10.1021/jp407701z.
(217) *IUPAC – Task Group on Atmospheric Chemical Kinetic Data Evaluation*. https://iupac.aeris-data.fr/ (accessed 2023-06-23).
(218) Baker, J.; Arey, J.; Atkinson, R. Rate Constants for the Gas-Phase Reactions of OH Radicals with a Series of Hydroxyaldehydes at 296 ± 2 K. *J. Phys. Chem. A* **2004**, *108* (34), 7032–7037. https://doi.org/10.1021/jp048979o.
(219) El Dib, G.; Sleiman, C.; Canosa, A.; Travers, D.; Courbe, J.; Sawaya, T.; Mokbel, I.; Chakir, A. First Experimental Determination of the Absolute Gas-Phase Rate Coefficient for the Reaction of OH with 4-Hydroxy-2-Butanone (4H2B) at 294 K by Vapor Pressure Measurements of 4H2B. *J. Phys. Chem. A* **2013**, *117* (1), 117–125. https://doi.org/10.1021/jp3074909.
(220) Messaadia, L.; El Dib, G.; Lendar, M.; Cazaunau, M.; Roth, E.; Ferhati, A.; Mellouki, A.; Chakir, A. Gas-Phase Rate Coefficients for the Reaction of 3-Hydroxy-2-Butanone and 4-Hydroxy-2-Butanone with OH and Cl. *Atmos. Environ.* **2013**, *77*, 951–958. https://doi.org/10.1016/j.atmosenv.2013.06.028.
(221) Bouzidi, H.; Aslan, L.; El Dib, G.; Coddeville, P.; Fittschen, C.; Tomas, A. Investigation of the Gas-Phase Photolysis and Temperature-Dependent OH Reaction Kinetics of 4-Hydroxy-2-Butanone. *Environ. Sci. Technol.* **2015**, *49* (20), 12178–12186. https://doi.org/10.1021/acs.est.5b02721.
(222) Cheramangalath Balan, R.; Rajakumar, B. Photo-Oxidation Reaction Kinetics and Mechanistics of 4-Hydroxy-2-Butanone with Cl Atoms and OH Radicals in the Gas Phase. *J. Phys. Chem. A* **2019**, *123* (20), 4342–4353. https://doi.org/10.1021/acs.jpca.9b00995.
(223) Petitjean, M.; Reyès-Pérez, E.; Pérez, D.; Mirabel, Ph.; Le Calvé, S. Vapor Pressure Measurements of Hydroxyacetaldehyde and Hydroxyacetone in the Temperature Range (273 to 356) K. *J. Chem. Eng. Data* **2010**, *55* (2), 852–855. https://doi.org/10.1021/je9004905.
(224) Lindenmaier, R.; Tipton, N.; Sams, R. L.; Brauer, C. S.; Blake, T. A.; Williams, S. D.; Johnson, T. J. Assignment of the Fundamental Modes of Hydroxyacetone Using Gas-Phase Infrared, Far-Infrared, Raman, and *Ab Initio* Methods: Band Strengths for Atmospheric Measurements. *J. Phys. Chem. A* **2016**, *120* (30), 5993–6003. https://doi.org/10.1021/acs.jpca.6b05045.
(225) Zhan, C.-G.; Nichols, J. A.; Dixon, D. A. Ionization Potential, Electron Affinity, Electronegativity, Hardness, and Electron Excitation Energy: Molecular Properties from Density Functional Theory Orbital Energies. *J. Phys. Chem. A* **2003**, *107* (20), 4184–4195. https://doi.org/10.1021/jp0225774.
(226) Messaadia, L.; El Dib, G.; Ferhati, A.; Roth, E.; Chakir, A. Gas Phase UV Absorption Cross-Sections for a Series of Hydroxycarbonyls. *Chem. Phys. Lett.* **2012**, *529*, 16–22. https://doi.org/10.1016/j.cplett.2012.01.044.
(227) Laidler, K. J. *Chemical Kinetics*, 3rd ed.; Harper & Row: New York, 1987.
(228) Debnath, A.; Rajakumar, B. Investigation of Kinetics and Mechanistic Insights of the Reaction of Criegee Intermediate (CH_2OO) with Methyl-Ethyl Ketone (MEK) under Tropospherically Relevant Conditions. *Chemosphere* **2023**, *312*, 137217. https://doi.org/10.1016/j.chemosphere.2022.137217.

(229) Kuo, M.-T.; Yang, J.-N.; Lin, J. J.-M.; Takahashi, K. Substituent Effect in the Reactions between Criegee Intermediates and 3-Aminopropanol. *J. Phys. Chem. A* **2021**, *125* (30), 6580–6590. https://doi.org/10.1021/acs.jpca.1c03737.
(230) Enders, J. J.; Cornwell, Z. A.; Harrison, A. W.; Murray, C. Termperature-Dependent Kinetics of the Reactions of the Criegee Intermediate CH_2OO with Aliphatic Aldehydes. *pending manuscript* **2024**.
(231) Dunning Jr., T. H. Gaussian Basis Sets for Use in Correlated Molecular Calculations. I. The Atoms Boron through Neon and Hydrogen. *J. Chem. Phys.* **1989**, *90* (2), 1007–1023. https://doi.org/10.1063/1.456153.
(232) Sheps, L.; Scully, A. M.; Au, K. UV Absorption Probing of the Conformer-Dependent Reactivity of a Criegee Intermediate CH_3CHOO. *Phys. Chem. Chem. Phys.* **2014**, *16* (48), 26701–26706. https://doi.org/10.1039/C4CP04408H.
(233) Taatjes, C. A.; Welz, O.; Eskola, A. J.; Savee, J. D.; Scheer, A. M.; Shallcross, D. E.; Rotavera, B.; Lee, E. P. F.; Dyke, J. M.; Mok, D. K. W.; Osborn, D. L.; Percival, C. J. Direct Measurements of Conformer-Dependent Reactivity of the Criegee Intermediate CH_3CHOO. *Science* **2013**, *340* (6129), 177–180. https://doi.org/10.1126/science.1234689.
(234) Smith, M. C.; Ting, W.-L.; Chang, C.-H.; Takahashi, K.; Boering, K. A.; Lin, J. J.-M. UV Absorption Spectrum of the C2 Criegee Intermediate CH_3CHOO. *J. Chem. Phys.* **2014**, *141* (7), 074302. https://doi.org/10.1063/1.4892582.